UNIVERSIDAD POLITÉCNICA DE MADRID
Escuela Técnica Superior de Ingeniería Aeronáutica y del Espacio

DESIGN, NUMERICAL SIMULATION, AND EXPERIMENTAL VALIDATION OF THE AIR COOLING SYSTEM OF A FUTURE PARTICLE DETECTOR OF THE ALICE EXPERIMENT

DOCTORAL THESIS

Submitted for the degree of Doctor by:

AITOR AMATRIAIN CARBALLO
MASTER IN ADVANCED MATHEMATICS

Madrid, 2024

UNIVERSIDAD POLITÉCNICA DE MADRID
Escuela Técnica Superior de Ingeniería Aeronáutica y del Espacio

Doctoral Degree in Aerospace Engineering

DESIGN, NUMERICAL SIMULATION, AND EXPERIMENTAL VALIDATION OF THE AIR COOLING SYSTEM OF A FUTURE PARTICLE DETECTOR OF THE ALICE EXPERIMENT

DOCTORAL THESIS

Submitted for the degree of Doctor by:

AITOR AMATRIAIN CARBALLO
MASTER IN ADVANCED MATHEMATICS

Under the supervision of:
Dr. GONZALO RUBIO CALZADO

Madrid, 2024

Title: Design, numerical simulation, and experimental validation of the air cooling system of a future particle detector of the ALICE experiment
Author: Aitor Amatriain Carballo
Doctoral Programme: Aerospace Engineering

Thesis Supervision: Dr. Gonzalo Rubio Calzado

External Reviewers:

Thesis Defense Committee:

Thesis Defense Date:

Abstract

In this thesis, research and development work for the air cooling system of the Inner Barrel of the Inner Tracking System 3 (ITS3 IB) is carried out. The ITS3 IB will be a future particle detector of the ALICE experiment at the Large Hadron Collider (LHC). Efficient cooling is crucial for maximizing the particle measurement quality. The cooling system introduces open-cell carbon foams as heat exchangers that combine conduction and convection for the first time in a high-level engineering application. The ITS3 IB will have an unprecedentedly low material budget, which is a requirement for particle detectors that aim at precise tracking at low particle momenta.

In the first chapter, the characterization of open-cell foams is performed. A multiscale model is developed that is applicable to a wide range of parameters. The microscopic geometry is based on a periodic model of the foam unit cell. The geometrical scales given by the model are validated with microscope images and computed tomography scans. The outputs of the microscopic model are the pressure loss, the thermal conductivity, and the Nusselt number. These values are used as inputs of the macroscopic model that determines the thermal performance at large scales. The multiscale model is concluded to provide accurate results with respect to the experimental data.

The results obtained in the previous study are used to select appropriate foams for the ITS3 IB and to design the cooling system in the second chapter. A prototype of the ITS3 IB is built and installed in a wind tunnel to determine the thermal performance. The analysis also uses numerical simulations. The numerical results show excellent agreement with the experiments, with mean deviations of less than 0.5 K in the temperature distribution attributed to uncertainties in the sensor installation. The results confirm the system adherence to the temperature requirements. Compared to the baseline design, it is shown that enhancements based on simulations can reduce up to half the maximum temperature variation of the detector layers.

The airflow applied to the low-mass structure of the ITS3 IB generates vibrations. This requires an aeroelastic analysis, which is done in the third chapter. A novel experimental approach is proposed using confocal sensors to measure the structural displacements of the prototype used for thermal analysis. A mathematical model for the fluid-structure interaction is developed. The results obtained in the experimental setup show that the mathematical model predicts the primary peaks of the spectrum of the structural displacements induced by the air flow. The validated model is used to analyze the real anticipated configuration of the future ITS3 IB, as well as possible adjustments arising from changes in detector cooling and installation requirements.

In the industrial context of computational fluid dynamics, Wall-Modeled Large Eddy Simulations (WMLES) and hybrid Reynolds-Averaged Navier Stokes (RANS)/LES models suffer from multiple shortcomings. The present thesis tackles this problem, and a Generalized WMLES (GWMLES) model is presented in the fourth chapter that enables the modeling of the entire log-layer. GWMLES is validated against models of different fidelities and experimental data. The model developed gives a level of accuracy similar to recent LES results with a much lower computational cost. It is demonstrated that it is more accurate than URANS even when the resolved portion of the energy spectrum is reduced, and that it requires up to half the computational cost compared to the Detached Eddy Simulation (DES) model.

Resumen

En esta tesis se realizan trabajos de investigación y desarrollo para el sistema de enfriamiento por aire del Inner Barrel del ALICE Inner Tracking System 3 (ITS3 IB), el cual será un futuro detector de partículas del experimento ALICE en el Gran Colisionador de Hadrones. El enfriamiento eficiente es crucial para maximizar la precisión de las mediciones de partículas. El sistema de enfriamiento introduce espumas de celdas abiertas como intercambiadores de calor que combinan conducción y convección por primera vez en una aplicación ingenieril de alto nivel. El ITS3 IB poseerá un valor bajo sin precedentes del presupuesto de material, el cual es un requerimiento para detectores de partículas que buscan un seguimiento preciso a valores bajos de momentos de partículas.

En el primer capítulo caracterizan las espumas de celdas abiertas. Se desarrolla un modelo multiescala que es aplicable a un rango amplio de parámetros. La geometría microscópica se basa en un modelo periódico de la celda unidad de la espuma. Las escalas geométricas que se obtienen en el modelo se validan con imágenes de microscopio y de tomografía axial computerizada. Los parámetros de salida del modelo microscópico son la pérdida de presión, la conductividad térmica, y el número de Nusselt. Estos valores se emplean como parámetros de entrada del modelo macroscópico que determina el rendimiento térmico en grandes escalas. Se concluye que el modelo multiescala aporta resultados precisos en comparación con datos experimentales.

Los resultados obtenidos en el estudio previo se emplean para seleccionar espumas apropiadas para el ITS3 IB y para diseñar el sistema de enfriamiento en el segundo capítulo. Se construye un prototipo del ITS3 IB y se instala en un túnel de viento para determinar el rendimiento térmico. En el análisis también se realizan simulaciones numéricas. Los resultados numéricos concuerdan de manera excelente con los experimentos, con desviaciones medias menores que 0.5 K en la distribución de temperatura que son atribuidas a incertidumbres en la instalación de los sensores. Los resultados confirman que el sistema cumple los requerimientos térmicos. En comparación con el diseño de referencia, se muestra que mejoras basadas en simulaciones pueden reducir hasta la mitad la máxima variación de temperatura de las capas del detector.

El flujo de aire aplicado a la estructura de baja masa del ITS3 IB causa vibraciones, lo cual requiere un análisis aeroelástico que se realiza en el tercer capítulo. Se propone un nuevo enfoque experimental haciendo uso de sensores confocales para medir los desplazamientos estructurales del prototipo empleado en el análisis térmico. Se desarrolla un modelo matemático para la interacción fluido-estructura. Se muestra que el modelo matemático predice los picos primarios del espectro de desplazamientos estructurales inducidos por el flujo de aire en el experimento. El modelo validado se emplea para analizar la configuración anticipada del futuro ITS3 IB, además de posibles ajustes procedentes de modificaciones en los requerimientos de enfriamiento e instalación del detector.

En el contexto industrial de la mecánica de fluidos computacional, los modelos Wall-Modeled Large Eddy Simulations (WMLES) e híbridos Reynolds-Averaged Navier Stokes (RANS)/LES sufren múltiples desventajas. La presente tesis aborda este problema, y se presenta un modelo WMLES generalizado (GWMLES) en el cuarto capítulo que permite la modelización de la capa logarítmica entera. GWMLES se valida con modelos de diferentes fidelidades y datos experimentales. El modelo desarrollado aporta un nivel de precisión similar al de resultados LES recientes con un coste computacional mucho menor. Se demuestra que es más preciso que URANS incluso cuando la parte resuelta del espectro de energía es reducida, y que además requiere hasta la mitad de coste computacional que el modelo Detached Eddy Simulation (DES).

Acknowledgements

First of all, I would like to thank my thesis director, Gonzalo Rubio. Gonzalo has guided me throughout a large part of my student period, starting as co-director of my bachelor's thesis, following as co-director of my master's thesis, and now as director of my doctoral thesis. We have also worked together on other projects, and my experience with him has been excellent. Gonzalo has always been approachable and emphatic, and his technical knowledge, together with his industrial and academic background, have been very useful to me. I have learned a lot from him.

My words of gratitude continue with the person who gave me the opportunity to start this adventure: my CERN supervisor Corrado Gargiulo. Corrado has also been approachable and emphatic, and at CERN I have felt like at home since the first day. I appreciate the trust that he has placed in me during this period, with a dynamic way of working. I have had no constraints related to putting ideas into practice, which is something I find highly positive for a doctoral student. I feel privileged to have worked with him and to have learnt from his wisdom.

One of the slogans of CERN is that being a member means working in a place like nowhere else on earth. I totally agree. I very much value CERN for the employee benefits provided, in particular the outstanding simulation and experimental resources, as well as courses, travels to conferences, and visit periods to the university. The international environment of both Prévessin and Meyrin sites of CERN has been a plus. This package offered by the organization for doctoral students is unique in the world, and I am grateful to have been able to take advantage of it.

Experiments are an important part of this thesis. Making the design and construction of prototypes a reality has been achieved thanks to the other members of the work package of mechanics and cooling of the ALICE Inner Tracking System 3. I would like to remark the figure of Massimo, who has helped me since the beginning when my experimental skills were basic. His expertise has been a key for success during this period in experimental testing and for generating new ideas.

Working at an international organization, and specifically on a particle detector that is integrated in a large and complex structure, is not easy in the beginning. There are many components, and the majority of them are not industry standards. However, I think I have not had a difficult adaptation; specifically, thanks to Elisa. Her support has been important for understanding many technical details and ways of working at CERN. I would also like to thank the designer of the working group, Gael, as well as the technicians Pieter, Greg, Fabio, Philippe, Vadim, Lee, and Shawaiz, for their collaboration during these years. Not only in terms of project goals, but also for contributing to the generation of a fantastic work environment.

The colleagues outside my working group at Buldings 25 and 166 of the Meyrin site are another source of good memories. Lunch breaks at Restaurant 1 at CERN have been every day a synonym of having a good time with my italian colleagues Francesco, Luca, and Lorenzo. It has been a pleasure to discuss many topics with them, and to learn about italian traditions. I appreciate the help of Andrés and Sole regarding many questions that I had before my move to the Geneva area, as well for the nice conversations during this time. The moments of sharing opinions with other colleagues, namely Youmin, Fernando, Mikko, Pascal, and Spyros, have also meant a lot to me.

My passion on multiphysics problems, and in particular on fluid mechanics, thermodynamics, and heat transfer, is in part thanks to my former Bachelor's and Master's theses director, Ignacio Parra. I consider that the training acquired at the School of Aeronautics of Universidad Politécnica de Madrid on these topics is remarkable; nevertheless, when I was a recent undergraduate, I was missing some links of ideas to understand the physics of engineering problems. I consider that Ignacio has been crucial for bridging that gap, and this has been a key of my progress.

All academic and professional achievements would not have been possible without the continuous support received from my friends and family, especially from my parents. Thank you for always being there.

Contents

Page

Abstract . . . iii

Acknowledgements . . . vii

Chapter 1. Introduction . . . 1
- §1. Motivation . . . 1
  - §1.1. Large Hadron Collider . . . 1
  - §1.2. Particle detectors and material budget . . . 3
  - §1.3. ALICE Inner Tracking System (ITS) . . . 5
- §2. Research background . . . 8
  - §2.1. Cooling systems of particle detectors . . . 8
  - §2.2. Open-cell foams . . . 10
  - §2.3. Numerical simulation of turbulent flows . . . 11
  - §2.4. Vibrations of structures . . . 14
- §3. Objectives and methodology . . . 15
- §4. Publications . . . 16

Chapter 2. Characterization of open-cell foams . . . 17
- §1. Methodology . . . 17
  - §1.1. Foam overview . . . 17
  - §1.2. Experimental setup . . . 19
  - §1.3. Multiscale model . . . 20
- §2. Results and discussion . . . 27
  - §2.1. Microscopic model . . . 27
  - §2.2. Macroscopic model . . . 31

Chapter 3. Thermal analysis . . . 35
- §1. Methodology . . . 35
  - §1.1. ALICE ITS3 IB cooling system . . . 35
  - §1.2. Experimental setup . . . 38
  - §1.3. Mathematical model . . . 41
- §2. Results and discussion . . . 42
  - §2.1. Model validation . . . 43
  - §2.2. Real configuration . . . 46

Chapter 4. Aeroelastic analysis . . . 49
- §1. Methodology . . . 49
  - §1.1. Experimental setup . . . 49
  - §1.2. Mathematical model . . . 51
- §2. Results and discussion . . . 56
  - §2.1. Model validation . . . 57
  - §2.2. Real configuration . . . 60

Chapter 5. Turbulence model for industrial applications . . . 65
- §1. Model description . . . 65

§1.1. Equations . . . 65
§1.2. Numerical implementation . . . 68
§2. Results and discussion . . . 71
§2.1. Subsonic round jet . . . 72
§2.2. Periodic channel . . . 75
§2.3. Ahmed body . . . 80
§2.4. Circular cylinder . . . 86

Chapter 6. Conclusions . . . 93

Appendix A. Turbulence models . . . 97
§1. Turbulence scales . . . 97
§1.1. Kolmogorov's hypotheses . . . 97
§2. Large Eddy Simulation . . . 99
§2.1. Implicit and explicit filtering . . . 100
§2.2. Residual stress tensor models . . . 101
§2.3. Wall-modeled LES . . . 102
§3. Reynolds-Averaged Navier Stokes . . . 102
§3.1. Spalart-Allmaras model . . . 103
§3.2. Two-equation models . . . 103
§3.3. Reynolds stress models . . . 107
§4. Detached Eddy Simulation . . . 108

Appendix B. Finite volume method . . . 111
§1. Discretization . . . 111
§1.1. Spatial discretization . . . 111
§1.2. Temporal discretization . . . 116
§1.3. Non-linear terms . . . 117
§1.4. Rhie-Chow interpolation . . . 117
§2. Pressure-velocity coupling . . . 119
§2.1. Segregated algorithms . . . 119
§2.2. Coupled algorithms . . . 121
§2.3. Extensions to compressible flow . . . 121
§3. Resolution of systems of linear algebraic equations . . . 121
§3.1. Iterative methods . . . 122
§3.2. Multigrid methods . . . 122
§3.3. Under-relaxation . . . 123
§3.4. Residuals . . . 124

Bibliography . . . 125

Chapter 1

Introduction

§1. Motivation

§1.1. Large Hadron Collider

The CERN accelerator complex is a succession of machines with increasingly higher energies (see Fig. 1.1). Each machine injects a beam into the next, and the beam energy increases as the particles are accelerated. The Large Hadron Collider (LHC) is the last element of this chain, where the particle beam energy can achieve values up to 13.6 TeV (achieved in 2022). Particle collisions are usually proton-proton (pp), proton-lead ion (pPb), and lead ion-lead ion (PbPb).

The starting point for proton collisions are hydrogen ions (H^-) that are accelerated in the Linear Accelerator 4 (LINAC 4, see Fig. 1.1), and then two electrons are removed using a strong magnetic field (Evans, 2009). The protons obtained from this process are injected into the Proton Syncroton Booster (PSB), and the beam is fed to the Proton Syncroton (PS) (CERN, 2021). Then, their energy is increased in the Super Proton Synchroton (SPS), and, finally, they are transferred to the LHC (see Fig. 1.1). The lead nuclei are produced from a purified lead sample heated to a temperature of about 500°C, and the lead vapor is ionized by an electron current. Many different charge states are produced with a maximum around Pb^{29+}. These nuclei are selected and accelerated in the LINAC 3 before passing through a carbon foil, which strips most of them to Pb^{54+}. The Pb^{54+} beam is accumulated, and then accelerated in the Low Energy Ion Ring (LEIR), which transfers it to the PS. The PS, which provides an additional energy source, sends the beam to the SPS, after passing it through a second foil where it is fully stripped to Pb^{82+}. Similarly to the case of the protons, the SPS accelerates the beam, and sends it to the LHC.

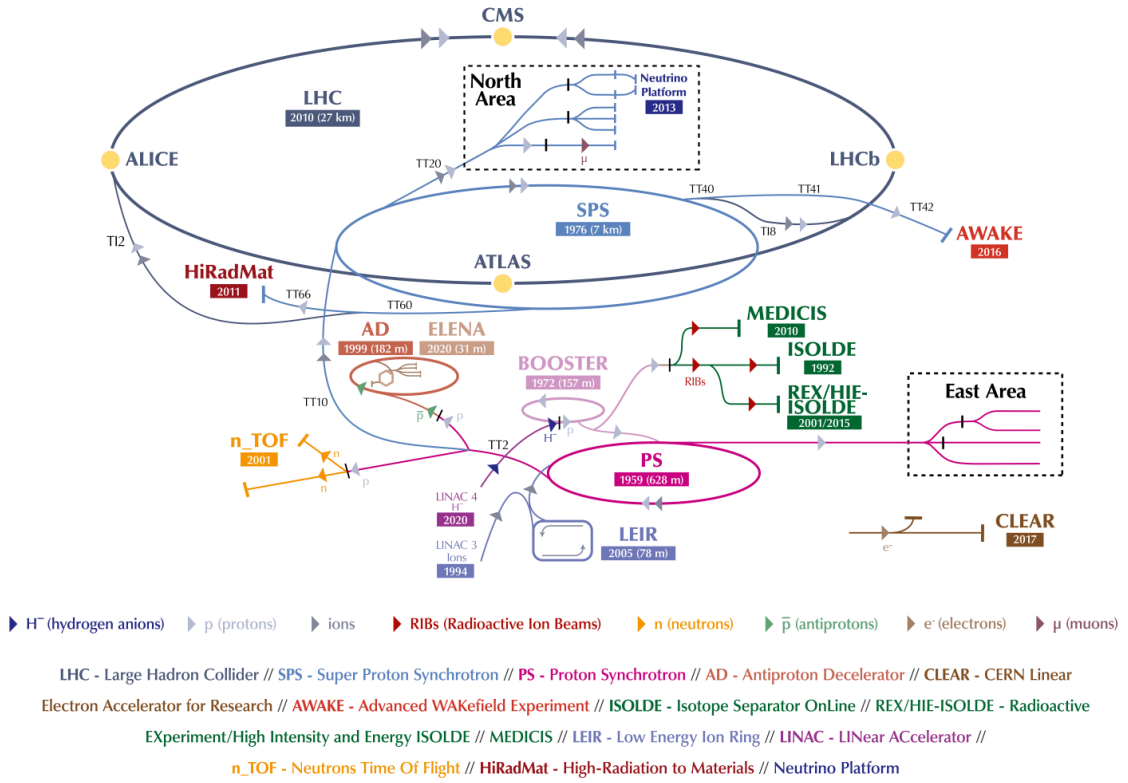

FIGURE 1.1: Schematic of the CERN particle accelerator complex. Image created by CERN.

The LHC is the world's largest and highest-energy particle collider. The main structure is a torus of 26.7 km of circumference that was built between 1998 and 2008, and from 50 to 175 metres underground around the french-swiss border. There are nine experiments in the LHC, each of which consists of different particle detectors. The main ones—called large experiments—are four: ATLAS and CMS were built for general purposes, and ALICE and LHCb are focused on specific physical phenomena. Each experiment is located at a different point in the LHC (see Fig. 1.2). There are other important points in the LHC, such as control centers for particle beams (Point 3), particle accelerators (Point 4), particle absorbers (Point 6), and cooling plants (Point 7).

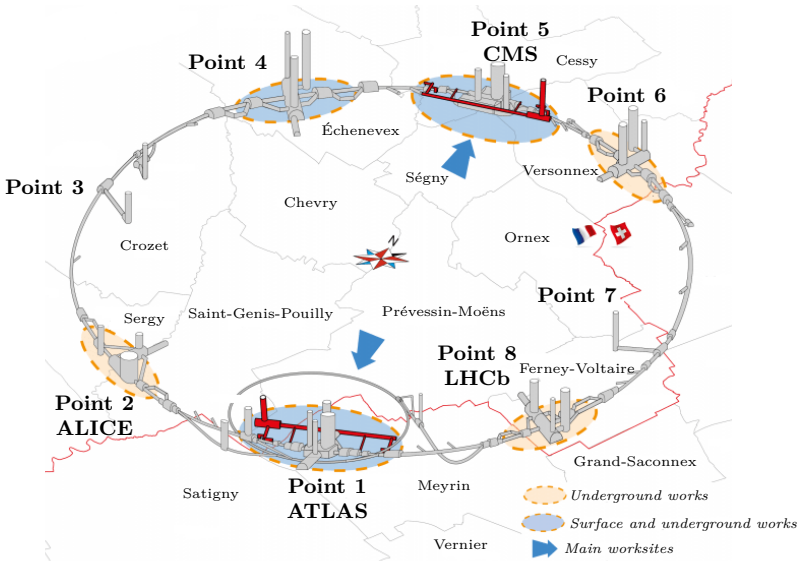

FIGURE 1.2: Map of the Large Hadron Collider. Image created by CERN.

The LHC aims to detect the particles that are generated after pp, pPb, and PbPb collisions with the highest energies ever achieved in a particle collider. The main reasoning behind the need of higher energies is that, considering the simplified equation of the special relativity, $E = mc^2$, collisions at higher energies can produce particles of high mass that have not been discovered before. The particle detectors of the LHC were designed to answer different open topics of the physics community, such as the origin of mass (ATLAS, CMS), the dark matter (ATLAS, CMS), the properties of the Quark-Gluon plasma (ALICE), and the matter-antimatter asymmetry (LHCb).

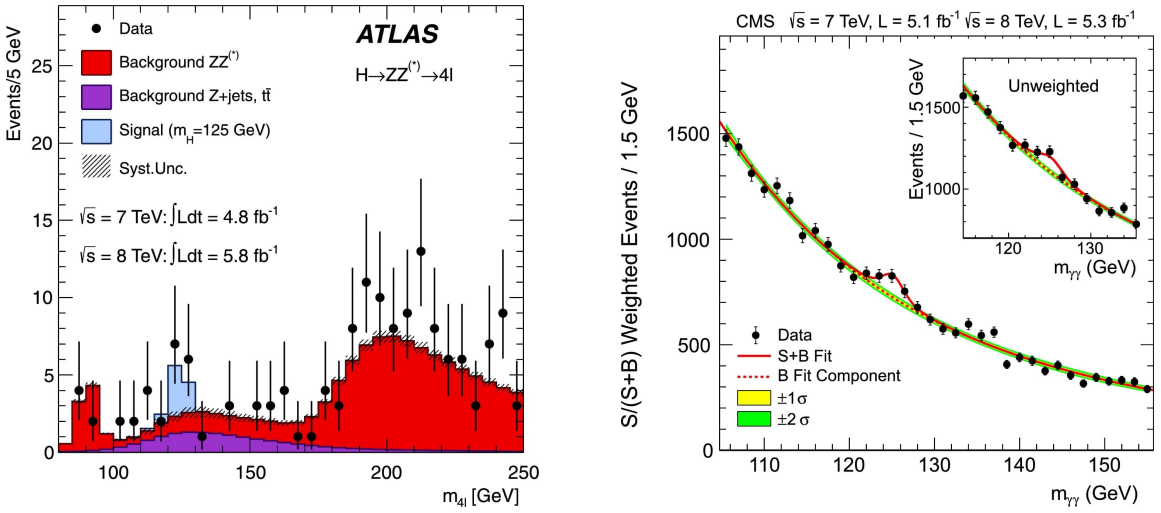

(A) Four-lepton invariant mass distribution (ATLAS Collaboration, 2012).

(B) Diphoton invariant mass distribution (CMS Collaboration, 2012).

FIGURE 1.3: Experimental data obtained by ATLAS and CMS particle detectors at the LHC.

Today, the most important findings come from the study of the origin of mass. In 1964, it was hypothesized that the mass of particles is proportional to the strength of their interactions, with an energy field called the Higgs field (Englert and Brout, 1964; Higgs, 1964). This field could be detected through its excitation, called the Higgs boson. The Higgs boson was searched in particle accelerators around the world, until it was found at the LHC in 2012 (ATLAS Collaboration, 2012; CMS Collaboration, 2012). Based on theory, once produced, the Higgs boson is expected to decay into known particles: one of the modes is the decay into two Z bosons, in turn decaying into four leptons ($H \to ZZ^* \to 4\ell$), and another is the decay into two photons ($H \to \gamma\gamma$). These channels were investigated by ATLAS and CMS, which led to a resonance around 125 GeV, indicating the production of a new particle (see Fig. 1.3). In addition, it was proved that the Higgs boson interacts with other particles with an intensity proportional to their masses, and that it is the first elementary scalar particle with zero spin. Subsequent studies have shown other production modes with weaker signals; for example, the decay into two bottom quarks ($H \to b\bar{b}$) (ATLAS Collaboration, 2018), or two muons ($H \to \mu\mu$) (CMS Collaboration, 2021). Recently, the uncertainty of the value of the mass of the Higgs boson has been reduced to 0.09% (ATLAS Collaboration, 2023).

§1.2. Particle detectors and material budget

The Higgs boson is unstable, and its properties cannot be measured directly; therefore, they are obtained from the products of its decays. This methodology is also applied in other studies, such as those leading to the discovery of *exotic hadrons* (LHCb Collaboration, 2021). The products of the collisions are detected by studying their interactions with matter. General purpose detectors are typically constructed in layers, each taking on a specific task (see Fig. 1.4).

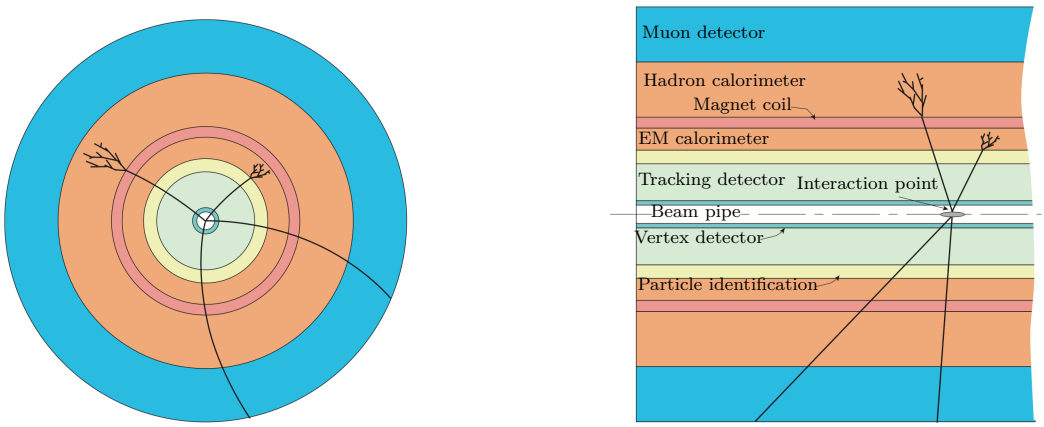

(A) Cut perpendicular to the beam. (B) Cut parallel to the beam.

FIGURE 1.4: Detector components in particle colliders (Kolanoski and Wermes, 2020).

Vertex and tracking detectors constitute the closest layers to the beam pipe, and measure the interaction (collision) points, as well as position and momentum of charged particles. A magnetic field created by magnets curves the trajectory of the particles, and the momentum of particles can be obtained from measurements of the curvature. The calorimeters are placed at intermediate positions to determine the energy of the high-energy particles as they interact with matter. Electromagnetic calorimeters measure the energy of particles that interact primarily via the electromagnetic interaction, namely electrons (e^-), positrons (e^+) and photons. Hadronic calorimeters quantify the energy of particles that interact primarily through strong force, such as protons, neutrons (n), kaons ($K^\pm$), and pions ($\pi^\pm$). The need for calorimeters for particle identification, rather than from momentum measurements, is because the relative momentum resolution deteriorates proportionally with increasing momentum, whereas the energy resolution of a calorimeter improves with increasing energy (Kolanoski and Wermes, 2020). Muon trackers constitute the outermost layers for the identification of muons, which are the most penetrating charged particles (see Fig. 1.5).

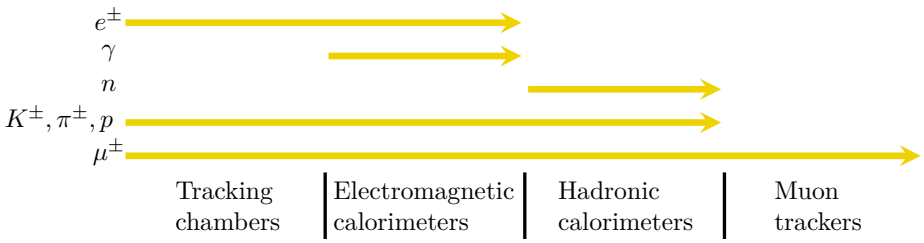

FIGURE 1.5: Particle trajectories in a general layout of a particle detector.

Particle detectors take advantage of different interactions of particles with matter such as ionization. When a medium is penetrated, charged particles lose energy after interacting with the atomic shell of the chemical elements. This is the dominant energy loss process of charged particles up to high momenta (~ 1 TeV/c), when radiation effects start to be important. In classical electrodynamics, the power radiated per unit time from an accelerated charge of energy E, atomic number Z, and mass m is given by Larmor's formula $\mathrm{d}P/\mathrm{d}t \sim Z^2E/m^2$ (Landau and Lifshitz, 1980). The quantum-electrodynamical analogue is the radiation of individual photons—called *bremsstrahlung*—and the energy loss through this process is given by an ordinary differential equation:

$$\frac{\mathrm{d}E}{\mathrm{d}x} = -\frac{E}{X_0} \longrightarrow E = E_0 \exp(-x/X_0), \tag{1.1}$$

where x is the arc length, and X_0 is the radiation length.

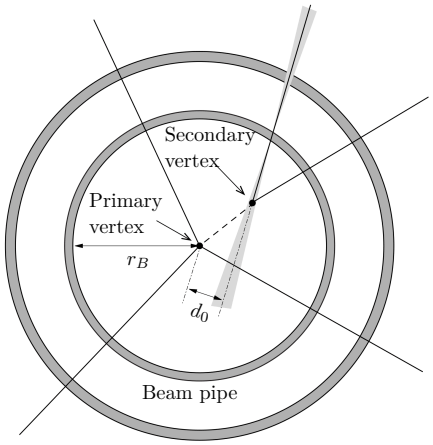

FIGURE 1.6: Influence of Coulomb scattering on the reconstruction of secondary vertices in the inner layers of particle detectors (Kolanoski and Wermes, 2020).

The value of the radiation length, which depends on the chemical element, is key in other types of interaction of particles with matter; for example, in the multiple scattering, which is produced after the passage of a particle through a material layer. A quantity n of scattering processes leads to a statistical distribution of the scattering angle relative to the original direction. For $n \to \infty$, according to the central limit theorem, the scattering distribution is Gaussian, whose standard deviation can be approximated as follows (Kolanoski and Wermes, 2020):

$$\theta_{ms} = \frac{13.6 \text{ MeV/c}}{p\beta} z \sqrt{\frac{X}{X_0}} \left(1 + 0.038 \ln \frac{X}{X_0}\right), \tag{1.2}$$

where p, β, and z are the particle momentum, velocity, and charge, respectively, and X is the layer thickness. Whether a particle track comes from a secondary vertex—an interaction point of secondary collisions—or not is indicated by the impact parameter d_0, which is the distance closest to the primary vertex of an extrapolated track in the plane perpendicular to the beam (see Fig. 1.6). Scattering at the first detector layer leads to a reconstruction error when extrapolating the track to the primary vertex, which is indicated by the shaded area in Fig. 1.6.

Material	ρ **(g/cm^3)**	ρX_0 **(g/cm^2)**	X_0 **(cm)**
Be	1.85	65.19	35.2
C	2.21	42.7	19.3
Si	2.33	21.82	9.36
Ti	4.5	16.16	3.59
Al	2.7	24.01	8.9
Fe	7.84	13.84	1.76
Cu	8.96	12.86	1.44

TABLE 1.1: Radiation length of materials (Gupta, 2010).

Assuming that the first detector layer can be placed on the beam pipe and that the spatial resolution of the detector is much smaller than the uncertainty caused by multiple scattering, the error on d_0 becomes $\varepsilon = \theta_{ms} r_B$. Accordingly, the distance of the first detector layer to the vertices should be as small as possible, and the layer thickness X should be as low as possible compared to the radiation length of the material X_0 (see Eq. (1.2)). The ratio X/X_0 is called *material budget*. Consequently, the accuracy of the particle measurements is maximized if the material budget is minimized. Beryllium is the solid material with the highest value of the radiation length (see Table 1.1), which justifies its use in beam pipes despite its toxicity and high price. In addition, since beam pipes are long and thin—usually less than 1 mm of thickness—buckling is a potential issue that is limited due to its high stiffness. Carbon is another interesting material, and its low radiation length is the reason why there is an ongoing process to replace the subsystems of particle detectors made of aluminum and steel with carbon-based structures. It is important to note that the characteristic parameter of each chemical element is ρX_0, while the relevant value for the accuracy of the measurements is X_0. Thus, for a fixed material, a density reduction—for example, in a form of porous medium—provides further reduction to the material budget.

§1.3. ALICE Inner Tracking System (ITS)

The ALICE (A Large Ion Collider Experiment) experiment has been designed to study Pb-Pb collisions at energies such that, after the collisions, temperatures of up to $\sim 10^{12}$ K are reached. In this order of magnitude the Hagedorn temperature T_H is defined, above which the structure of some elements of matter varies. For $T < T_H$, hadrons are made up of quarks that are bound thanks to the strong force, whose mediators are the gluons. When $T > T_H$, the strong force is no longer dominant and quarks and gluons are deconfined, constituting a new state of matter called Quark-Gluon plasma (Rafelski, 2016). The existence of the Hagedorn temperature is a limit temperature because, for high energies, the energy increase is translated into the creation of higher number of particles instead of producing particles with greater energy. The Quark-Gluon plasma is considered as a new state of matter that behaves as a nearly inviscid fluid (PHENIX Collaboration, 2019), and the characterization of its properties plays an important role in the theory of quantum chromodynamics. In the Standard Model, the Quark-Gluon plasma is representative of the conditions that existed at $t \sim 10^{-6}$ s after the Big Bang.

Since the start of the LHC operation in Run 1 (2009-2013), the ALICE detector has been upgraded during the Long Shutdown 1 (LS1, 2013-2015), and subsequently in the LS2 (2018-2021) after Run 2 (2015-2018). The structure of the ALICE detector during Run 3 that started in July 2022 is shown in Fig. 1.7 (ALICE 2). With dimensions of 26 m long, 16 m high, and 16 m wide, the detector contains multiple subsystems that can be divided into five categories: particle trackers (ITS, MCH, MFT, TPC, and TRD), particle identificators (HMPID, MID, and TOF), calorimeters (EMCAL, PGOS/CPV, ZDC), magnets (DM, L3M), and the absorber.

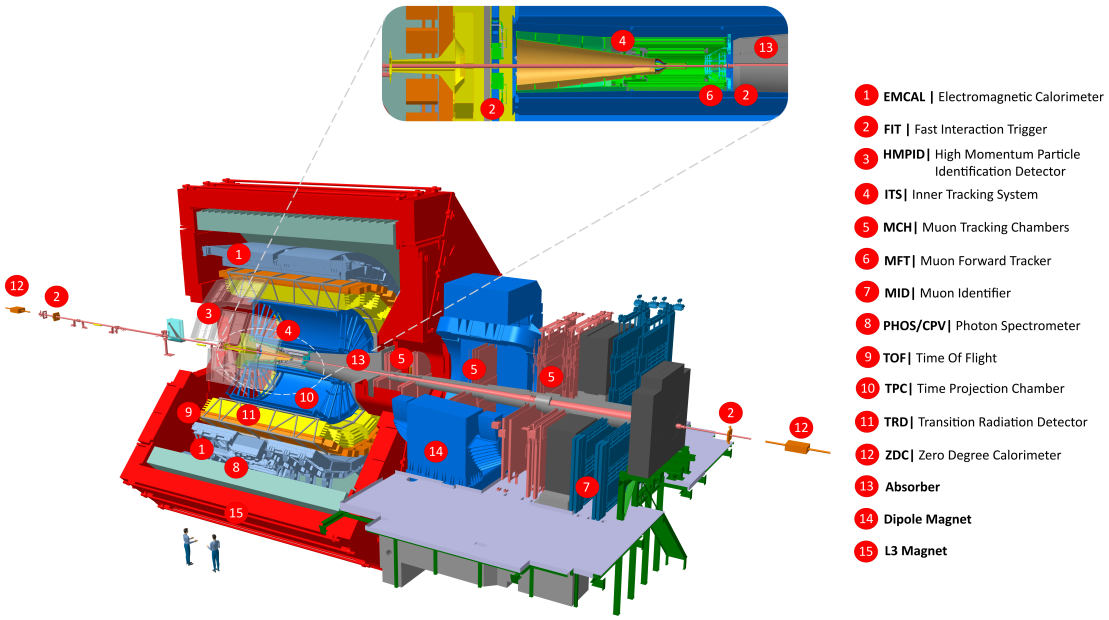

FIGURE 1.7: ALICE detector during Run 3 (ALICE 2). Image created by CERN.

The ALICE Inner Tracking System (ITS) is the closest detector to the beam pipe. Currently (ITS2), it is conceived as a two-barrel structure: the Inner Barrel (IB), formed by Layers 0 to 2, and the Outer Barrel (OB), formed by Layers 3-4 (middle layers) and Layers 5-6 (outer layers) (see Fig. 1.8a). The layers are azimuthally segmented into units called staves, which are mechanically independent. Each stave contains a Flexible Printed Circuit (FPC) that includes sensors and passive components: a Hybrid Integrated Circuit (HIC), cooling pipes, and a frame (see Fig. 1.8b).

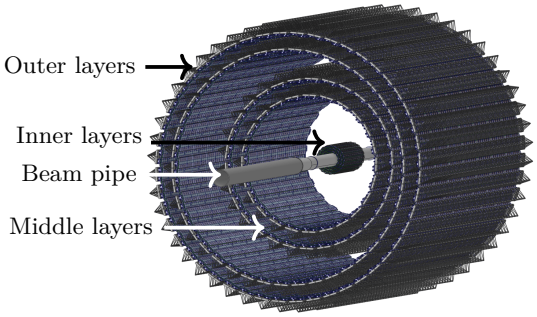

(A) Isometric view.

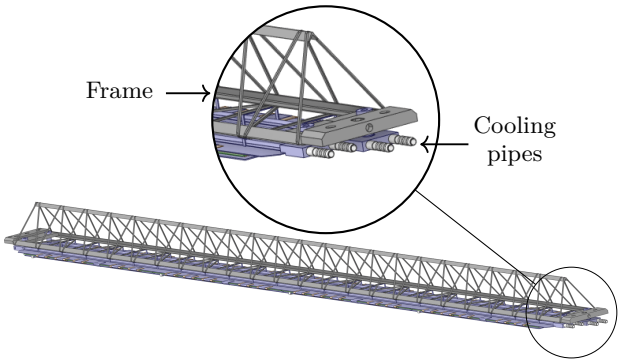

(B) Structure of the OB staves.

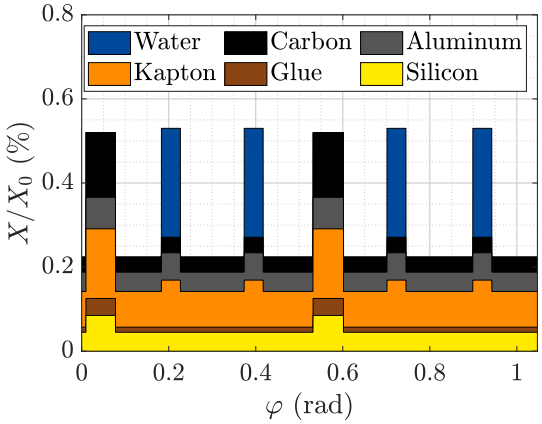

(C) Material budget of Layer 0 in the azimuthal direction.

FIGURE 1.8: ALICE Inner Tracking System 2.

Figure 1.8 gives the plot of the ITS2 material budget in the azimuthal direction. Silicon layers constitute only $X/X_0 \approx 0.05\%$ of the mean value of 0.35%, while the rest of the mean contributions are given by the cooling (water $\approx 0.04\%$), external data lines and power distribution (kapton + aluminum $\approx 0.17\%$), and mechanical supports (carbon + glue $\approx 0.17\%$).

During the Long Shutdown 3 (2026-2030), a new Inner Barrel (IB) with three inner layers (Layer 0 to Layer 2) will replace the current IB of the ITS2 (ALICE Collaboration, 2019); that is, the ITS3 will be composed of the same OB of the ITS2 and a new IB (ITS3 IB). The ITS3 IB will consist of two halves (half-barrels) to allow the detector to be mounted around the beam pipe (see Fig. 1.9a). Each half-barrel will incorporate three layers made of a single large silicon pixel chip of length 280 mm and thickness of 40 µm bent into half-cylindrical shape. The production of a single large chip will allow the removal of external data lines and power distribution, while the increased flexural stiffness from the bending of the silicon layers will lead to a significant reduction in the use of mechanical supports. Moreover, a beryllium beam pipe of inner radius of 16 mm and wall thickness of 500 µm will replace the one of the ITS2 of 870 µm of the same material.

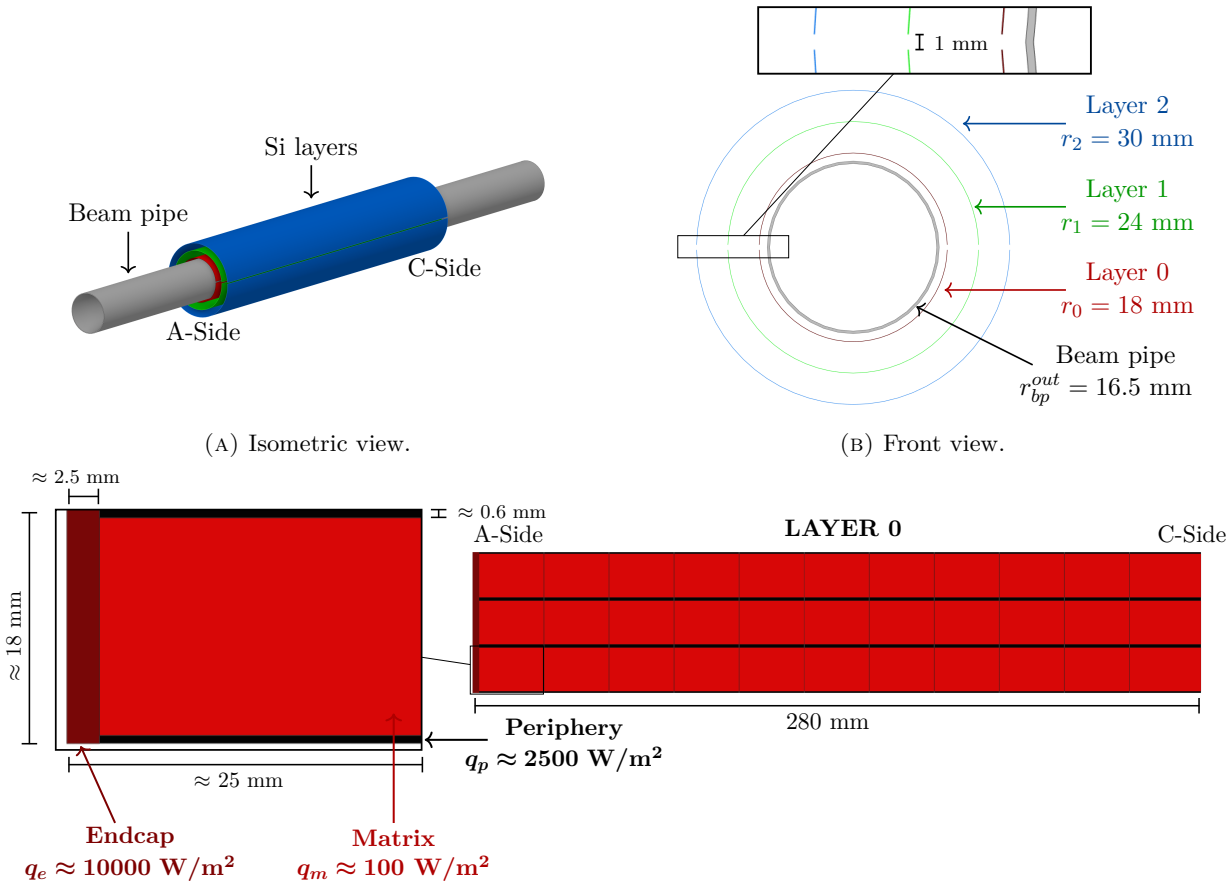

(A) Isometric view.

(B) Front view.

(C) Power dissipation of the silicon layers.

FIGURE 1.9: Schematic of the ALICE ITS3 Inner Barrel (IB).

Due to dimensional tolerances and space limitations in the detector installation, the half-layers will probably not be in contact, and the nominal distance between them is expected to be 1 mm (see Fig. 1.9b). At one of the edges (A-Side, see Fig. 1.9a), the silicon sensors will be electrically interconnected over a length of approximately 300 µm to a flexible printed circuit using aluminum wedge wire bonding. Additional electrical components will be needed in that zone—called *endcap*—whose extension in the longitudinal (z) direction will be approximately 2.5 mm. In the endcap, the heat flux in the silicon sensor due to the power dissipation of the electrical components will be the highest (see Fig. 1.9c). The rest of the sensor will be composed mainly by the *matrix*, which is the effective zone for particle detection, and where the heat flux is one order of magnitude lower than in the endcap. The power for the sensor operation will be transferred to the endcap region on the

longitudinal strips called *peripheries*. Each of the three layers of silicon Monolithic Active Pixel Sensors (MAPS) will be produced by stitching smaller parts (matrix + two peripheries) of total dimensions of around 18 mm × 24 mm, called stitching units (Kluge, 2022). Layer 0 is shown in Fig. 1.9c, and the same schematic applies to Layers 1 and 2. Heat dissipation in the beam pipe, q_{bp}, is also expected, and inputs received from other groups consider $q_{bp} \leq 1000$ W/m^2. The heat flux values mentioned in this paragraph are approximate, and, the power dissipation in the peripheries can depend on the longitudinal coordinate.

§1.3.1. ALICE ITS3 IB cooling system

The damage of radiation to the materials of a detector structure is proportional to the radiation intensity and the operating temperature of the detector. In ATLAS and CMS experiments the operating temperature is approximately -20 °C, as a consequence of the high radiation levels (absorbed doses) of the order of 1 MGy (ATLAS Collaboration, 2017a; CMS Collaboration, 2017). In the ALICE experiment the radiation levels are low ($\ll$ 1 MGy, (ALICE Collaboration, 2013)); therefore, like the current ALICE ITS2, the ALICE ITS3 will operate at ambient temperature of around 20 °C. Keeping the temperature of the silicon layers bounded is relevant to control the thermoelastic expansion, since the accuracy of silicon sensors is approximately 5 µm, and the displacements of the layers (possibly due to vibrations) should be kept lower than that value.

This thesis focuses on the development of the cooling system of the ALICE ITS3 IB. The system must ensure that the temperature variation of the layers is kept below a design limit that will be discussed in the following section, and that the displacements of the layers are lower than the sensor accuracy. To keep the layers in cylindrical shape and increase the structural stiffness, the design must include structural supports with the minimum contribution to the material budget.

§2. Research background

§2.1. Cooling systems of particle detectors

The designs of cooling systems involve facing Conjugate Heat Transfer (CHT) engineering problems; that is, heat transfer between liquids and solids with thermal coupling. These systems are frequently based on convection with single phase flows, namely in oil systems of turbofan engines (Chávez-Modena et al., 2023) and in turbine blades (Han, 2014). Two-phase flows are used for hybrid vehicle electronics (Mudawar et al., 2009), and conductive heat transfer is the main mechanism in superconducting magnet energy storage systems (Nagaya et al., 2012). The use of heat exchangers with single- and two-phase flows is extensive (Webb and Chung, 2005), since the design possibilities are wide, and different materials can be used depending on the requirements. In particular, materials such as open-cell foams are used. These are cellular structures that consist of a solid material that contains a ligament structure with a large number of pores (Wypych, 2022).

In the High-Luminosity phase of the Large Hadron Collider (HL-LHC), which will start in 2030, new particle detectors will be installed in two large experiments (ATLAS Collaboration, 2017a,b; CMS Collaboration, 2017). Similar to the ALICE ITS2, each of the layers will be built by assembling smaller structures. The cooling systems of the detectors cited will use carbon foams. Due to their high mechanical and thermal properties per unit of mass, these materials are an excellent choice for cooling applications (Wang et al., 2021). In the baseline design, the heat dissipated by the sensors will be transferred by conduction to an open-cell foam and a titanium pipe, to then be removed by convection with two-phase CO_2. Additional structures of reduced thickness of Carbon-Fiber-Reinforced Polymer (CFRP) will be added to increase structural stiffness (see Fig. 1.10). In the design of Fig. 1.10, the mean value of the material budget is $X/X_0 \approx 0.6\%$ (ATLAS Collaboration, 2017b). Improvements of the baseline design are being developed such as the use of microchannels (Kandlikar, 2012) and microvascular networks (Pety et al., 2017), although the reduction of the material budget is limited due to the use of support structures.

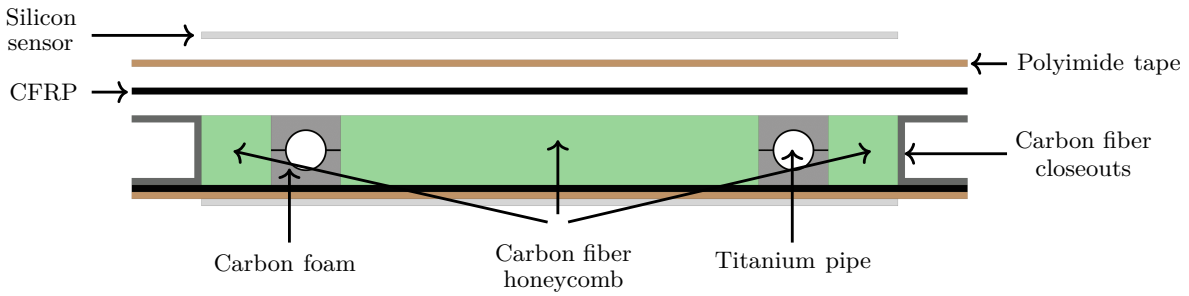

FIGURE 1.10: Stave core of the ATLAS ITk Strip Detector (ATLAS Collaboration, 2017b).

Obtaining material budget values lower than 0.25% requires the use of alternative cooling solutions. In current particle detectors, when the average power dissipation is lower than 1000 W/m^2, forced gas flow cooling emerges as an alternative. The requirement to install pipes around the detector is removed, providing the minimum material budget among the cooling systems mentioned. Forced gas cooling was used in the Heavy Flavor Tracker (HFT) of the STAR experiment at the Relativistic Heavy Ion Collider (RHIC), where the detector power dissipation was equal to 1700 W/m^2. With a flow with a freestream velocity $v_\infty = 10$ m/s, the maximum temperature variation in the detector was 15 K (Contin et al., 2018). However, the material budget in the inner layer was still high and non-uniform ($\approx 0.4\%$), as a result of the contributions of cables and mechanical supports. In the Mu3e experiment, helium at $v_\infty \approx 15$ m/s will be used to remove the heat flux of 2500 W/m^2 dissipated by the silicon tracker (Arndt et al., 2021; Rudzki et al., 2023). The use of aluminized kapton foils as structural supports will provide a lower material budget than the systems described previously ($X/X_0 \approx 0.11\%$).

As introduced in §1.3.1, the minimization of the thermal expansion of the silicon layers is a requirement for the cooling system of the ALICE ITS3 IB. Since the accuracy of the silicon sensors is approximately 5 µm, a thermal deformation of more than 5 µm is detrimental to the measurement quality. Furthermore, additional structures are required to keep the layers in cylindrical shape, and there is a mismatch between the thermal expansion coefficient of silicon (CTE $\approx 2.5\times10^{-6}$ K^{-1}) and the standard epoxy glues (CTE $\approx 50 \times 10^{-6}$ K^{-1}), which are needed for the interfaces between the layers and the mechanical supports. Thus, temperature gradients generate stresses that should not affect the performance of the system. A maximum layer temperature variation $\Delta T = T - T_\infty = 10$ K is the upper limit set, while values closer to 5 K are the target. The temperature variation is referred to the ALICE cavern (room) temperature T_∞, which is constant throughout the detector operation, and its absolute value does not affect the performance of the system. Consideration of relative temperatures is due to the fact that the detector is installed and calibrated at T_∞, and the cooling air is extracted from that region. Thus, the system is in zero-stress condition at $\Delta T = 0$, and in that situation the freestream air temperature is equal to the room temperature.

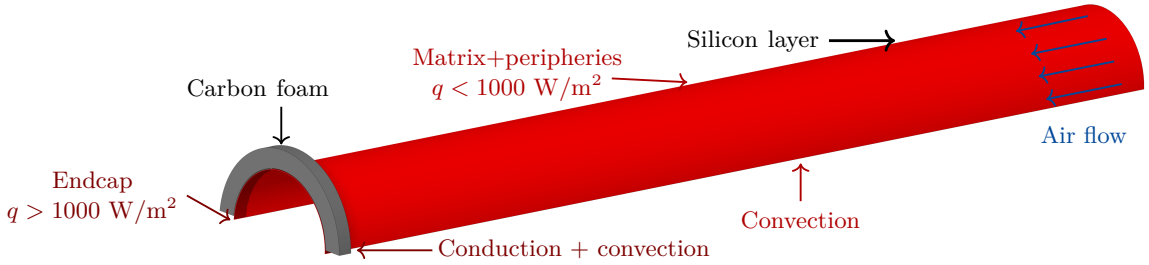

FIGURE 1.11: Graphical representation of the cooling system of the ALICE ITS3 IB.

In the ALICE ITS3 IB, the average power dissipation will be lower than the reference value of 1000 W/m^2 (see Fig. 1.9c), which motivates the use of forced air cooling. The ITS3 IB will be the first particle detector at CERN using a cooling system based on forced air convection. The

increased heat dissipated in the endcaps will be transferred by conduction to carbon foam rings, to be then removed by convection with an air flow (see Fig. 1.11). Additional foam structures will be used to keep the layers in cylindrical shape and minimize the structural displacements due to the air flow. The low density of foams and the reduced area covered by these structures is expected to lead to a mean material budget $X/X_0 \approx 0.07\%$. This is the lowest value ever achieved in a High-Energy Physics (HEP) particle detector, with a reduction of more than 80% with respect to the ITS2 ($X/X_0 \approx 0.35\%$, see Fig. 1.8).

§2.2. Open-cell foams

The selection and characterization of the thermal and structural foams for the ALICE ITS3 IB is a key part of the cooling system design. There are two different foam variants depending on the internal structure: open-cell and closed-cell foams (see Fig. 1.12). The former have a network of ligaments but no cell walls, while the cells of the latter are surrounded by thin cell walls and sealed off from neighboring cells. Owing to its fluid permeability, the open-cell structure is adequate for applications where fluid transport is demanded, while the isolated pores in the closed-cell structure offer potential advantages for thermal insulation purposes (Wypych, 2022). The properties of foams can be tuned by varying the precursor material and/or the production process. Given their potential benefits as heat exchangers, in what follows, only open-cell foams will be considered.

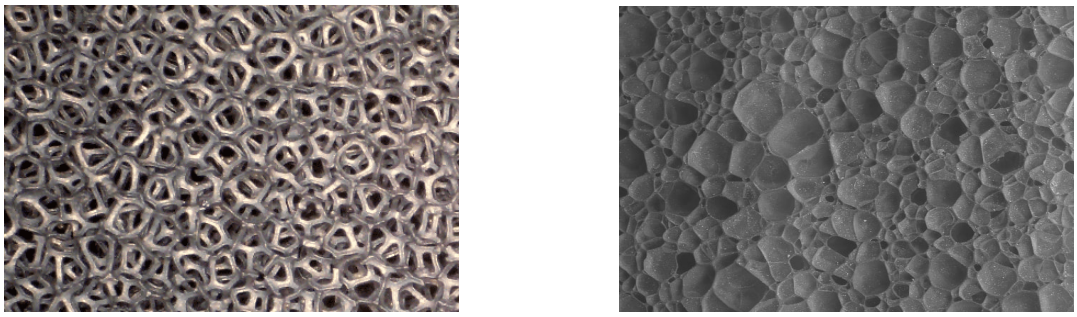

(A) Open-cell. (B) Closed-cell.

FIGURE 1.12: Microscope images of foams.

The possibility of producing (open-cell) foams with low cell sizes (down to $\ell \sim 10^{-4}$ m) and base materials of high thermal conductivity leads to their use as heat exchangers. When a foam is placed in contact with a material that dissipates heat, the heat can be transferred to the foam by conduction, and then removed from the foam with a fluid flow that can be a gas, a liquid, or a two-phase mixture. Systems using foams such as modern electronic devices (Li and Leong, 2011; Zhao, 2012), power plants (Kuruneru et al., 2020), and space heat sinks (Rawal et al., 2005) benefit from the combination of both heat transfer mechanisms. Recently, open-cell foams have been studied as potential candidates for improving the performance of heating, ventilation, and air conditioning (HVAC) systems (Hu et al., 2016; Rehman and Ali, 2020; Dongellini et al., 2022), electronic devices (De Schampheleire et al., 2013), and solar power plants (Ami Ahmadi et al., 2021).

The multiple applications of foams have motivated the realization of numerous experimental studies for the characterization of properties such as the thermal conductivity (Calmidi and Mahajan, 1999; Sadeghi et al., 2011; Paek et al., 2000), the pressure drop (Lacroix et al., 2007; Bonnet et al., 2008), and the heat transfer coefficient in natural convection (Phanikumar and Mahajan, 2002) and forced convection (Younis and Viskanta, 1993; Mancin et al., 2013). Experimental work has led to correlation-based models for the thermal conductivity (Boomsma and Poulikakos, 2001; Kumar and Topin, 2016), the pressure drop (Dukhan, 2006; Inayat et al., 2016), and the Nusselt number (Calmidi and Mahajan, 2000). Simulations have been performed to compute the heat transfer coefficient in aluminum foams with geometries extracted from computed tomography scans (Iasiello et al., 2020), although reduced domains are simulated; thus, fully developed flow regimes are not considered. Furthermore, the availability of foams with a wide range of cell sizes (from 250

µm up to 10 mm) and porosities (from $\Phi = 0.8$ to $\Phi = 0.97$) limits the precision of correlations and analytical models based on experimental data. The correlations consider different geometrical parameters as building blocks (Trilok et al., 2022). Since the repeatability of the foam production process is not close to 100%, and different measurement techniques are used to obtain them, the comparison between correlations of different foams is not straightforward.

The thermal performance of the joint between carbon foams and solid surfaces—and, in particular, the effect of the amount of glue that penetrates into the foam—is expected to play a major role in the thermal performance of foams, and has not been studied in depth. In this line, an initial study applied to the previously mentioned CO_2 cooling systems has been performed at CERN (Mussgiller, 2016), where a titanium-foam interface is considered. However, the applicability of this study to other configurations with different interfaces such as silicon-foam is unclear, since the direct contact between these materials can damage the silicon sensors. A different configuration of the interface is required, specifically including an additional component between the silicon and the foam to minimize the damage and the thermal resistance.

§2.3. Numerical simulation of turbulent flows

Turbulent flows are present in multiple industrial applications such as aircraft and vehicle aerodynamics, turbomachinery, medical devices, and weather prediction. The understanding of turbulent flow is important, since turbulence produces effects that include the increase in friction losses and heat transfer, the delay of separation in flows exposed to adverse pressure gradients, and the noise generation. The complete flow description is obtained with Direct Numerical Simulations (DNS), in which the entire turbulence spectrum is resolved. Estimates derived from Kolmogorov's hypotheses show that, for a turbulent flow above a flat plate of length L, the number of grid points is $N_{\mathrm{DNS}} \sim Re_L^{37/14}$ (Choi and Moin, 2012).

The computational cost of DNS is reduced with the Large Eddy Simulation (LES) models, which solve part of the turbulence spectrum and model the remainder (see Appendix A, §2). The dynamics of the large-scale motions, which are affected by the flow geometry and are not universal, are computed explicitly. The small scales have a universal character and follow the Kolmogorov hypotheses, and they are represented by simple models. As a general rule, LES simulations require a minimum of 80% of the turbulent kinetic energy to be resolved (Pope, 2000), which is restrictive in wall-bounded flows at high Reynolds numbers; for example, in the turbulent flow above a flat plate, the number of grid points is $N_{\mathrm{LES}} \sim Re_L^{13/7}$ (Choi and Moin, 2012). The scaling problem near the wall is reduced in the Wall-Modeled LES (WMLES) models, where a mixing length model or a wall function are used up to the inner part of the logarithmic layer. For a WMLES simulation of a turbulent flow above a flat plate, the number of grid points is $N_{\mathrm{WMLES}} \sim Re_L$ (Choi and Moin, 2012). The accuracy of current WMLES models is limited by the *log-layer mismatch* (LLM), which is the deviation of the velocity from the log-law, especially where the model switches from the wall function (or the mixing length model) to LES (Bose and Park, 2018). Multiple solutions have been proposed, including the addition of forcing terms in the momentum equations (Piomelli et al., 2003), although the constants of the forcing terms are not universal. This is partially solved in dynamic approaches that are based on control systems (Keating and Piomelli, 2006), although at the expense of an increase in complexity and numerical stability. The error of the LLM is proportional to the dimensionless wall distance $\tilde{y}^+$ of the first near-wall cell, and mesh refinement is not always possible due to the requirement of using cells with a low aspect ratio for resolved turbulence. If a mixing length model is used near the wall (Shur et al., 2008), the use of high aspect ratio cells is limited due to the reduced width in which the RANS model is applicable.

In the Reynolds-Averaged Navier Stokes (RANS) models, the computational cost does not depend on the Reynolds number (see Appendix A, §3). The entire energy spectrum is modeled, and since the equations contain mean quantities, temporal resolution is not required in the simulations. RANS models have shown great accuracy in wall-bounded attached flows, where the law of the wall establishes a reference for the derivation of the model constants. Two-equation models are currently the reference for industrial simulations, since they provide the optimum balance between

computational cost, stability, and accuracy. However, mean quantities are not well predicted in free shear flows (Yoder et al., 2015) and separated flows (Corson et al., 2009), which constitute an important part of industrial applications. Furthermore, due to their time-averaged formulation, RANS models are usually not suitable for predicting time-dependent quantities; for example, in acoustics simulations (Uzun et al., 2004), fluid-structure interaction (Breuer et al., 2012), and multiphase flows (Fox, 2012). There are particular cases—namely massively separated flows—where unsteady RANS simulations (URANS) provide unsteady solutions, and specifically part of the turbulence spectrum, although the accuracy is limited in these situations (Palkin et al., 2016).

In wall-bounded flows at high Reynolds numbers, the computational cost of LES is unaffordable for practical engineering applications. In contrast, the cost in RANS is several orders of magnitude lower, and the accuracy of these models for boundary layers without detachment is often acceptable for industrial applications. In free shear flows, much less computational power is required to perform LES simulations. A compromise solution in terms of accuracy and computational cost is given by hybrid RANS/LES models, where RANS is used in the boundary layers, and LES in the rest of the domain. The most popular model is the Detached Eddy Simulation (DES) and its variants, although these models have one or more shortcomings (see Appendix A, §4). The most important is the *grid-induced separation* (GIS), which consists of early separation in flows exposed to an adverse pressure gradient. Similarly to the LMM, the transition point from RANS to LES depends on the mesh size, and it can be produced in cases where the mesh is not fine enough for an LES simulation, leading to solution deterioration. In addition, the length of the transition area from RANS to LES is not negligible in practical applications. This is called *gray area* in the literature, since the turbulence model is not well defined there. Gray areas delay the generation of turbulent structures, and generate spurious buffer layers (Fröhlich and von Terzi, 2008) and the LLM (Spalart, 2009). Another weakness shared by all DES family is the reduced accuracy of the LES part. Assuming an equilibrium of the source terms of the RANS turbulence variables, it can be demonstrated that the LES formulation corresponds to a Smagorinsky model; specifically, for the original constant $C_{\mathrm{DES}} = 0.61$ (Strelets, 2001) used in DDES with the $k-\omega$ SST model as the RANS model (Menter, 1994), the corresponding Smagorinsky constant outside the boundary layers is $C_s \approx 0.175$. This value is too dissipative for free shear flows, for which $C_s \approx 0.1$ has been shown to be optimal (Yoshizawa, 1986). The DES family also inherits limitations from the Smagorinsky model, namely the need to adjust the model constant based on the specific flow being simulated. Another deficiency is the persistent presence of non-zero turbulent viscosity in standard laminar regions, including laminar shear layers, where it should ideally vanish.

Similar to the DES family, the Scale-Adaptive Simulation (SAS) model is a formulation that takes RANS equations as reference, and a second equation for the turbulence scale is reformulated (Menter and Egorov, 2010). This results in the inclusion of the second velocity space derivative in the RANS equations, so that the scale-equation is able to adjust to resolved scales in the flow. SAS has been shown to provide performance superior to those of unsteady RANS (URANS) models in flows with strong instabilities (Egorov et al., 2010; Xu et al., 2019). However, for a given mesh suitable for LES far from walls, when the flow instability is not enough to enable the LES model, SAS solves turbulent structures of sizes similar to those of URANS (Rezaeiha et al., 2019a), and the model can be less accurate than URANS (Davidson, 2006). Thus, in these cases, gray areas are produced, since the model does not solve the equations either in URANS or in LES mode. While in the DES family the properties the gray areas are reasonably known, in SAS that knowledge does not exist. Other hybrid RANS/LES models available in the literature solve the Partially-Averaged Navier Stokes (PANS) equations (Girimaji, 2006). The difference between RANS and PANS is that the latter contains modified parameters in the turbulence dissipation and diffusion terms, so that, under some restrictions, the required level of modeled-to-resolved turbulent kinetic energy and dissipation rate can be set. The PANS model does not include additional shielding functions, so the presence of gray areas, the LLM, and the GIS are potential problems. The exact transition point from RANS to LES can be defined with the Zonal RANS/LES methods, where RANS and LES are solved in different parts of the domain, and a synthetic turbulence generator transfers modeled RANS turbulence to resolved LES turbulence (Terracol, 2006). However, industrial applications in

which the location of the RANS/LES interface can be accurately defined are limited.

The Stress-Blended Eddy Simulation (SBES) approach has been developed by Ansys to overcome the deficiencies of the original DES model and its variants (Menter, 2018). The basis is the blending of the RANS and LES models at the stress level, which is equivalent to the blending of the turbulent viscosities if both models use the Boussinesq turbulent viscosity assumption. All RANS and LES models can be combined, which is relevant in the LES case, since more consistent models than the classical Smagorinsky model can be used. In addition, motivated by the higher time scale of the RANS turbulence quantities in comparison to the rest flow variables, in SBES the equations of RANS variables can be solved every 5-10 flow time steps. This benefit is obtained due to the decoupling of the RANS and LES turbulent viscosities, and leads to a computational cost similar to the WMLES/LES models, which is lower than the one of DES/DDES/IDDES that solve the equations of RANS variables at all time steps. Ansys claims that the blending function is defined such that the RANS model covers the entire boundary layer, without the GIS problem, and with gray areas of negligible size. It has been verified that the model switches to the WMLES mode depending on the mesh size and the turbulence content of the flow. However, the details of the formulation are not published, and it is available only in Ansys Fluent/CFX. SBES has shown similar or greater accuracy than IDDES/DDES in a mixing layer (Menter, 2018), automotive applications (Ekman et al., 2020), and multiphase flows (Wang et al., 2023).

Hybrid RANS/LES models can be applied to transitional flows with transition RANS models such as the $\gamma - Re_{\theta t}$ (see Appendix A, §3.2.2), which has been validated in turbomachinery applications (Langtry et al., 2006). The model has been shown to be capable of predicting some of the physics of the laminar-turbulent transition in further studies of wing profiles (Dong et al., 2019) and wind turbines (Rezaeiha et al., 2019b; Campobasso et al., 2022). However, in some cases, discrepancies with experimental data have been encountered in separated flow regions. Transitional flows have been studied with LES models, although significant errors have been observed in the early stages of separation bubbles (Lardeau et al., 2012). This is because the residual stress models do not detect the entire laminar regions in medium and coarse meshes, and the resolution needs to be increased to levels that are close to DNS simulations (Lehmkuhl et al., 2013). Alternatives have been proposed based on the use of sensors to detect the transition point (Bodart and Larsson, 2012), although this methodology implies modeling and the addition of uncertainties. Since the LES approach combines the high CPU cost and the modeling requirement, an interesting approach is to use a transition RANS model as a basis for a hybrid RANS/LES model. However, as noted in (Bouchard et al., 2022), the number of publications on this topic is reduced.

In the industrial context, DNS simulations are not an option in the near future, and LES is limited to free shear flows due to the high computing power required. Given its limited accuracy, RANS can only be used for preliminary simulations and/or non-complex turbulent flows. Thus, WMLES simulations for moderate Reynolds numbers and hybrid RANS/LES models for high Reynolds numbers are stated as the reference for industrial flows in the near future (Chaouat, 2017; Pont et al., 2018). In the hybrid RANS/LES case, provided there is no GIS, the requirement of solving the outer layer of the boundary layer in RANS can be dropped, since it is not universal and the mesh requirements are of the same order as in the freestream region. Even if the Reynolds numbers are not expected to be high in the ALICE ITS3 IB (see §2.4), air cooling is under consideration to be used in the future outer barrels of the ALICE 3 (ALICE Collaboration, 2022), which will replace the entire ALICE 2. Moreover, the characteristic lengths of the inner trackers of ATLAS and CMS trackers are one order of magnitude greater (ATLAS Collaboration, 2017a; CMS Collaboration, 2017) than in ALICE. This means that, if low material budgets are targeted for the next LHC upgrades, the use of air cooling will require the use of more efficient and accurate turbulence models. The reasoning also applies to future colliders, namely the electron-positron Future Circular Collider (FCC-ee), in which air cooling is expected to be one of the key areas of increased performance (Monteil and Wilkinson, 2021; Bacchetta et al., 2022).

§2.4. Vibrations of structures

Vibration control is a key in industrial applications to avoid failure of mechanical components. Relevant sources of vibration include pressure fluctuations coming from the environment (Powell, 1958), mass imbalances (Ramlau and Niebsch, 2009), irregular mechanical contacts (Rolek et al., 2016), and moving parts (Grega et al., 2017). Different solutions are frequently explored, namely the improvement of structural stiffness (Ng and Hui, 2008), or the addition of vibration absorbers that increase the damping of systems (Thompson, 2008). These solutions have limitations when applied to a wide range of frequencies and external loads, which motivate the development of variable stiffness devices (Yang et al., 2014; Hauser et al., 2017). A complex discipline in the study of vibrations is aeroelasticity, which consists of the coupling between aerodynamic loads and structural dynamics. Aeroelastic problems are present in multiple engineering applications, namely aircraft wings (Dowell and Hall, 2001), turbomachinery (Campbell and Paterson, 2011), and civil structures (Zhang et al., 2013). The structural response needs to be predicted in these applications, as positive feedback between structure motion and external forces can cause problems due to fatigue or large displacements (Bisplinghoff et al., 2013). For example, aeroelasticity is an important part of aircraft design, given that aeroelastic instabilities such as divergence (Townsend et al., 2019), flutter (Jonsson et al., 2019), and buffet (Lawson et al., 2016) can lead to structural failure.

In the LHC, magnetic fields are measured using a rotating coil system that induces vibrations (Mangiarotti et al., 2022). Future measurement needs will require an increase in the speed of the rotating components, which will imply an increase in vibration amplitudes (Brooks et al., 2008). The installation of new equipment during the LHC operation may affect the quality of the measurements for similar reasons (Guinchard et al., 2018). Other sources of noise during LHC operation are earth movements and humans, both commonly referred to as cultural noise (Di Girolamo et al., 2021). Since not all components of large experiments are built at CERN, vibrations due to transport loads are also an important concern (Zhang et al., 2022; Vallone et al., 2023). With attention to ALICE ITS3 IB, the design of the cooling system must ensure that not only the silicon layers do not break, but also that the displacements induced by the air flow are lower than the accuracy of the silicon sensors (≈ 5 µm). Thus, an aeroelastic study is needed to study the effect of the air flow on the mechanical behavior of the silicon layers. The maximum displacement target with respect to the equilibrium position is set conservatively at 1 µm.

Numerical simulations of the Fluid-Structure Interaction (FSI) require model selection for fluid and structural equations, as well as the definition of the coupling strategy. The universal approach to solving the structural problem consists of considering a spring-damper-mass system of equations, and the coefficients are built based on material stiffness, mass, and damping properties (Glück et al., 2001; Tong et al., 2007). The complexity of the fluid problem is higher due to the disparity between the small and large scales of fluid flows. In computational fluid dynamics, different equations are solved depending on mesh and accuracy requirements. DNS simulations provide the lowest modeling error, although the computational cost associated with these simulations is beyond the capabilities of current computing power within the industrial framework. The use of LES approaches reduces the computational cost by approximately one order of magnitude, which is still limiting for industrial cases, although recent investigations show promising results using the latest advances in numerical methods (Lahooti et al., 2023). RANS models are interesting alternatives in highly unstable flows or when the mean flow quantities are responsible for structural deformations. However, the required meshes are still too fine for practical applications, and large errors have been found for non-optimal meshes (Otter et al., 2022). Hybrid RANS/LES models take the advantages of RANS and LES and provide the optimum balance between computational cost and accuracy, although current studies at high Reynolds numbers are limited to coarse meshes (Šekutkovski et al., 2016). Thus, baseline tools in the aeronautical industry, where aeroelastic studies are common, comprise structural simulations with aerodynamic forces computed from simplified models such as the Blade Element Momentum Theory (BEMT, (Burton et al., 2011)), Free Vortex Methods (FVM, (Leishman et al., 2002)), and Theodorsen functions (Zhang et al., 2021).

In fluid simulations, equations are usually solved in Eulerian coordinates, while a Lagrangian

description is the standard approach for structural simulations. This leads to numerical challenges to solve the resulting system of equations, in which the coupling between the equations of fluid and structural problems plays an important role. The most popular coupling techniques are monolithic and partitioned. In the monolithic case, the fluid and structural domains are treated as a single continuum, and all equations are solved simultaneously (Ryzhakov et al., 2010; Liu et al., 2024). In partitioned solvers, the fluid and structural equations are solved separately, and the coupling is achieved through an iterative procedure (Wall et al., 2007; van Brummelen, 2011). Monolithic methods are more stable, although at the cost of increased complexity in implementation and computational cost (Degroote et al., 2009). In monolithic methods, different solutions exist to deal with the difference on the formulations of fluid and structural equations, ranging from fully Eulerian (Richter, 2013) to fully Lagrangian (Cornejo et al., 2021). Arbitrary Lagrangian-Eulerian (ALE) methods are intermediate options in which structural equations are solved in Lagrangian coordinates, and fluid equations are solved in an artificial coordinate system (Lozovskiy et al., 2019). Computational cost savings can also be obtained with the Immersed Boundary Methods (IBM), although their applicability for flows at high Reynolds numbers is limited due to their diffuse nature (Tschisgale et al., 2021). The accuracy and stability of the simulations are strongly influenced by the quality of the dynamic meshing approach used, especially when large displacements are considered (Stein et al., 2003; Bathe and Zhang, 2009). Even if there are some cases in which the computational cost of FSI simulations is affordable using reduced-size meshes, such as in medical applications (Bazilevs et al., 2010; Crosetto et al., 2011), the high computational cost of FSI problems usually motivates the decoupling of structural and fluid simulations in the partitioned approach. Loosely-coupled (or explicit) FSI simulations, in which only one iteration is performed at every time step, are an alternative to coupled FSI that provide successful results in particular cases without important nonlinearities (Dang et al., 2010; Zhao, 2012). Structural and fluid problems are solved separately in decoupled approaches, which provide a reasonable result for preliminary studies and/or when structural displacements are small (Mohmmed et al., 2020; Wijesooriya et al., 2021). Given the computing power limitations in the industry and the complexity of FSI simulations, experimental works are also extensive in aeroelasticity, especially in the study of wings (Sheta et al., 2002; Shangguan and Lu, 2004; Zarruk et al., 2014; Avin et al., 2022).

In the ALICE ITS3 IB, a characteristic Reynolds number based on channel height $h = 6$ mm (see Fig. 1.9b) and a reference freestream velocity $v_\infty = 10$ m/s used in other air-cooled particle detectors (see §2.1) is $Re_h \approx 4000$. Assuming that the circular pipe flow regimes are applicable, the fully-developed channel flow is transitional. In addition, foam rings used for cooling (see Fig. 1.11) and other structural supports can lead to the generation of free shear flows that are expected to be turbulent, since the transition Reynolds number is lower in free shear flows than in wall-bounded flows. To study the vibrations generated by the air flow, the use of simplified models such as those mentioned in the previous paragraph is discarded, since they have been developed for wing profiles. On the other hand, RANS turbulence models are unsuitable for free shear turbulent flows. Thus, more computationally-demanding simulations are required, such as LES, which is the choice for the current thesis. This implies the definition of fine meshes, which means that, in the industrial framework, a simplified and specially tailored model needs to be developed by taking into account the fundamental physics of the problem. In addition, the experimental validation of the displacements of the ALICE ITS3 IB layers is a challenge, as the tight tolerances and the low mass of the system do not allow the use of invasive devices such as accelerometers (Wagner et al., 2015). The standard non-invasive techniques used in engineering, namely laser triangulation sensors, have been verified by the author as unsuitable due to the tight tolerances of the system. Thus, more accurate devices are needed for this particular case.

§3. Objectives and methodology

The main goal of this thesis is to carry out research and development steps for the air cooling system of the ALICE ITS3 IB, which will include open-cell carbon foams as heat exchangers and

structural supports. As discussed in §2.2, foam selection depends on different properties whose values are uncertain or unknown to the manufacturer. To the author's knowledge, there is no numerical methodology available in the literature to compute these properties with reasonable accuracy in a general case. The studies cited provide great accuracy, but for a limited range of validity that is usually not specified. The present thesis tackles this problem, and proposes in Chapter 2 a multiscale foam model for the characterization of open-cell foams, as well as an experimental setup for validation. Moreover, the effect of the glue penetration on the temperature of the foam-silicon interface is studied in a case of practical application for the ALICE ITS3 IB.

Based on the bibliographic study conducted in §2.1, the use of open-cell foams as heat exchangers combining heat conduction and convection is still not present in high-level engineering applications. Using the results obtained in Chapter 2, this work presents in Chapter 3 a novel application of open-cell foams in HEP. In addition to the design process, the full thermal analysis process is carried out, with a methodology divided into two parts: the development of a mathematical model, and the construction of an experimental setup with a prototype of the ITS3 IB for validation purposes.

Taking as a reference the design presented and validated in terms of cooling requirements in Chapter 3, the structural response of the ALICE ITS3 IB under aerodynamic loads is studied in Chapter 4; in particular, the aeroelastic study consists of the development of a simplified model of the fluid-structure interaction, and the results given by the model are compared with experimental measurements performed in the prototype presented in Chapter 3 using a confocal chromatic sensor.

Given the limitations of the current simulation approaches and importance of efficient and accurate turbulence models in industrial applications, a Generalized Wall-Modeled Large Eddy Simulation model (GWMLES) is developed in Chapter 5, which unifies the classical WMLES and hybrid RANS/LES to a model that solves in RANS the viscous sublayer and/or the log-layer. Finally, the most important conclusions are drawn in Chapter 6.

§4. Publications

Journal articles published

- **Amatriain, A.**, Gargiulo, C., and Rubio, G. (2023). Numerical and experimental study of open-cell foams for the characterization of heat exchangers. *International Journal of Heat and Mass Transfer*, 217(124701). DOI: 10.1016/j.ijheatmasstransfer.2023.124701.
- **Amatriain, A.**, Angeletti, M., Gargiulo, C., and Rubio, G. (2024). Development of an air cooling system with low material budget for high-energy physics applications. *Applied Thermal Engineering*, 236(121699). DOI: 10.1016/j.applthermaleng.2023.121699.
- **Amatriain, A.**, Gargiulo, C., and Rubio, G. (2024). Generalized wall-modeled large eddy simulation model for industrial applications. *Physics of Fluids 36(015141)*. DOI: 10.1063/5.0180690.

Journal article under review

- **Amatriain, A.**, Angeletti, M., Gargiulo, C., and Rubio, G. (2024). Aeroelastic analysis of a future particle detector. Preprint submitted to Aerospace Science and Technology.

Chapter 2

Characterization of open-cell foams

In this chapter the characterization of open-cell foams is done to select adequate foams for the ALICE ITS3 IB; in particular, in terms of the pressure loss, the thermal conductivity, and the Nusselt number. Taking into account two geometric scales (microscopic and macroscopic), a multiscale foam model is proposed that can be applied to a wide range of porosities, cell sizes, and materials. Moreover, the effect of glue penetration on the temperature of the foam-silicon interface is studied numerically and experimentally in a case of practical application. This chapter is divided as follows: first, the methodology consisting of the development of an experimental setup and the multiscale model is explained in §1. Then, simulation and experimental results are discussed in §2.

§1. Methodology

Four types of foams will be considered, whose main features are shown in §1.1. The experimental setup built at CERN to obtain foam properties is described in §1.2. Then, in §1.3 the multiscale model is presented, which is applied to two geometric scales: the microscopic scale ℓ, which is representative of the characteristic foam cell size, and the macroscopic scale $\mathcal{L}$, which is representative of the characteristic length of the system where the foam is used. The microscopic model gives as output averaged properties. These properties are inputs to the macroscopic model, which is used to determine the thermal behavior of a macroscopic system.

§1.1. Foam overview

§1.1.1. Duocel® Al

Aluminum open-cell foams manufactured by ERG Aerospace (see Fig. 2.1a), with densities of 100-325 kg/m^3, and thermal conductivities of 2-7 W/(m $\cdot$ K). These foams are not planned to be used in the ALICE ITS3 IB. However, since extensive experimental results are available in the literature, these data will be used to validate the models developed for the calculation of the pressure loss, the thermal conductivity, the Nusselt number, and the overall heat transfer coefficient. The Nusselt number is referred to the (local) heat transfer coefficient h, while the overall heat transfer coefficient is related to the performance of a system on the macroscopic scale.

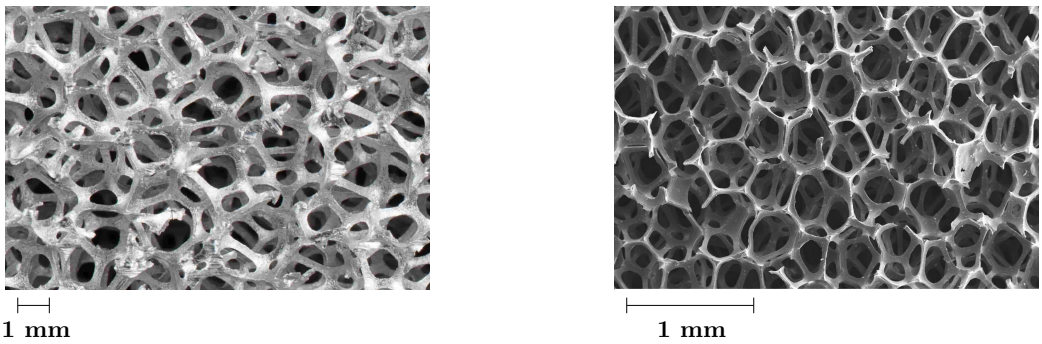

(A) Al-40 ($\Phi = 0.92$). (B) RVC 100 PPI.

FIGURE 2.1: Microscopy images of Duocel® foams obtained by the CERN EN-MME-MM section.

§1.1.2. Duocel® RVC

Open-cell foam manufactured by ERG Aerospace and made of Reticulated Vitreous Carbon (RVC), which is one of the morphological structures of vitreous carbon. The density $\rho_f = 45$ kg/m^3, with a number of 100 pores per inch (PPI) (see Fig. 2.1b). This foam is a thermal insulator ($\kappa_f \approx 0.05$ W/(m·K)); therefore, it cannot be used as a heat exchanger for thermal applications. However, the low density and high stiffness motivate its use as a structural part in the ALICE ITS3 IB. Thus, in this foam the only important result to be taken into account is the pressure loss.

§1.1.3. K9

The low thermal conductivity of the RVC foam is attributed to surface cracks that occur during heat treatment. Images of ligaments indicate that surface cracks are filled when the microstructure is coated by chemical vapor deposition (CVD) (Bonaad, 2012). This is the process carried out to produce the K9 foam manufactured by Lockheed Martin. The amount of carbon introduced determines the density of the resulting foam. In this thesis, the foam with $\rho_f \approx 200$ kg/m^3 is studied. Microscopy (SEM) images allow to notice the main microstructural difference between the RVC and the K9 foam: in the latter, the graphite coating is a new structure that increases the thickness of the filaments (see Fig. 2.2) and the thermal conductivity to $\kappa_f \approx 25$ W/(m · K).

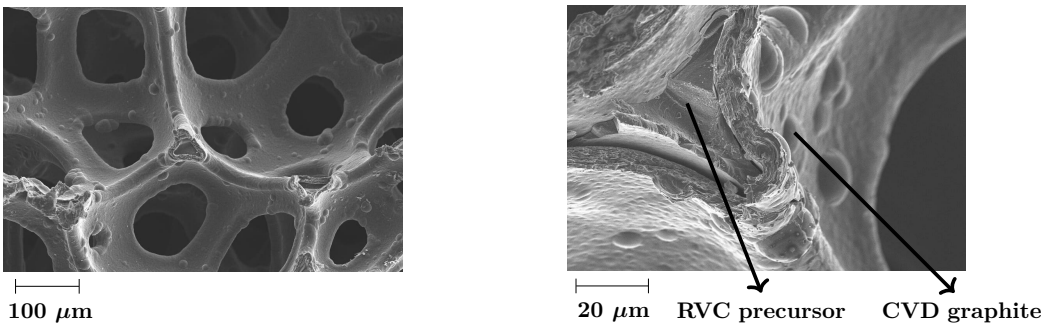

FIGURE 2.2: Microscopy images of the K9 foam obtained by CERN EN-MME-MM section.

§1.1.4. CFOAM® 35 HTC

Carbon foam of $\rho_f \approx 350$ kg/m^3 manufactured by CFOAM LCC that is made from mesophase pitch feedstock. Compared to the K9 foam, the CFOAM® 35 HTC has larger pores and more irregular surfaces, with multiple microcracks (see Fig. 2.3a). The structure is highly anisotropic, and the images have been taken from the most homogeneous zone. A CAD file has been obtained from a Computed Tomography (CT) scan performed at CERN (see Fig. 2.3b), which shows in the plane $x = 0$ that the cells are elongated in the z direction. The thermal conductivity in the y direction is 20-30 W/(m·K) is approximately twice as high as in the x and z directions. It has some closed cells, and is considered to be an alternative to the K9 foam to be used as a heat exchanger.

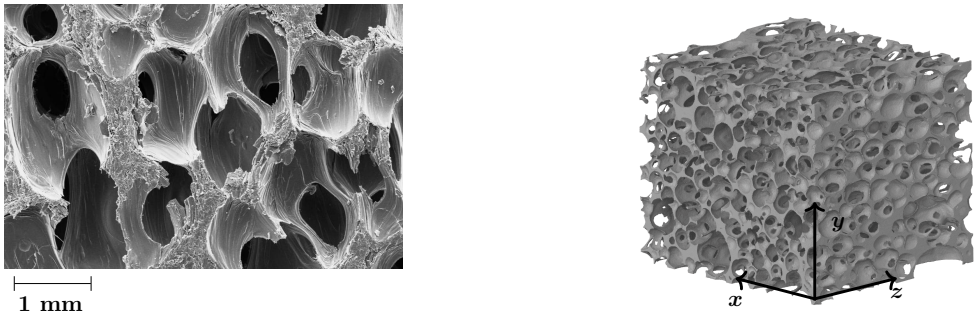

(A) Microscopy image. (B) CT scan.

FIGURE 2.3: Geometry of the CFOAM® 35 HTC foam obtained by CERN EN-MME-MM section.

§1.2. Experimental setup

An experimental setup has been built at CERN (see Fig. 2.4). The geometry of the tested foams are rectangular cubes of $l_x \times l_y \times l_z = 6 \times 60 \times 6$ mm that represent characteristic dimensions of the foams to be used in the ALICE ITS3 IB. The flow meter includes flow stabilizers at the inlet and at the outlet while providing a low pressure loss (275 Pa for $v_\infty = 10$ m/s) and an error of $\pm 0.07 v_\infty$. Simulations have been performed to deduce the minimum lengths of the different parts of the system, so that turbulence levels and non-uniformities do not affect the accuracy of the measurements. The pressure loss caused by the foam is measured by means of a differential pressure sensor of error ±50 Pa and whose ends are located at a distance of 50 mm to the center of the foam. The air temperature is measured by two PT1000 sensors of error ±0.15 K at a distance of 100 mm from the foam. To prevent air leaks, the 3D-printed flanges include rectangular cavities to place toric joints (see Fig. 2.4). The adapters, the flanges, and the frame are 3D printed in Accura 25 material, the circular pipe is made of CFRP, black PVC in the case of the frames, and the material of the rectangular pipes is black PLEXIGLAS®. The material selection—$\kappa < 0.2$ W/(m · K) in all of the heat transfer surfaces—has been done to maximize the thermal insulation of the system. In addition, Armaflex® ($\kappa = 0.03$ W/(m · K)) of 20 mm thickness has been added to reduce heat losses. To avoid the spread of carbon powder in the test room, the rectangular outlet pipe is connected with a vacuum cleaner. Data acquisition is done using LabVIEW software.

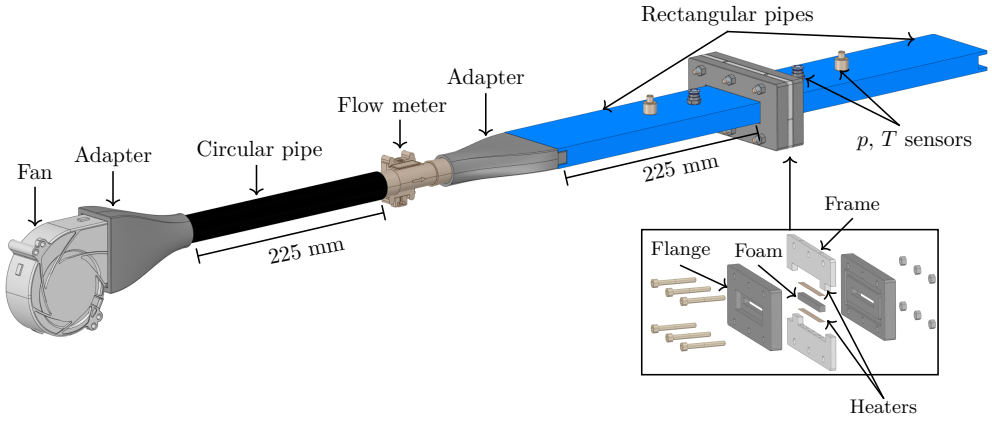

FIGURE 2.4: Experimental setup for foam characterization.

Two custom-made polyimide heaters of 100 µm of thickness—consisting of a copper layer of 5 µm surrounded by two polyimide layers ($\kappa = 0.2$ W/(m · K)) of 25 and 75 µm—are placed in contact with the foam in both sides to represent the heat dissipation of the silicon sensors (see Fig. 2.4), and the temperatures of the sides of the heater that are not in contact with the foam are measured by two PT1000 in each heater (see Fig. 2.5a). The PT1000s have planar dimensions of 1.6×1.2 mm, and are placed in the middle of the flow direction x. Assuming that the walls of the frame are adiabatic, $T_{\text{center}} = T_{\text{side}}$. However, soldered wires exit from the heaters near the wall, and the effective surface decreases in the neighbourhood of the soldering point. Thus, T_{side} gives additional information to determine possible gradients in the planar direction y.

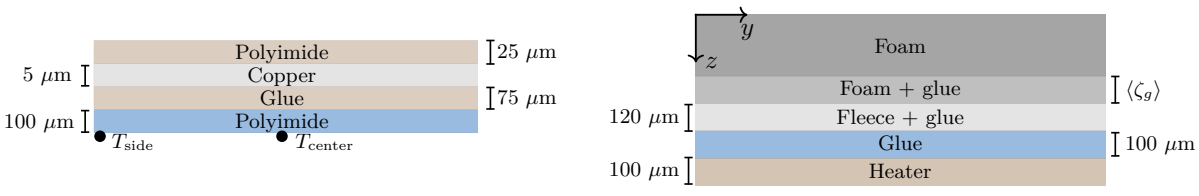

(A) Heater design.

(B) Foam-heater interface.

FIGURE 2.5: Details of foam samples used for foam characterization.

The setup aims to represent the thermal interface between the foams and the silicon layers of the ALICE ITS3 IB. Preliminary tests have shown that direct contact between foams and silicon sensors of 50 µm of thickness creates footprints on the sensor, which constitutes a risk of deterioration of measurement quality. To solve that issue, a carbon fleece of 120 µm of thickness and areal density of 8 g/m^2 is added between the foam and the heater. The fleece glued to the foam provides a smoother contact, with additional contact points to reduce the thermal resistance and increase the shear strength. The fleece also helps to control the thickness of the glue layer of mean thickness $\langle \zeta_g \rangle$ that penetrates into the foam (see Fig. 2.5b). In the assembly process, the foam is first glued to the fleece, and after the curing process, the resulting part is glued to the heater. The thickness of the glue layer between the fleece and the heater is 100 µm. The glue is the Epoxies® 50-3150 FR: an epoxy filled with alumina powder of 75 µm of mean diameter measured by the CERN EN-MME-MM section, and with a thermal conductivity measured at CERN $\kappa = 0.85$ W/(m · K).

§1.3. Multiscale model

The multiscale model is divided into two submodels (see Fig. 2.6):

- Microscopic model: in the microscopic domain Ω_f^ℓ, the geometry is based on a model of the unit cell of foams derived from the literature. After solving the Navier-Stokes equations in the microscopic domain with periodic boundary conditions, the pressure loss, the thermal conductivity, and the Nusselt number of foams are obtained.
- Macroscopic model: in the macroscopic domain $\Omega_f^\mathcal{L}$, mean variables are considered that are obtained by averaging fluid magnitudes in volume regions $\mathcal{L} > \ell^3$ for a sufficient $\mathcal{L}/\ell$ ratio that will be mentioned in the results section. This model uses a simplified geometry of the foam—which acts as a porous medium—and solves the Navier-Stokes equations with the addition of source terms. The source terms take into account the effect of the small scales of the order of ℓ on the large scales of the order of $\mathcal{L}$, and contain parameters obtained from the simulations of the microscopic model.

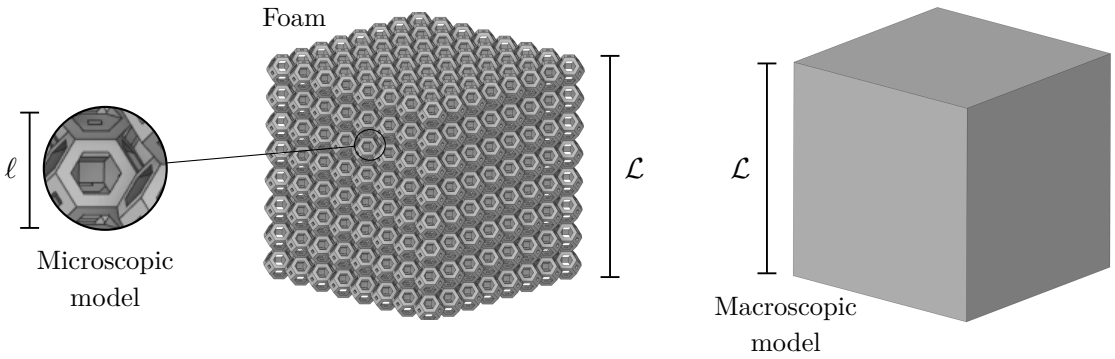

FIGURE 2.6: Geometric scales of the multiscale model.

§1.3.1. Microscopic model

Geometry

When looking for the space-filling arrangement of cells of equal volume that has minimum surface area, Lord Kelvin proposed a 14-sided truncated octahedron—named as tetrakaidecahedron by Kelvin—as a solution (Thomson, 1887). In the miscoscopic model, foams are modeled as uniformly-distributed cells of tetrakaidecahedrons. The starting point of the model is the completely solid geometry, and then volume is removed to obtain the frame structure (see Fig. 2.7).

Taking as references microscopy images of aluminum (Perrot et al., 2007) and graphite (Fig. 2.2) foams, triangular cross section is considered in the ligaments, with the same length of the sides of the rectangular and hexagonal faces. This implies that the size of the hexagonal and square

holes decreases as the porosity decreases. When $\Phi \approx 0.82$, the square holes disappear; therefore the model proposed is assumed to be valid for $\Phi > 0.82$. This result is applicable to the CFOAM, which has a lower number of holes per cell than the other foams considered (see Fig. 2.3a).

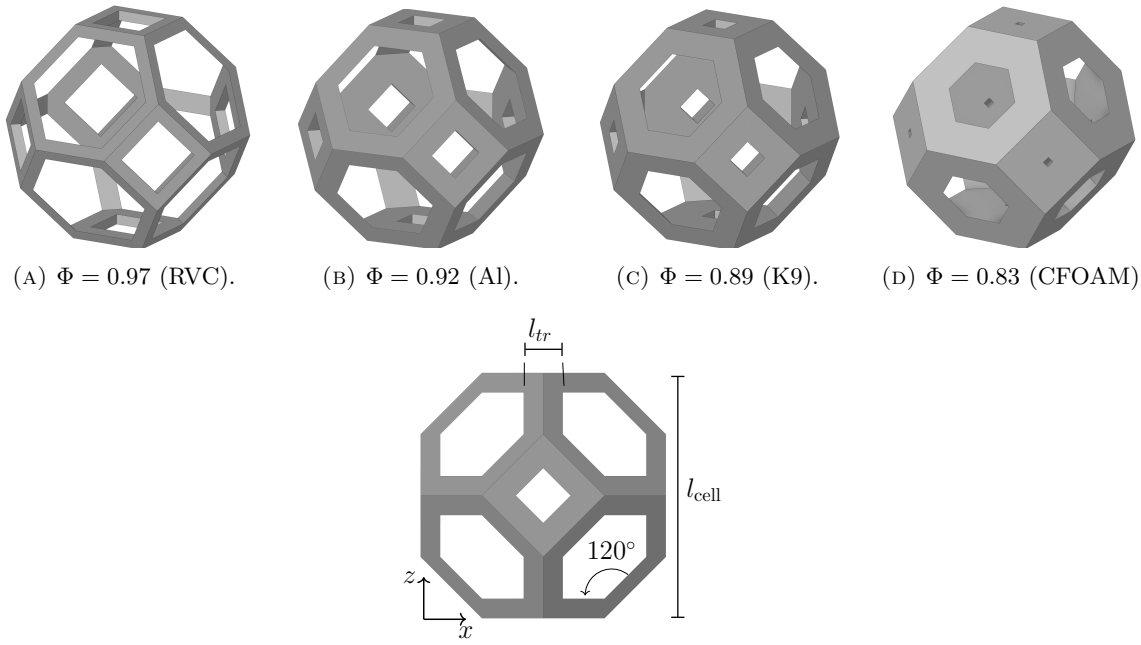

(A) $\Phi = 0.97$ (RVC). (B) $\Phi = 0.92$ (Al). (C) $\Phi = 0.89$ (K9). (D) $\Phi = 0.83$ (CFOAM).

(E) Front view for $\Phi = 0.92$ (Al).

FIGURE 2.7: Computational model of the microscopic geometry of the foams described in §1.1.

The dimensions of the unit cells are completely determined by specifying the values of the cell length l_{cell} and the ligament triangle side l_{tr}, which are derived from two inputs (see Fig. 2.7e):

- Porosity Φ: the ratio between the volume of the tetrakaidecahedron and the volume of the cube of edge length l_{cell}. It determines the amount of material that has to be removed from each tetrakaidecahedron so that the geometry is fixed up to a scaling factor.
- Specific surface area Σ_f: the ratio between the surface area of the tetrakaidecahedron and the volume of the cube of edge length l_{cell}. It determines the scaling factor that has to be applied to the geometrical model to obtain the completely defined geometry.

Foam	$\boldsymbol{\Phi}$	$\boldsymbol{\Sigma_f}$ **(1/m)**	$\boldsymbol{l_{\text{cell}}}$ **(μm)**	$\boldsymbol{l_{tr}}$ **(μm)**	**Experiments**	**Reference**
RVC	0.97	6600	390	35	$l_{\text{cell}} \approx 400$ μm	Fig. 2.1b
Al-10	0.92	750	5000	800	$l_{tr} \approx 640$ μm	(Perrot et al., 2007)
Al-20	0.92	1260	2975	475	$l_{tr} \approx 450$ μm	(Perrot et al., 2007)
Al-40	0.92	1800	2125	340	$l_{\text{cell}} \approx 2250$ μm	(Amani et al., 2018)
K9	0.89	14700	285	55	$l_{\text{cell}} \approx 300$ μm	Fig. 2.2
CFOAM	0.83	2500	3500	900	$l_{\text{cell}} \approx 3000$ μm	Fig. 2.3b

TABLE 2.1: Geometrical parameters of the microscopic model of the foams described in §1.1.

ERG Aerospace provides the values of the specific surface density of the Duocel® foams. The ligament thickness of the K9 foam is obtained at CERN by taking the mean value of the ligament thicknesses derived from microscope images (see Fig. 2.2), while the values of the CFOAM are obtained from the computed tomography scan performed at CERN (see Fig. 2.3b). The geometric parameters of the foams considered in this work are presented in Table 2.1. It is concluded that the values given by the computational model provide a reasonable approximation in all cases.

Equations

The incompressible Navier-Stokes equations for the air are (Pope, 2000):

$$\begin{cases} \nabla \cdot \boldsymbol{v} = 0 & (2.1) \\ \dfrac{\partial \boldsymbol{v}}{\partial t} + \boldsymbol{v} \cdot \nabla \boldsymbol{v} = -\dfrac{1}{\rho}\nabla p + \nabla \cdot [(\nu + \nu_t)\nabla \boldsymbol{v}] + \boldsymbol{M} & (2.2) \\ \dfrac{\partial T}{\partial t} + \boldsymbol{v} \cdot \nabla T = \nabla \cdot [(\alpha + \alpha_t)\nabla T] + Q, & (2.3) \end{cases}$$

where $\boldsymbol{v}$ is the velocity vector, t is the time, p is the pressure, ν is the dynamic kinematic viscosity, c_p is the specific heat capacity at constant pressure, T is the temperature, and α the thermal diffusivity. Eqs. (2.1) to (2.3) also contain the following assumptions, terms, and parameters:

- Implicitly-filtered Large Eddy Simulations (LES) are performed (see Appendix A, §2.1); therefore, all variables of the equations are implicity-filtered.
- The isotropic part of the *subgrid stress tensor* is included in the filtered pressure, and the *turbulent kinematic viscosity* ν_t derived from the Boussinesq assumption is provided by the WALE model with the wall constant $C_w = 0.325$ (see Appendix A, §2.2).
- The *viscous dissipation function* $\phi_v = \nabla \cdot (\tau \cdot \boldsymbol{v}) - \boldsymbol{v} \cdot (\nabla \cdot \tau)$ that contains the viscous stress tensor τ is neglected, since in terms of the Mach number $M^2/Re \ll 1$. Using the same reasoning, this term is also neglected in the equations of Chapter 3 and Chapter 4.
- The *turbulent thermal diffusivity* $\alpha_t = \nu_t / Pr_t$, where $Pr_t = 0.85$ is the turbulent Prandtl number (Kays, 1994). The value is shared by all models developed in this thesis.
- The *heat source* $Q = 0$.

Computation of the pressure loss, the thermal conductivity, and the Nusselt number

To compute the pressure loss, a single tetrakaidecahedron cell is used with periodic boundary conditions in the three spatial directions (see Fig. 2.8a). The pressure difference $\Delta p = p(x = l_{\text{cell}}) - p(x = 0)$ is periodic, and the numerical implementation is carried out with a body force in Eq. (2.2): $\boldsymbol{M} = \beta \hat{\mathbf{i}}$. The parameter β is the pressure gradient that is updated in each iteration of the numerical method, so that the mass flow rate is equal to $\dot{m} = \rho v_\infty l_{\text{cell}}^2$, where v_∞ is the freestream velocity. No-slip condition is imposed at the walls of the domain.

(A) Fluid domain. (B) Solid domain.

FIGURE 2.8: Geometry of the numerical simulations of the microscopic model.

Simulation results provide the pressure gradient that can be modeled as

$$\nabla p = \frac{\Delta p}{l_{\text{cell}}} = A v_\infty + B v_\infty^2 = \rho f \frac{v_\infty^2}{2 d_h} \tag{2.4}$$

for appropriate values of A and B (Bear, 2018). On the right-hand side of Eq. (2.4), f is the friction factor, and $d_h = 4\Phi/\Sigma_f$ is the hydraulic diameter.

The thermal conductivity of foams, κ_f, is also obtained from the simulation of a single tetrakaidecahedron (see Fig. 2.8b), which is in contact with two plates of negligible thermal resistance that are placed at $z_1 = 0$ and $z_2 = l_{\text{cell}}$ at temperatures T_1 and T_2. The heat equation is solved with the thermal diffusivity of the solid material $\alpha_s = \kappa_s/(\rho_s c_s)$, and adiabatic walls are considered except at the foam-plate contacts, where the equality of temperatures and heat fluxes is imposed. Regarding radiative heat transfer, previous studies for poliurethane (Coquard and Baillis, 2005) and metallic (Contento et al., 2014) foams—with cell sizes and porosities that are similar to the foams studied in this work—have shown that its contribution is $\kappa_r \sim 10^{-2}$ W/(m · K). Since the thermal conductivities of the foams used as heat exchangers $\kappa_f > 1$ W/(m · K) (see §1.1) and $\kappa_r/\kappa_f \ll 1$, then radiative heat transfer is neglected in the model. When simulations are finished, defining q as the heat flux between the plates, the thermal conductivity of the foam is calculated as follows:

$$\kappa_f = \frac{q l_{\text{cell}}}{(T_2 - T_1)}. \tag{2.5}$$

To compute the Nusselt number, periodic boundary conditions are applied in the momentum equation in the same way as in the calculation of the pressure gradient. In this case the Richardson number $Ri = g\beta\Delta T\mathcal{L}/v^2 \ll 1$ for the gravity acceleration $g \sim 10$ m/s^2, the air thermal expansion coefficient $\beta \sim 10^{-3}$ K^{-1}, $\Delta T \sim 10$ K, $\mathcal{L} \sim 1$ m and $v \sim 10$ m/s, which means that natural convection is negligible with respect to forced convection. Then, the Nusselt number is assumed to be a function of the Reynolds and Prandtl numbers, so the solid temperature distribution is assumed not to have an impact on the results. Based on the previous reasoning, the solid domain is not considered, and the fluid-solid surface temperature T_S is an input of the simulations that is set as constant. As air flows through the porous medium, its temperature approaches the wall temperature. At sufficient distance from the inlet, the fluid-to-wall temperature differences decay exponentially to zero. In the periodic thermally developed regime, the variable $\Theta = (T(\boldsymbol{x}) - T_S)/(\tilde{T}_\infty - T_S)$ is periodic (Patankar et al., 1977), where $\tilde{T}_\infty$ is the flux-weighted freestream temperature:

$$\tilde{T}_\infty = \frac{\displaystyle\int_{x=0} T|\rho\boldsymbol{v}\cdot \mathrm{d}\boldsymbol{\mathcal{S}}|}{\displaystyle\int_{x=0} |\rho\boldsymbol{v}\cdot \mathrm{d}\boldsymbol{\mathcal{S}}|}, \tag{2.6}$$

which is an input of the simulations. The heat transfer coefficient h is calculated at the surfaces of the microscopic domain $\partial\Omega_f^\ell$ as follows:

$$h = \frac{1}{A_p}\int_{\partial\Omega_f^\ell} \frac{q}{T_S - \tilde{T}_\infty}\,\mathrm{d}\mathcal{S} = \frac{1}{A_p}\int_{\partial\Omega_f^\ell} h\,\mathrm{d}\mathcal{S}, \tag{2.7}$$

where q is the heat flux, and A_p is the surface area of the porous medium. It has been verified that h defined in Eq. (2.7) does not depend on the values of the inputs T_S and $\tilde{T}_\infty$. The Nusselt number referred to the microscopic length scale ℓ is given by the following expression:

$$Nu_\ell = \frac{h\ell}{\kappa}. \tag{2.8}$$

§1.3.2. Macroscopic model

Geometry

The experiments considered in this work are rectangular channels with a foam that is placed at the origin of the coordinate system (see Fig. 2.9).

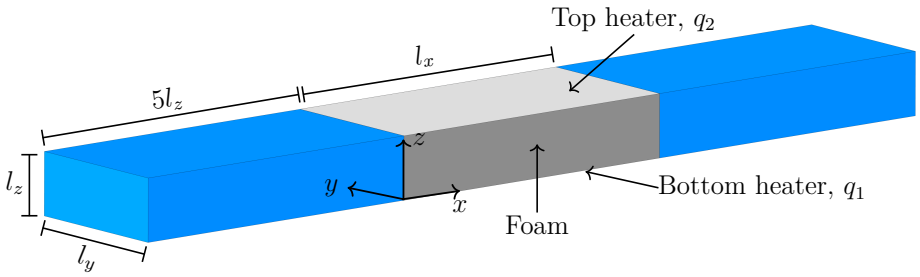

FIGURE 2.9: Geometry of the numerical simulations of the macroscopic model.

Equations

In the regions with no foam—colored in blue in Fig. 2.9— the equations are the same as those of the microscopic model (Eqs. (2.1) to (2.3)). In the foam region, some modifications are done:

- No turbulence model is considered; that is, $\nu_t = \alpha_t = 0$ in Eqs. (2.2) and (2.3).
- The *momentum source term* $\boldsymbol{M}$ takes into account the pressure loss of the foam (Bear, 2018):

$$\boldsymbol{M} = \Phi\left(\frac{\mu}{\mathcal{P}} + \frac{\Phi\rho C_d}{\sqrt{\mathcal{P}}}|\boldsymbol{v}|\right)\boldsymbol{v}\ \mathbf{1}_{\Omega_f^{\mathcal{L}}}, \tag{2.9}$$

  where $\mathbf{1}_{\Omega_f^{\mathcal{L}}}$ is the indicator function in the macroscopic domain $\Omega_f^{\mathcal{L}}$. The first component (Darcy's law) represents the drag of Stokes flows ($Re \ll 1$), while the second component (Forchheimer's law) provides the general expression for $Re \gg 1$, with $\mathcal{P}$ and C_d referring to the permeability and drag coefficients, respectively. Assuming that the flow reaches a steady state, and that viscous effects are negligible, the values are derived from Eq. (2.4):

$$\mathcal{P} = \frac{\mu}{A}, \quad C_d = \frac{B}{\rho}\sqrt{\frac{\mu}{A}}. \tag{2.10}$$

- The air and the solid material of the foam behave as a homogeneous mixture. Based on the theory of multiphase flows (Brennen, 2005), the specific enthalpy of the foam is:

$$\underbrace{\rho_f h_f}_{\text{Foam}} = \underbrace{\Phi\rho c_p(T - T_{ref})}_{\text{Air}} + \underbrace{(1-\Phi)\rho_s c_s(T_s - T_{ref})}_{\text{Solid}}, \tag{2.11}$$

  where $T_{ref} = 298.15$ K is the reference temperature, and T_s the solid temperature.

- The air temperature is given by Eq. (2.3) adapted to porous media (Bear, 2018):

$$\rho c_p\left(\Phi\frac{\partial T}{\partial t} + \boldsymbol{v}\cdot\nabla T\right) = \Phi\kappa\nabla^2 T + h\Sigma_f(T_s - T)\mathbf{1}_{\Omega_f^{\mathcal{L}}}. \tag{2.12}$$

  In Eq. (2.12), the heat transfer coefficient h obtained from the microscopic model (Eq. (2.7)) is used, and T_s refers to the solution of the energy equation in the solid:

$$(1-\Phi)\rho_s c_s\frac{\partial T_s}{\partial t} = \kappa_f\nabla^2 T_s + h\Sigma_f(T - T_s)\mathbf{1}_{\Omega_f^{\mathcal{L}}}. \tag{2.13}$$

Computation of the overall heat transfer coefficient

In the macroscopic model, the freestream velocity v_∞ and temperature T_∞ are the boundary conditions at the inlet, and zero gradient boundary conditions and pressure equal to the reference pressure for the flow variables at the outlet. Depending on the experiment considered, there are up to two copper heaters that provide a heat flux of q_1 and q_2. This is implemented with a source

term in the energy equation equal to the heat flux divided by the thickness of the heater. The plane $y = 0$ is considered to be a symmetry plane.

Two performance indicators of the system will be calculated: the mean temperature of the heaters T_w, which is the area-weighted average of the temperature of the mesh faces in contact with the heater surface, and the overall heat transfer coefficient (Mancin et al., 2013):

$$U = \frac{P_h}{A_h \Delta T_{log}}, \tag{2.14}$$

where $A_h = l_x l_y$ is the surface area of the heater, and P_h is the power supplied by the heater. Assuming that the walls of the domain are adiabatic, the energy equation in a control volume consisting of the domain of Fig. 2.9 states that all power is transferred to the air:

$$P_h = P_{\text{air}} = \dot{m}(h_0^{\text{out}} - h_0^{\text{in}}), \tag{2.15}$$

where h_0 is the air specific stagnation enthalpy. Since the sectional areas of the inlet and outlet are the same, Eq. (2.15) is reduced to

$$P_h = \dot{m} c_p (T^{\text{out}} - T_\infty) = \rho v_\infty l_y l_z c_p (T^{\text{out}} - T_\infty). \tag{2.16}$$

The last term of Eq. (2.14) to be defined is the logarithmic temperature difference ΔT_{log}:

$$\Delta T_{log} = \frac{(T_w^{\text{in}} - T_\infty) - (T_w^{\text{out}} - T^{\text{out}})}{\ln\left(\dfrac{T_w^{\text{in}} - T_\infty}{T_w^{\text{out}} - T^{\text{out}}}\right)}, \tag{2.17}$$

where T_w^{in} and T_w^{out} are the inlet and outlet temperature of the wall in contact with the foam, and T^{out} is the outlet air temperature.

Analytical solution

An analytical approach will be derived to study the influence of the parameters of the problem in preliminary studies. As a first approximation, the following assumptions are made:

- The air and the solid material of the porous medium are in thermal equilibrium.
- The flow is two-dimensional, and a steady condition is reached.
- The longitudinal (x) velocity v_∞ is the only non-zero component of the velocity vector.

In the thermal boundary layer, the energy equation and the boundary conditions are:

$$\begin{cases} v_\infty \dfrac{\partial T}{\partial x} = \alpha_f \dfrac{\partial^2 T}{\partial z^2} & \text{in } \Omega_f^{\mathcal{L}} \quad (2.18) \\ \kappa_f \dfrac{\partial T}{\partial z} = q & \text{in } \partial\Omega_f^{\mathcal{L}} \quad (2.19) \\ T \to T_c & \text{if } z \to \infty, \quad (2.20) \end{cases}$$

where $\alpha_f = \kappa_f/(\rho c_p)$ is the foam thermal diffusivity, and T_c is a characteristic temperature. Introducing the following self-similar variables

$$\eta = \sqrt{\frac{v_\infty}{\alpha_f}} \frac{z}{\sqrt{x}}, \qquad \Theta = \sqrt{\frac{v_\infty}{\alpha_f}} \frac{\kappa_f}{q} \frac{T - T_c}{\sqrt{x}}, \tag{2.21}$$

then the previous equation can be solved analytically to give:

$$\Theta = \frac{2}{\sqrt{\pi}} \exp\left(-\frac{\eta^2}{4}\right) - \eta \operatorname{erfc}\left(\frac{\eta}{2}\right), \tag{2.22}$$

where erfc is the complementary error function. The solution at the wall is:

$$T_w - T_c = 2q\sqrt{\frac{x}{\pi\rho c_p \kappa_f v_\infty}}. \tag{2.23}$$

§1.3.3. Numerical implementation

Mesh

In the microscopic model, the computational mesh uses octrees in the bulk region, with a polyhedral mesh near the walls. Two different cell sizes are considered: one for the bulk region, Δ, and other near the walls with the size obtained from a mesh-independence study. This mesh is used to calculate the pressure loss and the Nusselt number, while the mesh used for the calculation of the thermal conductivity has only one cell size equal to Δ. In what follows, all meshes considered in this thesis are obtained using the Ansys Fluent Meshing tool (Ansys Inc., 2023a).

The computational mesh of the simulations of the macroscopic model consists of octrees in the bulk region, which are connected to a layered prism mesh in the boundary layers with polyhedral elements. After performing a mesh-independence study, two different cell sizes are considered taking as a reference Fig. 2.9: one for the blue domain equal to $l_z/20$, and other for the foam (gray) domain equal to $l_z/40$. The number of prism layers in the boundary layers near the walls of the domain is equal to 15. Two identical domains are created for the air and solid regions of the foam, and Eq. (2.3) and Eq. (2.13) are solved in the corresponding domain. All solid layers with high aspect ratios such as the heaters are implemented using the Shell Conduction model. This model does not require that the wall thickness is taken into account in the mesh generator. The solid layers mentioned are automatically generated by the Ansys Fluent solver before the simulation starts (Ansys Inc., 2023a). The shells are adiabatic on the sides, where there is no physical contact with other components, and otherwise the equality of the temperatures and heat fluxes is imposed. In the shell-foam contacts, the shells are coupled with the solid domain of the porous medium.

Resolution of the equations

Equations are solved with the finite volume method (see Appendix B) that is implemented in Ansys Fluent 2023R1 (Ansys Inc., 2023a). Flow variables are stored at cell centers, and cell face values are obtained from interpolation schemes. The central differencing scheme is used for all terms of the equations (see Appendix B, §1.1.1), and Rhie-Chow interpolation is used to avoid pressure checkerboarding (see Appendix B, §1.4). Gradients are obtained with the least-squares procedure (see Appendix B, §1.1.2), and the temporal discretization is done with the second order implicit scheme (see Appendix B, §1.2). The pressure-velocity coupling is performed with the SIMPLEC algorithm (see Appendix B, §2.1), and in each iteration the linearized system of algebraic equations is solved with an algebraic multigrid (AMG) method (see Appendix B, §3.2). The simulations are performed from a precursor RANS simulation (steady-state solver with second-order upwind discretization in the convective terms), with a time step dt such that the cell convective Courant number $Co = v_{\text{cell}} dt / l_{\text{cell}} < 1$, with the globally-scaled residuals (see Appendix B, §3.4) $< 10^{-4}$ (continuity), $< 10^{-5}$ (momentum), and $< 10^{-8}$ (energy) at all time steps. These values, which are kept as references to numerical convergence in what follows, are lower than those given by default in Ansys Fluent of $< 10^{-3}$ (continuity, momentum) and $< 10^{-6}$ (energy). The simulations are finished when output variables reach a statistically steady state. The methodology is shared by all simulations performed during this thesis, with minor differences in other chapters related to the spatial discretization and the pressure-velocity coupling. Thus, in the following chapters, only those differences with respect to the content shown in this paragraph will be highlighted.

§2. Results and discussion

In this section, the accuracy of the microscopic model is first assessed in §2.1. Then, the validated outputs of the microscopic model are used in the macroscopic model, whose results are compared with experimental data and the analytical solution in §2.2.

Simulation parameters are shown in Table 2.2. The physical properties are obtained from (ASM, 1991) (Al and Cu), and by private communication with the supplier of the K9 foam, the polyimide (PI), and the glue. The density and thermal conductivity of the K9 material are those of the solid material (RVC+graphite). The value of the thermal conductivity of the glue tested at CERN is considered instead of the one provided by the official datasheet ($\kappa = 2.16$ W/(m · K)).

Symbol	Material	Parameter	Value	Units
c_p	Air	Specific heat at constant pressure	1006	J/(kg · K)
c_s	Al	Specific heat	900	J/(kg · K)
	Cu		385	
	Glue		1000	
	K9		710	
	PI		1100	
κ	Air	Thermal conductivity	0.025	W/(m · K)
	Al		218	
	Cu		385	
	Glue		0.85	
	K9		1500	
	PI		0.2	
μ	Air	Dynamic viscosity	1.837×10^{-5}	Pa · s
ρ	Air	Density	1.184	kg/m^3
	Al		2700	
	Cu		8930	
	Glue		1600	
	K9		1800	
	PI		1420	
	RVC		1500	

Table 2.2: Simulation parameters of the multiscale model.

The properties of Table 2.2 are taken at 298 K. In the simulations the air and solid temperatures vary between 298 K and 398 K. In this range, the properties whose variations are greater than 10% are the air thermal conductivity and dynamic viscosity (both $\approx 25\%$ higher at 398 K). This temperature dependence is neglected in the present model, since it is assumed that the error is of the same order as those of the simplifications of the multiscale model, the uncertainty on the foam production process, and the accuracy of the experimental devices.

§2.1. Microscopic model

The accuracy of the microscopic model will be tested for the pressure loss in §2.1.1, the thermal conductivity in §2.1.2, and the Nusselt number in §2.1.3.

§2.1.1. Pressure loss

First, a mesh independence study is done with four different mesh sizes. The mesh element length Δ near the walls is two times smaller than in the interior. Other different ratios have been tested such as 1/1, 1/4, and 1/8, and the 1/2 ratio provides the optimum balance between accuracy and computational cost. For error estimation, the mean (time-averaged) pressure loss $\langle \nabla p \rangle$ is approximated with a second-order series expansion as a function of the interior mesh element length. Based on Table 2.3, the mesh of 2.5×10^5 elements is chosen for subsequent simulations, whose error is estimated to be around 8% from the series expansion. It is verified that the differences between the results obtained with the WALE model and without modeled turbulence are lower than 1% (see Table 2.3). The reason why LES is considered in all foams is that, for Duocel® Al foams, the Reynolds number increases to $Re_{l_{\text{cell}}} = 3500$ in the cases that will be considered in this section. For $Re_{l_{\text{cell}}} > 250$ the flow in foams is expected to be turbulent (Hall and Hiatt, 1996; Della Torre et al., 2014), with a Kolmogorov length scale that satisfies $l_{\text{cell}}/\eta \sim Re_{l_{\text{cell}}}^{3/4} \sim 10^2$; therefore, $\eta \sim 10\Delta$. Simulations have been performed with cubes consisting of multiple unit cells in each direction and without periodic boundary conditions. The results have lead to the conclusion that the error of the periodic model is lower than 5% when the real geometry of the foam has more than eight cells in each direction; that is, with the geometric scales illustrated in Fig. 2.6, entrance and exit effects are considered to be negligible for $\mathcal{L}/\ell \geq 8$.

Mesh element length		**Mesh element number**	$\langle \nabla p \rangle$ **(Pa/mm)**	$\langle \nabla p \rangle$ **(Pa/mm)**
Walls	**Interior**		**(LES)**	**(No model)**
$l_{\text{cell}}/50$	$l_{\text{cell}}/25$	5.5×10^4	174.2	173.6
$l_{\text{cell}}/100$	$l_{\text{cell}}/50$	2.5×10^5	181.2	181.2
$l_{\text{cell}}/200$	$l_{\text{cell}}/100$	1.4×10^6	187.9	187.9
$l_{\text{cell}}/400$	$l_{\text{cell}}/200$	9.5×10^6	191.7	191.7

TABLE 2.3: Results of the mesh independence study for the RVC foam at $Re_{l_{\text{cell}}} = 275$.

Experiments performed at CERN in the setup described in §1.2 and data provided on the official ERG website are taken as references for comparison of the results. Figure 2.10 compares the numerical results given by the macroscopic model and experimental data. The test and simulation results show significant agreement at all values of the freestream velocity for the Duocel® and K9 foams, with discrepancies that are of the order of the sensor error, although the simulations overpredict the pressure loss in the Al-20 foam for $Re_{l_{\text{cell}}} > 1250$. However, the porosities of the RVC and K9 samples have been measured at CERN with precision balances, but the exact value of Duocel® Al foams tested by the manufacturer (ERG) is unknown. Thus, small deviations from the nominal value can lead to differences as those shown in Fig. 2.10b. The maximum pressure loss that the fan can provide is 3400 Pa, while the pressure loss of a sample of the K9 foam of $6 \times 60 \times 6$ mm is $750 \times 6 = 4500$ Pa (see Fig. 2.10c). To obtain the value of the pressure loss of the K9 foam at $Re_{l_{\text{cell}}} = 175$, a sample of $3 \times 60 \times 6$ mm is tested. Since the cell size of the K9 foam is 285 µm, in 3 mm length there are $3/0.285 \approx 10$ cells. This value is higher than the number of 8 cells from which the error of the periodic assumption is considered to be negligible.

Figure 2.10d shows that the homogeneous tetrakaidecahedron model does not correctly predict the pressure loss of the CFOAM®. The characteristic cell size obtained from the CT scan is approximately 3 mm, and the foam length is 6 mm, which means that there are two unit cells in the longitudinal direction. Thus, the periodic assumption is not justified. However, experimental data give values that are one order of magnitude higher than the simulation values, which is a large deviation even if the periodicity error is considered. This is attributed to the reduced number of pores and the presence of closed cells in the CFOAM (see Fig. 2.3). The CFOAM is not an entirely open-cell foam; therefore, the microscopic model is not applicable to this foam.

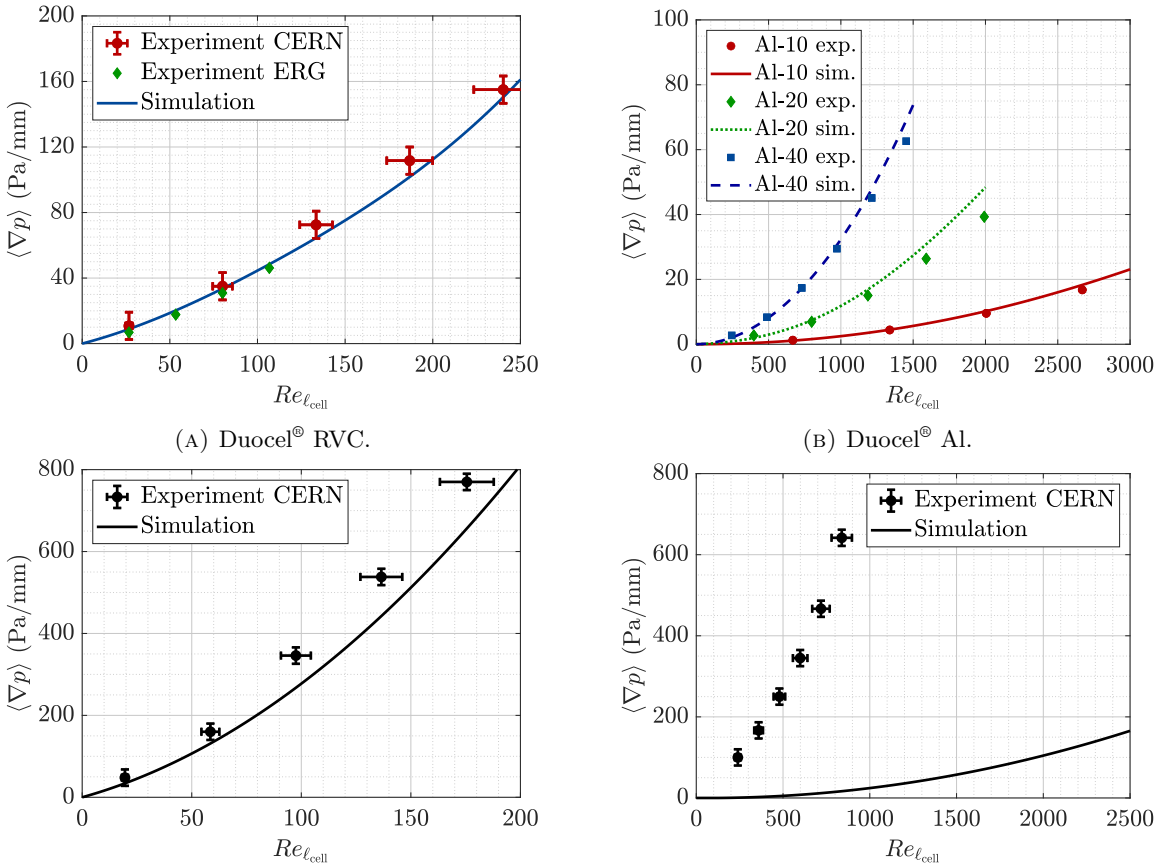

(A) Duocel® RVC.

(B) Duocel® Al.

(C) K9.

(D) CFOAM® 35 HTC.

FIGURE 2.10: Simulation and experimental results of the pressure loss produced by open-cell foams.

§2.1.2. Thermal conductivity

Figure 2.11a compares the thermal conductivity given by the microscopic model and experimental data of aluminum foams, which has been obtained with the direct contact method: (Calmidi and Mahajan, 1999) (Experiment 1), (Paek et al., 2000) (Experiment 2), (Sadeghi et al., 2011) (Experiment 3), and (Amani et al., 2018) (Experiment 4). Experiments 1 to 3 assume that the foams are isotropic, although in Experiment 4 differences between the planar and vertical directions were claimed, which are represented by the two values in Fig. 2.11a. The simulation results are interpreted as average values in all directions.

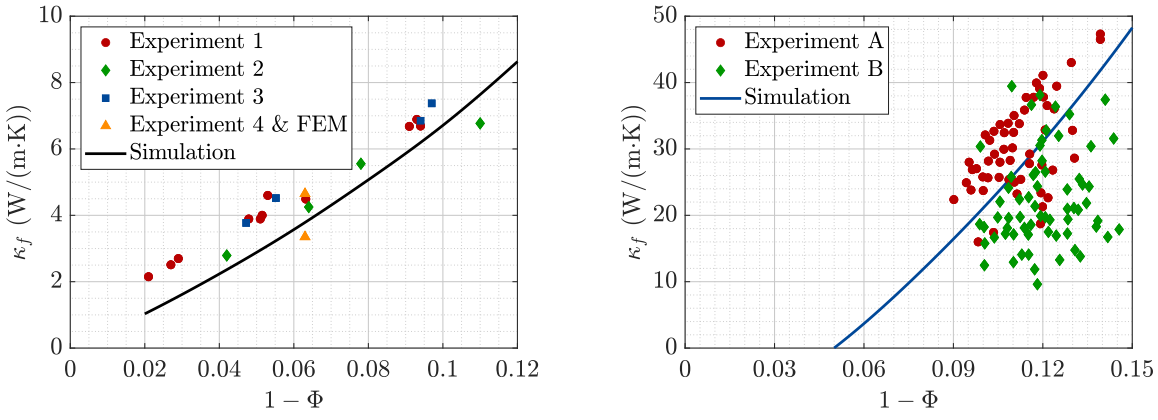

(A) Duocel® Al.

(B) K9.

FIGURE 2.11: Simulation and experimental results of the thermal conductivity of open-cell foams.

Figure 2.11b depicts the experimental results obtained from the laser flash method (Gilchriese et al., 2012) (Experiment A), from the direct contact method (Experiment B performed by the manufacturer), and from the simulations of the K9 foam. The scattering of the experimental data is due to the lack of repeatability of the production process. Assuming that there are no errors in the measurements, it is suspected that the differences between the methods are because the laser flash method is not accurate in foams. In this method, the thermal conductivity is obtained from the time derivative of the fundamental solution of the heat equation, which is based on the assumption that Fourier's law of heat conduction is valid. However, recent experiments in metal foams have shown that Fourier's law underpredicts the time derivatives of the temperature distributions (Kovács et al., 2022). Thus, as a conservative approach, in what follows, the values obtained from the direct contact method will be taken as references. The simulations predict approximately the mean value of the experimental data for all values of Φ, and in particular $\kappa_f \sim (1-\Phi)^2$, which is the case of the experimental results when broader ranges of porosities are considered (Gilchriese et al., 2012).

§2.1.3. Nusselt number

To validate the results of the Nusselt number given by the microscopic model, the correlation obtained from experiments of Duocel® Al foams (Mancin et al., 2013) will be used:

$$Nu_{l_{tr}} = ARe_{l_{tr}}^{n} Pr^{1/3}, \tag{2.24}$$

where the constants $A = 0.418$ and $n = 0.53$, the Nusselt number $Nu_{l_{tr}} = h\ell_{tr}/\kappa$, the Reynolds number $Re_{l_{tr}} = \rho v_\infty l_{tr}/(\mu\Phi)$, and the Prandtl number $Pr = \mu c_p/\kappa$.

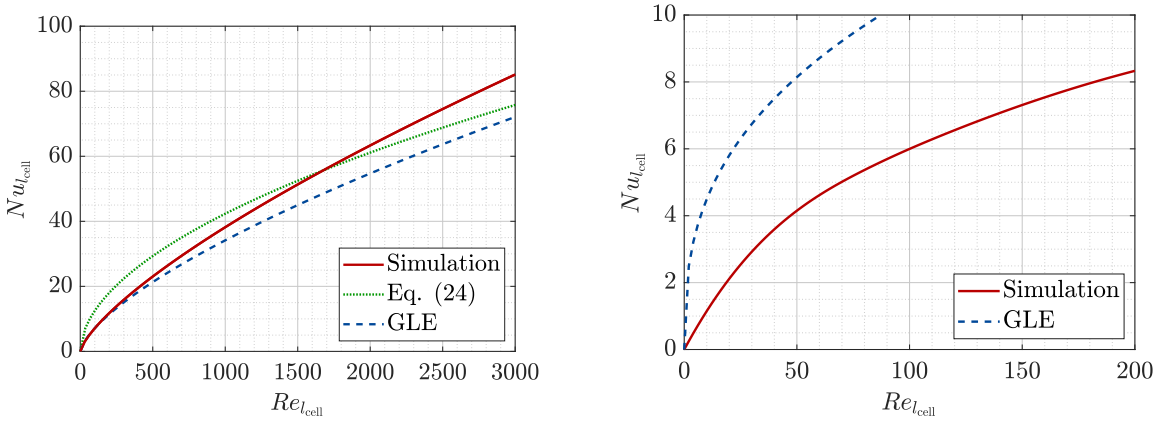

(A) Duocel® Al. (B) K9.

FIGURE 2.12: Simulation and correlation results of the Nusselt number of open-cell foams.

The measurement of heat (and mass) transfer coefficients is usually more complicated than the measurement of the pressure loss. Thus, the accuracy of the Generalized Lévêque Equation (GLE) will also be considered, which provides a general expression of the heat transfer coefficient as a function of the coefficients of the pressure loss curve (Martin, 2002):

$$Nu_{l_{\text{cell}}} = 0.404(\chi f d_h/l_{\text{cell}})^{1/3} Re_{l_{\text{cell}}}^{2/3} Pr^{1/3}, \tag{2.25}$$

where the friction factor f is given by Eq. (2.4), and $\chi = (f-B)/f$ is the fraction of the pressure loss due to viscous forces with B defined in Eq. (2.4). Given that Eqs. (2.24) and (2.25) are referred to different Reynolds numbers, the identity $l_{\text{cell}} = 6.25 l_{tr}$ derived from Table 2.1 is used to refer all Reynolds numbers to the same length scale.

The comparison between the numerical results and the correlation in Fig. 2.12a shows that the heat transfer coefficient increases as the cell size decreases, since $Nu_{l_{tr}} \sim Re_{l_{tr}}^{n}/l_{tr} \sim l_{tr}^{n-1}$ and $n-1 < 1$ from Eq. (2.25). The numerical values of the Nusselt number of all variants of Al foams are the same for a fixed $Re_{l_{\text{cell}}}$, and agree well with Eqs. (2.24) and (2.25), with maximum differences

of 20%, which are reasonable given the assumptions done in the model, the uncertainties related to the foam production process, and the errors of the measurement systems. Satisfactory results were also obtained with the correlation in previous studies applied to foams with similar geometrical parameters (Incera Garrido et al., 2008). The opposite conclusion can be drawn from Fig. 2.12b. The reason for the discrepancy can be that in Eq. (2.25) the product χf is approximately constant in the cases considered in Fig. 2.12a, while for the K9 foam χf is strongly dependent on $Re_{l_{\text{cell}}}$ and alters the $Re_{l_{\text{cell}}}^{2/3}$-dependency of the GLE equation. An improvement of the GLE could be based on considering variations of the expression for low Rynolds numbers.

The correlation given by Eq. (2.24) applied to the numerical results gives constants $a \approx 0.12$ and of $n \approx 0.75$ for the Duocel® Al foams, while $a = 0.11$ and $b = 0.55$ for the K9 foam. These exponents are similar to the values of the laminar flow in a flat plate ($n = 0.5$), and the turbulent flow in a flat plate and in a circular tube ($n = 0.8$ in both cases) (Schlichting, 1979). Since there are no significant variations in the heat transfer coefficient among the foams studied ($h \sim 10^2$ W/(m$^2 \cdot$K)), what makes the difference in the thermal performance—apart from the foam thermal conductivity—is the specific surface area (see Eq. (2.13)). This is because the surface areas of foams differ by up to one order of magnitude (see Table 2.1). Variations in the Nusselt as a function of the foam porosity have been verified to be negligible.

§2.2. Macroscopic model

The pressure loss, thermal conductivity, and Nusselt number obtained from the microscopic model are used to validate the results given by the macroscopic model. Two values will be analyzed in this work: the overall heat transfer coefficient of Duocel® Al foams in §2.2.1, and the temperature of the heaters in contact with the K9 foam in §2.2.2.

§2.2.1. Overall heat transfer coefficient

The overall heat transfer coefficient U of Duocel® Al foams has been experimentally measured (Mancin et al., 2013). The lengths are $l_x = 100$ mm, $l_y = 50$ mm, and $l_z = 20$ mm (see Fig. 2.9), and $L = l_z$ for the calculation of the Reynolds number Re_L. In the plane $z = l_z$, an aluminum plate of 10 mm is placed in contact with the foam, and a heater made of copper of $\xi = 7$ mm of thickness is placed in in contact with the aluminum plate. The heater provides a heat flux $q_2 = 2.5 \times 10^4$ W/m^2 ($q_1 = 0$). In Eq. (2.17), the inlet and outlet wall temperatures are defined at $x^{\text{in}} = 20$ mm and $x^{\text{out}} = 80$ mm, respectively. In the experiment, the air outlet temperature is measured by six temperature sensors placed after a mixer in the plane $x \approx 200$ mm. In the simulations it is considered to be the area-weighted temperature in that plane. The thermal conductivity and the Nusselt number used in the simulations are obtained from Fig. 2.11a and Fig. 2.12a.

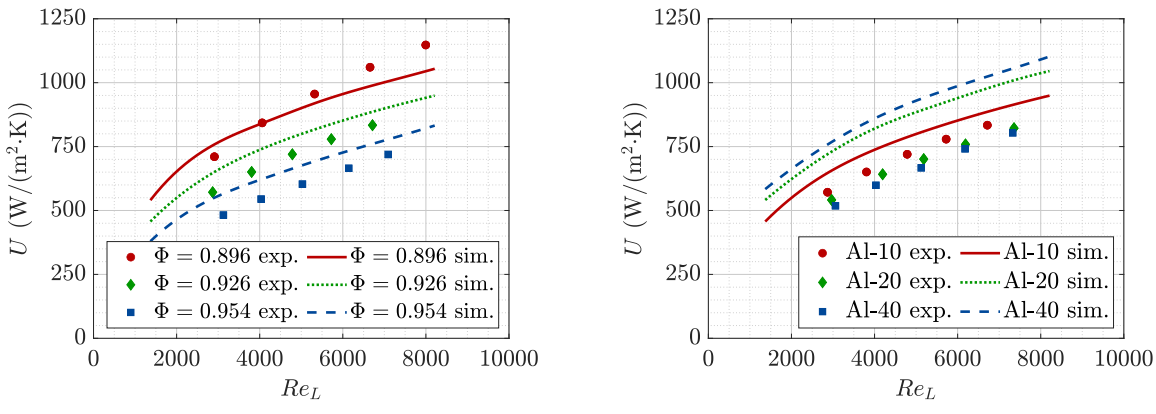

(A) Al-10. (B) $\Phi \approx 0.93$.

FIGURE 2.13: Simulation and experimental results of the overall heat transfer coefficient of Duocel® Al foams.

Experimental and simulation results of the overall heat transfer coefficient defined by Eq. (2.14) are compared in Fig. 2.13a. The maximum error of the simulations is 15%, and leads to the conclusion that the results given by the macroscopic model are accurate. The shape of the curve is better approximated when $\Phi = 0.926$ and $\Phi = 0.954$, although the increase in the slope of the curve at $Re_L \approx 2000$ is captured correctly in all cases. This behavior is closely related to the decrease of the Nusselt number for low values of the Reynolds number (see Fig. 2.12a).

Figure 2.13b depicts the numerical and experimental results of three variants of the Duocel® foams for $\Phi \approx 0.93$. The differences between simulations and experiments increase as the cell size is decreased, since the experimental results predict that the overall heat transfer coefficient decreases as the cell size decreases, while the model developed provides the opposite trends. For a fixed Reynolds number, the heat transfer coefficient increases as the cell size decreases (see §2.1.3), and the thermal conductivity does not depend on the cell size (Amani et al., 2018); therefore, the correct dependency is expected from the numerical results. The anisotropic thermal conductivity (see §2.1.2) and the lack of repeatability of the production process may play an important role in the mentioned discrepancies. In addition, errors related to the model developed and the experimental data add additional uncertainties to the comparison. Other sources of error may come from the fact that the overall heat transfer coefficient defined in Eq. (2.17) depends on four temperature measurements, and that the ln function (Eq. (2.17)) is sensitive to small perturbations.

§2.2.2. Heater wall temperature

Due to its higher specific surface area and thermal conductivity with respect to the Duocel® Al foams, the K9 foam is concluded to be the one that provides the best thermal performance among the foams studied. The experimental setup described in §1.2 is used to determine the thermal performance of the K9 foam in a case of practical application.

To understand the effect of the glue penetration, six samples of mean glue penetration $\langle \zeta_g \rangle = 30, 80, 130, 180, 280$ and 380 µm are tested in the setup. Based on Fig. 2.5b, in the simulations the foam-heater interface is modeled as a layer of $100 + 120 = 220$ µm of thickness, with the thermal conductivity equal to the one of the glue. The heat fluxes are $q_1 = q_2 = q$, and the reference heat flux is $q_0 = 10^4$ W/(m · K). Since the pressure loss that the fan can provide is limited, seven equispaced holes of 1.5 mm are drilled in the foam that provide a 20% of reduction in the pressure loss. In the simulations the $y = 0$ and $z = 0$ planes are symmetry planes, so the lengths of the computational domain are $l_x \times l_y \times l_z = 6 \times 30 \times 3$ mm, and $L = l_z$. The thermal conductivity is given by the simulation curve (see Fig. 2.11b) for $\Phi = 0.89$ (see Table 2.1). During the tests, it has been verified that Eq. (2.14) holds with a difference of less than 5% between the two terms.

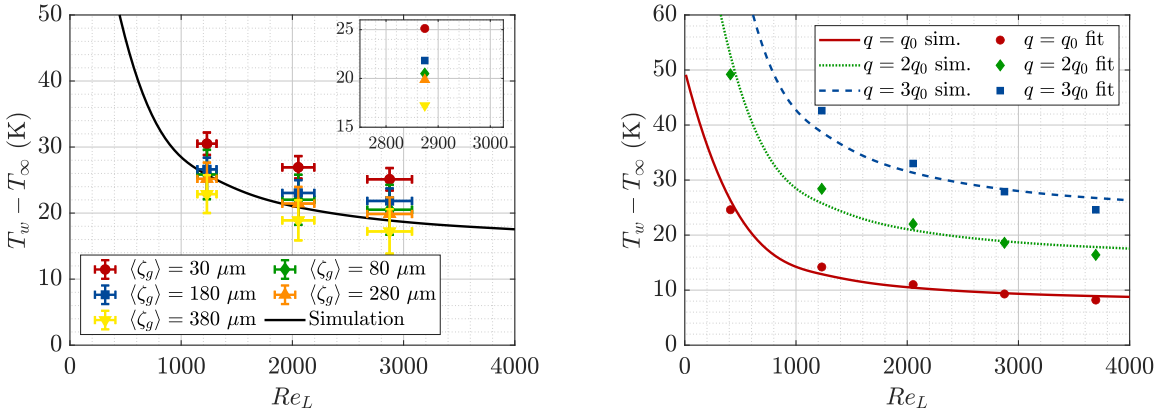

(A) Effect of glue penetration for $q = 2q_0$.

(B) Effect of the heat flux.

FIGURE 2.14: Simulation, experimental, and analytical results of the heater wall temperature difference with respect to the freestream temperature in the K9 foam.

Figure 2.14a illustrates the difference between the heater wall temperature and the freestream temperature for different Reynolds numbers. The wall temperature values (T_w) are those of the temperature sensors located at the center of the heater T_{center} (see Fig. 2.5a). The values of T_{side} are in all cases around 15% lower. This temperature non-uniformity is because the total surface area of the heaters is lower than 6×60 mm due to the presence of soldering points for the cables. The case of $\langle\zeta_g\rangle = 30$ µm gives the highest temperature values, and is expected to be sensitive to variations in the glue thickness, therefore it is discarded for the future. The heater wall temperature decreases when the penetration of the glue increases because the thermal resistance is reduced. The compromise between thermal performance and material budget is concluded to be $\langle\zeta_g\rangle = 280$ µm, which is in line with the value $\langle\zeta_g\rangle = 250$ µm obtained by the CMS Collaboration ((Mussgiller, 2016)). However, unlike in the CMS tests, the temperature variations are reasonably bounded in all cases with the proposed assembly procedure explained in §1.2.

The boundary layers of the two heaters interact, and from Eq. (2.20) it is deduced that $T_c \neq T_\infty$. This means that the analytical solution (Eq. (2.23)) is not able to provide a good approximation of the heater wall temperature. However, based on the analytical expression, the numerical results have been fitted to a curve as follows:

$$T_w - T_\infty = \sqrt{C}\frac{q}{\sqrt{v_\infty}} \tag{2.26}$$

for a constant $C = 6.04 \times 10^{-6}$ K$^2\cdot$m^5/(W$^2\cdot$s) that is obtained from minimization of the differences of the numerical results and Eq. (2.26) in a least-squares sense.

Figure 2.14b shows the variation of the heater wall temperature for different values of the dimensionless heat dissipation given by the macroscopic model (lines) and the fit of Eq. (2.26) (points). It is deduced that the analytical solution provides correct trends of the wall temperature as a function of the heat flux and the freestream velocity. In addition, the analytical solution predicts that $T_w - T_\infty \sim 1/\sqrt{\kappa_f}$, which means that the uncertainty in the thermal conductivity of the K9 foam (see Fig. 2.11b) is not expected to produce a great impact on the results.

Chapter 3

Thermal analysis

As mentioned in the Introduction, efficient cooling is crucial for maximizing the particle measurement quality in the LHC. In this chapter the cooling system of the ALICE ITS3 Inner Barrel (IB) is developed, consisting of a novel application in HEP using open-cell foams as heat exchangers and structural supports for the minimization of the material budget. In §1 the different design steps are carried out, which are applicable to other engineering areas. The process is based on following numerical and experimental approaches, and the corresponding results are compared and discussed in §2. This section also includes parametric studies and a proposal for design improvement.

§1. Methodology

The development of the ALICE ITS3 IB cooling system is divided into three parts: first, the design is explained in §1.1, which is focused on the thermal and structural parts to be used in the silicon half layers; then, the design proposed is built and installed in a wind tunnel setup that is presented in §1.2; finally, a mathematical model is developed in §1.3 that is used to numerically validate the thermal performance of the design.

§1.1. ALICE ITS3 IB cooling system

The heat dissipated by the sensors will be removed with an air flow. To reduce the temperature gradients in the endcap region (see Fig. 1.9c), the proposed design considers the use of thermally-conductive open-cell carbon foam rings in that zone; specifically, in contact with the silicon sensors. The foams act as heat exchangers, so the heat is transferred from the sensors to the foams by conduction, and then it is removed from the foams by air convection. The carbon foam rings in the endcap region are not sufficient to keep the silicon sensors in cylindrical shape, and the design includes additional foam parts that act as mechanical supports. These aspects of the design are detailed in §1.1.1. Since there are four air flow channels in the detector, the second decision is related to the air flow distribution system in §1.1.2.

§1.1.1. Design

Two open-cell carbon foams are selected to be used in the system: first, the Reticulated Vitreous Carbon (RVC) Duocel® (see Chapter 2, §1.1.2) as structural support, thanks to its extremely low density and high specific Young modulus obtained from tests performed by the manufacturer (see Table 3.1); second, the K9 (see Chapter 2, §1.1.3), whose high specific thermal conductivity, low density, and high heat transfer coefficient justify its use as a heat exchanger.

Foam	ρ **(kg/m^3)**	Φ	l_{cell} **(m)**	Σ_f **(1/m)**	κ_f **(W/(m·K))**	E **(GPa)**
RVC	45	0.97	3.9×10^{-4}	6600	0.05	0.1
K9	200	0.89	2.85×10^{-4}	14700	25	0.4

TABLE 3.1: Main parameters of the foams to be used in the ALICE ITS3 IB cooling system.

In the baseline design, RVC and K9 foams are used as follows (see Fig. 3.1a):

- A-Side: three rings made of the K9 foam are placed. The length of the rings in the z direction is 6 mm, which is the same as the distance between the layers. This is a conservative value

determined from mechanical tests at CERN so that there are no risks of breaking the foams in the assembly process. It is not possible to place a fourth ring in the 1.5 mm height channel between the beam pipe and Layer 0 due to design tolerances and fragility of the carbon foams.

- Plane $y = 0$: no thermal performance is required in that zone; therefore, longerons made of the RVC foam are used near the edges of the silicon sensors. The length in the y direction of these foams is 2.5 mm.
- C-side: since there is no endcap region, rings of the same geometry of those of the A-Side made of RVC foam are installed.

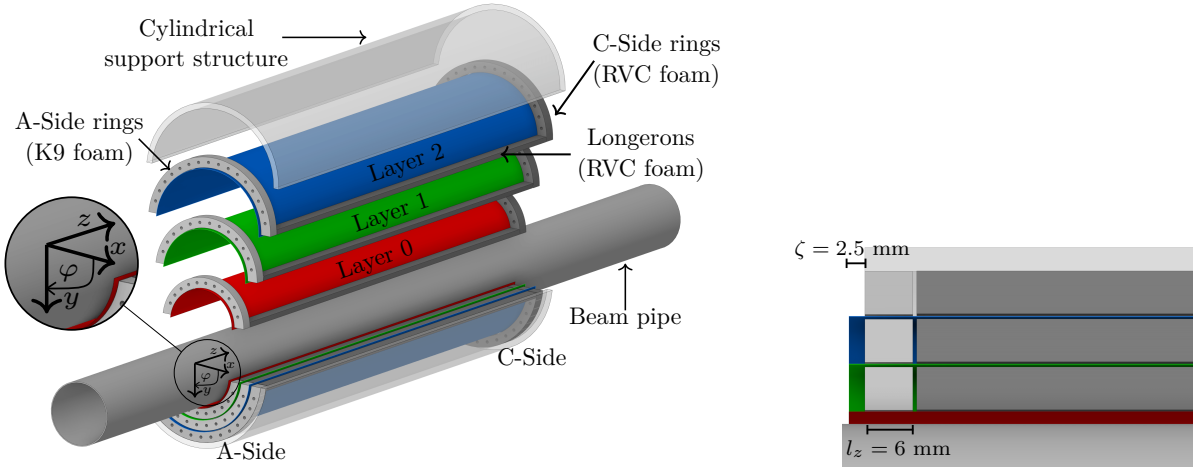

(A) Isometric view. (B) Top view (half-barrel).

FIGURE 3.1: Foam structures of the ALICE ITS3 IB.

To leave space for the wire bonding procedure, as a conservative approach, the A-side rings are not placed in contact with the endcap region, and a spacing ζ of 2.5 mm is left (see Fig. 3.1b); that is, there is no contact between the 2.5 mm long endcap and K9 foam. In regard to the foam-silicon interface, following previous studies, carbon fleece of 120 µm of thickness and areal density of 8 g/m^2 is placed between the silicon layers and the foams, a glue layer of 100 µm between the fleece and the heater, and a glue penetration of 250 µm in the foam (see Chapter 2). The Araldite 2011 epoxy glue is used in the RVC foam, and the Epoxies® 50-3150 FR (same glue used in the experimental setup described in Chapter 2, §1.2) in the K9 foam. The material budget of the ALICE ITS3 IB is shown in Fig. 3.2, with a mean value of $\approx 0.07\%$ in both directions, which gives a 80% reduction in this value relative to the one of the ALICE ITS2 IB (see Fig. 1.8).

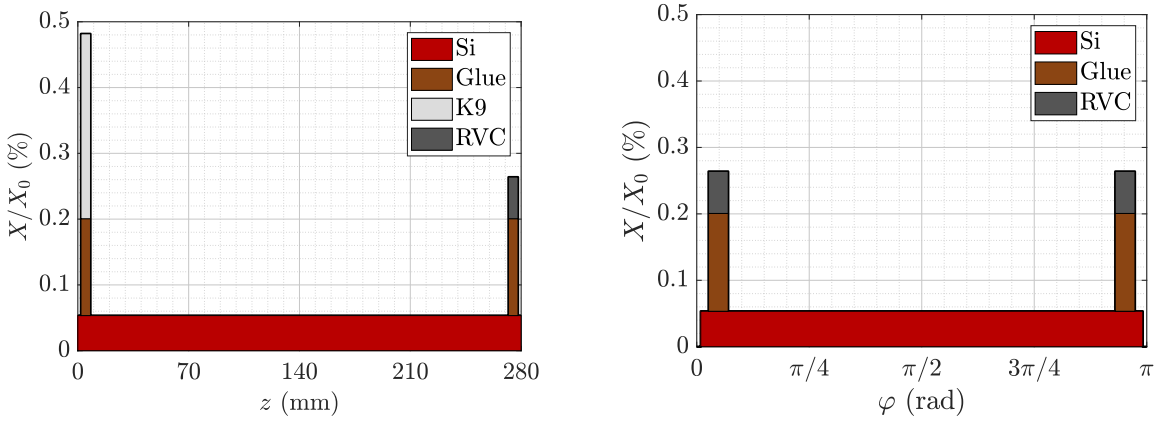

(A) Longitudinal direction. (B) Azimuthal direction.

FIGURE 3.2: Material budget of the ALICE ITS3 IB.

Due to the complexity of the installation of the ITS3 IB in the ALICE cavern, the system is not expected to be completely isolated; therefore, the pressure drop of the foams should be minimized to reduce leaks. This also reduces the power required by the flow distribution system. To this end, holes are drilled into the foams as shown in Fig. 3.1a. The diameter of the holes is 1.5 mm.

§1.1.2. Air flow distribution

In terms of ease of installation and integration with other subsystems, the simplest approach is to use a single channel at the inlet. This configuration is sketched in Fig. 3.3. The flow direction is from the C-Side to the A-Side (see Fig. 3.1a).

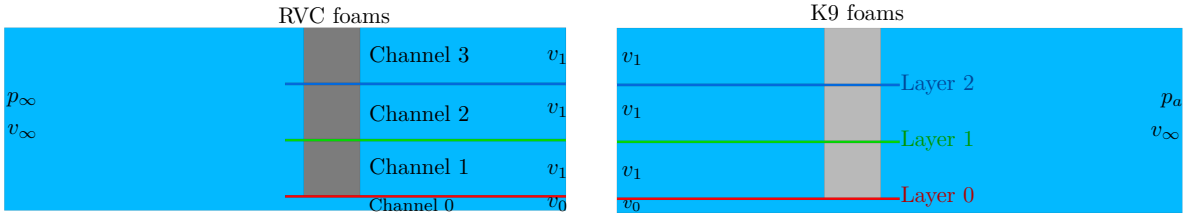

(A) Inlet. (B) Outlet.

FIGURE 3.3: Single flow distribution configuration of a half-inner barrel of the ALICE ITS3. Cut with the plane $x = 0$.

Since carbon foam rings produce pressure losses, the flow distribution in the four channels is a priori unknown. An estimation can be obtained by making the following assumptions:

- The flow is steady and one-dimensional.
- The pressure loss due to friction forces on the walls of Channels 1, 2, and 3 is negligible compared to the pressure loss induced by the foams.
- The pressure loss of a foam with 1.5 mm holes is 20% lower than that of a foam without holes (see Chapter 2, §2.2.2).
- The velocity in the three outermost channels is the same and equal to v_1. This is because the channel height and the foams used in each channel are the same; thus, it is reasonable to assume that the friction resistance is the same in all three channels.
- The flow in Channel 0 is turbulent with a Reynolds number $\rho v_0 h_0/\mu > 10^3$, and the pressure loss is given by the Darcy–Weisbach equation with a conservative friction factor $f = 0.1$ (McKeon et al., 2005), where $h_0 = 1.5$ mm is the height of Channel 0.
- The pressure at the outlet p_a is the same for the four channels.

v_∞ (m/s)	v_0 (m/s)	v_1 (m/s)
2	27.12	1.22
4	46.45	2.86
6	64.55	4.56
8	82.21	6.29
10	99.64	8.03

TABLE 3.2: Flow distribution in the ALICE ITS3 IB with a single flow distribution channel.

The flow distribution is such that the pressure loss $p_\infty - p_a$ is minimized across the channels. The velocity in the Channel 1 (v_0) and the one in the Channels 1, 2, and 3 (v_1), which is reached

at a sufficient distance downstream of the rings, is shown in Table 3.2. Since v_0 is one order of magnitude greater than v_1 in all cases, it is not possible to have an adequate control of the velocity distribution. It is concluded that it is necessary to have a minimum of two distribution channels: one for Channel 0, and another for Channels 1, 2, and 3.

§1.2. Experimental setup

An experimental setup has been built at CERN to study the thermal performance of the design explained in §1.1.1. Moreover, the assembly procedure—which is not described in this work— is a crucial part of the design, and this setup contributes to the process optimization. The silicon bending and the realization of the in-house gluing procedure explained in Chapter 2, §1.2 require the use of parts with tight tolerances, as well as high-precision tools such as optical microscopes.

Figure 3.4a shows the core of the setup, which consists of a prototype of a half-barrel of the design of Fig. 3.1a and a carbon sandwich cover based on CFRP, specifically with a layout consisting of CFRP + thermally-insulating foam + CFRP. The cover has an inner radius of 40 mm, instead of the 36 mm required (30 mm of radius of Layer 2 shown in Fig. 1.9b + 6 mm of the foam). This is because it was previously manufactured for a preliminary model of 40 mm of inner radius, and it was decided to adapt it to the current design. To solve the mismatch in the dimensions, a thermally-insulating closed-cell carbon foam is introduced to cover the remaining 4 mm of thickness (see Fig. 3.4c). The final prototype used in the ALICE experiment will be manufactured as a single part of CFRP. All thermal interfaces with the aluminum supports have a thick layer of a thermally-insulating epoxy glue to reduce the thermal losses of the system. The choice of aluminum instead of 3D-printed parts for the support is related to the tolerances of the assembly process.

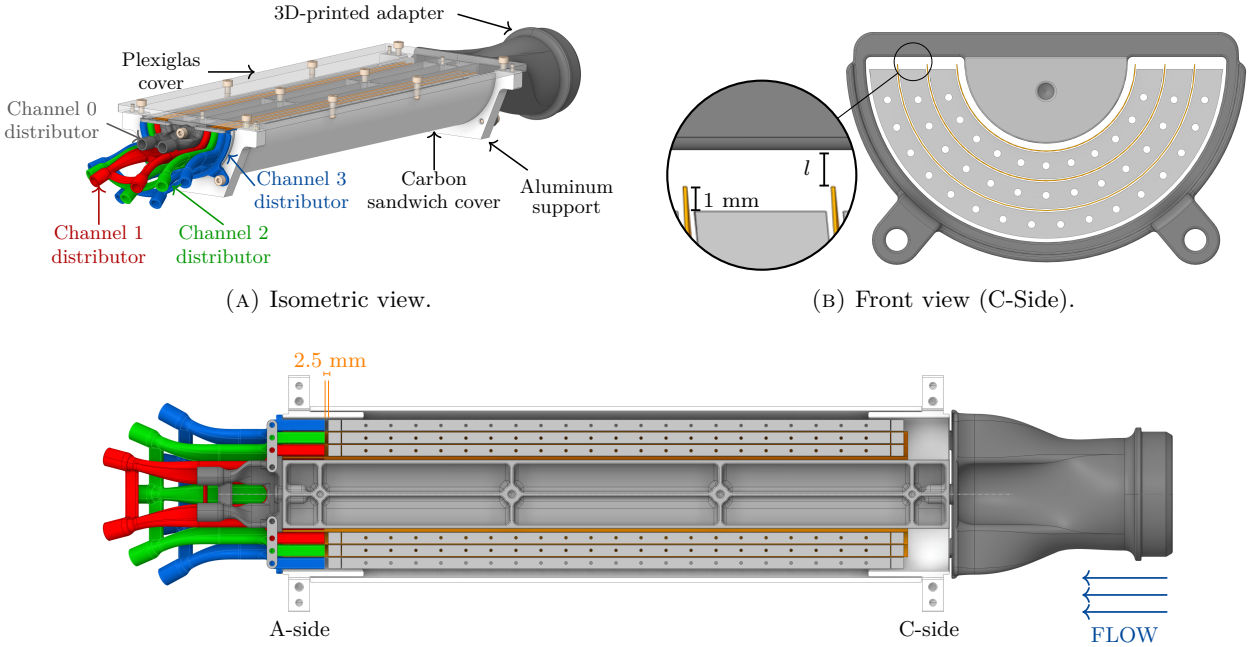

(A) Isometric view.

(B) Front view (C-Side).

(C) Top view.

FIGURE 3.4: ALICE ITS3 inner half-barrel prototype of the experimental setup.

A flow distribution system consisting of four separate channels has been designed (see Fig. 3.4a). The longitudinal distance from the 3D-printed air distributors to the foams is 2.5 mm (see Fig. 3.4c), which is the minimum to allow a that a space of 2.5 mm of the endcap region is left for the wire bonding procedure. As shown in Fig. 3.4b, the foam rings cover an azimuth angle—defined in Fig. 3.1a—of $\varphi_0 < \varphi < \varphi_1$ with $\varphi_0 > 0$ and $\varphi_1 < \pi$, since in the assembly process a gap of 1 mm is required at the edges (see Fig. 3.4b). The distribution system is such that it covers also $\varphi_0 < \phi < \varphi_1$; therefore, it cannot be seen from the C-side (see Fig. 3.4b). This configuration has

been chosen to minimize the air flow in the zone of height $l + 1$ mm and maximize the amount of air that flows through the foams at the A-side. The distance between the edge of the layers and the PLEXIGLAS® cover is $l = 1.5$ mm in the experimental setup, although in the real detector the distance to the symmetry plane will be $l = 0.5$ mm (see Fig. 1.9b). The gap of approximately 1 mm between the outermost ring and the cover shown in Fig. 3.4b is filled with glue. At the C-side, the transition from a circular pipe of 25 mm of radius to the prototype of 16.5 mm of inner radius and 36 mm of outer radius is done with a 3D-printed adapter. The detailed geometry of the adapter is not relevant for the current work, since the RVC foam acts as a flow straightener because of the low cell size (see Table 3.1). Moreover, the flow that passes through the foam holes is independent of the inlet flow, because the characteristic length is lower than the one in the channel flow, as well as the high velocity gradients that are generated when the air flows through the holes. In addition, the pressure loss induced by the adapter is negligible compared to the foam pressure loss.

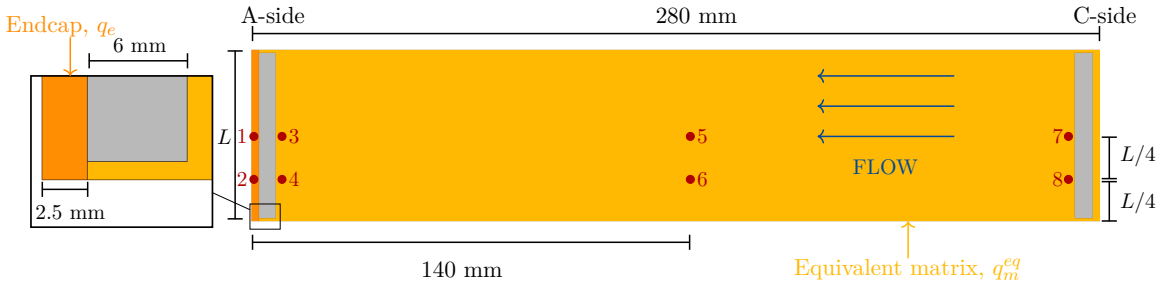

FIGURE 3.5: Location of the temperature sensors in each layer of the integrated heaters produced by the CERN EP-DT-DD Micro-Pattern Technologies (MPT) group.

The heat dissipated by the sensors is modeled with integrated heaters that contain a silicon wafer of 40 µm, a copper heater of 5 µm, and three polyimide layers of 12.5 µm (polyimide-silicon-polyimide-copper-polyimide) that are joined with an epoxy glue. The measured total thickness of the heaters is 160 - 170 µm, and the exact thickness of each of the glue layers is unknown. Since the thermal conductivity of epoxy glues is approximately the same as the one of polyimide ($\kappa = 0.2$ W/(m·K)), glue layers are considered as an additional thickness of 27.5 µm of the polyimide layers. Thus, the equivalent system of the simulations consists of five layers, with a thickness of 40 µm of the polyimide layers, and a total thickness of 40 µm (silicon) + 3 × 40 µm (polyimide) + 5 µm (copper) = 165 µm. As shown in Fig. 3.5, the heater of each layer is divided into two resistors. The first is the endcap with a heat flux equal to q_e. The periphery region is not considered, and its effect is included as an additional power dissipation in the second resistor called "equivalent matrix", with a heat flux equal to q_m^{eq}. The layout of the foam-integrated heater interface is the same as the one explained in Chapter 2, §1.2, but replacing the silicon by the integrated heater. The temperature of the polyimide layer in contact with the silicon layer is measured with eight PT1000 temperature sensors with an uncertainty of ±0.15 K. These sensors are joined to polyimide layers using the same glue used in the foam-heater interface (see Fig. 3.5). Sensors 1 to 4 are placed in contact with the foam. Holes of 1.5 mm in diameter are drilled in the longerons so that the wires of the temperature sensors (four per sensor) can exit the system (see Fig. 3.4c).

A computed tomography (CT) scan has been performed at CERN to verify the cilindricity of the layers of the experimental setup. Figure 3.6a shows a comparison between the scan (white) and the layers from the CAD model (red, green, and blue), and shows that the proposed design ensures the correct shape of the silicon sensors. The results have been post-processed with CAD software. The conclusion is that the difference between the CAD model and the experimental setup is negligible in all regions except small zones near the edges; in particular, at the edge of Layer 0, where the maximum deviation is 300 µm. The cause of this deviation is attributed to a non-optimal mechanical interface between the RVC foam and the silicon sensors, as shown in Fig. 3.6a. This problem can be solved by increasing the contact surface between the foam and the silicon; that is, either increasing the size of the foam, or using a denser foam. The CT-scan also shows that the gluing process developed at CERN ensures to have uniform glue layers (see Fig. 3.6b).

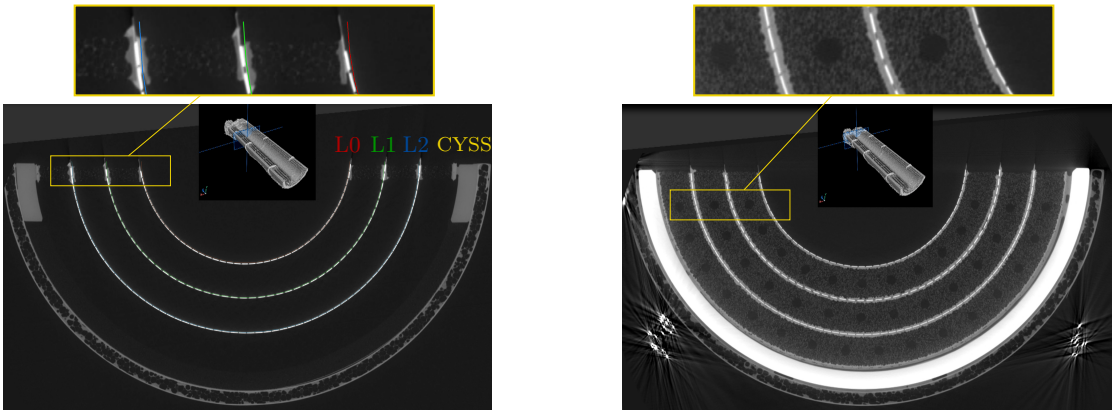

(A) CT scan and CAD comparison - Matrix.

(B) CT Scan - A-side (K9 foam).

FIGURE 3.6: Results of the Computed Tomography scan of the ITS3 prototype performed by the CERN EN-MME Materials, Metrology and Non-Destructive Testing (MM) section.

The air flow is generated by a fan that can provide up to 2×10^4 Pa for a freestream velocity of 20 m/s, and includes a frequency inverter so that the operating point can be set manually or with a computer. All channels are equipped with an aluminum valve and the same mass flow meter used in the setup described in §1.2. Channel 3 uses two mass flow meters due to limitations in the range of the device. The mean freestream velocity in the four channels $v_{\infty,i}$ (i from 0 to 3) is obtained by mass conservation assuming that the flow is steady and incompressible. The valves have been designed and produced at CERN to minimize the pressure loss in that area. Due to space limitations in the installation of the ITS3 IB in the ALICE cavern, the fan must be placed close to the A-side. Thus, the fan operates such that the flow direction is from the C-side to the A-side (see Fig. 3.4c); that is, the air expands when flowing through the system. This decision is justified because, under the opposite operating condition—where the fan blows air—the inlet temperature is higher than the room temperature. This is a consequence of the non-isentropic compression that is produced by the fan, which is not desirable.

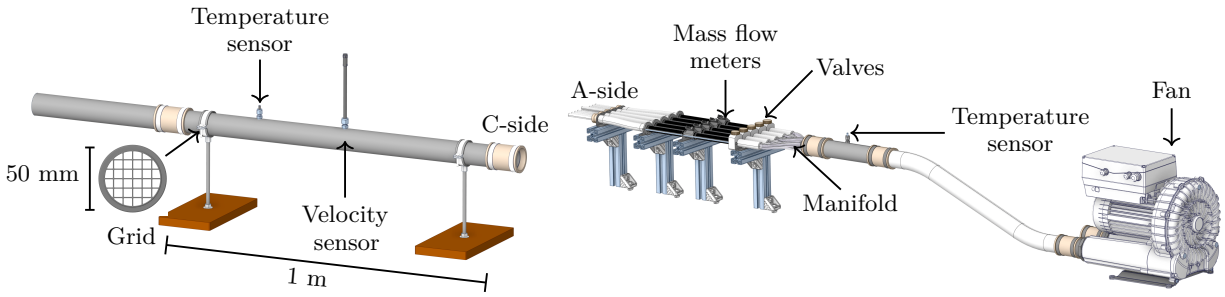

(A) Inlet.

(B) Outlet.

FIGURE 3.7: Components of the wind tunnel used for experimental testing.

The inlet of the system is a pipe of 50 mm of inner diameter that contains a grid to straighten the flow and reduce the turbulence levels (see Fig. 3.7a). The inlet and outlet temperatures are measured by temperature sensors of the same model as the one of the heaters. A velocity sensor is placed to verify that there are no leaks in the system, and that the values given by the mass flow meters are correct. The measured difference between the mass flow given by the velocity sensor and the sum of the values obtained from the mass flow meters is 5%, which is of the order of the sensor accuracy. The straight pipes where the temperature sensors are installed are made of PVC, and the flexible pipe that joins the fan and the outlet straight pipe is made of silicon. The same material is used for the white pipes that connect the 3D-printed manifold and the valves, while the black pipes connected at both sides of the mass flow meters are 3D-printed.

§1.3. Mathematical model

The mathematical model consists of the governing equations introduced in §1.3.1 that are closed by the boundary conditions defined in §1.3.2. The numerical implementation is explained in §1.3.3.

§1.3.1. Equations

The incompressible Navier-Stokes equations are given by Eqs. (2.1) to (2.3) with the following assumptions, terms, and parameters:

- The flow regime depends on the air freestream velocity, since $Re_h \in [0, 4000]$ for $v_\infty \in [0, 10]$ m/s and $h = 6$ mm. The model assumes that the flow is turbulent in all cases, and RANS turbulence modeling is considered (see Appendix A, §3). The turbulent viscosity μ_t is provided by the $k-\omega$ SST turbulence model (see Appendix A, §3.2).
- The *momentum source term* $\boldsymbol{M}$ that takes into account the pressure loss of foams is given by Eq. (2.9). The permeability and drag coefficients obtained from Fig. 2.10a and Fig. 2.10c are $\mathcal{P}^{\text{RVC}} = 3.32 \times 10^{-9}$ m^2, $\mathcal{P}^{\text{K9}} = 5.97 \times 10^{-10}$ m^2, $C_d^{\text{RVC}} = 7.81 \times 10^{-2}$, and $C_d^{\text{K9}} = 1.02 \times 10^{-1}$.
- The air and the solid material of the foams are considered to be a homogeneous mixture, and the *specific enthalpy* of the foam is given by Eq. (2.11).
- In the foam domains, the air temperature is given by Eq. (2.3), and the *heat source* $Q = h\Sigma_f(T_s - T)\mathbf{1}_{\Omega_f}$. Since the RVC foam is a thermal insulator (see Table 3.1), the heat flux from the silicon layers to the RVC foam is negligible, and in this foam the thermal equilibrium model is considered, so $T = T_s$. In the K9 foam, the heat transfer coefficient h is obtained from the Nusselt number $Nu = hl_{\text{cell}}/\kappa = C_h Re_{l_{\text{cell}}}^n$, where $C_h = 0.56$ and $n = 0.51$ derived from Fig. 2.12b. The variable T_s refers to the solution of the energy equation in the solid material of the foam (Eq. (2.13)).
- All layers of the heaters are thermally coupled to the foams and the fluid domain. The interfaces between the foams and the heaters are modeled as a single layer of glue of equivalent thickness of 220 µm derived from the studies of Chapter 2. The dissipated heat is implemented as a source term equal to the heat flux divided by the layer thickness.

§1.3.2. Boundary conditions

Boundary conditions are defined at the inlet, the outlet, the walls, and the symmetry plane.

Inlet

The inlet is placed at the outlet of the 3D-printed adapter shown in Fig. 3.4a. The numerical results are not sensitive to variations of the geometry, as expected from the arguments explained in §1.2. At the inlet, the pressure is set to the reference pressure, and a Neumann boundary condition is used for the velocity and the turbulence variables. The static temperature is equal to T_∞.

Outlets

The geometry is simplified in this region by extending the length of the channels 128 mm away from the A-side foam. This value is such that the flow is uniform at the outlets based on preliminary simulations. Simulations have been performed with the real geometry of the distribution channels (see Fig. 3.4a), and the $\Delta T = T - T_\infty$ values in the eight locations of the temperature sensors (see Fig. 3.5) have been compared. The temperature values given by the two geometries differ less than 1%. This difference is assumed to be lower than the error related to other assumptions of the model, such as those of the modeling of the interfaces between different materials. With the simplified geometry of Fig. 3.8, the mass flow rate is defined at the four outlets, where the velocity

is equal to the freestream velocity v_∞. Zero-gradient boundary conditions are used for the pressure, the temperature, the turbulent kinetic energy, and the turbulent specific dissipation rate.

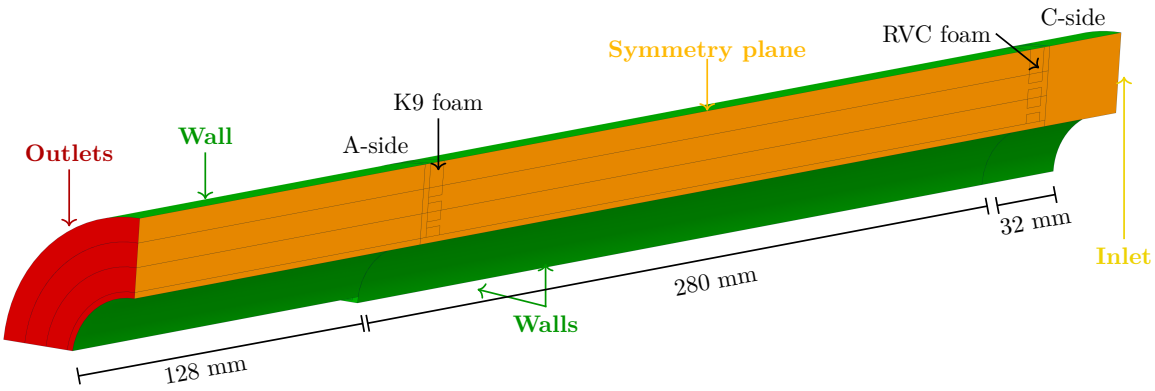

FIGURE 3.8: Computational domain of the thermal simulations of the inner half-barrel of the ALICE ITS3.

Walls

No-slip condition and adiabatic boundary conditions are imposed, and the turbulent kinetic energy is set to zero. The dimensionless wall-parallel velocity is given by the solution in the viscous sublayer: $v_\parallel^+ = \tilde{y}^+$ (see Appendix B, §2.3). The boundary condition for ω is obtained from a perturbation analysis of the ω-equation: $\omega^+ = 85/(\tilde{y}^+)^2$ (see Appendix B, §3.2.1).

Symmetry

The plane $x = 0$ (see Fig. 3.1a) is considered a symmetry plane.

§1.3.3. Numerical implementation

The mesh consists of octrees in the bulk region, a high-quality layered poly-prism mesh in the boundary layers, and general polyhedral elements that connect both meshes. The coarsest size is set in the fully-developed region of the flow between the silicon layers, while the finest size is defined in the A-side. This is due to the strong interaction between the wake of the flow downstream of the carbon foams and the one downstream of the channels of height $l + 1 = 2.5$ mm illustrated in Fig. 3.4b. In the remaining flow regions, namely the fully-developed region of the channels of $l + 1 = 2.5$ mm in height, intermediate cell sizes are used. At all walls 10 cells are defined along the thickness of the boundary layers, with the wall $\tilde{y}^+ < 5$. All solid layers with high aspect ratio are implemented using the Shell Conduction model (see Chapter 2, §1.3.3).

Equations (2.1) to (2.3) are solved with the finite volume method that is implemented in Ansys Fluent 2023R1, with the baseline methods listed in Chapter 2, §1.3.3. Some modifications are carried out; first, the convective terms of Eq. (2.2), Eq. (2.3), and the $k-\omega$ SST equations (Eqs. (A.37) and (A.38)) are discretized with a second-order upwind scheme (see Appendix B, §1.1.1); second, a Coupled algorithm (see Appendix B, §2.2) is used that follows the pseudo-transient approach (see Appendix B, §3.3.1) for the pressure-velocity coupling. Temperature values are monitored at every pseudo time step in the eight sensor locations (see Fig. 3.5), and simulations are terminated when these values do not vary and the globally-scaled energy residual $< 10^{-8}$.

§2. Results and discussion

First the accuracy of the model developed in §1.3 is assessed in §2.1 by comparing numerical results with data obtained from the experiment described in §1.2. The validated model is then used to simulate the real configuration of the ITS3 and to perform a parametric study in §2.2.

Symbol	Material	Parameter	Value	Units
c_s	Be	Specific heat	1825	$J/(kg \cdot K)$
	Si		710	
q_{bp}	Be	Heat flux in the beampipe	0	W/m^2
q_m^{eq}	Si	Heat flux in the equivalent matrix	250	W/m^2
q_e	Si	Heat flux in the endcap	10000	W/m^2
κ	Be	Thermal conductivity	216	$W/(m \cdot K)$
	Si		149	
ρ	Be	Density	1850	kg/m^3
	Si		2329	

TABLE 3.3: Simulation parameters for the thermal analysis of the ALICE ITS3 IB.

Simulation parameters are shown in Tables 2.2 and 3.3. The additional physical properties used for thermal analysis are obtained from (Boss, 1991) (Be), (Masolin et al., 2013) (Si). Material properties are taken at $T_\infty = 298$ K, and their temperature dependence is neglected, since the temperature range of the simulation results is limited (298 - 318 K). The importance of considering relative temperatures has been stressed in the Introduction; therefore, all results presented hereafter are temperature variations with respect to the freestream temperature, $\Delta T = T - T_\infty$. As mentioned in §1.2, the integrated heaters do not contain periphery regions, and their effect is considered by applying a heat flux equal to the area-weighted average of the heat flux in the periphery ($q_p = 2500$ W/m^2) and in the matrix ($q_m = 100$ W/m^2). The surface areas of each region are calculated from the dimensions of the stitching unit (see Fig. 1.9c).

§2.1. Model validation

§2.1.1. Mesh independence study

Three meshes of different element sizes are considered, with minimum and maximum element lengths equal to $\delta_{\min}$ and $\delta_{\max}$, respectively. These values refer to the distance between the layers ($h = 6$ mm). In each mesh, the total number of cells considered in the study contains the cells generated by the Shell Conduction model. The freestream velocity $v_\infty = 5$ m/s, and the monitored temperature values are referred to Layer 1 in the locations shown in Fig. 3.5.

$\delta_{\min}$	$\delta_{\max}$	Number of cells	ΔT_1 (K)	ΔT_3 (K)	ΔT_5 (K)	ΔT_7 (K)
$h/12$	$d/2$	1.1 M	7.11	2.62	3.93	1.46
$h/24$	$d/4$	4.6 M	7.37	2.69	3.77	1.38
$h/48$	$d/8$	18.3 M	7.43	2.71	3.74	1.33

TABLE 3.4: Results of the mesh independence study of the thermal analysis of the ALICE ITS3 inner half-barrel prototype.

Table 3.4 shows that the temperature values vary only marginally when the mesh size is increased, halving $\delta_{\min}$ and $\delta_{\max}$, and even smaller differences are obtained by halving them further, demonstrating the tendency to converge. This is a reasonable result, since the flow around the layers is not complex, and in all cases the boundary layers contain 10 elements in the wall normal direction. This ensures consistent behavior of the velocity and the turbulent variables in the context

of RANS turbulence modeling. The medium mesh of 4.6 M cells is chosen due to the significant differences between the coarse and fine meshes in ΔT_1.

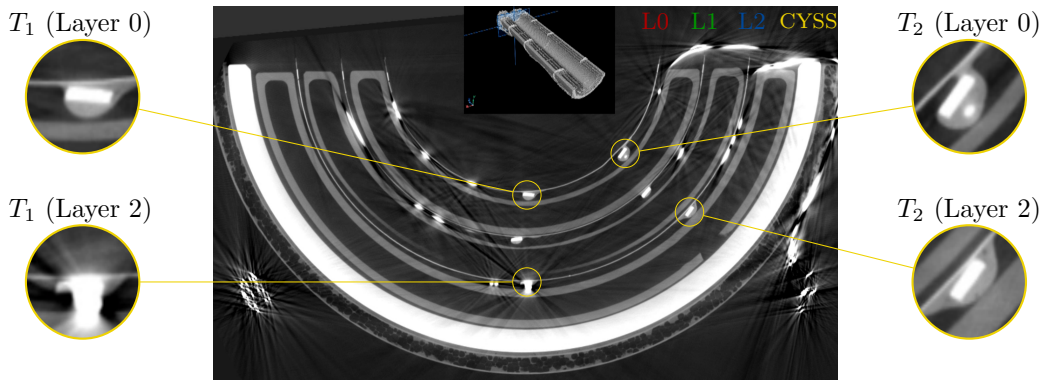

FIGURE 3.9: Results of the CT scan of the ITS3 inner half-barrel prototype in the endcap region.

§2.1.2. Comparison with experimental data

Figures 3.11a, 3.11c and 3.11e depict the temperature in the endcap region measured in the experiments and the one predicted by the numerical model proposed in this work. The differences (in L_1 norm) between the simulation curves and the temperature sensor value with lowest thermal resistance (highest temperature) are bounded by 0.5 K. The simulations overpredict the temperature values in most cases, which is attributed to the thermal resistance produced by the glue between the polyimide layer and the temperature sensors. While the experimental values of ΔT_3 and ΔT_4 differ less than 0.25 K, there are noticeable differences between ΔT_1 and ΔT_2, especially in Layers 0 and 2. The reason in Layer 0 is that T_2 is not correctly glued (see Fig. 3.9), which leads to the increase of thermal resistance, and therefore to the temperature decrease. In Layer 2, the differences are because T_1 and T_2 are not aligned in the longitudinal direction. Indeed, the output of the CT Scan is a video that gives images of the front view along the longitudinal direction (from the A-Side to the C-Side), and a flash is seen at the edge of the sensors, which is a metallic surface. This flash disappears when the scan points to the effective surface of the sensor, which is made of ceramic. In Layer 2, while the image shown points to the edge of T_2, in T_1 it points to the effective surface. Thus, T_2 is closer to the edge, leading to the temperature increase, since it is further away from the foam. In addition, the planar dimensions of the sensors (1.6 x 1.2 mm) are of the same order as the endcap length (2.5 mm), leading to additional uncertainty in the measurements.

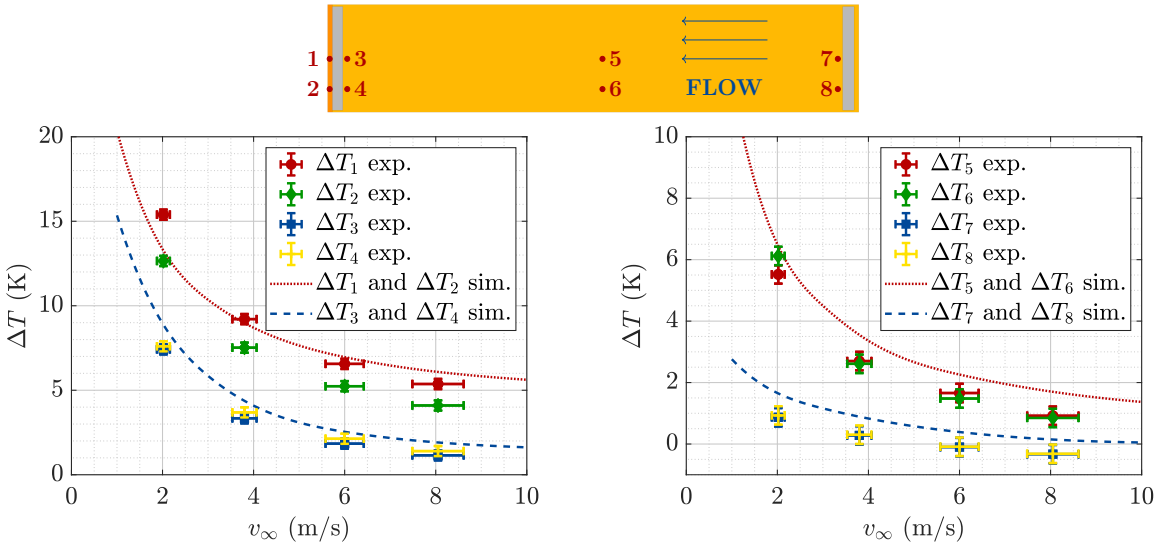

(A) Layer 0 - Endcap.

(B) Layer 0 - Matrix.

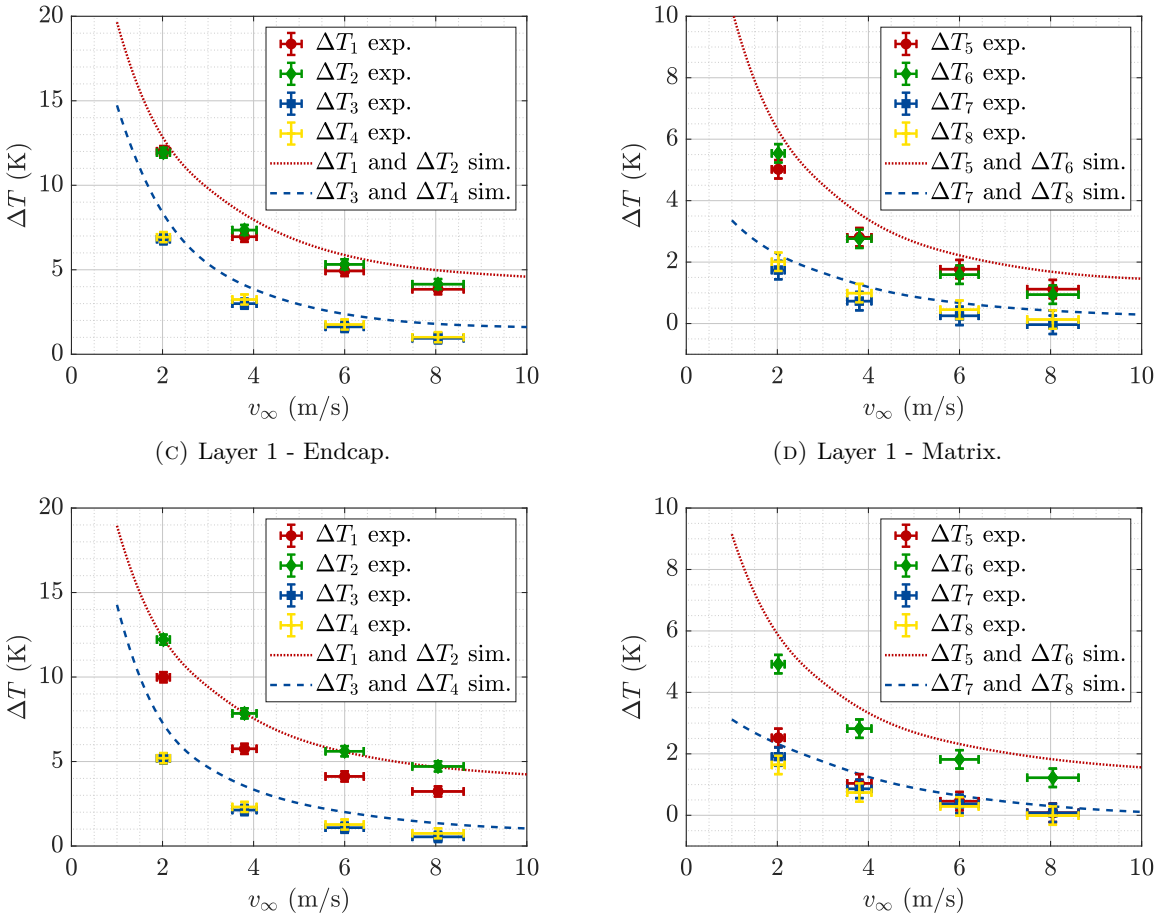

(C) Layer 1 - Endcap.

(D) Layer 1 - Matrix.

(E) Layer 2 - Endcap.

(F) Layer 2 - Matrix.

FIGURE 3.11: Simulation and experimental results of the temperature variation with respect to the freestream temperature in the polyimide-silicon interface of the ALICE ITS3 inner half-barrel prototype.

Figures 3.11b, 3.11d and 3.11f show the results given by the experiments and the simulations in the matrix region. Similar conclusions to those of the endcap region can be drawn when comparing the experimental and numerical results. The temperature discrepancy between the sensors placed at constant values of the z coordinate are negligible except from ΔT_5 and ΔT_6 in Layer 2. In that case, the low ΔT_5 values are due to a poor contact between the sensor and the polyimide layer. It should be noted that some of the experimental ΔT values are negative, which can be ascribed in part to the limited accuracy of the temperature sensors. Even if their accuracy is stated to be ± 0.15 K by the official datasheet, when the heat dissipation is set to zero, a difference of 0.6 K has been obtained between the minimum and maximum values among all (26) temperature sensors. Thus, the uncertainty of the temperature values of Fig. 3.11 is ± 0.3 K. In addition, differences have been observed between the time scales of the inlet temperature and the temperature of the sensors, since the temperature of the test room is not constant during the tests.

Another important aspect to be taken into account is that, for Channels 1, 2, and 3 (see Fig. 3.3), the Reynolds number of the fully-developed channel flow $Re = \rho v_\infty h/\mu = 2000$ for $v_\infty = 5$ m/s. Assuming that the division of flow regimes in circular pipes (Schlichting, 1979) is applicable to the current geometry, the fully-developed channel flow is laminar for $v < 5$ m/s, and transitional for $v_\infty > 5$ m/s. Simulations have been performed to study the accuracy of the RANS model in the heat transfer of a periodic channel flow. The laminar case considers $\mu_t = 0$ with the use of the central differencing scheme for the convective terms of the momentum equation to minimize the numerical diffusion. Laminar and RANS solutions have been compared, leading to the conclusion that the error introduced by the RANS model is negligible. This is reasonable, since $\mu_t/\mu \ll 1$ in the cases simulated with the turbulence model. The reason for using a RANS turbulence model

in all cases is that the velocity increases in the region around the foam holes, and the resulting shear flow is turbulent for approximately $v_\infty > 1$ m/s in the mesh considered. In these cases, if a LES approach is followed, the simulations do not reach a steady state due to the reduction in the turbulent viscosity. Performing unsteady simulations implies a large increase in the computational cost, which is discarded because of the reasonable accuracy of RANS in laminar heat transfer, as well as that no time-dependent quantities are analyzed in the current study.

§2.2. Real configuration

The temperature increase in the endcap region is the main point of concern, since the ΔT values are more than twice those in the matrix region. However, the layout described in §1.2 is not the same as the one of the real configuration that will be installed in the ALICE cavern, since the heaters include polyimide and glue layers that act as a thermal barrier. As previously mentioned, the distance to the symmetry plane will be $l = 0.5$ mm instead of $l = 1.5$ mm (see Fig. 3.4b). In addition, the detector will consist of two half-layers instead of one, with three zones of different power dissipation in the layers: the endcap, the periphery, and the matrix, unlike in the experimental setup, where only the endcap and the "equivalent matrix" are considered.

In this section the real configuration of the ITS3 will be simulated. Apart from the $x = 0$ plane, in the current simulations the plane $y = 0$ is also a symmetry plane (see Fig. 3.1a); that is, 1/4 of the geometry is simulated. The dimensions and values of the heat fluxes in the three regions are given in Fig. 1.9c; in particular, the heat fluxes are $q_e = 10000$ W/m^2, $q_p = 2500$ W/m^2, and $q_m = 100$ W/m^2, which give the same total power dissipation as in the simulations of §2.1.2. In this configuration, the main objective is to verify in §2.2.1 that $\Delta T < 10$ K in all layers. Then, a parametric study is performed in §2.2.2 focused on the heat dissipation of the layers, and, finally, the weak point of the design is identified and improved in §2.2.3.

§2.2.1. Thermal analysis

The ΔT distribution in the silicon layers of the real configuration is shown in Fig. 3.12. In comparison to the results of Fig. 3.11, the ΔTs in the endcap and matrix of the real configuration are 1 K higher. This is explained from the thermal resistance produced by the polyimide layers and the localized increase of power dissipation. Even with these differences, it can be concluded that the experimental setup represents a realistic temperature distribution of the real detector.

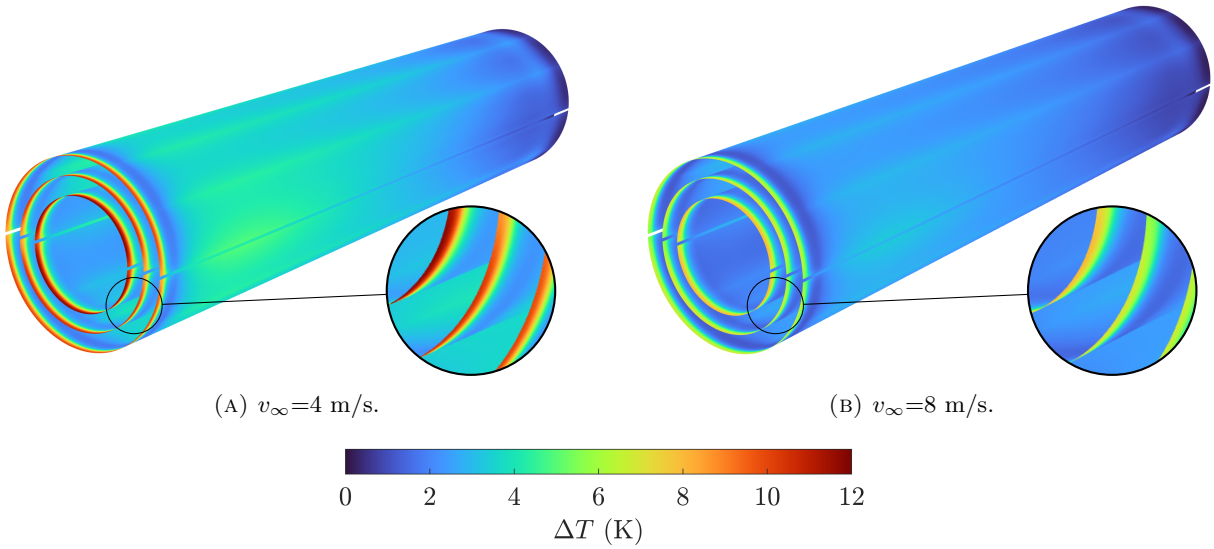

(A) v_∞=4 m/s. (B) v_∞=8 m/s.

FIGURE 3.12: Simulation results of the temperature variation with respect to the freestream temperature in the silicon layers of the real configuration of the ITS3 IB.

The highest temperature values in the matrix and periphery regions are obtained close to $\varphi = 0$ at the C-side, since the longerons (thermally-insulating foams) reduce the heat transfer rate in that region. Another reason is that the trajectory of the air that flows through the channel of height 1.5 mm is deviated near the A-side. This is because, as previously pointed out, the flow distribution system does not cover the full π radians of the azimuth angle φ. In addition, there is no contact between the foam and the periphery region at $\varphi \approx 0$. It is deduced that values of $v_\infty > 4$ m/s are required to achieve $\Delta T < 5$ K in the matrix and periphery regions. An analogous conclusion can be drawn in the endcap, and, in particular, for approximately $v_\infty > 5$ m/s, the maximum temperature variation is lower than 10 K. Therefore, the design requirement stated in the Introduction is met.

§2.2.2. Parametric study

No significantly higher heat dissipation values than those used in the simulations are expected. However, as mentioned in the Introduction, the heat fluxes used in the simulations are approximate values averaged on the surfaces. Since the maximum ΔT in the endcap is close to the design limit of 10 K, it is essential to study the influence of the power dissipation in the endcap. In addition, the effect of the power dissipation of the beam pipe on the temperature distribution needs to be assessed, since it can be of the same order as the matrix power dissipation.

Endcap

Taking as a reference the baseline value of the endcap heat flux $q_0 = 10000$ W/m^2, the influence of this value on the mean (in space) endcap temperature variation is shown in Fig. 3.13. The dependence as a function of the heat flux and the freestream velocity follows the same behavior predicted by the analytical solution obtained in Chapter 2, §1.3.2: $\Delta T = T_e - T_\infty \sim q/\sqrt{v_\infty}$. As illustrated in Fig. 3.12, Layer 0 is the layer with the maximum temperature variation in all cases, and for $q \geq 3q_0/2$ it is not possible to achieve temperature differences lower than 10 K.

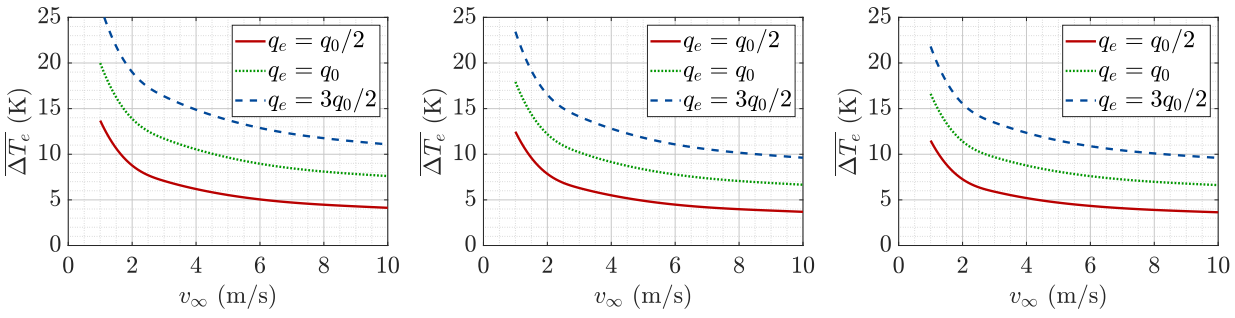

(A) Layer 0. (B) Layer 1. (C) Layer 2.

FIGURE 3.13: Simulation results of the ALICE ITS3 IB Layer 0 endcap mean temperature variation with respect to the freestream temperature for different endcap power dissipation values.

The temperature variation is negligible in the foam-silicon contact surface (see Fig. 3.12). However, in the baseline configuration, where the endcap length is 2.5 mm and the foam is placed at a distance $\zeta = 2.5$ mm from the edge of the layer (see Fig. 3.1b), there is no physical contact between the foam and the endcap. This limits the performance of the system, as the layer thickness is only 40 µm and the conductive heat transfer is not effective despite the high thermal conductivity of silicon.

Beam pipe

Another key aspect mentioned in Introduction is that the beam pipe is likely to dissipate heat. Cooling the beam pipe is not a design requirement, although the power dissipation of the beam pipe leads to a temperature increase in the silicon layers. The effect of the power dissipation of the beam pipe is addressed by considering three cases in the range mentioned in the Introduction.

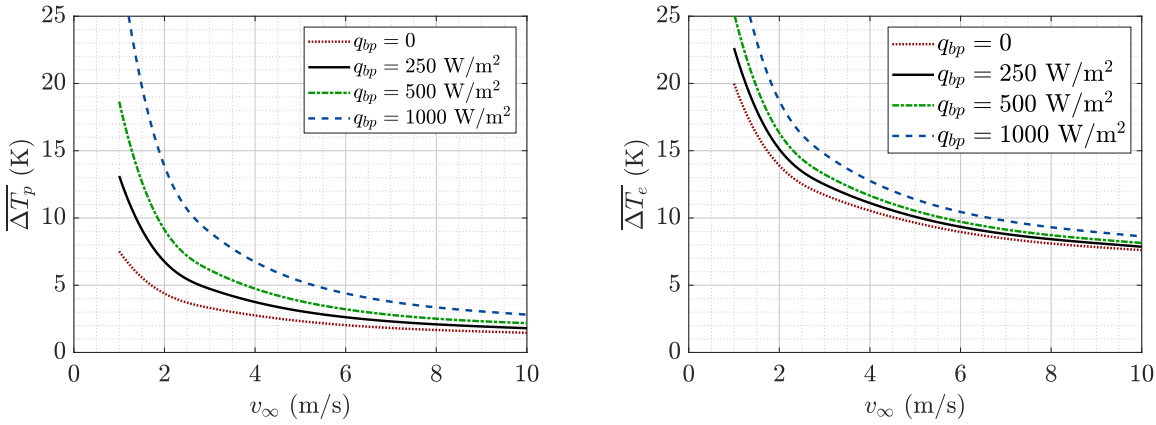

(A) Periphery. (B) Endcap.

FIGURE 3.14: Simulation results of the mean temperature variations of ALICE ITS3 IB Layer 0 of the with respect to the freestream temperature for different beam pipe power dissipation values.

Figure 3.14a shows the influence of the power dissipation of the beam pipe, which increases when the freestream velocity is decreased. This is justified because the thickness of the thermal boundary layers is inversely proportional to this parameter, and the reduced distance between the beam pipe and Layer 0 contributes to heat transfer. The effect is less pronounced in the endcap (see Fig. 3.14b), since the power dissipation in that zone is one order of magnitude higher than in the beam pipe. However, given that the temperature variation in Layer 0 is close to the design limit of 10 K, the effect of the beam pipe cannot be neglected.

§2.2.3. Design improvement

The baseline design, in which the distance from the K9 foam to the edge $\zeta = 2.5$ mm (see Fig. 3.1b), is highly conservative. The wire bonding region extends 300 µm in the z direction, and the wire bonding procedure will be performed prior to the gluing of the carbon foam. Therefore, there will be no limitations in terms of spacing needed for the wire bonding. Thus, it is reasonable to move the carbon foams closer to the layer edge, to allow a physical contact between the endcap and the foam. The theoretical maximum length of the contact region is 2.2 mm: that is, 2.5 mm of the endcap minus 300 µm of the wire bonding. However, achieving this value is a challenge, since the wire bonding region is delicate. Consequently, apart from the baseline design where the endcap-foam contact length is zero ($\zeta = 2.5$ mm), two additional configurations will be studied. A limit case is considered by setting $\zeta = 0.5$ mm, which means a contact length of 2 mm between the foam and the silicon. The intermediate case is $\zeta = 1.5$ mm, which means a contact length of 1 mm.

$\boldsymbol{\zeta}$ **(mm)**	$\overline{\boldsymbol{\Delta T_e}}$ **(K)**
2.5	8.12
1.5	5.39
0.5	4.06

TABLE 3.5: Simulation results of the mean endcap temperature variation of ALICE ITS3 IB Layer 0 with respect to the freestream temperature for different K9 foam positions ($v_\infty = 8$ m/s, $q = q_0$).

Table 3.5 shows that the endcap temperature depends strongly on the K9 foam position in the A-side. This means that there is a high margin of improvement in the temperature variation in the endcap region. If a value of $\zeta \approx 1$ mm can be set, with the baseline power dissipation of $q_e = 10000$ W/m^2, $q_p = 2500$ W/m^2, and $q_m = 100$ W/m^2, and a freestream velocity $v_\infty = 8$ m/s, then the ΔT would be approximately uniform along the layers. Moreover, it would be bounded by 5 K, which would imply almost a 50% reduction over the baseline configuration shown in Fig. 3.12b.

Chapter 4

Aeroelastic analysis

In this chapter, the interaction between the air flow and the ALICE ITS3 IB layers is analyzed. A methodology consisting of experimental and numerical approaches is explained in §1. The use of confocal chromatic sensors is proposed for the experimental part. On the basis of thorough market research, they provide up to one order of magnitude greater accuracy than laser displacement sensors. To the author's knowledge, this is the first research study on the use of confocal sensors in a high-level engineering application. In §1.1, the experimental setup employing confocal sensors to measure the displacements of the layers in a prototype of the ALICE ITS3 IB is presented. Next, in §1.2 a mathematical model for the fluid-structure interaction (FSI) is developed; in particular, it is focused on decoupling the fluid and structural problems. The results of the study are detailed in §2. Initially, the mathematical model is compared with the experimental values for validation. Subsequently, the model is used to analyze the real configuration of the future ITS3 IB setup, as well as potential modifications due to changes in detector cooling and installation requirements.

§1. Methodology

The aeroelastic study of the ALICE ITS3 IB is divided into two parts. First, in §1.1 the experimental setup is presented. Confocal sensors are installed in this setup to measure layer displacements in a prototype of the ALICE ITS3 IB. Second, §1.2 describes the development of a mathematical model for the FSI. This model aims to determine the aeroelastic performance of the system by decoupling the fluid and structural problems with a simplified geometry of the fluid domain.

§1.1. Experimental setup

The experimental setup presented in Chapter 3, §1.2 for thermal analysis is used to measure the displacements of Layer 2 (see Fig. 1.9b), which exhibits the highest displacements in the setup. This point will be explained later. Since the carbon sandwich cover of the prototype is glued to the foams (see Fig. 3.4), it cannot be replaced by a new one; thus, two holes of 12 mm diameter are drilled at $x = 0$ (see Fig. 4.1). These holes are subsequently covered by a transparent glass, so that the displacements of Layer 2 can be measured with a confocal chromatic sensor.

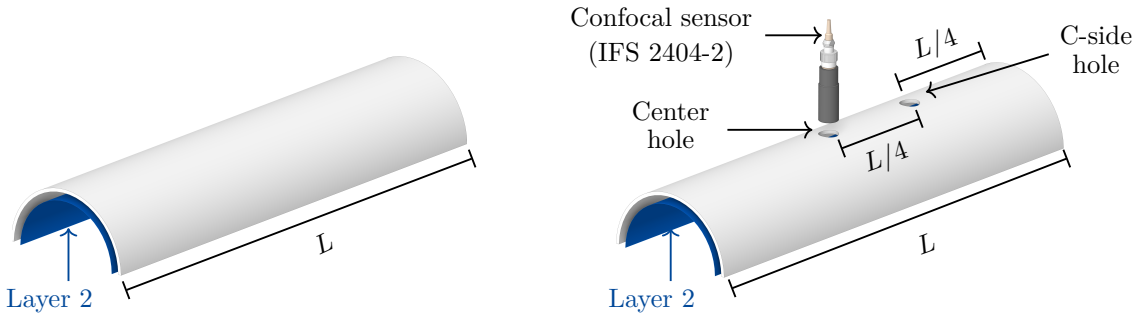

(A) Thermal analysis.

(B) Aeroelastic analysis.

FIGURE 4.1: Update to the ITS3 inner half-barrel prototype of Fig. 3.4 to measure Layer 2 displacements.

§1.1.1. Confocal chromatic sensors

Confocal chromatic sensors use white light to measure distances and thicknesses of materials. These sensors contain a multilens optical system that disperses the polychromatic white light into a rainbow of monochromatic wavelengths (from 380 nm to 780 nm) by controlled chromatic dispersion. The measuring range is given by the distance between the apices of the triangles of the ultraviolet and red lights (see Fig. 4.2a). Lights of different wavelengths are reflected from the measuring object, but a system consisting of a semipermanent mirror and a pinhole ensures that only the beams of the focused wavelength are not blocked. The sensors are connected by optical fiber to another device—the controller—which contains a spectrometer. The wavelength is seen as a peak in the intensity of the spectrometer, and a linear correlation obtained by the manufacturer gives as output the distance to the measuring object.

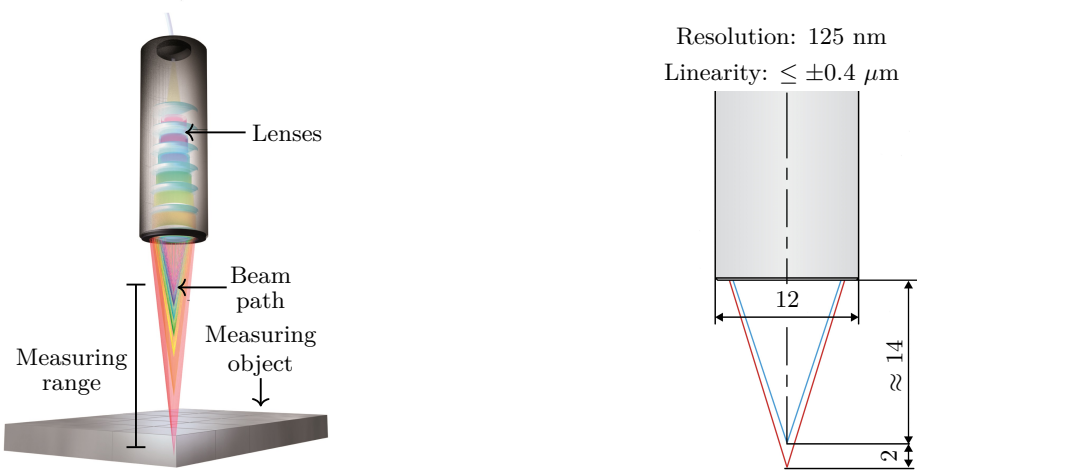

(A) Measuring principle. (B) Lengths in mm of IFS2404-2 (Micro-Epsilon, 2023).

FIGURE 4.2: Details of confocal chromatic sensors.

The measuring range of confocal sensors, as well as the diameter of the cone generated by the beam, is not the same for all devices. The first limitation in the sensor selection is the distance from the sensor to the target. In the case of Layer 2, the minimum distance is the sum of Channel 3 width (6 mm), the thickness of the closed-cell foam used next to the cover (3 mm), and the thickness of the cover (4 mm) (see §1.2). This implies that the start of the sensor measurement range must be greater than 6+3+4=13 mm, which is the case for the Micro-Epsilon confocalDT IFS2404 (see Fig. 4.2b). The start of the measurement range is given by the height of the blue triangle ($\approx$ 14 mm), while the height of the red triangle represents the end of the measurement range (14+2=16 mm). The diameter of the holes is such that the entire beam passes through it. Smaller holes lead to a reduction of the intensity of the wavelength peak in the spectrometer, which can lead to the deterioration of the accuracy.

The error of confocal chromatic sensors is the combination of the resolution and the linearity:

- Resolution: the smallest size that the sensor can detect. In dynamic measurements it is higher than in static measurements. Static displacements are not considered in this work; thus, the value given in Fig. 4.2b is the dynamic resolution given by the official datasheet.

- Linearity: the error of the linear correlation of the distance as a function of the wavelength. Each sensor has a linearity curve that gives the deviation from the linear correlation along the measuring range (see Fig. 4.3). In this work, the linearity of the sensor is defined as the peak-to-peak value of this curve. In the sensor used it is lower than the one given in the official datasheet (±1 µm), which is the maximum value among all sensors manufactured. It should be noted that linearity is defined for measurements of absolute distances of the order of the domain of Fig. 4.3 (from 0 to 800 µm), while the current study is focused on

relative distances—with respect to the equilibrium position—of ~ 1 µm. This implies that considering the sensor error to be equal to the linearity is a conservative assumption.

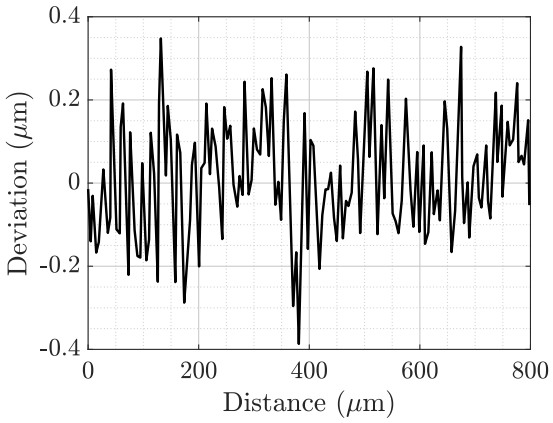

FIGURE 4.3: Linearity curve of the IFS 2404-2 confocal chromatic sensor used for testing.

§1.2. Mathematical model

In this section, the mathematical model for the FSI problem for the system described in the previous section is presented. The displacements of the layers can be divided into two parts: the static displacements produced by pressure differences in the mean flow of different channels, and the dynamic displacements generated by the pressure fluctuation due to turbulence.

In this work, steady displacements are not taken into account. This is reasonable in Channels 1, 2, and 3, since the pressure loss is dominated by the foams (see Chapter 3), whose length is the same in all channels. In addition, the channel flow distributors shown in Fig. 3.4 are designed so that the pressure loss is the same in all of them, ensuring a minimum pressure difference between the channels. In Channel 0, a static structural analysis using the pressure forces obtained from the order-of-magnitude analysis of Chapter 3, §1.1.2, including a safety factor of 5, has shown that the displacements are of the order of 10^{-4} µm, which concludes the justification that static displacements are negligible with the present geometry and flow parameters.

In terms of dynamic displacements, as discussed in the Introduction (§2.4), the maximum permissible displacement for the layers is 5 µm, and ideally with values lower than 1 µm with respect to the equilibrium position (peak to peak value of 2 µm). Therefore, a decoupled FSI strategy remains valid provided these displacements do not interfere with the fluid flow; specifically, if both the undeformed and deformed geometries result in identical aerodynamic forces. A standard mesh requirement for accurate LES simulations is that the dimensionless wall distance of the first near-wall cell is $\tilde{y}_w^+ \leq 1$. The wall distance of the first near-wall cell such that $\tilde{y}_w^+ \leq 1$ can be estimated using the Schlichting correlation for the skin friction coefficient of a flat plate (Schlichting, 1979). For $Re_h = 3000$ ($v_\infty = 8$ m/s), the estimated wall distance of the first near-wall cell such that $\tilde{y}_w^+ = 1$ is $\tilde{y} = 25$ µm. This value is one order of magnitude higher than the characteristic displacements, which means that the effect of structural displacements on the fluid flow can be neglected. In summary, it is justified to consider a decoupled FSI in the model. If the characteristic displacements given by this method are much higher than the sensor accuracy, then the model accuracy is reduced. However, this is irrelevant, since the detector cannot be installed under those conditions. In this case, design improvements or the reduction of the air freestream velocity would be required to match the targets set by the ALICE experiment.

§1.2.1. Fluid simulations

Equations

The incompressible Navier-Stokes equations (Eqs. (2.1) to (2.3)) are solved within the implicitly-filtered LES approach and the WALE turbulence model. The momentum source term is given by

Eq. (2.9), with the values of the permeability and drag coefficients specified in Chapter 3, §1.3.1.

Geometry and boundary conditions

The computing power available does not allow for the performance of the fluid simulation of the entire geometry of Fig. 3.4. The mesh required to solve at least 80% of the turbulent kinetic energy (Pope, 2000) requires a high cell count. This implies the use of a small time step, while the number of simulated time steps is high due to the large ratio between the channel length and width (280 mm/6 mm ≈ 50, see Fig. 4.4). To reduce the computational cost, the first additional assumption consists of considering that the flow in the four channels is independent. This is equivalent to stating that there is no flow between the layers, which is the case when the longerons are considered to be walls (no air can penetrate through them), and that the gap of 1.5 mm of Fig. 3.4b to the symmetry plane (0.5 mm in the real ITS3, see Fig. 1.9b) does not exist. This assumption allows the simulation of each channel separately, reducing the computational cost of the fluid simulations.

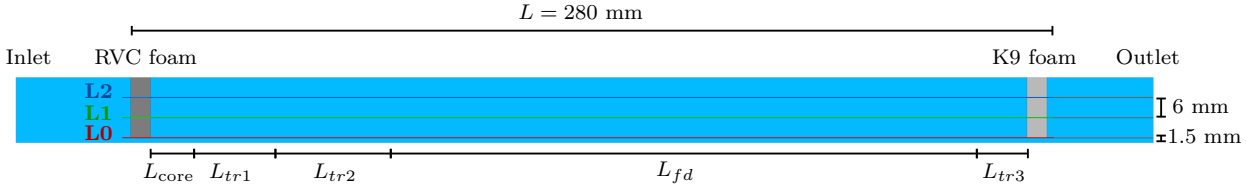

FIGURE 4.4: Cut with the plane $y = 0$ of an inner half-barrel of the ALICE ITS3.

In free shear flows, turbulence is generated at much lower Reynolds numbers than in wall-bounded flows. This fact motivates the assumption that the free shear flow after the air passes through the holes of the foams is responsible for the pressure fluctuations in the silicon layers. These fluctuations begin at the potential core during the spatial development of the Kelvin-Helmholtz instability, in a region of length L_{core} (see Fig. 4.4). Then, the fluctuations reach their maximum intensity in a region of length L_{tr1}, to then be reduced in a region of length L_{tr2}, in which the channel flow starts to develop. After a distance from the holes of $L_{\text{core}} + L_{tr1} + L_{tr2}$, the fully developed channel flow regime is reached, and this behavior holds for a distance of L_{fd}, in particular until a distance of L_{tr3} before the K9 foam, in which the flow is accelerated locally near the holes.

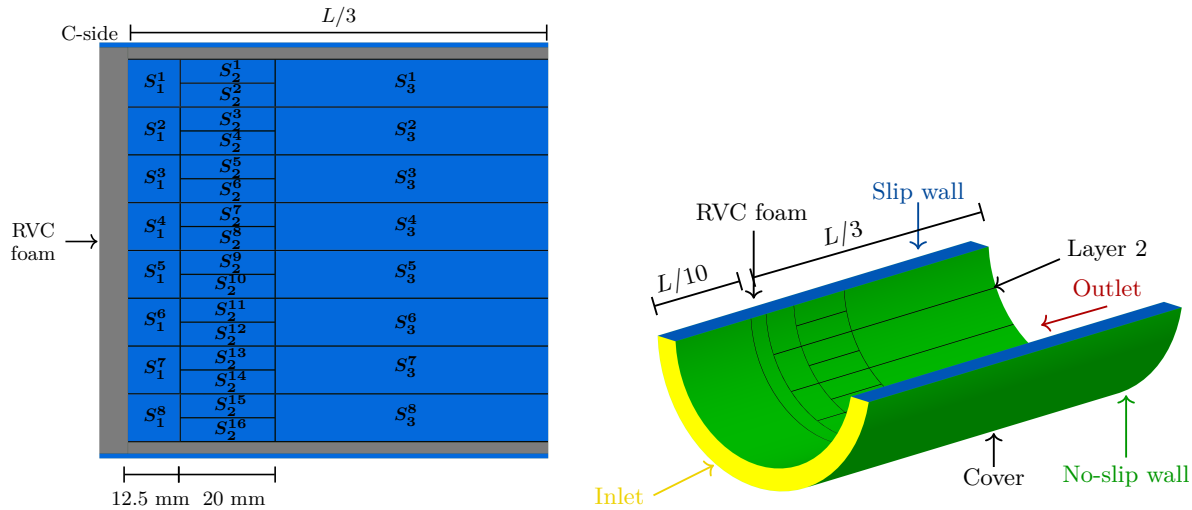

(A) Sub-surfaces of Layer 2.

(B) Isometric view of Channel 3.

FIGURE 4.5: Geometry of the fluid simulations for the calculation of the aerodynamic forces in Layer 2.

The second additional assumption consists of reducing the length of the computational domain. It is assumed that the displacements are mainly caused by the pressure fluctuations in the region

of length L_{tr1}, and the computational domain extends from the inlet of Fig. 4.4 until the flow is fully developed at a distance to the foam of $L_{\text{core}} + L_{tr1} + L_{tr2} = L/3$. The total value of $L/3$, as well as the length of $L/10$ from the inlet to the foam (see Fig. 4.5b), have been derived from preliminary LES simulations with a coarse mesh. Inlet turbulence levels are assumed not to affect the downstream solution, since the RVC foam acts as a flow straightener due to its low cell size. Its effect on the free shear flow generated in the holes is assumed to be of the same order as the error related to other assumptions of the model. In addition, since the heights of Channels 1, 2, and 3 are the same (and in Channel 0 there is no free shear flow due to the absence of foams), it is reasonable to assume that the aerodynamic loads produced in Layer 0, Layer 1, and Layer 2 are similar. Since the displacements are inversely proportional to the structural stiffness, for the same aerodynamic loads in all layers, the highest displacements are expected in Layer 2. As a consequence, this work will focus only on the displacements of Layer 2, which means that only Channels 2 and 3 will be simulated, and the pressure at Layer 2 will be obtained as the difference between the wall pressure obtained in the simulation of Channel 3 and the one of the simulation of Channel 2.

The procedure to transfer the pressure loads obtained from fluid simulations to structural simulations is an important part of the model. Generating the same computational mesh for both simulations is discarded, since fluid simulations require a much smaller mesh size, and generating a mesh with small size for structural simulations notably increases the computational cost of these simulations. An alternative is to generate meshes of different sizes to project pressure values from the fine (fluid) mesh to the coarse (structural) mesh. However, the current situation is such that this process cannot be automated in Ansys Mechanical/Fluent, which is the software used in the current work. As a solution, a division of Layer 2 into sub-surfaces is proposed, so that average values over these sub-surfaces are extracted and used as inputs for structural simulations. Considering the unbent Layer 2 for the ease of illustration, the division in the longitudinal direction is made into three sections, including a first part of length $L_{\text{core}} = 12.5$ mm (S_1), a second part of length $L_{tr1} = 20$ mm (S_2), and a third part of length $L_{tr2} = L/3 - 20 - 12.5$ mm (S_3, see Fig. 4.5a). The division in the orthogonal direction is done taking as reference the number of holes of the foam (16). As mentioned previously, pressure fluctuations are expected to be dominant in the region of length $L_{tr1} = 20$ mm; therefore, S_2 sub-surface is divided into 16 additional sub-surfaces; that is, two times greater number of elements than S_1 and S_3. These divisions and lengths have been obtained after performing the preliminary LES simulations mentioned in the previous paragraph.

The boundary conditions of the fluid simulations are sketched in Fig. 4.5b. The velocity at the inlet is set to the freestream velocity v_∞, whereas the outlet pressure is set to the reference pressure. No-slip condition is imposed on all walls of the domain except the wall in contact with the longerons, in which a slip boundary condition is applied. The same reasoning applies to the simulations of Channel 2.

Numerical implementation

The mesh consists of octrees in the bulk region, a high-quality layered poly-prism mesh in the boundary layers, and general polyhedral elements that connect both meshes. The computational mesh is generated with two different cell sizes. The fine mesh size Δ is defined in the S_1 and S_2 surfaces (see Fig. 4.5a), while in S_3 the mesh size is equal to 2Δ. It has been verified in preliminary simulations that the results given by this mesh are the same as those obtained with a uniform mesh of size Δ. In the no-slip walls, the poly-prism mesh of the boundary layer is defined such that $\tilde{y}_w^+ \leq 1$ and the aspect ratio of the first near-wall cell is less than 3.

The resolution of the equations is done with the baseline methods listed in Chapter 2, §1.3.3. Simulations start at $t = t_0$ from a precursor RANS simulation, and the time step is selected so that the maximum cell convective Courant number $Co < 1$. This same time step is used in all simulations of the mesh independence study. The simulations are completed when the flow statistics (pressure forces) reach a statistically steady state at $t = T$. Pressure forces are extracted at the same frequency as the sampling frequency of the confocal sensor (30 kHz).

§1.2.2. Structural simulations

Equations

The displacements $\boldsymbol{d}$ of Layer 2 are obtained from the following equation:

$$\boldsymbol{M}\frac{\partial^2 \boldsymbol{d}}{\partial t^2} + \boldsymbol{C}\frac{\partial \boldsymbol{d}}{\partial t} + \boldsymbol{K}\boldsymbol{d} = 0 \tag{4.1}$$

where $\boldsymbol{M}$ is the mass matrix, $\boldsymbol{C}$ is the damping matrix, and $\boldsymbol{K}$ is the stiffness matrix.

The mass and stiffness matrices are obtained from known material properties, while the damping matrix is, a priori, unknown. Rayleigh approximation is considered, in which the damping matrix is a linear function with respect to the mass and stiffness matrices (Zienkiewicz et al., 2005):

$$\boldsymbol{C} = \alpha\boldsymbol{M} + \beta\boldsymbol{K}, \tag{4.2}$$

with α and β referring to the mass and stiffness multipliers, respectively. These values relate the damping ratio at a particular natural frequency, ζ_i, with the natural frequency f_i (Dorf and Bishop, 2016):

$$\zeta_i = \frac{\alpha}{4\pi f_i} + \pi\beta f_i. \tag{4.3}$$

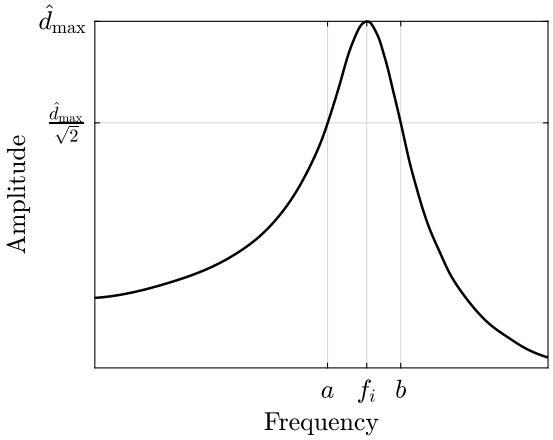

FIGURE 4.6: Half-bandwidth method for the calculation of the damping ratio.

The values of α and β are closed with the damping ratios of two natural frequencies of the system. The damping ratio is estimated using the half-power bandwidth method (Papagiannopoulos and Hatzigeorgiou, 2011), which uses the experimental frequency response of the geometry under consideration as a reference. For a natural frequency f_i whose corresponding amplitude is $\hat{d}_{\max}$, then $\zeta_i = 2(b-a)/f_i$, where a and b are the frequencies such that the amplification is equal to $\hat{d}_{\max}/2$ (see Fig. 4.6).

Geometry and boundary conditions

The geometry of the transient structural simulations is shown in Fig. 4.7. The entire Layer 2 is simulated, with the pressure forces obtained from the fluid simulations as boundary conditions. At the surface of length $L - L/3 = 2L/3$ —not considered in the fluid simulations—the mean value (in space) of the pressure at the S_3 sub-surfaces (see Fig. 4.5a) is applied, representing an approximation of the fully developed channel flow (see Fig. 4.4). The bonding between foams and silicon layers is assumed to be infinitely stiff; therefore, silicon-foam surfaces are fixed supports.

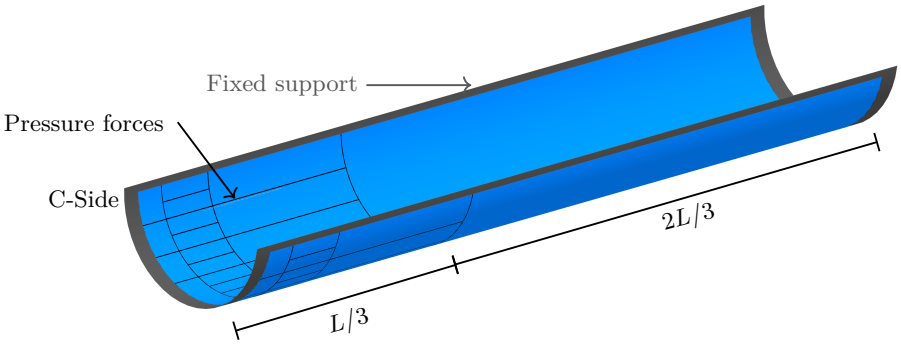

FIGURE 4.7: Geometry and boundary conditions of the structural simulations of Layer 2.

Numerical implementation

Equation (4.1) is solved with the finite element method that is implemented in Ansys Mechanical 2023R1 (Ansys Inc., 2023b). Since the thickness of the layer is negligible with respect to the other dimensions, particularly to the radius of curvature of the bent layer, shell elements are used (Reddy, 2006). This allows the generation of a two-dimensional mesh, in which quadrilateral elements are used with a uniform size equal to δ. In the simulations of the experimental setup, the heater layout explained in Chapter 3, §1.2, including the glue, is taken as a reference, and the copper layer is neglected as a first approximation. This is because the copper layer has the geometry of a "serpentine" (see Fig. 4.8), and the direction of the serpentine is such that the contribution to the bending stiffness of the structure in the y direction (normal to the unbent layer) is considerably reduced with respect to a fully-solid layer. The contacts between the layers of the integrated heaters are assumed to be ideal; that is, there is no separation nor sliding between the layers.

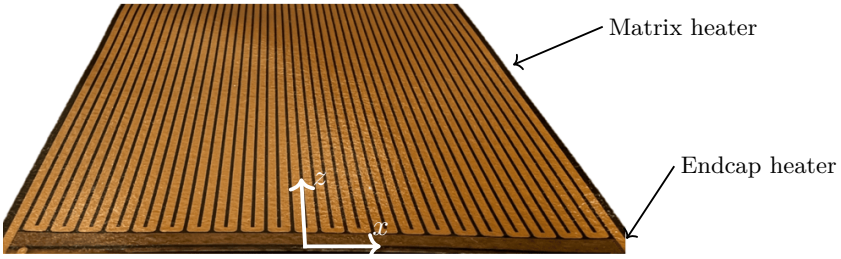

FIGURE 4.8: Layers with integrated heaters used in the ITS3 half-inner barrel prototype.

The mass and stiffness matrices are given as follows (Zienkiewicz et al., 2005):

$$\boldsymbol{M} = \rho \int_{V_e} \boldsymbol{N}^T \boldsymbol{N} \, \mathrm{d}\mathcal{S}, \qquad \boldsymbol{K} = \int_{V_e} \boldsymbol{B}^T \boldsymbol{D} \boldsymbol{B}, \tag{4.4}$$

where ρ is the material density, and the matrices are defined as follows:

- $\boldsymbol{N}$: relates the nodal displacements $\boldsymbol{u}$ and the displacements of a general point:

$$\boldsymbol{w} = \boldsymbol{N}\boldsymbol{u}. \tag{4.5}$$

- $\boldsymbol{B}$: relates the strains $\boldsymbol{\varepsilon}$ to the nodal displacements:

$$\boldsymbol{\varepsilon} = \boldsymbol{B}\boldsymbol{u}. \tag{4.6}$$

- $\boldsymbol{D}$: the elastic stiffness matrix that relates stresses $\boldsymbol{\sigma}$ and strains:

$$\boldsymbol{\sigma} = \boldsymbol{D}\boldsymbol{\varepsilon}, \tag{4.7}$$

and whose local components in the directions $\hat{x}$, $\hat{y}$, and $\hat{z}$ for an orthotropic material are:

$$\begin{bmatrix} \sigma_{\hat{x}\hat{x}} \\ \sigma_{\hat{y}\hat{y}} \\ \sigma_{\hat{z}\hat{z}} \\ \sigma_{\hat{y}\hat{z}} \\ \sigma_{\hat{z}\hat{x}} \\ \sigma_{\hat{x}\hat{y}} \end{bmatrix} = \begin{bmatrix} \frac{1}{E_{\hat{x}}} & -\frac{\nu_{\hat{y}\hat{x}}}{E_{\hat{y}}} & -\frac{\nu_{\hat{z}\hat{x}}}{E_{\hat{z}}} & 0 & 0 & 0 \\ -\frac{\nu_{\hat{x}\hat{y}}}{E_{\hat{x}}} & \frac{1}{E_{\hat{y}}} & -\frac{\nu_{\hat{z}\hat{y}}}{E_{\hat{z}}} & 0 & 0 & 0 \\ -\frac{\nu_{\hat{x}\hat{z}}}{E_{\hat{x}}} & -\frac{\nu_{\hat{y}\hat{z}}}{E_{\hat{y}}} & \frac{1}{E_{\hat{z}}} & 0 & 0 & 0 \\ 0 & 0 & 0 & \frac{1}{G_{\hat{y}\hat{y}}} & 0 & 0 \\ 0 & 0 & 0 & 0 & \frac{1}{G_{\hat{z}\hat{x}}} & 0 \\ 0 & 0 & 0 & 0 & 0 & \frac{1}{G_{\hat{x}\hat{y}}} \end{bmatrix}^{-1} \begin{bmatrix} \varepsilon_{\hat{x}\hat{x}} \\ \varepsilon_{\hat{y}\hat{y}} \\ \varepsilon_{\hat{z}\hat{z}} \\ \varepsilon_{\hat{y}\hat{z}} \\ \varepsilon_{\hat{z}\hat{x}} \\ \varepsilon_{\hat{x}\hat{y}} \end{bmatrix}. \tag{4.8}$$

All materials considered in this study are assumed to be isotropic except from silicon, which is orthotropic. In each point of the unbent Layer 2, following the global coordinate system shown in Fig. 3.1a, the $\hat{z}$ axis is defined in the along the 280 mm-length layer, the $\hat{y}$ axis in the normal direction to the layer, and the $\hat{x}$ axis such that it leads to a cartesian right-handed coordinate system (see Fig. 4.8).

Symbol	Material	Parameter	Direction	Value	Units
E	Al	Young modulus		70	GPa
	Cu			130	
	Glue			2	
	PI			2.4	
	Si		$\hat{x}$	169	
	Si		$\hat{y}$	130	
	Si		$\hat{z}$	169	
G	Si	Shear modulus	$\hat{x}\hat{y}$	79.6	GPa
	Si		$\hat{x}\hat{z}$	50.9	
	Si		$\hat{y}\hat{z}$	79.6	
v_∞	Air	Freestream velocity	z	8	m/s
γ	Al	Poisson ratio		0.33	
	Cu			0.36	
	Glue			0.33	
	PI			0.34	
	Si		$\hat{x}\hat{y}$	0.28	
	Si		$\hat{x}\hat{z}$	0.064	
	Si		$\hat{y}\hat{z}$	0.36	

TABLE 4.1: Simulation parameters for the aeroelastic analysis.

§2. Results and discussion

Simulation parameters are given in Tables 2.2, 3.3 and 4.1. The components of the stiffness matrix of the p-type (100) silicon wafer have been obtained from (Hopcroft et al., 2010). It has been shown in Chapter 3, §2.2.1 that values of $v_\infty > 5$ m/s are required to meet the thermal design

requirements, while values of $v_\infty > 8$ m/s do not provide significant improvements in thermal performance while leading to large pressure loss. Thus, as a realistic conservative assumption, the freestream velocity is fixed to 8 m/s.

§2.1. Model validation

The first study is done in the fluid simulations. Since there are no relevant mean quantities of interest in the flow, the study will be focused on the spectral content. The time history of the pressure $p = p(t)$ is extracted from $t = 0$ to $t = T$ on the surfaces S_1^4, S_2^8, and S_3^4 (see Fig. 4.5a), and the variance of the signal $\sigma^2(p(t))$ is used as a convergence indicator (Norton and Karczub, 2003). The value $\sigma^2(p_i^j)$ will be referred to S_i^j. The consideration of the variance is because the power spectral density (PSD), S_{pp}, will be analyzed in the comparison with experimental data, and both variables are related in the frequency domain as follows:

$$\sigma^2(p) = \int_0^\infty S_{pp}(f)\ \mathrm{d}f - \mu(p)^2, \tag{4.9}$$

where μ is the mean value of $p(t)$, and S_{pp} represents the signal power:

$$S_{pp}(f) = \frac{1}{T}|\hat{p}(f)|^2 = \frac{1}{T}\left|\int_0^\infty p(t)e^{-2\pi i f t}\ \mathrm{d}t\right|^2, \tag{4.10}$$

with $\hat{p}(f)$ referring to the Fourier transform of the function $p = p(t)$.

Three meshes of different sizes are considered in the simulations, which are referred to the channel height h in Table 4.2. The study is conducted only in Channel 3, given the similarities between the geometries of Channels 2 and 3 (see Fig. 3.4). The results show that the differences between the variance values decrease as the size of the mesh decreases, leading to convergent behavior. The mesh of 15.7 M of cells is considered for the following simulations, in which the aspect ratio of the first near-wall cell is 2.5 to achieve $\tilde{y}_w^+ = 1$, which is acceptable for LES simulations.

$\boldsymbol{\Delta}$	**Number of cells**	$\boldsymbol{\sigma^2(p_1^4)}$ **(Pa²)**	$\boldsymbol{\sigma^2(p_2^8)}$ **(Pa²)**	$\boldsymbol{\sigma^2(p_3^4)}$ **(Pa²)**
$h/25$	2.8 M	0.099	0.282	0.026
$h/37.5$	5.4 M	0.128	0.349	0.027
$h/50$	15.7 M	0.141	0.387	0.027

TABLE 4.2: Results of the mesh independence study of the fluid simulations of Channel 3.

The variances obtained prove that pressure fluctuations are dominant in the S_2 surfaces, and that the effect of the periodic channel flow (S_3) on the displacements of Layer 2 is negligible. These results support the assumption of reducing the length of the fluid domain.

$\boldsymbol{\delta}$	**Number of cells**	$\boldsymbol{f_1}$ **(Hz)**	$\boldsymbol{d_{p-p}^{\text{center}}}$ **(μm)**
h	0.9 K	660	0.6
$h/2$	2.9 K	599	0.35
$h/6$	25 K	586	0.3

TABLE 4.3: Results of the mesh independence study of the structural simulations of Layer 2.

Using the pressure forces obtained from the fluid simulations performed with the fine mesh, structural simulations have been carried out with three different mesh sizes. The first natural frequency obtained from a modal analysis (f_1) and the peak to peak value of the displacements

at the center point (d_{p-p}^{center}) are used for result comparison. Table 4.3 shows that a convergent behavior is achieved, and the mesh of $\delta = h/6$ is used for the structural simulations.

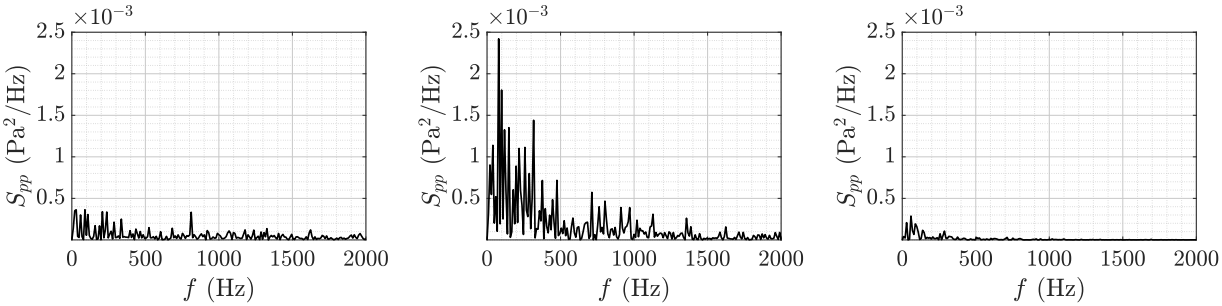

(A) S_1^4. (B) S_2^8. (C) S_3^4.

FIGURE 4.9: Power spectral densities of the pressure on Layer 2 obtained from Channel 3 simulation.

§2.1.1. Comparison with experimental data

Fig. 4.10a compares the results given by the confocal sensor and the mathematical model developed in this chapter at the center point. The model provides the main peak of the PSD at 586 Hz in the simulation, which corresponds to the first natural frequency of Layer 2 of the prototype. This can be verified in Fig. 4.11a, in which only the natural frequencies with displacements in at least one of the two measurement points are illustrated. The model also predicts significant contributions of the eighth and twelfth natural frequencies (see Figs. 4.11c and 4.11d). The former is also present at approximately the same frequency in the experiments, but with decreased amplitude, while the latter is not identified. As expected, the smallest contribution is given by the fifth natural frequency, given that the displacement at the center point is negligible (see Fig. 4.11b). Since the dominant frequencies of the aerodynamic forces are lower than the first natural frequency (see Fig. 4.9), the risk of failure of the system due to mechanical resonance is reduced.

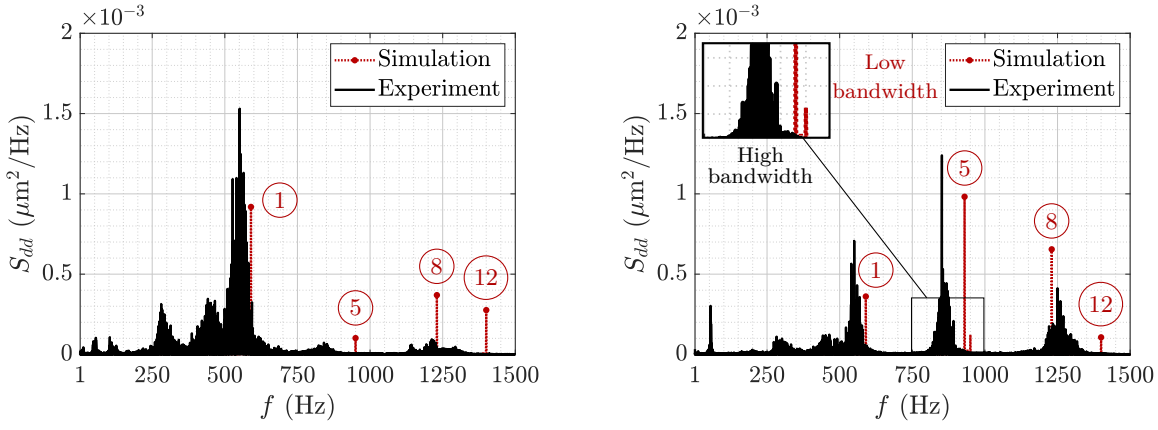

(A) Center point. (B) C-side point.

FIGURE 4.10: Power spectral densities of Layer 2 displacements of the ITS3 half-barrel prototype obtained from experiment and simulation.

The displacement PSDs obtained at the C-Side point are given in Fig. 4.10b. In both approaches the most relevant contribution is given by the fifth natural frequency, while the peaks of the first and eighth natural frequencies are of the same order of magnitude. In the same way as at the center point, the simulation predicts a peak at approximately 1400 Hz that is not noticed in the experiments. Moreover, a mode appears at 55 Hz with reduced damping in the experiments, which is not present in the simulation. Since this value is much lower than the first natural frequency of the layer, it is assumed that this is a part of the vibrations of the whole wind tunnel due to

external noise. Indeed, multiples of 55 Hz are also identified at the center point (275 Hz and 440 Hz). This is a characteristic behavior of structures connected mechanically to engines (Scheffer and Girdhar, 2004), which is the case in the current experimental setup (see Chapter 3, §1.2). Given that the displacements of the structures connected to the prototype do not vanish, it is expected that the experiment overpredicts the values of the displacements of the layers. To determine the damping coefficients (Eq. (4.2)), experimental data at the C-side point (fifth natural frequency) and at the center point (first natural frequency) have been used, leading to a value of $\zeta = 0.001$ for both natural frequencies, which in turn is equivalent to $\alpha = 4.19$ and $\beta = 2.2 \times 10^{-7}$.

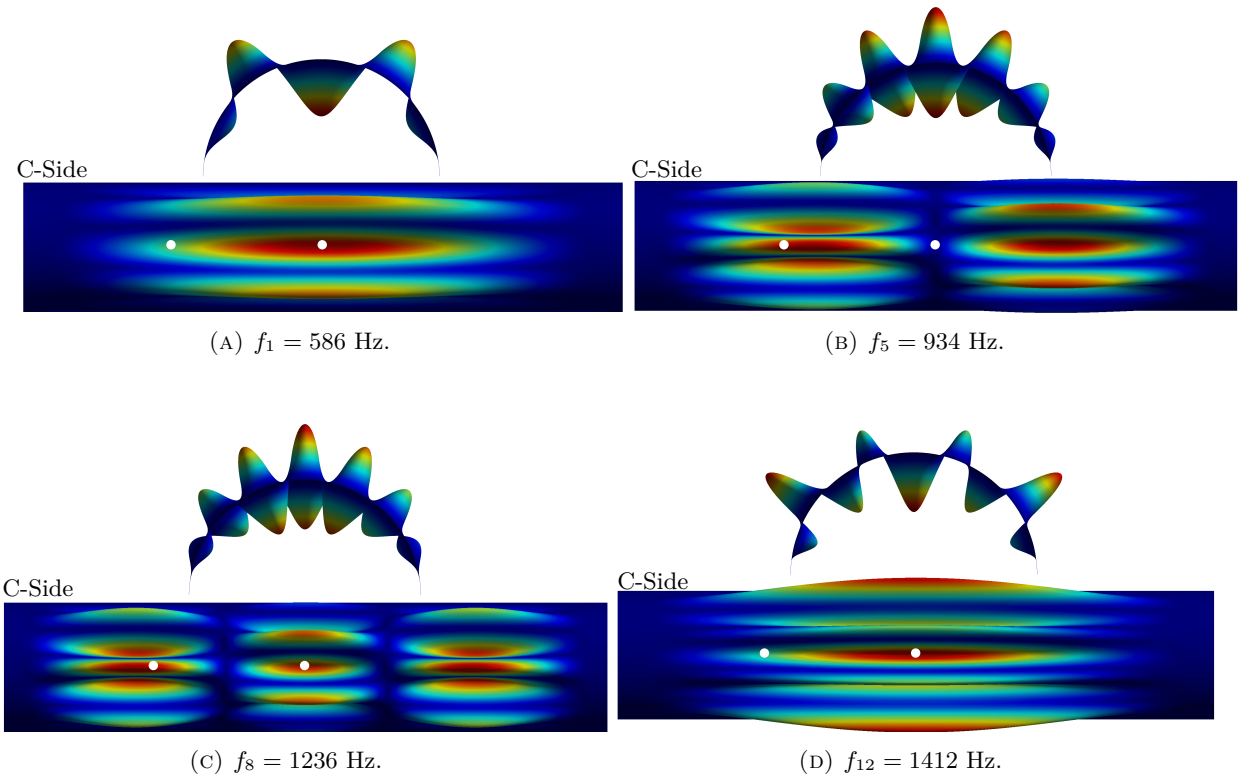

(A) $f_1 = 586$ Hz. (B) $f_5 = 934$ Hz.

(C) $f_8 = 1236$ Hz. (D) $f_{12} = 1412$ Hz.

FIGURE 4.11: Side and top view of the natural frequencies of Layer 2 of the ITS3 inner half-barrel prototype with relevant displacement in the measurement points (highlighted in white bullets).

Figure 4.12 shows the time histories of the PSDs of Fig. 4.10a during one second, which is the simulation time in which the displacement values are extracted. Simulations provide a peak-to-peak value $d_{p-p}^{\text{center}} \approx 0.3$ µm, while, in the experiments, $d_{p-p}^{\text{center}} \approx 1$ µm. As anticipated in the previous paragraph, the main reason is that the displacements of the entire wind tunnel are responsible for the contributions for $f < 550$ Hz and possibly for higher frequencies. Another important aspect is related to the damping term of Eq. (4.1). In the experimental data of Fig. 4.10b, the peaks at the natural frequencies are approximately a Dirac delta for values of the PSD higher than the peak value divided by $\sqrt{2}$, which is the limit value used in the half-power bandwidth method. This also occurs in the simulations. However, the contribution of the natural frequencies for which the value of the PSD is lower than the limit is negligible in the simulation, leading to low bandwidth; in the experiments the bandwidth is significantly large (see the zoom of Fig. 4.10b). Apart from the limitations of the modeling approach, it cannot be ruled out that the structure of the entire wind tunnel has a damping ratio much higher than the one of the silicon layer, which would explain the experimental results. In addition, it should be noted that the resolution of the sensors (0.125 μm) is of the same order as the differences between the experimental and numerical results, and the linearity (± 0.4 μm) adds additional error. Without air flow, the displacements measured by the sensor are $d_{p-p}^{\text{center}} \approx 0.2$ μm due to a combination of sensor error and external noise in the test room.

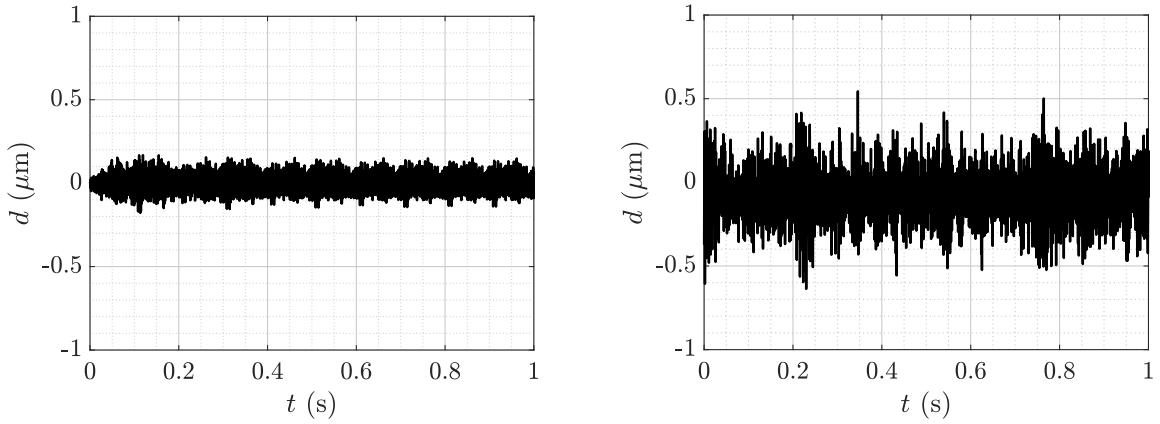

(A) Simulation. (B) Experiment.

FIGURE 4.12: Time history of the displacements of Layer 2 of the ITS3 inner half-barrel prototype at the center hole.

§2.1.2. Influence of the layout

The proposed model gives an acceptable approximation of the first measured natural frequencies, with differences lower than 10% (see Table 4.4). Neglecting the Cu layer is an intermediate assumption, as the contributions to the mass, damping, and stiffness matrices are not taken into account. Even if the thickness of the copper layer is only 5 μm, the high density of this material (see Table 4.1) leads to a significant contribution to the system mass. Consequently, it is crucial to study the influence of the modeling assumption. The most conservative approach is to consider that Layer 2 consists of a Si layer of 40 µm and a uniformly distributed mass equal to the sum of the contributions of the glue, PI, and Cu layers. Contrarily, the ideal situation occurs when the Cu layer is added to the baseline layout. Table 4.4 shows that the baseline configuration provides the closest prediction to the experimental data in the natural frequencies. In addition, the effects of modifying the layout on the values of the natural frequencies are significant, with differences up to 50% in f_1 between the Si + mass and Baseline + Cu. As expected, when only the Si layer contributes to the system stiffness, the displacements increase.

Layout	$\boldsymbol{d_{p-p}^{\text{center}}}$ **(μm)**	$\boldsymbol{d_{p-p}^{\text{cside}}}$ **(μm)**	$\boldsymbol{f_1}$ **(Hz)**	$\boldsymbol{f_5}$ **(Hz)**	$\boldsymbol{f_8}$ **(Hz)**	$\boldsymbol{f_{12}}$ **(Hz)**
Experiment	1	0.9	550	850	1250	–
Baseline	0.3	0.3	586	934	1236	1412
Si + mass	0.45	0.45	438	692	888	1003
Baseline + Cu	0.2	0.2	709	1091	1452	1798

TABLE 4.4: Natural frequencies and displacements of Layer 2 of the ITS3 half-barrel prototype for different layouts.

§2.2. Real configuration

After confirming the accuracy of the mathematical model using experimental results obtained in a prototype, in this section the expected real configuration of the future ITS3 IB will be studied. This real configuration differs from the one of the prototype in the materials used in the layers. In addition, possible adjustments required due to changes in detector cooling and installation requirements are also investigated in §2.2.1.

The Si layers used in the ITS3 IB will not contain the integrated heaters used in the experimental setup. The reference design for the real detector uses Si layers of 40 µm of thickness, although other alternatives are under consideration if that thickness cannot be achieved in the design for performance reasons: these include Si layers of 50 µm, or Si layers of 40 µm with an additional

Al layer of 10 µm deposited with physical vapor deposition. Using the model developed in this work, the aerodynamic loads are the same as those obtained in the simulations of the experimental prototype, but the setup of the structural simulation changes.

Layout	d_{p-p}^{center} **(µm)**	d_{p-p}^{cside} **(µm)**	f_1 **(Hz)**	f_5 **(Hz)**	f_8 **(Hz)**	f_{12} **(Hz)**
Si 40 µm (baseline)	0.5	0.5	766	1209	1551	1752
Si 50 µm	0.35	0.35	861	1355	1816	2074
Si+Al (40+10 µm)	0.55	0.55	761	1192	1592	1828

TABLE 4.5: Natural frequencies and displacements of Layer 2 of the real ALICE ITS3 IB for different layouts.

Table 4.5 shows the natural frequencies and displacements for different layouts. As predicted from the theory of rectangular plates (Reddy, 2006), for a given material and planar dimensions, the natural frequencies are proportional to the thickness, which leads to the increase of the values for thicker layers. Given the similar density of Al and Si, the system mass remains approximately constant in the Si+Al layout as opposed to the Si case of 50 µm. However, the stiffness decreases due to the significantly lower Young modulus of Al. Similar conclusions can be extracted from the displacements, with maximum differences of up to 40% between the layouts considered.

The frequency response of Layer 2 for the baseline layout of the real configuration is given in Fig. 4.13; only the first natural frequency is present in Fig. 4.13a, while the first and fifth frequencies are responsible for the C-side point displacements (Fig. 4.13a). The reduced number of relevant frequencies is because of the eighth and twelfth natural frequencies are higher than 1500 Hz, and in this range, the amplitudes of pressure forces are negligible (see Fig. 4.9b). The shape of the PSD and the values of the displacements are similar to those of the experimental setup, which means that the results obtained with experimental setup are representative of the real behavior of the ALICE ITS3. The design requirement ($d_{p-p} < 2$ µm) is met in all cases.

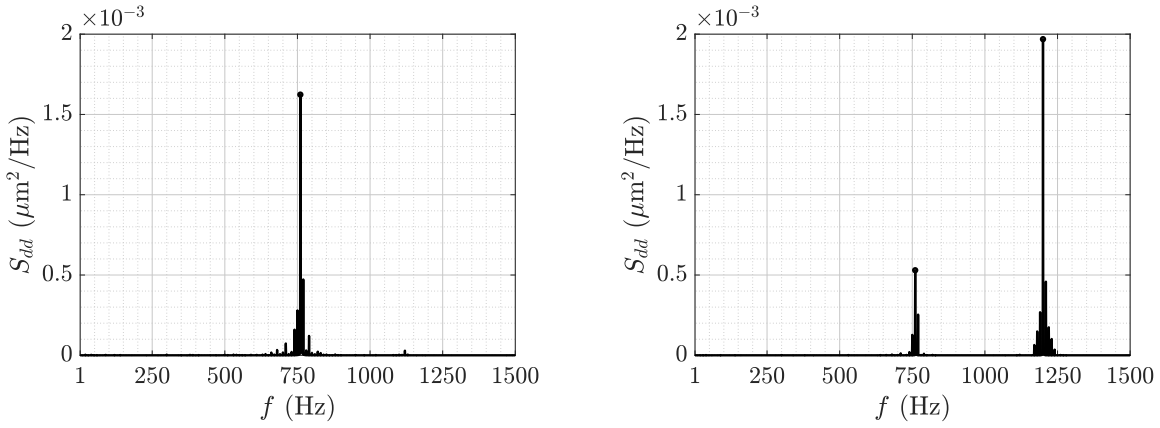

(A) Center point. (B) C-side point.

FIGURE 4.13: Simulation results of of Layer 2 displacements of the baseline layout of the ALICE ITS3 IB.

§2.2.1. Design modifications

As mentioned in Chapter 3, §1.1.1, holes of 1.5 mm of diameter are drilled in the foams of the ITS3 IB prototype to reduce the pressure loss. This aspect is relevant for two reasons: first, the system will work without interruption for many months, and the power consumption of the air flow generator should be minimized; second, because the gap of 1 mm between the half-barrels (see Fig. 1.9b) will lead to a loss of air flow to the environment that increases as the foam pressure loss increases. Moreover, the ALICE ITS3 installation will be challenging due to the reduced free

space in the ALICE cavern and the tight design tolerances; therefore, this gap could be increased up to 2 mm, leading to further increase of the leak rate. To reduce the foam pressure loss, two modifications are proposed: increasing the diameter of the hole to 2 mm (Fig. 4.14b) and generating 1.5 mm height slots (Fig. 4.14c). It has been verified that these modifications applied to the K9 foam lead to an increase of up to 1 °C at the surface in contact with the foam, and thermal design requirements are met even with this increase.

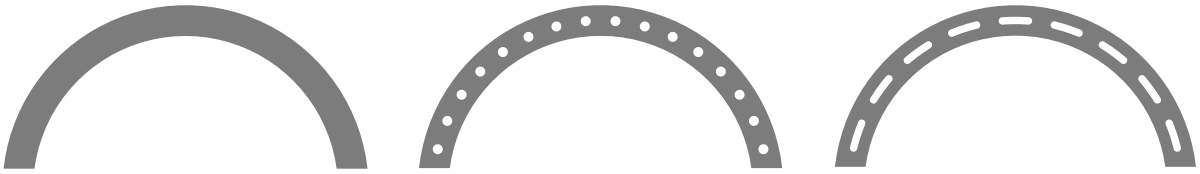

(A) No holes/slots. (B) Holes (diameter 2 mm). (C) Slots (height 1.5 mm).

FIGURE 4.14: Different foam designs used for simulation.

Table 4.6 shows that drilling holes of 2 mm and slots of 1.5 mm decrease the pressure loss through the foam $(\nabla p)_f$ 15% and 30%, respectively, compared to the baseline design. However, the displacements of the layers increase significantly. In these configurations, even if the maximum velocity is reduced with respect to the baseline case, the amount of air that passes through the foam cells is reduced. Since the foam acts as a turbulence reducer due to the low cell characteristic cell size, turbulence levels increase as foam material is eliminated. If no material is removed from the foam, no turbulence is generated, and vibrations are negligible in a channel flow at a Reynolds number of 3000. However this configuration entails a higher pressure loss than the baseline setup. It should be noted that decreasing the ratio between the foam (filled with cells) sectional area and the channel section, $\mathcal{S}$, does not lead to increased structural displacements for all values of $\mathcal{S}$. This is because in the limit $\mathcal{S} \to 0$ the foam is no longer present, and the flow is the same channel flow that leads to almost vanishing layer displacements mentioned before. These cases for which $\mathcal{S} \ll 1$ are not considered due to the fragility of foams and the compromised thermal performance. However, intermediate cases could be considered if the thermal design requirements are relaxed.

Design	$(\nabla p)_f$ **(Pa/mm)**	d_{p-p}^{center} **(μm)**	d_{p-p}^{cside} **(μm)**
Holes 1.5 mm (baseline)	110	0.5	0.5
Holes 2 mm	90	0.7	0.7
Slots 1.5 mm	75	1	1
No holes and/or slots	130	≈ 0	≈ 0

TABLE 4.6: Foam pressure loss and Layer 2 displacements of the baseline layout of the ALICE ITS3 IB for different foam designs.

Figure 4.15 illustrates the turbulent structures obtained from iso-surfaces of the Q-criterion, which is one of the invariants of the $\nabla \boldsymbol{v}$ tensor (Jeong and Hussain, 1995). As predicted in the model developed in §1.2.1, the flow instability is generated after the air passes through the holes, and the size of the turbulent region is of the order of the hole diameter in S_1 (defined in Fig. 4.5a). This leads to no interaction with Layer 2, and, as a consequence, to negligible pressure fluctuations (see Fig. 4.15a). Then, in S_2 the turbulent length scale increases and the jet mixing leads to maximum turbulence levels. After this point, turbulent structures are damped, giving rise downstream to the fully developed channel flow. The picture is similar in the case of 2 mm holes (Fig. 4.15b), with increased pressure fluctuations due to the increased amount of air that is accelerated.

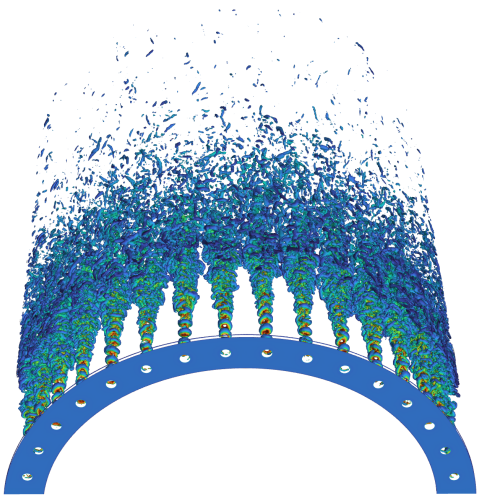

(A) Baseline (Holes, diameter 1.5 mm).

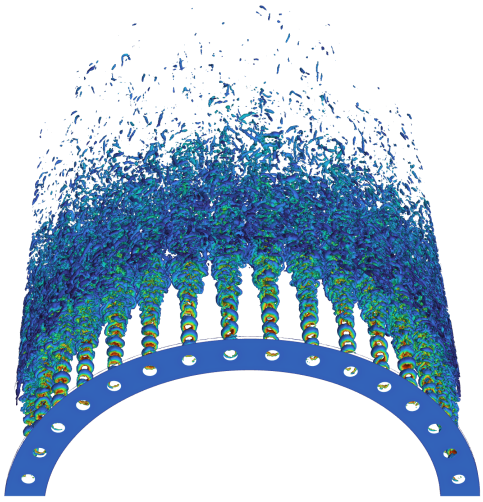

(B) Holes (diameter 2 mm).

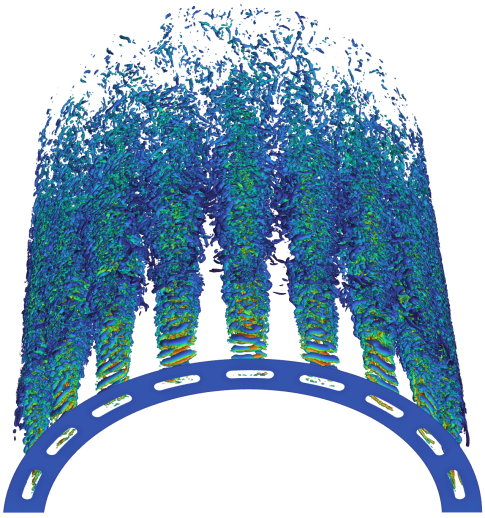

(C) Slots (height 1.5 mm).

(D) No holes and/or slots.

FIGURE 4.15: Iso-surfaces of $Q = 5 \times 10^7$ s^{-2} of the Channel 3 flow for different foam designs.

The large turbulent scales provide the dominant contribution to the turbulent kinetic energy (Pope, 2000); thus, higher displacements are obtained in the case with slots (see Fig. 4.15c). Another consequence of the higher energy of the jets is that the interaction and subsequent damping are produced further away from the foam. When no holes and/or slots are defined, there are no turbulence sources (see Fig. 4.15d), and consequently, layer displacements vanish. It has been verified that the PSDs of the pressure forces of different foam designs on the surface with the highest fluctuations (S_2) are essentially Fig. 4.9b scaled by a factor, that is, with similar dominant frequencies. Another deduction is that the peak to peak values of the displacements are proportional to the peak to peak values of the pressure forces, which is in line with the predictions of classical analytical theories that consider steady variables (Reddy, 2006).

Chapter 5

Turbulence model for industrial applications

In this chapter a generalized WMLES formulation (GWMLES) is developed that extends the classical WMLES approach. The model is divided into two separated formulations: $\text{GWMLES}_{\text{sub}}$, where turbulence is modeled up to the inner part of the log-layer, and $\text{GWMLES}_{\text{log}}$, where the viscous sublayer and the entire log-layer are modeled. $\text{GWMLES}_{\text{sub}}$ aims to improve current WMLES models, while the purpose of the $\text{GWMLES}_{\text{log}}$ is to reduce the computational cost of the DES family, as well as to eliminate the shortcomings that lead to solution deterioration (see Fig. 5.1). The GWMLES model is based on the SBES approach of blending the turbulent viscosities, but with two key differences: first, that in $\text{GWMLES}_{\text{log}}$ the RANS model does not cover the outer layer of the boundary layer, which is not universal; and second, that the selection between $\text{GWMLES}_{\text{log}}$ and $\text{GWMLES}_{\text{sub}}$ is done by the user and not depending on the mesh size. The remaining requirements for the blending function are shared with SBES to overcome the deficiencies of the DES family, namely the dissipative LES part, GIS, and the gray areas. First, the model is presented in §1; second, in §2, the results given by the model are compared with DDES, IDDES, SBES, and URANS, as well as with experimental data and DNS/LES/WMLES results available in the literature; in particular, in four test cases that represent industrial applications: a free shear flow, two turbulent wall-bounded flows, and a laminar-turbulent transitional flow.

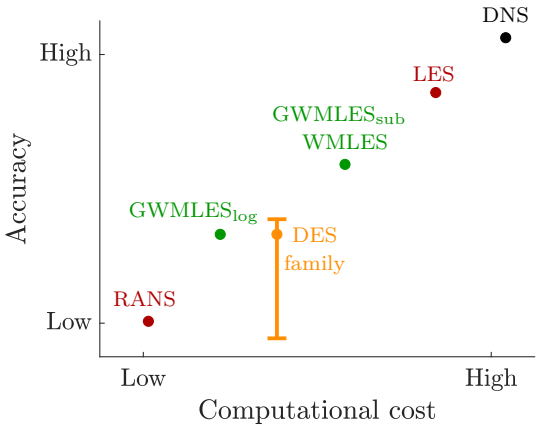

FIGURE 5.1: Overview of the main approaches for simulating turbulent flows. The differences between the models are not in real scale, since they are Reynolds number dependent.

§1. Model description

The model equations are listed in §1.1, which are closed with the expression of the blending function that is developed in §1.1.1. The numerical implementation is discussed in §1.2, including, in §1.2.3, the definition of quality estimators used in numerical simulations for model validation.

§1.1. Equations

The compressible Navier-Stokes equations are (Pope, 2000):

$$\begin{cases} \dfrac{\partial \rho}{\partial t} + \nabla \cdot (\rho \boldsymbol{v}) = 0 & (5.1) \\ \dfrac{\partial (\rho \boldsymbol{v})}{\partial t} + \nabla \cdot (\rho \boldsymbol{v} \otimes \boldsymbol{v}) = -\nabla p + \nabla \cdot \tau & (5.2) \\ \dfrac{\partial (\rho e)}{\partial t} + \nabla \cdot (\rho \boldsymbol{v} e) = -p \nabla \cdot \boldsymbol{v} + \phi_v + \nabla \cdot ((\kappa + \kappa_t) \nabla T). & (5.3) \end{cases}$$

Equations (5.1) to (5.3) contain the following assumptions, terms, and parameters:

- The *viscous stress tensor* τ uses the Boussinesq turbulent viscosity assumption (Pope, 2000):

$$\tau_{ij} = (\mu + \mu_t)\left(2S_{ij} - \frac{2}{3}\frac{\partial v_k}{\partial x_k}\delta_{ij}\right) - \frac{2}{3}\rho k \delta_{ij}, \tag{5.4}$$

  where δ_{ij} is the Kronecker delta, $S_{ij} = (\partial v_i/\partial x_j + \partial v_j/\partial x_i)/2$ are the components of the strain rate tensor, and k is the turbulent kinetic energy.

- The *turbulent viscosity* μ_t blends the RANS and LES formulations (Menter, 2018):

$$\mu_t = \mu_t^{\text{RANS}} f_{\text{GWMLES}} + \mu_t^{\text{LES}}(1 - f_{\text{GWMLES}}). \tag{5.5}$$

  Unless otherwise specified, μ_t^{RANS} is given by the $k-\omega$ SST model, and μ_t^{LES} by the WALE model with a constant $C_w = 0.325$. The blending function f_{GWMLES} is presented in §1.1.1. Since the RANS and LES formulations are used in different domain zones, it is considered that the flow variables are Reynolds-averaged in the RANS regions ($f_{\text{GWMLES}} = 1$) and implicitly-filtered in the LES regions ($f_{\text{GWMLES}} = 0$).

- The *production terms* of the RANS equations—which are proportional to μ_t^2—use the turbulent viscosity μ_t^{RANS} in the entire domain (and not μ_t, see Eq. (5.5)), even in the zones where $f_{\text{GWMLES}} = 0$. This ensures that f_{GWMLES} does not depend explicitly on the mesh size, since, as shown hereafter, f_{GWMLES} is a function of the RANS turbulence variables.

- The *viscous dissipation function* $\phi_v = \nabla \cdot (\tau \cdot \boldsymbol{v}) - \boldsymbol{v} \cdot (\nabla \cdot \tau)$.

§1.1.1. GWMLES blending fuction

The expression for f_{GWMLES} is developed to provide two different formulations: $\text{GWMLES}_{\text{log}}$, where $f_{\text{GWMLES}} \to 1$ up to the outermost part of the log-layer and $f_{\text{GWMLES}} \to 0$ elsewhere, and $\text{GWMLES}_{\text{sub}}$, where $f_{\text{GWMLES}} \to 1$ up to the inner part of the log-layer and $f_{\text{GWMLES}} \to 0$ elsewhere. The starting point is the F_2 function of the $k-\omega$ SST model (see Appendix A, §3.2):

$$F_2 = \tanh\left\{\left[\max\left(\frac{2\sqrt{k}}{\beta^* \omega \tilde{y}}, \frac{500\nu}{\tilde{y}^2 \omega}\right)\right]^2\right\} = \tanh\left\{\left[\max\left(\text{arg}_1, \text{arg}_2\right)\right]^2\right\}, \tag{5.6}$$

that is, $F_2 \to 1$ if arg_1 or $\text{arg}_2 \gg 1$, while $F_2 \to 0$ if arg_1 and $\text{arg}_2 \ll 1$. In arg_1, $\beta^* = 0.09$ is a model constant, and $\tilde{y}$ is the wall distance. The expressions of arg_1 and arg_2 are based on perturbation analyses of the boundary layer (see (Menter, 1994; Wilcox, 2006)):

- arg_1: the equations of k and ω can be simplified in the log-layer by making the same assumptions done in the derivation of the law of the wall. As a result, the turbulence length scale $l_t = \sqrt{k}/(\beta^* \omega) \approx 2.5\tilde{y}$ in the log-layer. This means that $\tanh[(\sqrt{k}/(\beta^* \omega \tilde{y}))^2] \approx \tanh(2.5^2) \approx 1$ holds in the log-layer for the $k-\omega$ SST model. In Eq. (5.6), the coefficient equal to 2 acts as safeguard to ensure that $F_2 \to 1$ in the log-layer of all flows.

- arg_2: the equations of k and ω in the viscous sublayer are obtained as a limit $\tilde{y} \to 0$ of the log-layer equations. This expansion yields $\omega = \omega_{\text{sub}} \approx 85\nu/\tilde{y}^2$ for the $k-\omega$ SST model. The coefficient equal to 500 in Eq. (5.6) avoids that $F_2 = 0$ in the buffer layer.

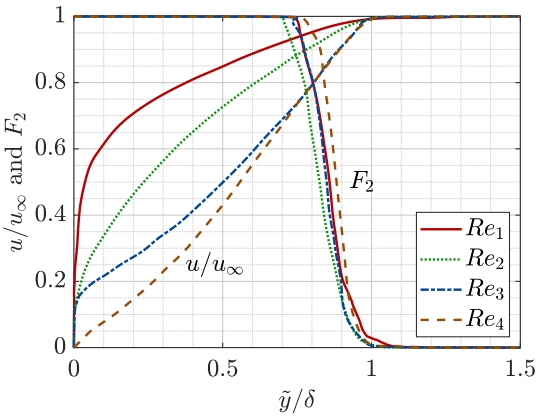

FIGURE 5.2: Blending function F_2 and velocity profiles at different Reynolds numbers, in flows exposed to an adverse pressure gradient. Adapted from (Menter, 1992).

The F_2 function does not depend on the mesh size if an asymptotic solution is reached in the RANS equations, thus not requiring a fine mesh due to their diffusive nature. This means that GIS is eliminated by definition. The function for different velocity profiles is shown in Fig. 5.2. It covers the viscous sublayer and the log-layer with separate terms, and switches from 1 to 0 between $0.7-0.8\delta$ and δ, which means that the transition from RANS to LES is done in a region with a characteristic length of $0.2\delta-0.3\delta$. This is not optimal for GWMLES because the gray area covers approximately the entire outer layer.

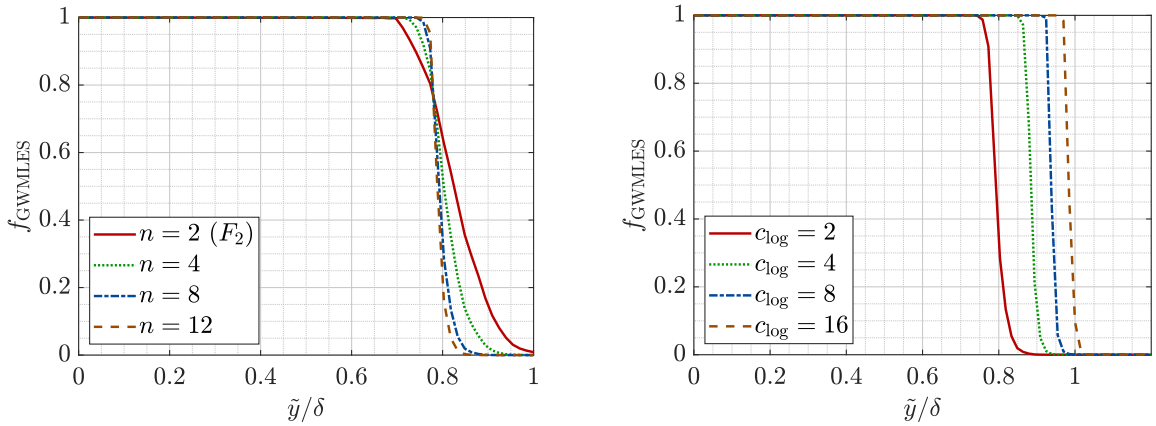

(A) $c_{\log} = 2$, $c_{\text{sub}} = 500$ and varying n.

(B) $c_{\text{sub}} = 500$, $n = 8$, and varying $c_{\log}$.

FIGURE 5.3: GWMLES blending function for different combinations of model constants.

The F_2 function is taken as reference for the development of the blending function f_{GWMLES} proposed in this chapter:

$$f_{\text{GWMLES}} = \tanh\left\{\left[\max\left(c_{\log}\frac{\sqrt{k}}{\beta^*\omega\tilde{y}}, c_{\text{sub}}\frac{\nu}{\tilde{y}^2\omega}\right)\right]^n\right\}, \tag{5.7}$$

where the constants n, $c_{\log}$, and c_{sub} are constants that are derived as follows:

- $\boldsymbol{n}$: it controls the length of the gray area. The F_2 function of Fig. 5.2 with the largest gray area of length 0.3δ is taken as reference, which corresponds to Re_2. The reduction of the gray area implies that $n > 2$. The case $n = 8$ gives a gray area of 0.1δ, while a further increase to $n = 12$ does not provide relevant differences. The value of n chosen for the GWMLES$_{\log}$ is $\boldsymbol{n_{\log} = 8}$. A mesh size $\Delta = 0.1\delta$ is considered representative of a GWMLES$_{\log}$ simulation in the outer layer; therefore, the transition takes place in one cell of the computational mesh. In the GWMLES$_{\text{sub}}$ mode the choice is less universal, since the ratio $\delta_{\text{sub}}/\delta$—with δ_{sub} referred to the thickness of the viscous sublayer—depends on the Reynolds number. In GWMLES$_{\text{sub}}$,

considering that the mesh size $\Delta = 0.01\delta$, then a similar reasoning to that of the GWMLES$_{\log}$ model leads to a constant $\boldsymbol{n_{sub} = 16}$.

- $\boldsymbol{c_{log}}$: it controls the value of $\tilde{y}/\delta$ in which the transition from RANS to LES occurs. In wall-bounded flows, the viscous sublayer and the log-layer constitute the universal part of the boundary layer, and the mesh requirements in the outer layer are of the same order as in the freestream region. Thus, it is assumed that for a mesh intending to solve 80% of the turbulence spectrum, the outer layer is solved in LES mode: thus, taking Fig. 5.3a as reference, $\boldsymbol{c_{log} = 2}$ is chosen for the GWMLES$_{\log}$ mode. The model also allows to cover the entire boundary layer in RANS for coarse meshes by setting $c_{\log} \geq 16$ (see Fig. 5.3b).

- $\boldsymbol{c_{sub}}$: in both GWMLES$_{\text{sub}}$ and GWMLES$_{\log}$ models, the goal is to solve the viscous sublayer and the buffer layer in RANS mode. This is the same idea behind the development of the $k-\omega$ SST model; therefore, the second argument of f_{GWMLES} (Eq. (5.7)) is proposed to be the same as the one of the F_2 function (Eq. (5.6)), which means that $\boldsymbol{c_{sub} = 500}$. The GWMLES$_{\text{sub}}$ mode is activated by setting $c_{\log} = 0$, and in this case $f_{\text{GWMLES}} = 1$ only up to the inner part of the log-layer. The ratio between the thickness of the viscous sublayer $\tilde{y}_{\text{sub}}$ and δ depends strongly on the Reynolds number; therefore, in the GWMLES$_{\text{sub}}$ mode, the transition point $\tilde{y}_{\text{sub}}/\delta$ from RANS to LES is not universal.

The parameters of GWMLES derived from the previous analyses are given in Table 5.1.

Formulation	$\boldsymbol{c_{sub}}$	$\boldsymbol{c_{log}}$	$\boldsymbol{n}$
GWMLES$_{\text{sub}}$	500	0	16
GWMLES$_{\log}$	500	2	8

TABLE 5.1: Parameters of the two formulations of the GWMLES model.

§1.2. Numerical implementation

Ansys Fluent 2023R1 is used, which incorporates Eq. (5.5) by default. The f_{GWMLES} blending function defined in Eq. (5.7) is implemented with a external code written in C (User-Defined Function, UDF) which is used in the in-built compiler of Ansys Fluent.

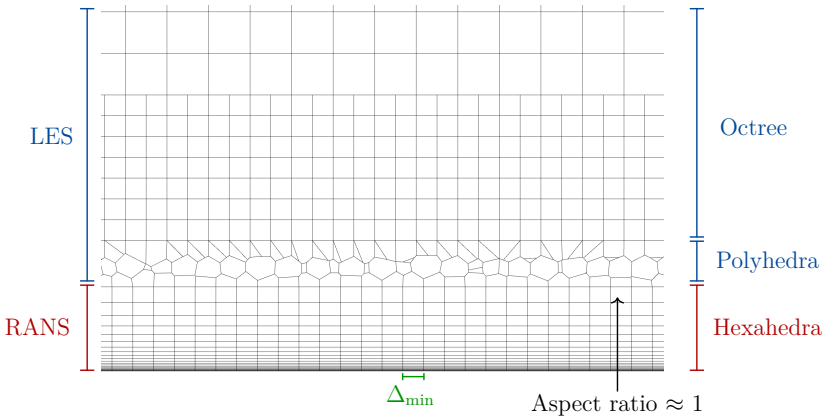

FIGURE 5.4: Poly-hexcore mesh used in the simulations performed in this work. The schematic is applicable to both GWMLES$_{\text{sub}}$ (where the RANS part covers up to the inner part of the log-layer) and GWMLES$_{\log}$ (where the RANS part covers up to the outermost part of the log-layer).

§1.2.1. Mesh

The poly-hexcore method of Ansys Fluent is used for meshing, which creates a mesh with octrees in the bulk region, and keeps a layered hexahedral mesh in the boundary layers. These elements

are connected with general polyhedral elements (see Fig. 5.4), which have been used successfully in LES simulations of jets (Bres et al., 2018) and external aerodynamics (Lozano-Durán et al., 2022). The computational mesh is generated with different cell sizes Δ ranging from $\Delta_{\min}$ to $\Delta_{\max}$, and the finest cell size is placed near the most relevant walls of the computational domain (see Fig. 5.4).

The use of cells with an aspect ratio greater than 1 has been shown to deteriorate the accuracy of scale-resolving simulations (Nishizawa et al., 2015; Kolmogorov et al., 2021b; Abe, 2021). Thus, the mesh is generated so that $f_{\text{GWMLES}} = 1$ (RANS) in the hexahedral cells with an aspect ratio greater than 1, and LES is considered in the rest of the domain. For flows at high Reynolds numbers, the instantaneous profile of f_{GWMLES} is expected to be time-dependent due to velocity fluctuations. To take this into account and avoid that LES is solved in cells of high aspect ratios, the transition ratio of the boundary layer cells is adapted so that the aspect ratio of the outermost hexahedral cells is close to 1 (see Fig. 5.4). It should be noted that the mean (time-averaged) contour of the function f_{GWMLES} is obtained after a precursor RANS simulation; that is, no unsteady simulations are needed to adapt the mesh to achieve the right numerical setup. The selection between $\text{GWMLES}_{\text{sub}}$ and $\text{GWMLES}_{\log}$ is done so that $f_{\text{GWMLES}} = 0$ (LES) in a computational cell if and only if the cell aspect ratio is close to 1; in particular, based on the references cited, values lower than 2 are considered acceptable. As a consequence of the above, the set of constants of Table 5.1 is not optimal for all cases; for a given mesh, $\text{GWMLES}_{\log}$ may lead to solving in RANS large regions suitable for LES, while $\text{GWMLES}_{\text{sub}}$ may lead to solving in LES a region that should be solved in RANS (with the corresponding risk of GIS). In those cases, the modification of the constant c_{sub} is proposed. The effect of this modification will be evaluated in one of the test cases studied in §2.

§1.2.2. Resolution of the equations

Equations (5.1) to (5.3) are solved with the finite volume method that is implemented in Ansys Fluent 2023R1, with the baseline methods listed in Chapter 2, §1.3.3. A central difference interpolation scheme is used in all terms of the equations except for the convective terms of the k and ω equations of the $k-\omega$ SST model. Ansys Fluent does not allow the definition of non-diffusive schemes for these equations, although this is considered to be not relevant, since the equations for RANS turbulence variables are inherently diffusive. In the SBES and GWMLES models, the equations of the RANS turbulence variables (k and ω) are solved every five time steps. Simulations are finished at $t = t_1$ when the flow statistics reach a statistically-steady state (see Algorithm 1).

Algorithm 1 Generalized wall-modeled LES algorithm

```
t = t_0                                          ▷ Precursor RANS simulation is converged
while t < t_1 do                                 ▷ LES solution not statistically steady
    if mod(t/dt, 5) = 0 then                     ▷ RANS solved every 5 time steps
        μ_t^RANS ← k − ω SST model               ▷ different RANS model can be used
    end if
    μ_t^LES ← WALE model                         ▷ different LES model can be used
    f_GWMLES ← Eq. (5.7)                         ▷ implemented as UDF in Fluent
    μ_t ← Eq. (5.5)                              ▷ included in Ansys Fluent
    Solve Navier-Stokes equations ← Eqs. (5.1) to (5.3)
    t = t + dt
end while
```

The simulations are performed in an eight-node cluster, with each node consisting of a 16-core AMD EPYC 7302 processors, which gives a total number of 128 cores. For each test case, the computational cost is obtained taking the following flow parameters as references:

- **Dimensionless time step, $\hat{dt}$**: ratio between the simulation time step dt and the characteristic time $t_c = L_c/v_\infty$, $\hat{dt} = dt/t_c$, where L_c is the flow characteristic length.

- **Dimensionless domain length, $\hat{L}_\Omega$**: ratio between the length of the simulation domain L_Ω and the characteristic length scale, $\hat{L}_\Omega = L_\Omega / L_c$.
- **Number of iterations per time step, N_{iter}**: for a given dimensionless time step, it is defined as the number of iterations performed by the numerical scheme before reaching the convergence conditions shown in previous paragraphs. As previously noted, the number of equations solved is not the same in all time steps for the case of SBES and GWMLES models; therefore, the value given is assumed to be the average value.
- **Iteration time t_{iter}**: computational time required to perform one iteration.
- **Number of flow times during transition N^{tr}_{flow}**: number of times that the mean flow passes through the computational domain before the extraction of flow statistics starts.
- **Number of flow times during data extraction, N^{dat}_{flow}**: number of times that the mean flow passes through the computational domain while the flow statistics are extracted.
- **Simulation time t_{sim}**: time required to perform the entire simulation, including the extraction of flow statistics. It is calculated as $t_{sim} = (\hat{L}_\Omega / \hat{dt})(N^{tr}_{\text{flow}} + N^{dat}_{\text{flow}}) N_{iter} t_{iter}$.

§1.2.3. Quality estimators

Three parameters related to the accuracy of the simulations will be considered.

- **Resolution quality, $\mathcal{Q}_r$**: an estimate of the resolved turbulence spectrum (Pope, 2000):

$$\mathcal{Q}_r = \frac{\overline{k}}{\overline{k} + k_r}, \tag{5.8}$$

  where $\overline{k} = (u'^2 + v'^2 + w'^2)/2$ is the resolved turbulent kinetic energy, and k_r is the residual kinetic energy obtained from the kinetic energy transport model (Menon et al., 1996):

$$k_r = \frac{\mu_t^2}{C_k^2 \rho^2 \Delta^2}, \tag{5.9}$$

  for a value of the constant $C_k = 0.05$ derived from simulations and experimental data (Menon et al., 1996). It is worth noting that, with additional equilibrium assumptions, the value of C_k can be also obtained from the Smagorinsky model (Sullivan et al., 1994). For a typical range of the Smagorinsky constant $C_s \in [0.1, 0.2]$, the corresponding range of C_k is $\in [0.05, 0.12]$, which means that the value chosen from (Menon et al., 1996) gives a conservative prediction of the resolution quality.

- **Number of computational cells per integral length scale, N**: since there is no universal method for estimating the resolution quality, another method will be considered that consists of computing the integral length scale, which is obtained as follows (Pope, 2000):

$$L_{ii} = \frac{1}{R_{ii}(0, \boldsymbol{x}, t)} \int_0^\infty R_{ii}(\boldsymbol{e_i} \boldsymbol{r}, \boldsymbol{x}, t) \, \mathrm{d}\boldsymbol{r}, \tag{5.10}$$

  where $R_{ii}(\boldsymbol{r}, \boldsymbol{x}, t) = \langle v_i(\boldsymbol{x}, t) v_i(\boldsymbol{x} + \boldsymbol{r}, t) \rangle$ are the components of the two-point correlation tensor, with $\boldsymbol{e_i}$ referring to the unit vector in the x_i coordinate direction, and $\langle v_i \rangle$ to the time-averaged value of v_i. In this work, the spanwise integral length scale L will be calculated; therefore, $i = 3$, and $L = L_{33}$. The number of computational cells per integral length scale N is used as an indicator for the quality of a LES simulation (Davidson, 2011); in particular, in a subdomain $\mathcal{S}_1 \subset \Omega$ of the computational domain Ω:

$$N_{\mathcal{S}_1} = \frac{L_{\mathcal{S}_1}}{\Delta}. \tag{5.11}$$

An approximation of N/Δ can be obtained for the particular case of a slight variation of the von Kármán spectrum (Von Kármán, 1948). The assumption that four cells are needed for a particular wavelength—which is considered as the characteristic length of the eddies—leads to a value of $N \approx 4$ for $\mathcal{Q}_r = 0.5$, and $N \approx 10$ for $\mathcal{Q}_r = 0.8$.

- **Q criterion, $\boldsymbol{Q}$**: second invariant of $\nabla \boldsymbol{v}$ (Jeong and Hussain, 1995):

$$Q = \frac{1}{2}(||\mathcal{W}||^2 - ||\mathcal{S}||^2), \tag{5.12}$$

where $\mathcal{W}$ is the vorticity tensor, and $||\mathcal{W}|| = [\mathrm{tr}(\mathcal{W}\mathcal{W}^t)]^{1/2}$ and $||\mathcal{S}|| = [\mathrm{tr}(\mathcal{S}\mathcal{S}^t)]^{1/2}$. The iso-surfaces of Q allow the visualization of the turbulence structures.

- **Taylor microscale, $\boldsymbol{\lambda}$**: length scale that represents the onset of the turbulence dissipation range, which is defined from the two-point correlation function (Pope, 2000):

$$\lambda_{ii} = \frac{\sqrt{2}}{\sqrt{-\left.\dfrac{\partial^2 R_{ii}}{\partial x_i^2}\right|_{(0,\boldsymbol{x},t)}}}. \tag{5.13}$$

The calculation of the Taylor microscale for meshes that differ more than one order of magnitude from the Kolmogorov scale can lead to large uncertainties, since the number of points close to $\boldsymbol{r} = 0$ is reduced. An approximation for the Taylor microscale will be used to estimate the cutoff limit of the turbulence spectrum of numerical solutions (Pope, 2000):

$$\lambda = \sqrt{10\nu\frac{\overline{k}}{\overline{\varepsilon}}}, \tag{5.14}$$

where $\overline{\epsilon} = \nu||S||^2$ is the resolved turbulent dissipation rate.

- **Normalized error, $\boldsymbol{\epsilon}$**: in each test case, the numerical result g_{num} will be compared with the reference experimental or DNS data g_{ref} in a subdomain $\mathcal{S}_2 \subset \Omega$ of the computational domain Ω. The normalized error ϵ is defined as follows:

$$||\epsilon(g)||_{\mathcal{S}_2} = ||\epsilon(g)||_{L^2(\mathcal{S}_2)} = \frac{||g_{num} - g_{ref}||_{L^2(\mathcal{S}_2)}}{||g_{ref}||_{L^2(\mathcal{S}_2)}}. \tag{5.15}$$

§2. Results and discussion

The accuracy of the GWMLES model will be compared hereafter with other models such as SBES, DES family, and URANS, as well as with results from LES/WMLES simulations available in the literature. DNS or experimental results will be taken as a reference in each case. First, the subsonic round jet is studied in §2.1 to verify the requirement that the blending function does not activate in turbulent regions far from walls, which is equivalent to showing that it gives a LES solution in a free shear flow; second, the periodic channel in §2.2 serves as a reference for the validation of the classical WMLES mode, which is given by $\mathrm{GWMLES}_{\mathrm{sub}}$; third, the flow around the Ahmed body is studied in §2.3, which is a complex turbulent wall-bounded flow used to test the $\mathrm{GWMLES}_{\log}$ model; finally, the capabilities of using a transition RANS model in the $\mathrm{GWMLES}_{\log}$ approach are evaluated by studying the flow around a circular cylinder around the critical regime in §2.4.

§2.1. Subsonic round jet

The subsonic round jet has been extensively studied in the literature to obtain the acoustic properties of jets (Viswanathan, 2004), which are key in the design of future aircraft engines Bridges and Wernet (2021). Taking experimental data as reference (Bridges and Wernet, 2011), simulation results will be compared with LES results obtained in the present thesis, as well as with WMLES results available in the literature (Stich et al., 2022).

Domain and boundary conditions

The axisymmetric domain with respect to the x axis is shown in Fig. 5.5. The Mach number $M = 0.5$; therefore, the pressure at the outlet of the convergent nozzle is equal to the ambient pressure. The model assumes that the turbulence at the nozzle outlet is negligible compared to that produced by the Kelvin-Helmholtz instability. Thus, the nozzle is not part of the computational domain, and no turbulence fluctuations are defined at the inlet. The dimensions of the computational domain have been deduced after performing a domain independence study with a coarse mesh.

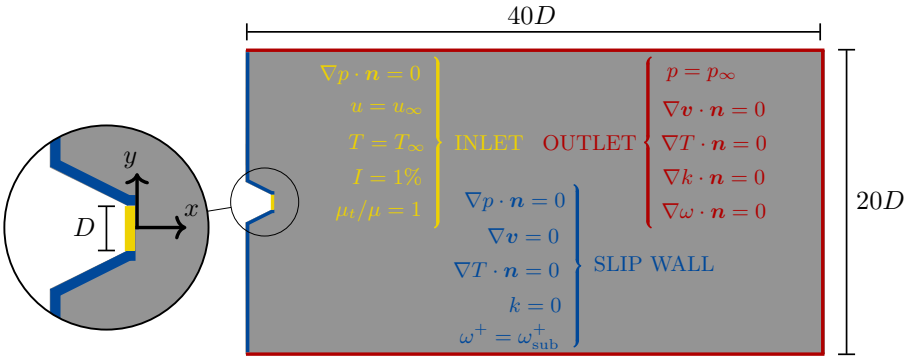

FIGURE 5.5: Computational domain Ω_{jet} and boundary conditions of the subsonic round jet.

The ambient pressure and temperature are $p_\infty = 101325$ Pa and $T_\infty = 298.15$ K, while the Reynolds number $Re_D = 2.8 \times 10^5$ referred to $D = 25.4$ mm and the ambient density, which is obtained with the ideal gas law. At the inlet, the turbulence boundary conditions are referred to the RANS turbulence variables, so that the turbulent kinetic energy and the turbulent specific dissipation rate can be calculated. The turbulence intensity $I = \sqrt{2k/3}/u_\infty$ is obtained from (Bridges and Wernet, 2011), although it has been verified that the value of the inlet (RANS) turbulent quantities do not have an impact on the results. The boundary condition for the turbulent specific dissipation rate is the asymptotic solution in the viscous sublayer. Non-reflecting boundary conditions (Thompson, 1987) are applied at the inlet and the outlet.

§2.1.1. Results

Mesh independence study

Three different meshes are considered, with $\mathcal{Q}_r$ (Eq. (5.8)) ranging from 0.5 to 0.8 in the region inside the edge of the shear layer. Table 5.2 shows that the estimation $N = 10$ (Eq. (5.11)) for $\mathcal{Q}_r = 0.8$ estimated in §1.2.3 is met, so that both methods show that the resolution of the fine mesh is acceptable for a LES simulation. The normalized error decreases as the mesh size decreases. The differences between the fine and the medium mesh are lower than those between the medium and the coarse mesh; therefore, a convergent behavior is achieved.

$\boldsymbol{\Delta_{min}}$	$\boldsymbol{\Delta_{max}}$	**Number of cells**	$\boldsymbol{\mathcal{Q}_r}$	$\boldsymbol{N_{\mathcal{S}_{jet1}}}$	$\boldsymbol{\|\|\epsilon(\langle u \rangle)\|\|_{\mathcal{S}_{jet2}}}$	$\boldsymbol{\|\|\epsilon(u')\|\|_{\mathcal{S}_{jet2}}}$
$D/20$	D	0.4 M	0.5	2.3	0.062	0.253
$D/40$	$D/2$	2.6 M	0.6	5.1	0.048	0.177
$D/80$	$D/4$	17.3 M	0.8	9.5	0.039	0.142

TABLE 5.2: Results of the mesh independence study of the subsonic round jet performed with the $\text{GWMLES}_{\text{log}}$ model. The number of cells per integral length is obtained in $\mathcal{S}_{\text{jet1}} = \{\boldsymbol{x} \in \Omega_{\text{jet}} \mid x/D = 10,\ y = 0,\ z/D \leq 1\}$, while the comparison with experimental data is made on the axis of revolution: $\mathcal{S}_{\text{jet2}} = \{\boldsymbol{x} \in \Omega_{\text{jet}} \mid x/D \leq 20,\ y = 0,\ z = 0\}$. Experimental data obtained from (Bridges and Wernet, 2011).

In the fine mesh, the normalized error in the fluctuations is lower than 15%, which is related to the $\mathcal{Q}_r$ value that is reasonably uniform along the jet (see Fig. 5.6b). Performing a Richardson extrapolation does not lead to $\epsilon \to 0$ for $\Delta \to 0$, which is explained by two reasons: first, neglecting the turbulence content from the nozzle flow is expected to lead to errors that are important when $\mathcal{Q}_r \to 1$; second, as shown in the comparison with experimental data, the experimental curve is the mean of several measurements; thus, for $\mathcal{Q}_r \to 1$ the uncertainty of the measurements dominates against the normalized error related to the simulations.

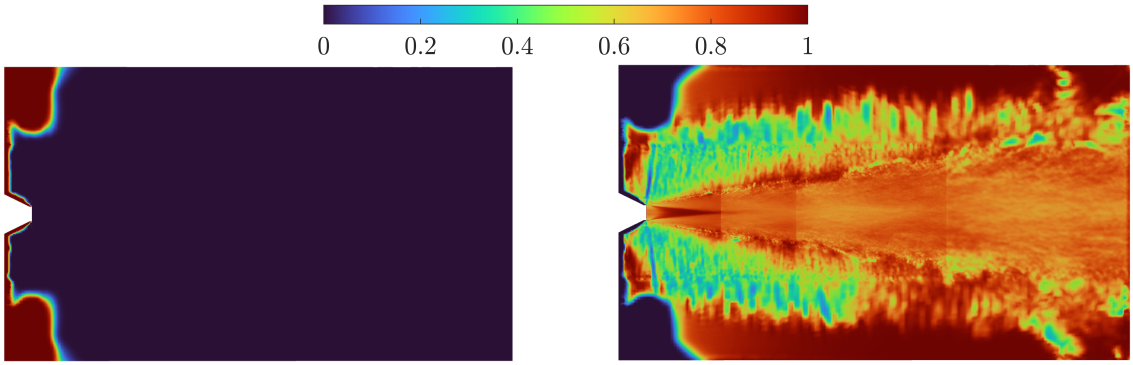

(A) $f_{\text{GWMLES}_{\text{log}}}$. (B) $\mathcal{Q}_r$.

FIGURE 5.6: Turbulence variables of the $\text{GWMLES}_{\text{log}}$ model on the plane $z = 0$ of the subsonic round jet.

Comparison between simulations and experimental data

Comparisons with experimental data will be shown for the fine mesh in all test cases. Figure 5.7 shows the results of the mean and fluctuating axial velocities given by different models. The mean differences between $\text{GWMLES}_{\text{log}}$ and SBES are lower than 2%, and closer to experimental data than DDES in Fig. 5.7d. Even if $f_{\text{GWMLES}_{\text{log}}}$ is activated far from the jet region (see Fig. 5.6a), LES results (WALE) are shown to verify that the regions with $f_{\text{GWMLES}_{\text{log}}} > 0$ do not affect the results. The data available in the literature are for a WMLES case that includes the nozzle region, for a fine mesh consisting of $\sim 10^2$ M elements. As expected, its accuracy is higher than the one of the simulations performed in this work. URANS gives a reasonable prediction of the mean flow, although this model significantly underpredicts the fluctuations. The normalized errors (Table 5.2) of the URANS solution obtained with the fine mesh are larger than those given by $\text{GWMLES}_{\text{log}}$ with the coarse mesh in the velocity fluctuations; therefore, for free shear flows, the use of the $\text{GWMLES}_{\text{log}}$ model is recommended over URANS even for coarse meshes.

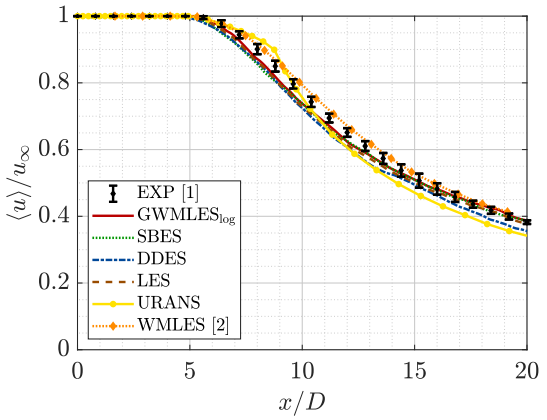

(A) Mean x-velocity on the x axis.

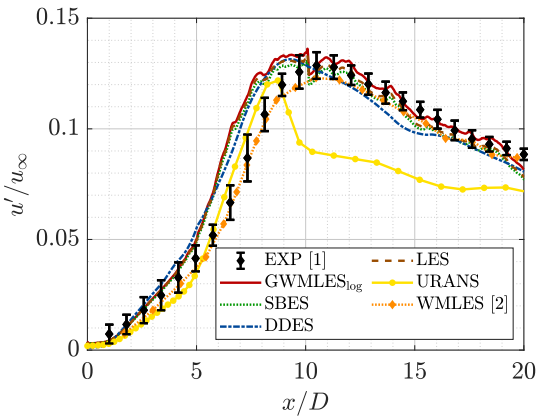

(B) Fluctuating x-velocity on the x axis.

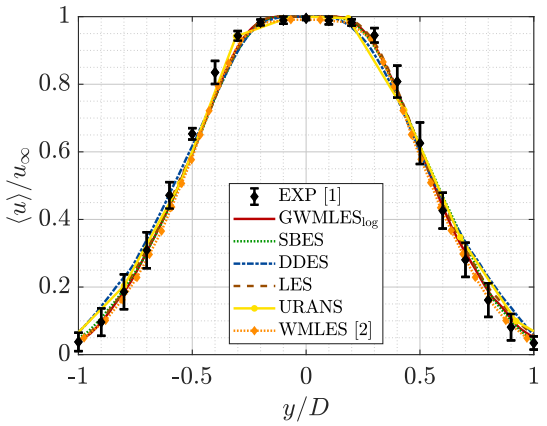

(C) Mean x-velocity at $(x/D, z/D) = (4, 0)$.

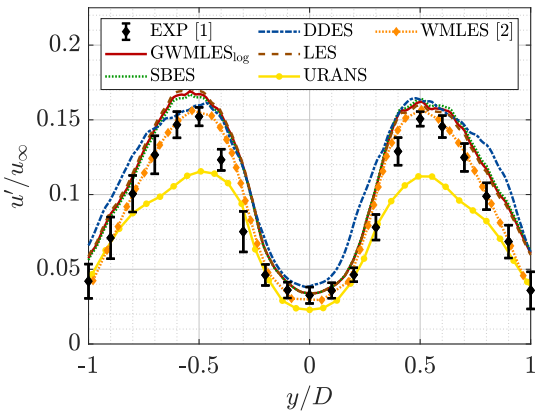

(D) Fluctuating x-velocity at $(x/D, z/D) = (4, 0)$.

FIGURE 5.7: Velocity statistics of the subsonic round jet. [1] (Bridges and Wernet, 2011). [2] (Stich et al., 2022).

Using a different residual stress model in GWMLES$_{\log}$ (WALE) and DDES (Smagorinsky) does not lead to important variations in the results. However, as previously mentioned, the model constant used in the DDES model is too dissipative in free-shear flows. This is translated into the resolution of coarser turbulence structures, in particular near the nozzle (see Fig. 5.8).

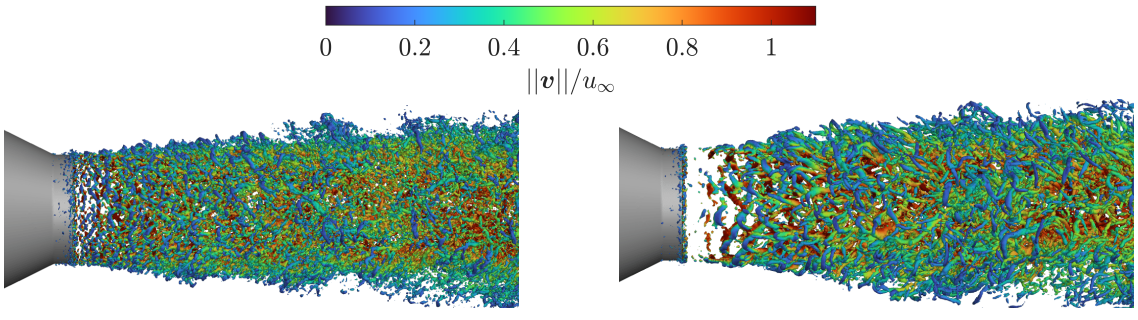

(A) GWMLES$_{\log}$.

(B) DDES.

FIGURE 5.8: Iso-surfaces of Q=5×10^9 s^{-2} of the subsonic round jet.

The increased dissipation produced by DDES can be verified by looking at the turbulence spectrum at $\boldsymbol{x}/D = (10, 0, 0)$ (see Fig. 5.9a), which is outside the potential core of the jet. Both turbulence models give almost the same spectrum for high wavenumbers. However, the cutoff limit is higher in GWMLES$_{\log}$, which is an important feature for acoustics calculations. This can be further verified quantitatively by calculating the Taylor microscale (see Eq. (5.13)). The higher values of λ close to $y = 0$ in the case of $x/D = 2$ are because this zone is inside the potential core of the jet, where the development of the turbulence structures is limited. Analyzing the Q-criterion,

the turbulence spectrum, and the Taylor microscales leads to the same conclusion: $\text{GWMLES}_{\text{log}}$ solves finer turbulence structures than DDES.

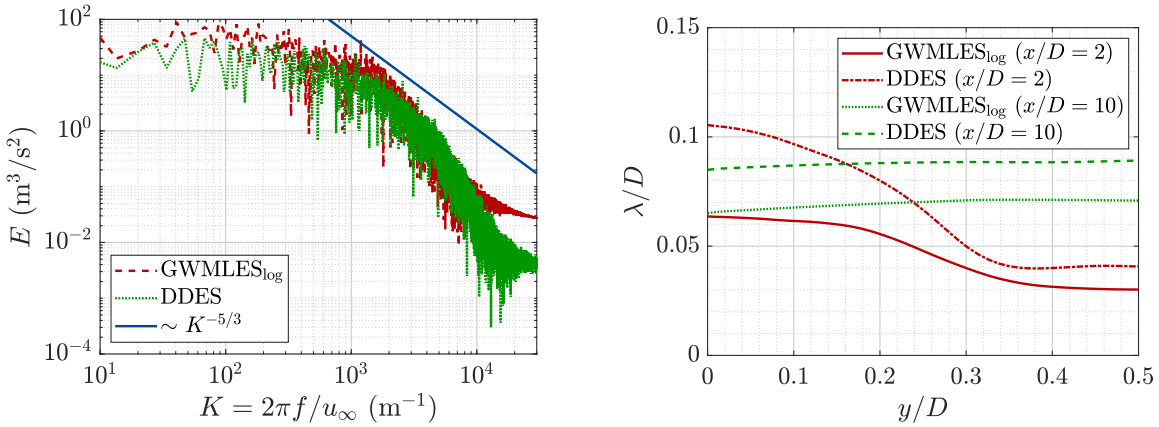

(A) Spectrum of the resolved turbulent kinetic energy at $\boldsymbol{x}/D = (10, 0, 0)$.

(B) Dimensionless Taylor microscale at $z/D = 0$.

FIGURE 5.9: Turbulence statistics of the subsonic round jet.

It has been verified that, for the same mesh, $\text{GWMLES}_{\text{log}}$ requires 30% lower computational cost than DDES, and 10% more computing time than LES (see Table 5.3). The reason is that, in $\text{GWMLES}_{\text{log}}$, RANS equations are solved every 5 time steps, while in DDES they are solved at all time steps, and no additional equation is solved for LES. Considering that the number of cores (128) is moderate, the simulation time is reasonable for an industrial framework.

Model	$\hat{\boldsymbol{dt}}$	$\hat{\boldsymbol{L}}_{\boldsymbol{\Omega}}$	$\boldsymbol{N_{iter}}$	$\boldsymbol{t_{iter}}$ **(s)**	$\boldsymbol{N^{tr}_{\text{flow}}}$	$\boldsymbol{N^{dat}_{\text{flow}}}$	$\boldsymbol{t_{sim}}$ **(days)**
$\text{GWMLES}_{\text{log}}$	3.4×10^{-3}	40	6	0.6	4	4	3.9
DDES	3.4×10^{-3}	40	6	0.9	4	4	5.9
LES	3.4×10^{-3}	40	6	0.55	4	4	3.6

TABLE 5.3: Simulation parameters of the subsonic round jet for a characteristic length scale $L_c = D$.

§2.2. Periodic channel

The periodic channel flow is a benchmark case that provides extensive information on near-wall turbulence without the requirement of simulating a large and/or complex domain. DNS results will be taken as reference (Hoyas and Jiménez, 2006; Bernardini et al., 2014), and the accuracy of the $\text{GWMLES}_{\text{sub}}$ model will also be compared with WMLES results obtained by other authors (Lodato et al., 2014). The influence of the constant c_{sub} appearing in Eq. (5.7) on the performance of the model will be studied by considering two simulation approaches: the baseline with $c_{\text{sub}} = 500$ ($\text{GWMLES}^{500}_{\text{sub}}$) and a variation with $c_{\text{sub}} = 1000$ ($\text{GWMLES}^{1000}_{\text{sub}}$).

Domain and boundary conditions

In what follows, the air is assumed to be incompressible. The domain is a rectangular periodic channel (see Fig. 5.10), with the dimensions validated in (Lozano-Durán and Jiménez, 2014) against larger domains. In the longitudinal (x) direction, the mass flow rate $\dot{m}$ is defined from the freestream velocity v_∞, while in the spanwise direction (z) the mass flow rate vanishes. In the no-slip walls, the wall-parallel velocity is given by the solution in the viscous sublayer (Wilcox, 2006). The Reynolds numbers $Re = 2\rho u_\infty h/\mu = 8.7 \times 10^4$ and $Re_\tau = \rho u_\tau h/\mu = 2000$, where u_τ is the friction velocity.

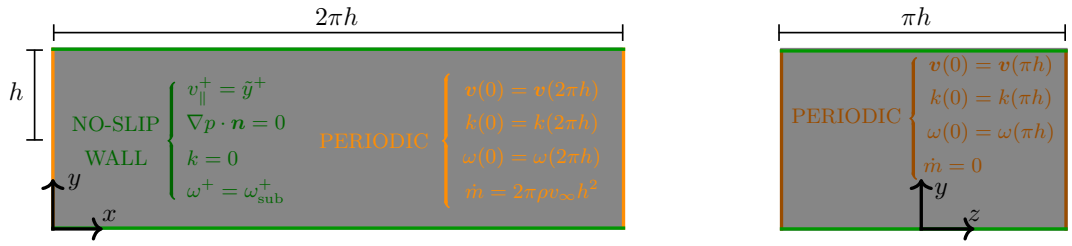

FIGURE 5.10: Computational domain Ω_{ch} and boundary conditions of the periodic channel.

§2.2.1. Results

Mesh independence study

The results of the mesh-independence study are shown in Table 5.4. The values given by GWMLES$^{500}_{\text{sub}}$ converge to a value whose normalized error is lower than 10% in all variables. This error is lower than 20% in the coarse mesh, even if the resolution quality is only 60%. This is attributed to the fact that this test is one of the classical benchmarks that are used to validate numerical methods and turbulence models, with no particular complex flow features such as recirculation or separation zones. The value of the (time-averaged) $\tilde{y}_w^+ = 1$ is uniform due to the periodicity of the flow, and 10 cells normal to the wall are defined where $f_{\text{GWMLES}} = 1$. Following the trends shown before, solving 80% of the turbulence spectrum corresponds to defining approximately ten computational cells per integral length scale. It can be concluded that both mesh quality indicators are related, with a relationship $N(\mathcal{Q}_r = 0.8) \approx 10$. Thus, in the following mesh independence studies, only the resolution quality will be specified.

$\boldsymbol{\Delta^+_{\text{min}}}$	$\boldsymbol{\Delta^+_{\text{max}}}$	**Number of cells**	$\boldsymbol{\mathcal{Q}_r}$	$\boldsymbol{N_{\mathcal{S}_{ch1}}}$	$\boldsymbol{\|\|\epsilon(\langle u\rangle)\|\|_{\mathcal{S}_{ch2}}}$	$\boldsymbol{\|\|\epsilon(u')\|\|_{\mathcal{S}_{ch2}}}$	$\boldsymbol{\|\|\epsilon(\langle C_f\rangle)\|\|_{\mathcal{S}_{ch2}}}$
100	400	1.8 M	0.6	2.4	0.039	0.193	0.08
50	200	7.2 M	0.7	7.9	0.015	0.123	0.02
25	100	28.9 M	0.85	14.7	0.009	0.087	0.01

TABLE 5.4: Results of the mesh independence study of the periodic channel performed with the GWMLES$^{500}_{\text{sub}}$ model. The number of cells per integral length is obtained in $\mathcal{S}_{ch1} = \{\boldsymbol{x} \in \Omega_{ch} \mid x/h = \pi,\ y/h = 1/8,\ 0 \leq z/h \leq 1/4\}$, while the comparison with DNS is done in the boundary layer $\mathcal{S}_{ch2} = \{\boldsymbol{x} \in \Omega_{ch} \mid x/h = \pi,\ 0 \leq y/h \leq 1,\ z = 0\}$. DNS data obtained from (Hoyas and Jiménez, 2006) (u) and (Bernardini et al., 2014) (C_f).

As expected from the reasoning followed in §1.1.1, most of the domain is solved in LES mode (see Fig. 5.11a). Details of the transition from RANS to LES will be given below. The resolution quality is uniform in all meshes considered (see Fig. 5.11b).

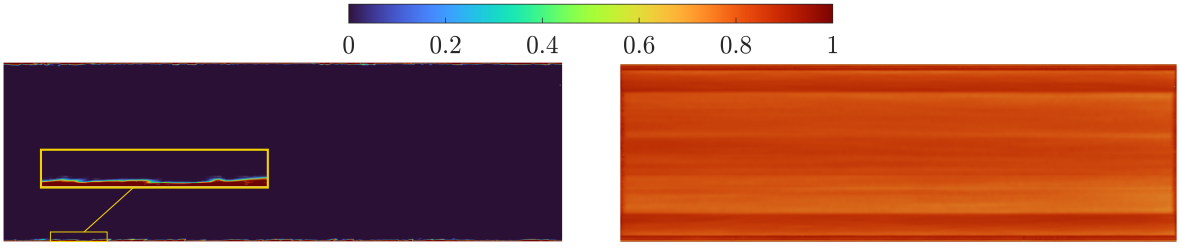

(A) $f_{\text{GWMLES}_{\text{sub}}}$. (B) $\mathcal{Q}_r$.

FIGURE 5.11: Turbulence variables of the GWMLES$^{500}_{\text{sub}}$ model on the plane $z = 0$ of the periodic channel.

Comparison between simulations and experimental data

The comparison between velocity statistics in the boundary layer given by different simulations is illustrated in Fig. 5.12. The agreement with DNS data is excellent in the $\text{GWMLES}_{\text{sub}}$ and SBES models, while IDDES predicts a 50% lower thickness of the log-layer (see Fig. 5.12a). The WMLES results (Lodato et al., 2014) are obtained with a wall function approach and provide correct agreement in the log-layer, although errors up to 20% in the mean dimensionless x-velocity are noticed in the viscous sublayer and the buffer layer.

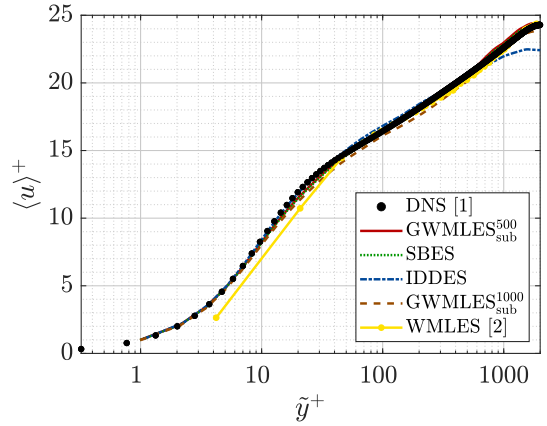

(A) Mean dimensionless x-velocity.

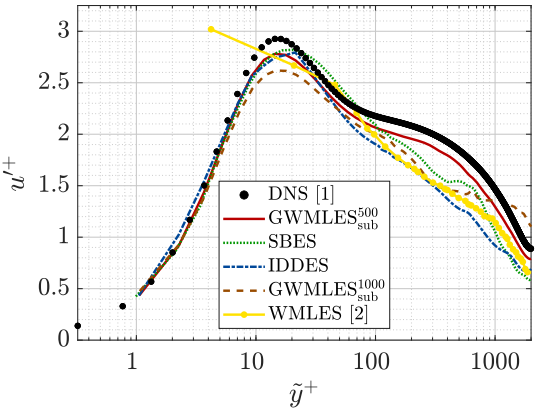

(B) Fluctuating dimensionless x-velocity.

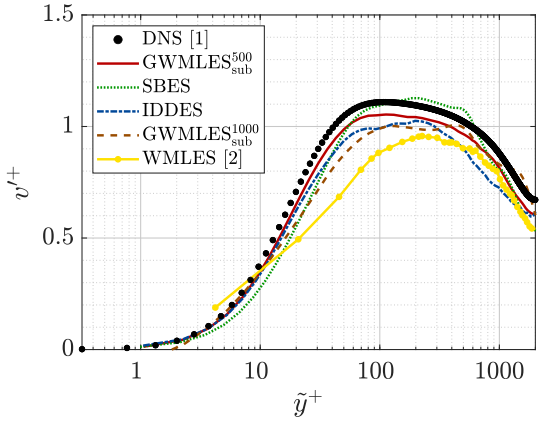

(C) Fluctuating dimensionless y-velocity.

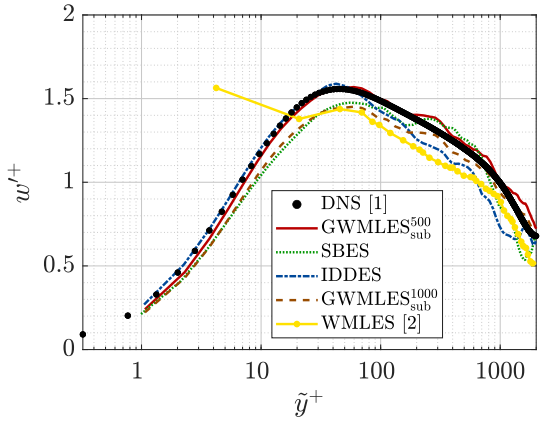

(D) Fluctuating dimensionless z-velocity.

FIGURE 5.12: Velocity statistics in the boundary layer of the periodic channel. [1] (Hoyas and Jiménez, 2006). [2] (Lodato et al., 2014).

The deviations between different methods are more pronounced in the fluctuating variables. $\text{GWMLES}_{\text{sub}}$, SBES, and IDDES results differ up to 20% in Fig. 5.12b, although they are significantly more accurate than WMLES (see Figs. 5.12b to 5.12d). The mesh is coarser in the simulation of (Lodato et al., 2014) ($\Delta^+_{\text{min}} = 79$), but this is partially balanced by the fifth-order spectral difference method used. Independently of the mesh and the numerical method, the issues of the wall function approach have been remarked in the Introduction (§2.3). This is relevant, since the fluctuations in the buffer layer are of the same order of magnitude as those in the log-layer. Even if RANS models are calibrated for steady cases, it is demonstrated that the model developed in this work is able to capture the velocity fluctuations that are produced in the viscous sublayer and the log layer, while the wall function approach leads to errors that are as high as 50% in Fig. 5.12b. Solving the viscous sublayer and the buffer layer in RANS leads to a higher computational cost than with the wall function-based approach. Nevertheless, in these zones the cell aspect ratio is much higher than 1; therefore, both mesh sizes are of the same orde of magnitude.

URANS simulations have also been performed, leading to a deviation lower than 1% in the mean velocity with respect to DNS, but with negligible fluctuations. Starting from a precursor RANS

simulation, the high dissipation of URANS does not lead to fluctuations. The same conclusion is extracted after sufficient time if the URANS simulation is initialized from a $\text{GWMLES}_{\text{sub}}$ solution. This could be anticipated before performing the simulation, since all parts of the domain are inside the boundary layer, with no relevant flow instabilities. Given that in $\text{GWMLES}_{\text{sub}}$ the normalized error of the mean values obtained with the coarse mesh is lower than 4% (see Table 5.4), and that URANS predicts negligible fluctuating variables, overall $\text{GWMLES}_{\text{sub}}$ provides more accurate results than URANS in the periodic channel flow for all meshes considered.

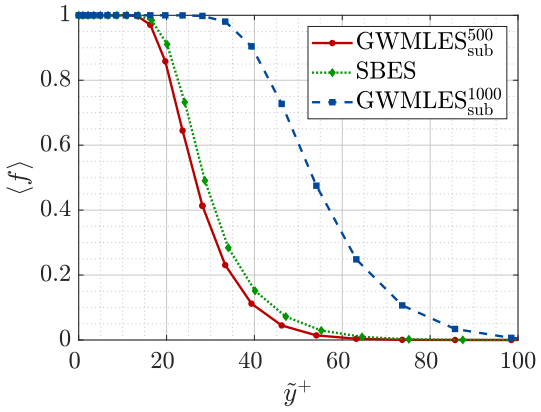

FIGURE 5.13: Mean blending functions in the boundary layer of the periodic channel.

Parameter → Simulation ↓	$\langle C_f \rangle$ $(\times 10^{-3})$
DNS [3]	4.375
$\text{GWMLES}^{500}_{\text{sub}}$	4.385
$\text{GWMLES}^{1000}_{\text{sub}}$	4.392
SBES	4.381
IDDES	4.396
URANS	4.391

TABLE 5.5: Mean skin friction coefficient of the periodic channel. [3] (Bernardini et al., 2014).

The increase of c_{sub} defined in Eq. (5.7) leads to a RANS-LES transition at higher $\tilde{y}^+$ (see Fig. 5.13). The transition region of the mean value of the blending function contains more than two cells. However, as illustrated in Fig. 5.11a, the fluctuations in the blending function are important because of the high resolution quality, which means that the time-averaged value is smoothed with respect to the instantaneous value; that is, in Fig. 5.13, the transition region is of the order of $\tilde{y}^+$, while Fig. 5.11a shows that the instantaneous transition region is much thinner. The mean SBES blending function is essentially the $\text{GWMLES}^{500}_{\text{sub}}$ function translated approximately by $\tilde{y}^+ = 5$. In $\text{GWMLES}^{1000}_{\text{sub}}$, the $\tilde{y}^+$ in which RANS-LES transition takes place is twice the one of $\text{GWMLES}^{500}_{\text{sub}}$, with a lower slope of the function. No LLM is noticed in Fig. 5.12a, and the velocity fluctuations are underpredicted, which is attributed to the higher dissipation as a consequence of the extended RANS region. The satisfactory accuracy of the $\text{GWMLES}_{\text{sub}}$, SBES, and IDDES models is also shown in the mean skin friction coefficient, which is predicted with an error lower than 5% in all models (see Table 5.5). This study confirms the potential of the proposed model to improve the classical wall-function and mixing-length approaches for WMLES.

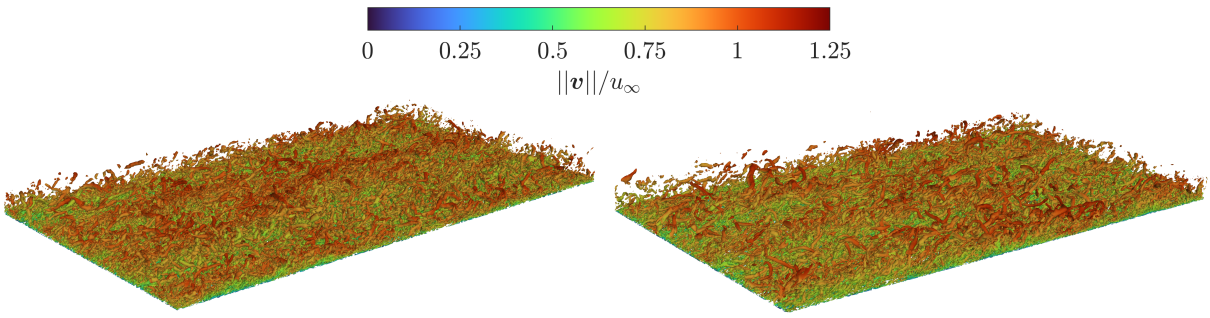

(A) $\text{GWMLES}^{500}_{\text{sub}}$. (B) IDDES.

FIGURE 5.14: Iso-surfaces of Q=10^6 s^{-2} in the boundary layer of the periodic channel.

The IDDES model has been particularly calibrated for periodic channel flows (Shur et al., 2008). Moreover, there are no transition regions, which means that the transition from modeled to resolved turbulence is not as relevant as in other more complex wall-bounded flows. This can be verified in

the size of the resolved turbulence structures, in which no qualitative differences can be observed between $\text{GWMLES}_{\text{sub}}$ and IDDES (see Fig. 5.14). Quantitative results derived from the Taylor length scale distribution lead to the same conclusion (see Fig. 5.15).

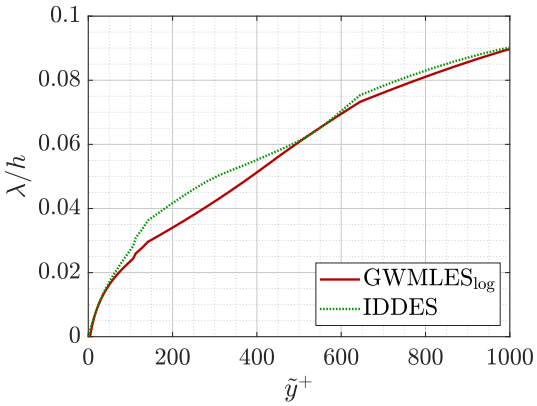

FIGURE 5.15: Dimensionless Taylor microscale in the boundary layer of the periodic channel.

The computational cost of $\text{GWMLES}_{\text{sub}}$ (same as for SBES) is around 35% lower than the one of DDES (Table 5.6). The reduction is greater than in the subsonic round jet case, since in compressible flow RANS equations represent $2/7 = 28\%$ of the total number of equations, while in incompressible flow without heat transfer the ratio is $2/6 = 33\%$. The computational cost is of the same order as the one of the simulations of the subsonic round jet (see Table 5.3). The higher cell count and lower time step used in this case, as well as the large number of time steps required for the turbulence structures to be fully developed, are compensated by the reduced numbers of iterations per time step and dimensionless length of the computational domain.

Model	$\hat{dt}$	$\hat{L}_\Omega$	N_{iter}	t_{iter} (s)	N^{tr}_{flow}	N^{dat}_{flow}	t_{sim} (days)
$\text{GWMLES}_{\text{sub}}$	1.4×10^{-3}	2π	3	0.9	15	5	2.8
IDDES	1.4×10^{-3}	2π	3	1.35	15	5	4.2

TABLE 5.6: Simulation parameters of the periodic channel for a characteristic length scale $L_c = h$.

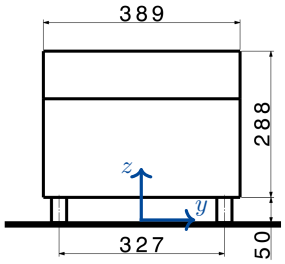

(A) Back view.

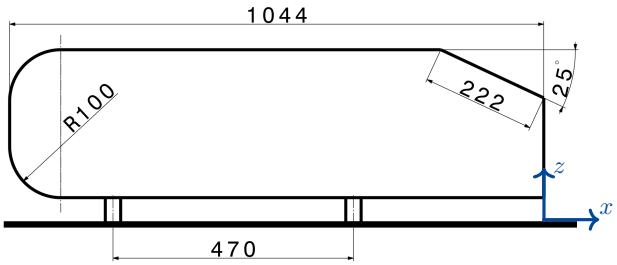

(B) Lateral view.

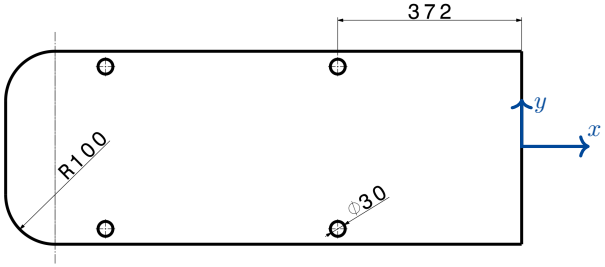

(C) Bottom view.

FIGURE 5.16: Geometry of the Ahmed body (Ahmed et al., 1984). Dimensions in mm.

§2.3. Ahmed body

The Ahmed body is a model of a generic road car (Ahmed et al., 1984) (see Fig. 5.16). The flow shares some features with the real cars such as a large three-dimensional recirculation zone at the back of the geometry, and the interaction of two counter-rotating vortices that are generated on the slant edges. For slant angles lower than the critical angle of 30°, the flow separates in the beginning of the slant, and it reattaches downstream, leading to complex flow features. Taking experimental data as references (Ahmed et al., 1984; Lienhart et al., 2002; Conan et al., 2011; Rossitto et al., 2016), simulation results will be compared with the results obtained from LES and WMLES simulations available in the literature (Lehmkuhl et al., 2019; Kolmogorov et al., 2021a).

Domain and boundary conditions

The computational domain is a 3/4 open wind tunnel with the dimensions of the cross section obtained from (Lienhart et al., 2002) (see Fig. 5.17). The lengths upstream and downstream of the Ahmed body have been obtained after performing a domain independence study with a coarse mesh. The Reynolds number $Re_L = 2.7 \times 10^6$, and the turbulence intensity u'/u at the inlet, which is used to calculate the turbulent kinetic energy and the turbulent specific dissipation rate, is obtained from experimental data (Lienhart et al., 2002).

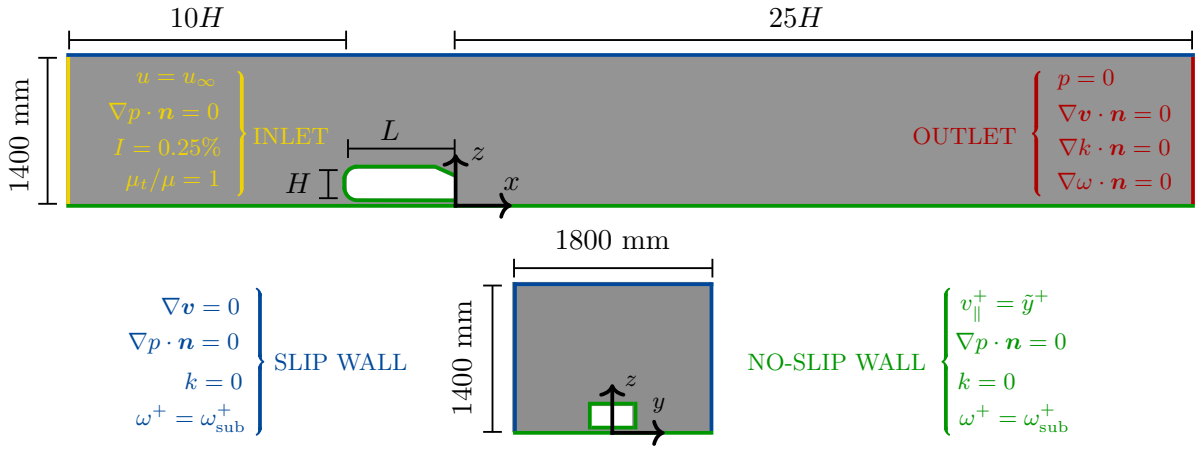

FIGURE 5.17: Computational domain Ω_{ahmed} and boundary conditions of the Ahmed body.

§2.3.1. Results

Mesh independence study

Three different meshes are considered, with $\mathcal{Q}_r$ on the slant region ranging from 0.5 to 0.8. Coarser meshes lead to numerical instabilities when the low-dissipation discretization methods mentioned in §1.2.2 are used. Table 5.7 shows that the error in the velocities of the boundary layer decreases as the mesh size decreases, and a convergent behavior is achieved.

Δ^+_{min}	Δ^+_{max}	Number of cells	$\mathcal{Q}_r$	$\|\|\epsilon(\langle u \rangle)\|\|_{\mathcal{S}_{\text{ahmed}}}$	$\|\|\epsilon(u')\|\|_{\mathcal{S}_{\text{ahmed}}}$	$\langle C_d \rangle$	$\langle C_{d,f} \rangle$
375	6400	2.4 M	0.5	0.194	0.488	0.346	0.057
275	4800	4.5 M	0.65	0.167	0.351	0.340	0.056
175	3200	11.5 M	0.8	0.149	0.264	0.335	0.056

TABLE 5.7: Results of the mesh independence study of the Ahmed body performed with the GWMLES$_{\text{log}}$ model in the boundary layer of the slant: $\mathcal{S}_{\text{ahmed}} = \{\boldsymbol{x} \in \Omega_{\text{ahmed}} \mid x = -0.043,\ y = 0,\ 0.25 \leq z \leq 0.4\}$. Experimental data obtained from (Lienhart et al., 2002).

The drag parameters—with $\langle C_{d,f} \rangle$ referring to the friction component of the drag coefficient—are not compared with experimental data; the reason is that there is no consensus based on different experiments. In the normal direction of the boundary layers 20 cells are defined, with $\tilde{y}_w^+ < 2$ in the turbulent boundary layers (see Fig. 5.18a). These conditions imply small differences in the quantities that strongly depend on the RANS model, such as the friction component of the drag coefficient. In contrast, there are separation and reattachment processes, and the drag coefficient and the fluctuating values are mainly determined by the accuracy of the LES region. This is the reason why these variables are more sensitive to mesh refinement. In the fine mesh $\Delta_{\min} < 0.1\delta$, even though, as noted in (Menter and Kuntz, 2004), the flow is not exposed to a strong adverse pressure gradient on the roof; therefore, GIS is not a problem for the present geometry.

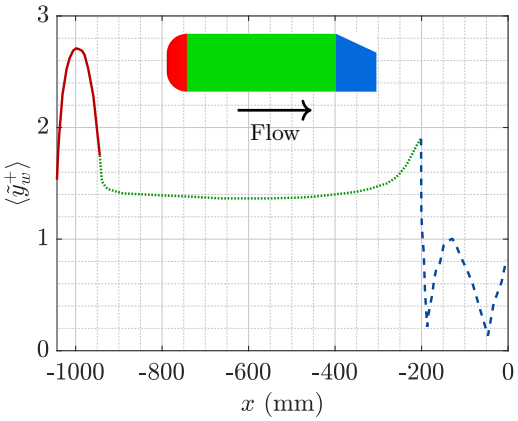

(A) Mean dimensionless wall distance of the first near-wall cell.

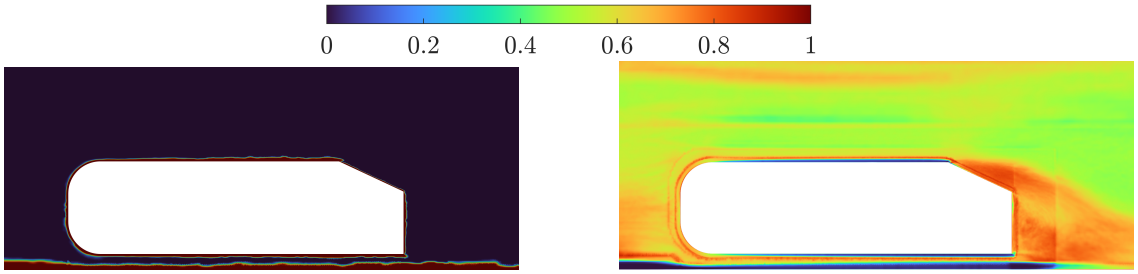

(B) $f_{\text{GWMLES}_{\log}}$.

(C) $\mathcal{Q}_r$.

FIGURE 5.18: Turbulence variables of the $\text{GWMLES}_{\log}$ model on the plane $y = 0$ of the Ahmed body.

It should be noted that the normalized error of the fluctuating velocity of the fine mesh is still 26%. Two universal reasons are related to the use of a RANS model in the boundary layers, as well as the limited resolution of the turbulence spectrum. Even if $\mathcal{Q}_r \approx 0.8$ on the slant, there are some regions in the wake where the value is $0.6 - 0.7$ (see Fig. 5.18c). In addition, in the experimental data available, there are only 10 data points in the boundary layer, which are only spaced by 4 mm. This means that the accuracy of the measuring technique could play an important role in the comparison, as well as the manufacturing tolerances of the body. The results will be compared with data available in the literature in the following paragraphs, so that a better picture can be obtained regarding the accuracy of the model developed in this chapter.

GWMLES$_{log}$ blending function

The mean profiles of the x-velocity and the $\text{GWMLES}_{\log}$ blending function in different positions of the roof of the Ahmed body are presented in Fig. 5.19. The equilibrium solutions in the viscous sublayer $\langle u_{\text{sub}}^+ \rangle = \tilde{y}^+$ and the log-layer $\langle u_{\log}^+ \rangle = C^+ + \log(\tilde{y}^+)/\kappa$ for values of the von Kármán constant $\kappa = 0.41$ and $C^+ = 5$ (Wilcox, 2006) are plotted as reference. Figure 5.19a shows that the boundary layer is not fully developed in the first three reference points. The transition point

from RANS to LES depends on the x-coordinate (see Fig. 5.19b), since the log-layer thickness is proportional to the distance to the leading edge when the flow is not fully developed. At $x = -250$ mm, the profile obtained from the numerical simulations matches the law of the wall. The mesh size in the roof region is $\Delta \approx 0.05\delta$ (half of the size used on the slant region), and the transition from RANS to LES takes place in around 2 cells. This is the expected result, given that the reference considered in §1.1.1 was 1 cell for $\Delta \approx 0.1\delta$. In the fully-developed case ($x = -250$ mm), the transition point is located near the end of the log-layer, as predicted.

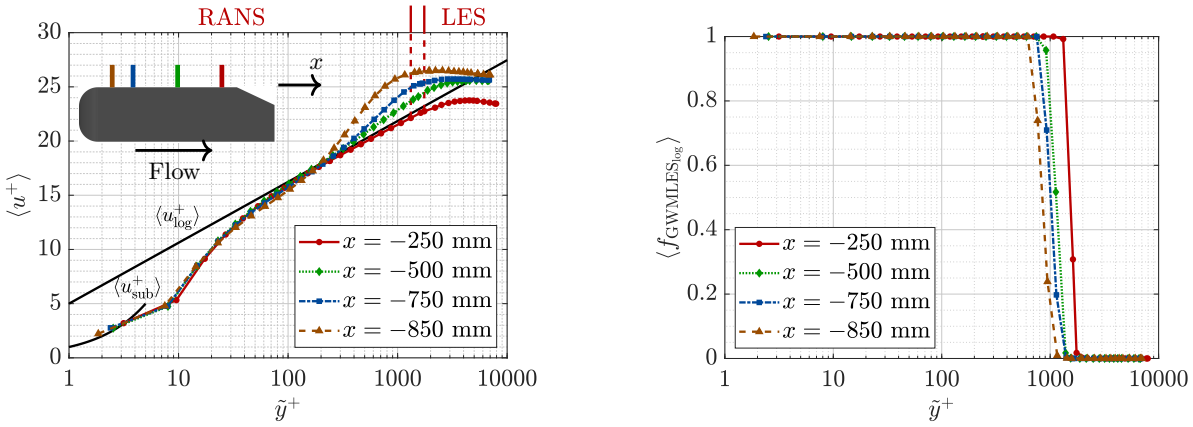

(A) Dimensionless x-velocity. (B) Blending function.

FIGURE 5.19: Mean boundary layer profiles on the plane $y = 0$ of the Ahmed body.

Comparison between simulations and experimental data

Fig. 5.20 compares the streamwise velocity statistics on the slant region of the symmetry plane (see Fig. 5.16) with experimental data, LES, and WMLES simulations. The results of LES and WMLES simulations are those obtained with the fine mesh used in the corresponding work. The differences between $\text{GWMLES}_{\log}$, SBES, and DDES are lower than 5% at almost all points, especially in the mean velocity. These models are more accurate than WMLES in the mean values, although the deviation from the experimental data is more pronounced than in the LES simulations. Even if the accuracy of all models compared is similar in the fluctuating velocity, at $x = -203$ mm there are some fluctuations predicted by the $\text{GWMLES}_{\log}$, SBES, and LES models that are not present in the DDES model and in the experimental data. URANS fails to determine the velocity profiles, with negligible temporal fluctuations; in fact, in URANS the normalized errors (Table 5.7) are greater than those obtained with $\text{GWMLES}_{\log}$ and the coarse mesh.

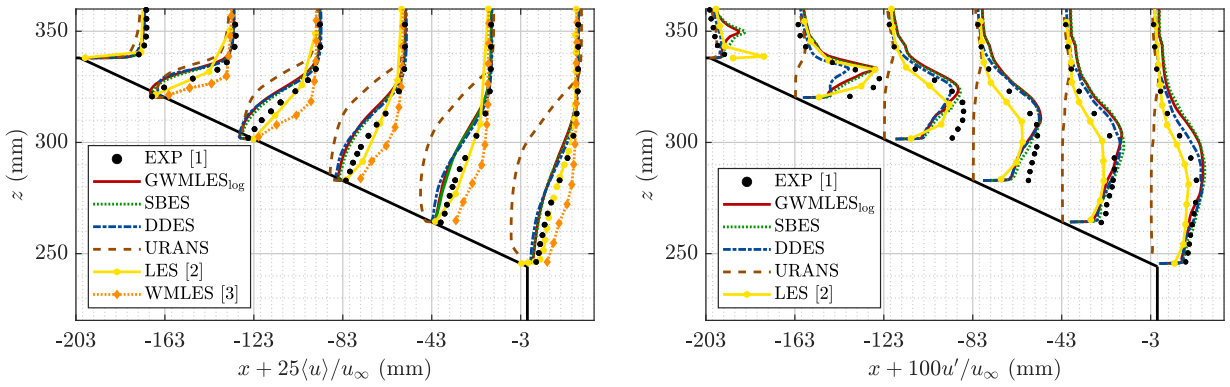

(A) Mean x-velocity. (B) Fluctuating x-velocity.

FIGURE 5.20: Velocity statistics on the plane $y = 0$ of the Ahmed body. [1] (Lienhart et al., 2002). [2] (Lehmkuhl et al., 2019). [3] (Kolmogorov et al., 2021a).

Figure 5.20a allows the detection of the separation and reattachment point from different models. In the attached flow, the streamwise velocity component is positive, while the opposite occurs when the flow is separated. Except from URANS, in which the flow is separated along the entire slant, the separation at the beginning of the slant and the subsequent reattachment before the end are predicted by all models. However, $\text{GWMLES}_{\text{log}}$, SBES, and DDES models overpredict the width of the separated zone, while LES and WMLES provide the opposite behavior. It should be noted that a positive streamwise velocity component is not a sufficient condition for the flow to be attached. It has been verified that in these cases the vertical (z) velocity component is negative, as required to deduce that the flow is attached.

Parameter	**EXP [4]**	**EXP [5]**	**EXP [6]**	**$\text{GWMLES}_{\text{log}}$**	**SBES**	**DDES**	**LES [3]**	**URANS**
$\langle C_d \rangle$	0.285	0.343	0.356	0.335	0.331	0.347	0.295	0.298
$\langle C_{d,f} \rangle$	—	0.051	—	0.055	0.057	0.052	0.037	0.052

TABLE 5.8: Drag parameters of the Ahmed body. [3] (Lehmkuhl et al., 2019). [4] (Ahmed et al., 1984). [5] (Conan et al., 2011). [6] (Rossitto et al., 2016).

The importance of an accurate prediction of the transition point will be analyzed in the drag parameters. Among the models that give a reasonable prediction of the velocity statistics, since the separated region is the largest in the DDES results, it is expected that DDES provides the highest drag coefficient value. In contrast, the lowest should be given by the LES model given the overprediction of the attached region by this model. This is indeed shown in Table 5.8. As previously anticipated, the value of the drag coefficient is not clear taking previous articles as references. The quality of the test sample has a strong influence on the drag coefficient (Rossitto et al., 2016); it has been shown that small roundings in the upper edge of the slant lead to a decrease of the drag coefficient, and, in particular, the drag coefficient does not depend on the radius of curvature in the cases studied. That is, there is a reference value in the body with a sharp edge, 0.356, which is similar to the one obtained in (Conan et al., 2011). The drag coefficient reduces to 0.297 with a rounded edge, which is closer to the one of (Ahmed et al., 1984).

Another key parameter is the friction component of the drag. The values given by $\text{GWMLES}_{\text{log}}$, SBES, and DDES models differ by less than 10%, and agree with the value given in (Ahmed et al., 1984). LES results provide a low value of the friction component, which may be a reason for the discrepancy in $\langle C_d \rangle$ with respect to (Conan et al., 2011) and (Rossitto et al., 2016). Since friction effects are dominant in the attached flow, the friction component given by URANS is in line with the one given by $\text{GWMLES}_{\text{log}}$, SBES, and DDES. Given the large deviations of the URANS results with respect to experimental data in the velocity statistics, it is expected that the friction coefficient predicted by URANS deviates significantly. This is not the case, since friction effects are not dominant on the slant, which is where the accuracy of URANS is reduced.

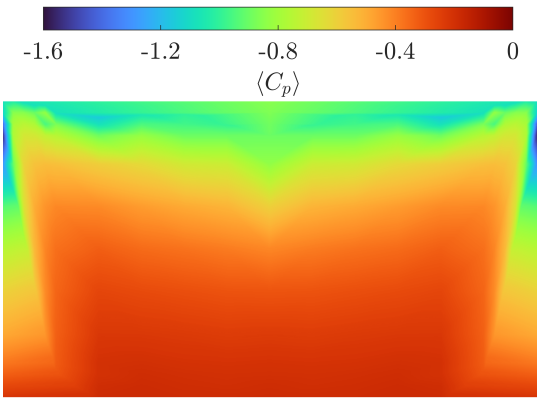

(A) Experiment (Lienhart et al., 2002).

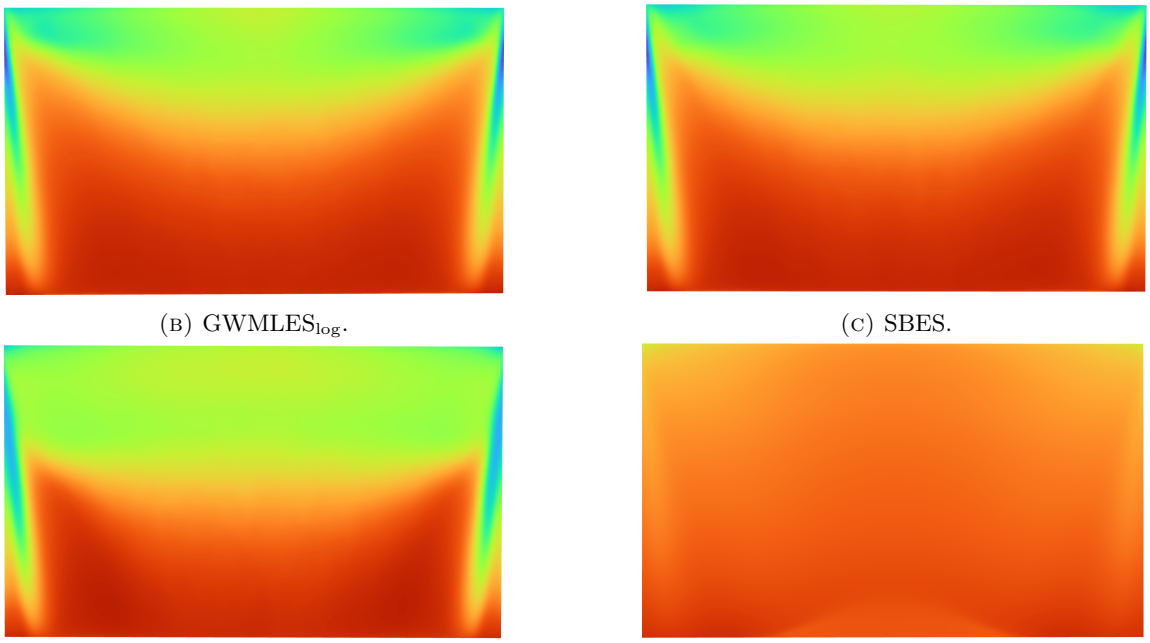

(B) $\text{GWMLES}_{\text{log}}$. (C) SBES.

(D) DDES. (E) URANS.

FIGURE 5.21: Pressure coefficient on the slant of the Ahmed body. Due to the limited number of sampling points of the LDA measurements, the contours cover the spanwise domain $0.1875 \leq y \leq 0.1875$, which is smaller than the width of the Ahmed body ($0.1945 \leq y \leq 0.1945$).

Even if the drag coefficient is not obtained in the experiments taken as reference in Fig. 5.20 (Lienhart et al., 2002), the pressure coefficient distributions on the slant and the rear surface of the Ahmed body are available. Figure 5.21 compares numerical and experimental results on the slant, and shows that simulation values provide an accurate overall picture of the distribution. However, errors up to $\approx 20\%$ are obtained in the numerical simulations (see Table 5.9). As expected from the comparison of velocity statistics, the prediction of URANS is of reduced accuracy, since this model does not predict clearly two of the main flow physics: the separation and subsequent reattachment, as well as the two counter-rotating vortices, which are extremely weak (see Fig. 5.21e). It has been verified that the normalized errors obtained with the coarse mesh in $\text{GWMLES}_{\text{log}}$ are lower than those of URANS in the fine mesh, which leads to the same conclusion as in the previous cases: GWMLES provides more accurate results than URANS even in coarse meshes.

Parameter	**EXP [1]**	**$\text{GWMLES}_{\text{log}}$**	**SBES**	**DDES**	**URANS**
$\langle C_p^{\text{slant}} \rangle$	-0.585	-0.499	-0.487	-0.534	-0.365
$\langle C_p^{\text{rear}} \rangle$	-0.161	-0.161	-0.158	-0.171	-0.171

TABLE 5.9: Pressure coefficients of the Ahmed body. [1] (Lienhart et al., 2002).

The contours of the pressure coefficient are less accurate at first sight on the rear of the body, which corresponds to the plane $x = 0$ (see Fig. 5.22). However, the area-averaged value is highly accurate in all cases, even in URANS (see Table 5.9); the latter is considered to be a coincidence, since the pointwise contour of URANS (Fig. 5.22e) deviates significantly from the experimental data (Fig. 5.22a). Assuming that there is no error in the remaining surfaces, from the results of Table 5.9 it is deduced that $\text{GWMLES}_{\text{log}}$ underpredicts the drag obtained in the experiments of (Lienhart et al., 2002). This enforces the assumption that the correct drag coefficient is around 0.34, so that the hybrid RANS/LES models would provide a better accuracy than the LES model for a much lower computational cost. In that situation, $\text{GWMLES}_{\text{log}}$ model is more accurate than the SBES, which can be due to solving the outer layer in LES mode instead of in RANS.

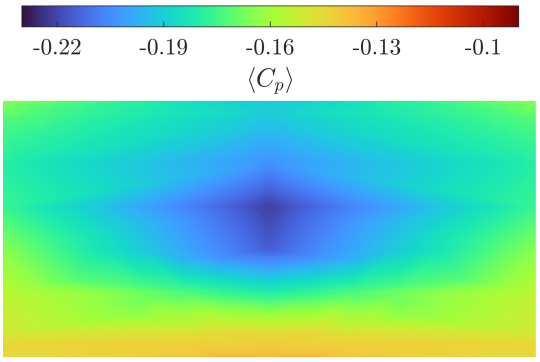

(A) Experiment (Lienhart et al., 2002).

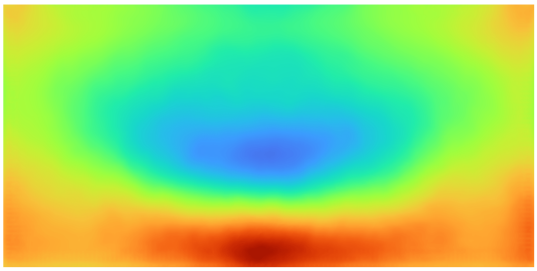

(B) $\text{GWMLES}_{\text{log}}$.

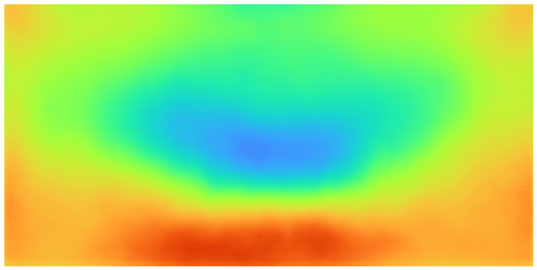

(C) SBES.

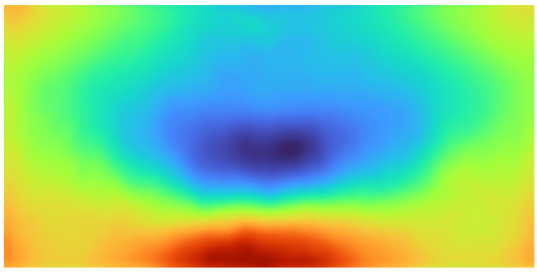

(D) DDES.

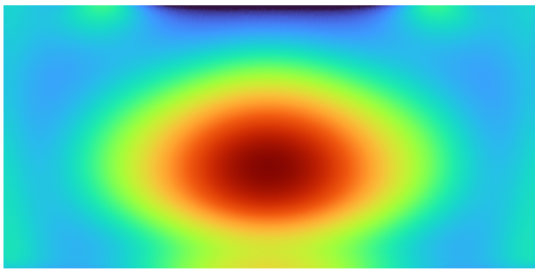

(E) URANS.

FIGURE 5.22: Mean pressure coefficient on the rear of the Ahmed body.

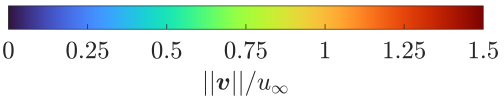

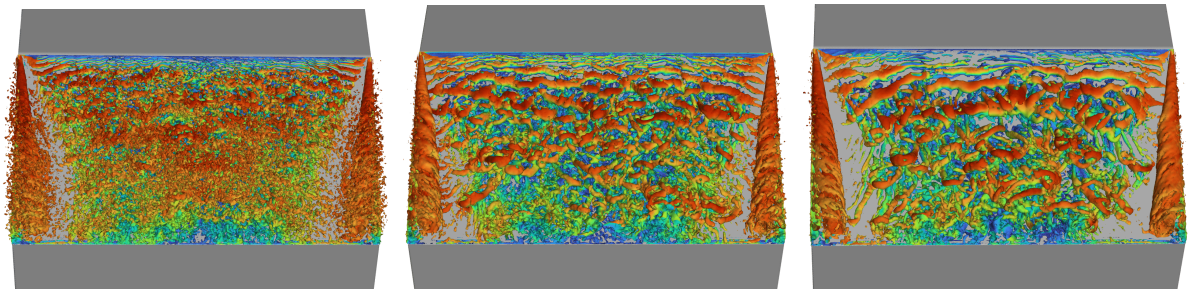

(A) $\text{GWMLES}_{\text{log}}^{\text{WALE}}$.

(B) $\text{GWMLES}_{\text{log}}^{\text{SMAG}}$.

(C) DDES.

FIGURE 5.23: Iso-surfaces of Q=2.5×10^6 s^{-2} on the slant of the Ahmed body.

In addition to the baseline $\text{GWMLES}_{\text{log}}$ with the $k-\omega$ SST RANS model and the WALE residual stress model ($\text{GWMLES}_{\text{log}}^{\text{WALE}}$), another simulation has been performed with the $k-\omega$ SST and Smagorinsky models ($\text{GWMLES}_{\text{log}}^{\text{SMAG}}$). This allows to study separately the effect of the subgrid-scale model and $f_{\text{GWMLES}_{\text{log}}}$ on the resolved turbulence structures. The Smagorinsky constant $C_s = 0.175$, which is equal to the equivalent Smagorinsky constant of the DDES model, as mentioned in the Introduction (§2.3). Even if the accuracy of $\text{GWMLES}_{\text{log}}$ and DDES in terms of mean and fluctuating variables has been shown to be similar, Fig. 5.23 shows that both the use

of a more consistent subgrid stress model (WALE) and the reduction of gray areas contribute to the increased resolution. In fact, the differences in the size of the turbulence structures between $\text{GWMLES}_{\text{log}}^{\text{WALE}}$ and DDES are more noticeable than in the previous test cases, with a reduced computational cost required by the $\text{GWMLES}_{\text{log}}$ with respect to DDES (see Table 5.10).

Model	$\hat{dt}$	$\hat{L}_\Omega$	N_{iter}	t_{iter} (s)	N_{flow}^{tr}	N_{flow}^{dat}	t_{sim} (days)
$\text{GWMLES}_{\text{sub}}$	1.3×10^{-3}	35	5	0.5	5	5	7.8
DDES	1.3×10^{-3}	35	5	0.75	5	5	11.7

TABLE 5.10: Simulation parameters of the Ahmed body for a characteristic length scale $L_c = H$.

§2.4. Circular cylinder

The flow around a circular cylinder at $Re \approx 10^5$ is representative of the laminar-turbulent transition process (Schlichting, 1979), with the type of transition depending on Re and the particular conditions of the experiments. In this test case, experimental data (Cantwell and Coles, 1983) and LES results (Breuer, 2000; de la Llave Plata et al., 2019) will be used for comparison. The work (Breuer, 2000) considers many cases with different spanwise lengths, mesh sizes and turbulence models. The case with the same spanwise length as in this work ($2D$), the fine mesh, and the dynamic Smagorinsky residual stress model is considered as reference. Two simulation approaches will be tested within the $\text{GWMLES}_{\text{log}}$ model: the standard $k-\omega$ SST model for turbulent boundary layers ($\text{GWMLES}_{\text{log}}^{\text{SST}}$), and the $\gamma - Re_{\theta t}$ model for boundary layers with laminar-turbulent transition ($\text{GWMLES}_{\text{log}}^{\gamma-Re_{\theta t}}$). The latter adds two additional transport equations for the intermittency γ and the transition momentum thickness Reynolds number $Re_{\theta t}$ (see Appendix A, §3.2.2). In both cases the residual stress model used is the baseline WALE model.

Domain and boundary conditions

The computational domain is a circular cylinder with periodic boundary conditions in the spanwise direction (see Fig. 5.24). The distance between the periodic boundaries has been deduced from a domain-independence study. The definition of the inlet boundary conditions for the RANS turbulence variables has been done with the aim of representing laminar freestream conditions, which correspond to the LES results used for comparison and the aim of the experiment taken as reference (Cantwell and Coles, 1983). The Reynolds number of the flow $Re_D = 1.4 \times 10^5$.

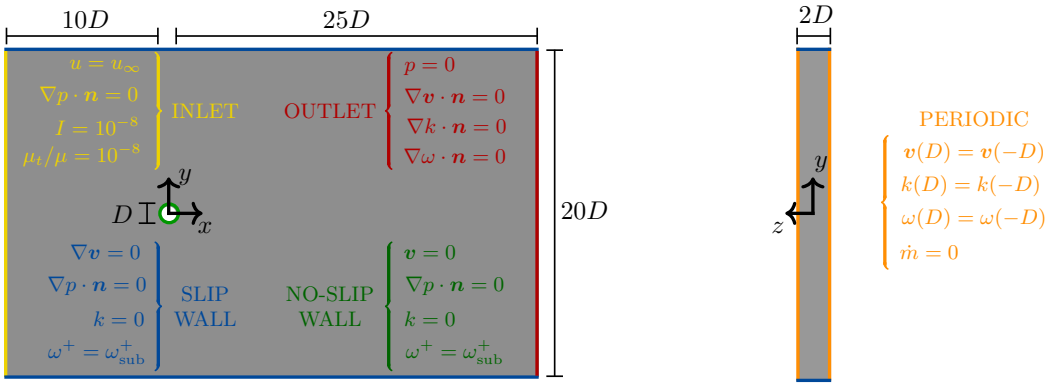

FIGURE 5.24: Computational domain Ω_{cyl} and boundary conditions of the circular cylinder.

§2.4.1. Results

Mesh independence study

Three different meshes are considered, with $\mathcal{Q}_r$ in the wake of the cylinder ranging from 0.6 to 0.8. Table 5.11 shows that the error in the velocity statistics and the mean drag coefficient converges to a constant value. In the following paragraphs, the reason why $\epsilon \not\to 0$ when $\mathcal{Q}_r \to 0$ will be explained. The increase of the mesh resolution does not have a strong impact on the results, which is attributed to the low y_w^+ value that is kept constant in all meshes (see Fig. 5.25), as well as the definition of 20 boundary layer cells in the normal direction. This study also allows to conclude that RANS zones play an important role in the flow.

$\boldsymbol{\Delta_{\min}}$	$\boldsymbol{\Delta_{\max}}$	**Number of cells**	$\mathcal{Q}_r$	$\|\|\epsilon(\langle u \rangle)\|\|_{\mathcal{S}_{\text{cyl}}}$	$\|\|\epsilon(u')\|\|_{\mathcal{S}_{\text{cyl}}}$	$\|\|\epsilon(\langle C_d \rangle)\|\|_{\mathcal{S}_{\text{cyl}}}$
$D/125$	$D/4$	2.4 M	0.6	0.114	0.402	0.502
$D/175$	$D/4$	4.8 M	0.7	0.134	0.373	0.61
$D/250$	$D/4$	12.1 M	0.8	0.129	0.365	0.674

TABLE 5.11: Results of the mesh independence study of the circular cylinder performed with the $\text{GWMLES}_{\text{log}}^{\gamma - Re_{\theta t}}$ model in the wake axis $\mathcal{S}_{cyl} = \{\boldsymbol{x} \in \Omega_{cyl} \mid 1 \leq x/D \leq 8,\ y/D = 0,\ z/D = 0\}$. Experimental data obtained from (Cantwell and Coles, 1983).

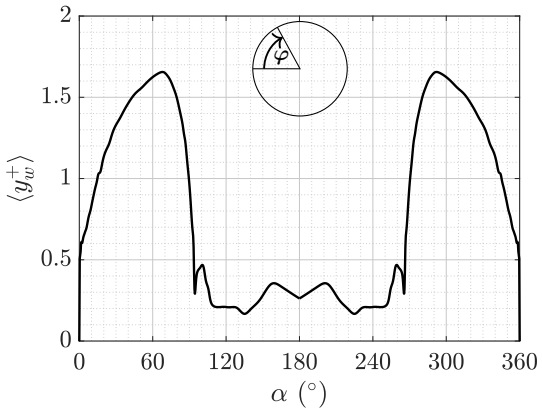

FIGURE 5.25: Mean dimensionless wall distance of the first near-wall cell of the circular cylinder.

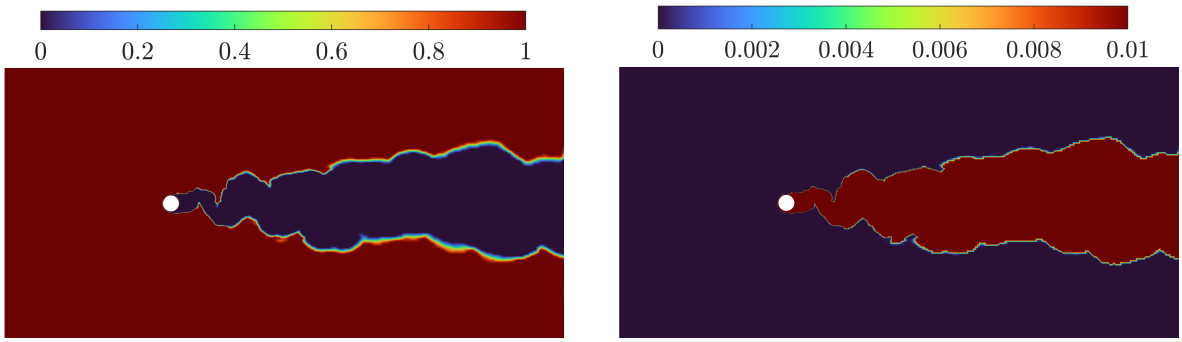

(A) $f_{\text{GWMLES}_{\text{log}}}$. (B) μ_t/μ.

FIGURE 5.26: Turbulence variables of the $\text{GWMLES}_{\text{log}}$ model on the plane $z = 0$ of the circular cylinder.

Figure 5.26a illustrates that $\text{GWMLES}_{\text{log}}^{\gamma - Re_{\theta t}}$ runs in LES mode only in the wake of the cylinder, which is not the expected behavior. However, the RANS zones outside the boundary layers are

fully resolved, since there $\mu_t/\mu \ll 1$ (see Fig. 5.26b). The turbulence variables k, ω, and μ_t almost vanish at the inlet. These values are not significantly increased outside the boundary layer or the wake, since the production terms in the k and ω equations are proportional to the strain rate that vanishes in these zones. This is because there is no wall or other turbulence generator than can produce velocity gradients. Thus, the second argument of the blending function defined in Eq. (5.7) activates without compromising the accuracy of the modeling approach.

Comparison between simulations and experimental data

Figure 5.27 shows the velocity statistics on the longitudinal axis and on one of the vertical axes close to the cylinder surface. The GWMLES$^{\text{SST}}_{\text{log}}$, SBES, and DDES models are more accurate than the LES cases considered in Figs. 5.27a and 5.27c, with mean differences with respect to experimental data lower than 20%. The opposite occurs in Figs. 5.27b and 5.27d; therefore, no clear conclusion about the accuracy of the models can be extracted. GWMLES$^{\gamma-Re_{\theta t}}_{\text{log}}$ results deviate significantly with respect to other data in the fluctuating variables, and provide the lowest turbulence levels, while the highest levels are obtained with the LES simulations.

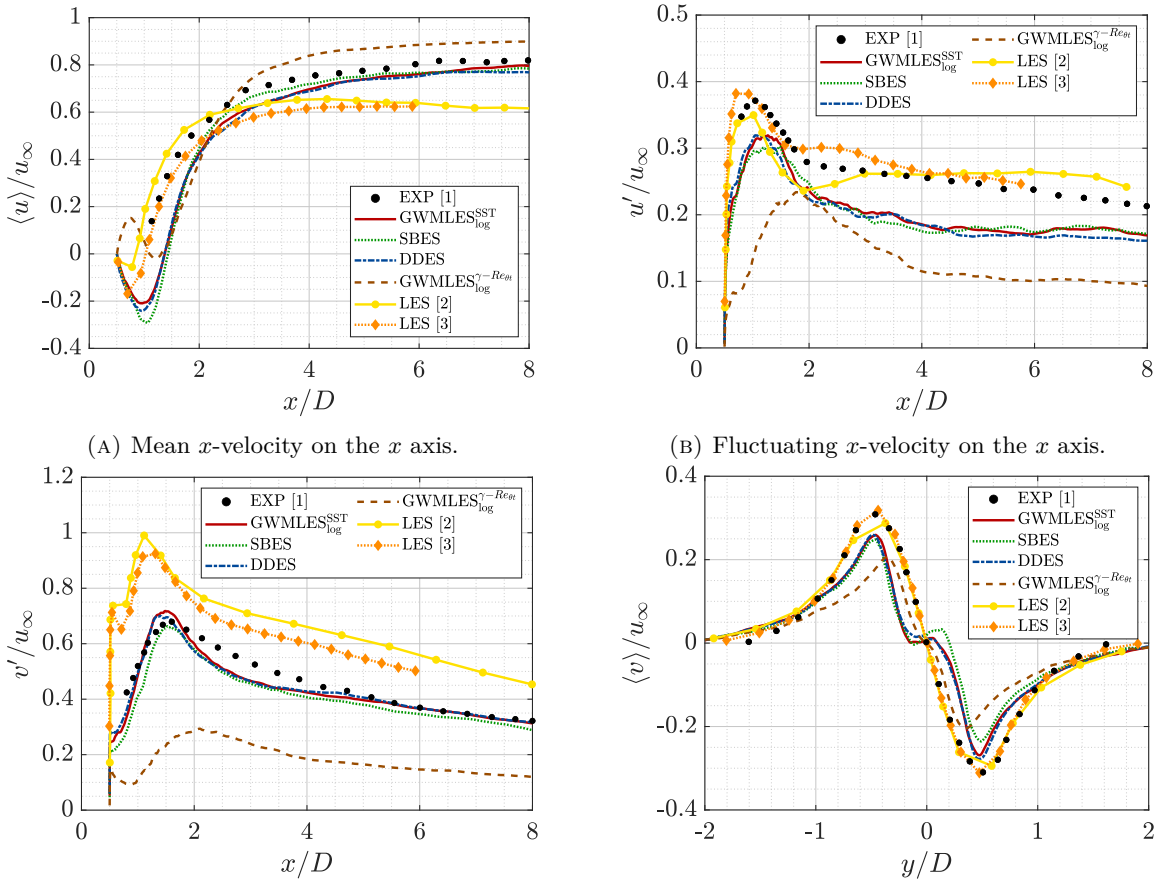

(A) Mean x-velocity on the x axis.

(B) Fluctuating x-velocity on the x axis.

(C) Fluctuating y-velocity on the x axis.

(D) Mean y-velocity at $(x, z) = (D, 0)$.

FIGURE 5.27: Velocity statistics of the circular cylinder on the plane $z = 0$. [1] (Cantwell and Coles, 1983). [2] (Breuer, 2000). [3] (de la Llave Plata et al., 2019).

Further comparison of flow parameters is presented in Table 5.12. Defining the separation angle φ_{sep} as the value at the inflection point of the pressure coefficient, in LES the flow separates at the lowest value of φ, leading to increased drag, while the opposite occurs in GWMLES$^{\gamma-Re_{\theta t}}_{\text{log}}$. GIS is not a problem for DDES in the meshes considered, since $\Delta_{\min} > 0.3\delta$ due to the thin boundary layer. The differences in the mean base pressure coefficient $\langle C_{p,b} \rangle = \langle C_p \rangle (\varphi = 180°)$ follow the same trends as in the drag coefficient, and the Strouhal number increases notably in the

laminar-turbulent transitional flow, in line with the data available in the literature (Schlichting, 1979).

Parameter	**EXP [1]**	**GWMLES$^{\mathbf{SST}}_{\mathbf{log}}$**	**SBES**	**DDES**	**GWMLES$^{\boldsymbol{\gamma-Re_{\theta t}}}_{\mathbf{log}}$**	**LES [2]**	**LES [3]**
$\langle C_d \rangle$	1.24	0.79	0.79	0.84	0.4	1.45	1.43
$\langle C_{p,b} \rangle$	-1.21	-0.85	-0.84	-0.83	-0.39	-1.76	-1.59
St	0.18	0.24	0.25	0.24	0.33	0.2	0.19
$\langle \varphi_{\text{sep}} \rangle$ (°)	90	105	105	110	120	—	95

TABLE 5.12: Parameters of the flow around the circular cylinder on the plane $z = 0$. [1] (Cantwell and Coles, 1983). [2] (Breuer, 2000). [3] (de la Llave Plata et al., 2019).

The discrepancies of the model developed in this work in the velocity statistics are translated into the pressure coefficient statistics. The time-averaged C_p is well predicted until $\varphi = 60°$, and after this point all models overpredict the absolute value of the pressure minimum (see Fig. 5.28a). One reason for the lack of accuracy of GWMLES$^{\text{SST}}_{\text{log}}$, SBES, and DDES may be that the flow is laminar in the experiment, and then the separation-induced transition to turbulence occurs around $\varphi = 90°$. In that case, turbulence models treat all the boundary layer as fully turbulent, which leads to the failure of the prediction of the transition point. This reasoning is not applicable to GWMLES$^{\gamma-\text{Re}_{\theta t}}_{\text{log}}$, which solves the Navier-Stokes equations without modeled turbulence at least in a portion of the boundary layer. Additional variables need to be studied to understand the physical reasoning behind the delayed separation point provided by this model.

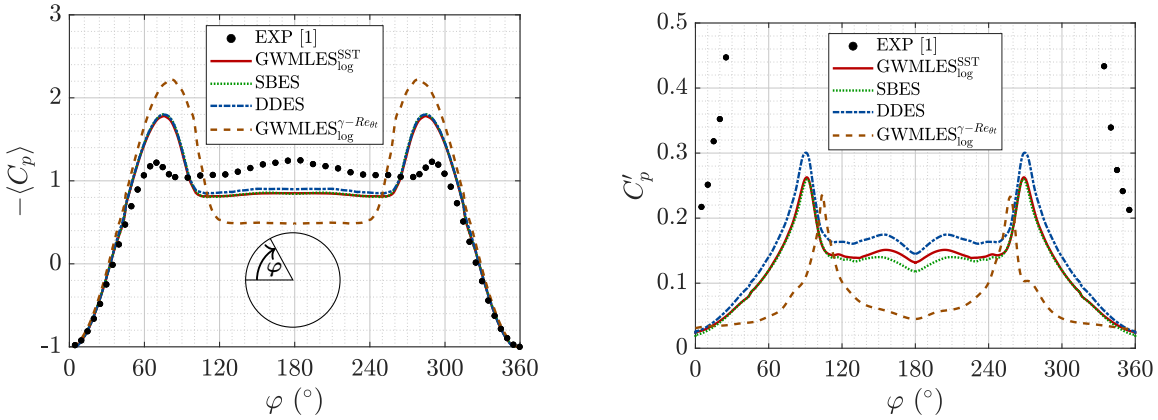

(A) Mean value.

(B) Fluctuating value.

FIGURE 5.28: Pressure coefficient statistics of the circular cylinder on the plane $z = 0$.

Even if no data of the fluctuating component of the C_p is presented, the article (Cantwell and Coles, 1983) provides the peak-to-peak values of the pressure coefficient, C_p^{p-p}. The experimental $C_p^{'}$ value given by Fig. 5.28b has been obtained assuming that the $C_p = C_p(t)$ function is sinusoidal, and in this case $C_p^{'} = C_p^{p-p}/\sqrt{2}$, which serves as an approximation. Figure 5.28b shows that the fluctuations are much higher in the experiments than in the simulations in the entire domain; in particular, in the region of favorable pressure gradient, which is supposed to be laminar, and the high experimental $C_p^{'}$ calls this into question. If the transition mechanism in the experiment is due to the separation-induced transition, then a laminar separation bubble would be expected, which is not the case, although possibly due to the lack of resolution of the experimental devices.

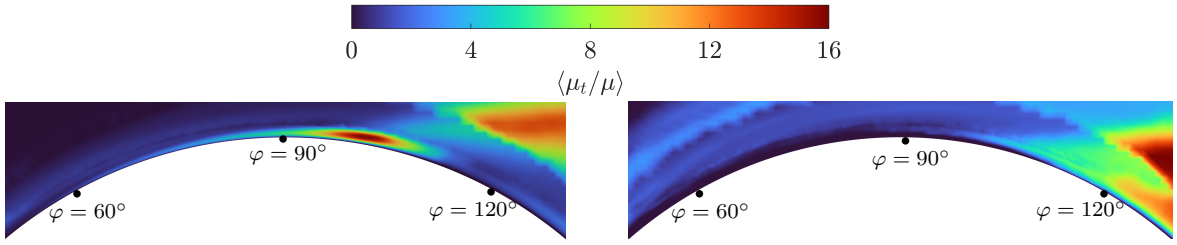

(A) $\text{GWMLES}^{\text{SST}}_{\text{log}}$. (B) $\text{GWMLES}^{\gamma-Re_{\theta t}}_{\text{log}}$.

FIGURE 5.29: Mean turbulent viscosity ratio in the boundary layer of the circular cylinder (plane $z = 0$).

Based on the laminar boundary conditions considered, the flow is laminar at the leading edge of the cylinder. $\text{GWMLES}^{\text{SST}}_{\text{log}}$ provides $\mu_t > 0$ even at $\varphi < 60°$ (see Fig. 5.29a), while $\text{GWMLES}^{\gamma-Re_{\theta t}}_{\text{log}}$ keeps $\mu_t \approx 0$ up to $\varphi \approx 110°$ inside the thin boundary layer. In $\text{GWMLES}^{\text{SST}}_{\text{log}}$, from $\varphi = 0°$ the intensity of the pressure fluctuations increase as φ increases, while in $\text{GWMLES}^{\gamma-Re_{\theta t}}_{\text{log}}$ this happens notably for $\varphi = 60°$ (see Fig. 5.28b). Thus, the transition model is expected to capture from $\varphi \approx 60°$ some unstable Tollmien-Schlichting waves that are the mechanism of the natural laminar-turbulent transition process. This can be verified in Fig. 5.30b.

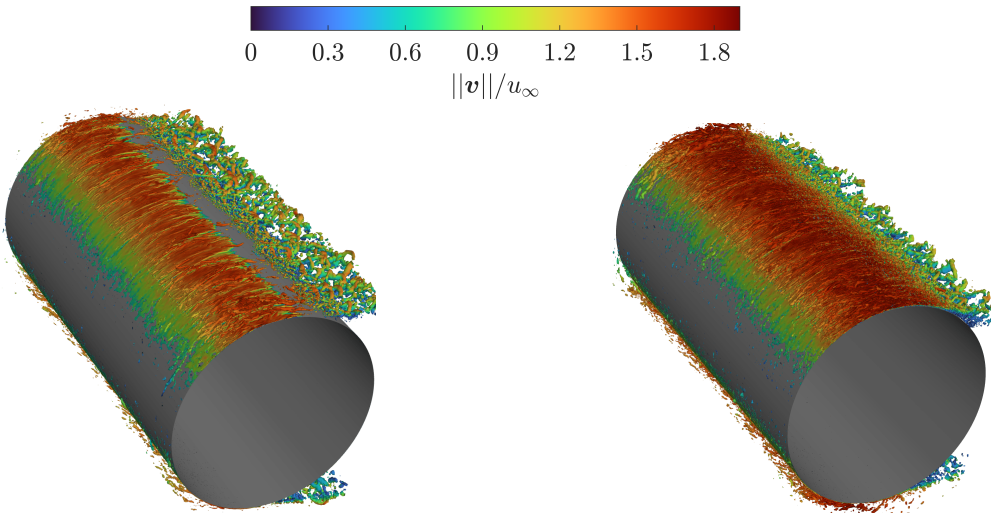

(A) $\text{GWMLES}^{\text{SST}}_{\text{log}}$. (B) $\text{GWMLES}^{\gamma-Re_{\theta t}}_{\text{log}}$.

FIGURE 5.30: Iso-surfaces of Q=2.5×10^7 s^{-2} in the boundary layer of the circular cylinder.

Since the resolution quality $\mathcal{Q}_r \sim \mu_t^2$ (see Eq. (5.8)), $\text{GWMLES}^{\gamma-Re_{\theta t}}_{\text{log}}$ keeps $\mathcal{Q}_r \approx 1$ up to $\varphi = 110°$ (see Fig. 5.31b). In contrast, in $\text{GWMLES}^{\text{SST}}_{\text{log}}$, the turbulence production terms activate and the resolution quality deteriorates from $\varphi = 60°$, even for $\mu_t/\mu < 5$ (see Fig. 5.29a). This translates into the resolution of coarser turbulent structures, which are notably damped around the separation point. Thus, flow separation is a consequence of the low resolution in $\text{GWMLES}^{\text{SST}}_{\text{log}}$, SBES (SST), and DDES. This fact explains the delayed separation of $\text{GWMLES}^{\gamma-Re_{\theta t}}_{\text{log}}$, since in this model the resolution drops only after the flow is fully separated. These findings emphasize the importance of using a low-dissipation numerical scheme. DDES can also be coupled with the $\gamma - Re_{\theta t}$ ($\text{DDES}^{\gamma-Re_{\theta t}}$), but in this case the number of RANS equations is four, while the total number of equations is eight. This means that $\text{GWMLES}^{\gamma-Re_{\theta t}}_{\text{log}}$ provides up to 50% of reduction of the computational cost with respect to $\text{DDES}^{\gamma-Re_{\theta t}}$ (see Table 5.13).

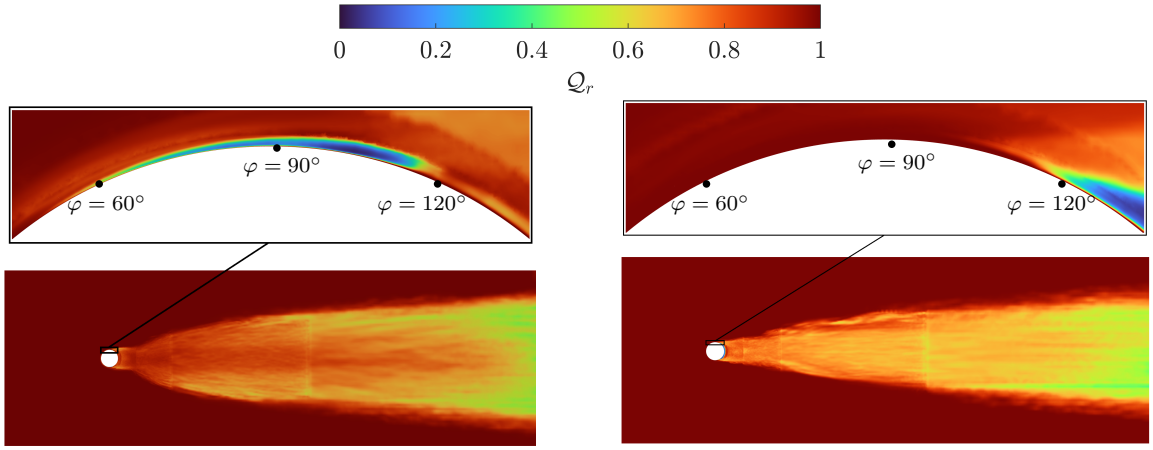

(A) $\text{GWMLES}^{\text{SST}}_{\text{log}}$. (B) $\text{GWMLES}^{\gamma-Re_{\theta t}}_{\text{log}}$.

FIGURE 5.31: Resolution quality on the plane $z = 0$ of the circular cylinder.

Model	$\hat{dt}$	$\hat{L}_\Omega$	N_{iter}	t_{iter}(s)	N^{tr}_{flow}	N^{dat}_{flow}	t_{sim} (days)
$\text{GWMLES}^{\gamma-Re_{\theta t}}_{\text{log}}$	10^{-3}	35	6	0.6	5	5	14.6
$\text{DDES}^{\gamma-Re_{\theta t}}$	10^{-3}	35	6	1.2	5	5	29.2

TABLE 5.13: Simulation parameters of the circular cylinder for a characteristic length scale $L_c = D$.

Even if the results given by $\text{GWMLES}^{\gamma-Re_{\theta t}}_{\text{log}}$ have physical sense, the generation of turbulent structures for $\Phi < 90°$ is not consistent with the prediction of the transition point given by the correlation implemented in the $\gamma - Re_\theta$ model. In fact, Fig. 5.29b shows that $\mu_t > 0$ (which means $\gamma > 0$) for $\Phi < 90°$, so that the correlation predicts laminar flow for $\Phi < 90°$, which coincides with the laminar separation claimed by the authors of the experiment taken as reference (Cantwell and Coles, 1983). With the numerical method used in this work, a flow instability is produced that leads to an early natural laminar-turbulent transition. This can be a particular feature of the flow, but it cannot be discarded that it is a consequence of the instability of the numerical scheme. Indeed, hybrid discretizations using a blended formulation between the central differencing and first-order upwind schemes (see Appendix B, §1.1.1) with low blending coefficients (up to 0.25 for the first-order upwind) have been tried, leading to the conclusion that the transition point is a function of the numerical diffusion of the scheme. This is the same conclusion extracted from a dedicated study on this phenomenon, in which it is shown that, in a similar solver based on the finite volume method, the central differencing scheme generates non-physical instabilities that lead to early natural laminar-turbulent transition (Smith and Ventikos, 2019). In addition, taking as reference DNS data, the article cited shows that, for under-resolved simulations, the transition point can be correctly predicted using a hybrid discretization; in particular, tuning the blending constant to a value that depends on the mesh, which is far from optimal. The instability of the central differencing scheme is well known for a long time (Swanson and Turkel, 1992; Shyy et al., 1992). These instabilities are also expected to be produced in turbulent flows, although in these cases the flow instability is stronger than the instability generated by the numerical scheme, so that using a central difference scheme is not detrimental for the quality of the results in these cases. In contrast, in flows with laminar-turbulent transition, the numerical instability can dominate against the physical instability, leading to the failure of the prediction of the transition point.

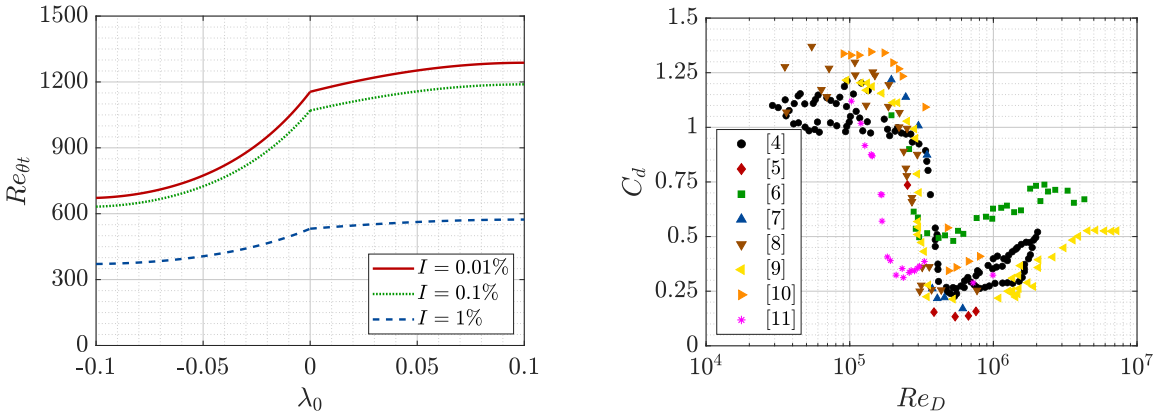

(A) Correlation of $Re_{\theta t} = f(\lambda_\theta, I)$ (Abu-Ghannam and Shaw, 1980).

(B) Drag coefficient of the circular cylinder.

FIGURE 5.32: Experimental data on laminar-turbulent transition [4] (Delany and Sorensen, 1953). [5] (Spitzer, 1965). [6] (Achenbach, 1968). [7] (Bursnall and Loftin, 1951). [8] (Vaz et al., 2007). [9] (Schewe, 1983). [10] (Wieselsberger, 1922). [11] (Fage, 1930).

The discrepancies between simulations and the experiment can also be explained from the uncertainties of the experiment. Apart from turbulence sources such as surface imperfections or measurement devices, a key aspect in laminar-turbulent transition is the freestream turbulent intensity. The work cited (Cantwell and Coles, 1983) says that $I \leq 0.6\%$, while in the numerical simulations $I = 10^{-8}\%$. From classical correlations that relate the transition momentum thickness Reynolds number with the dimensionless pressure gradient λ_θ and the freestream turbulence intensity, $Re_{\theta t} = f(\lambda_\theta, I)$, it is known the high sensitivity of the correlation with respect to the freestream turbulence intensity (see Fig. 5.32a). Thus, a range of $0 \leq I \leq 0.6\%$ is restrictive for comparison between numerical and experimental data. Indeed, as shown in Fig. 5.32b, there is a wide spread in the values obtained from different experiments (Delany and Sorensen, 1953; Spitzer, 1965; Achenbach, 1968; Bursnall and Loftin, 1951; Vaz et al., 2007; Schewe, 1983; Wieselsberger, 1922; Fage, 1930), which means that the flow is highly sensitive to the experimental setup.

Chapter 6

Conclusions

In this thesis research and development steps for the air cooling system of the Inner Barrel of the Inner Tracking System 3 (ITS3 IB) have been carried out. The ITS3 IB will be a future particle detector of the ALICE experiment at the Large Hadron Collider (LHC), which will consist of three silicon layers of thickness 40 µm and length 280 mm bent into cylindrical shape. The cooling system introduces open-cell carbon foams as heat exchangers that combine conduction and convection for the first time in a high-level engineering application. The ITS3 IB is designed to have an unprecedentedly low material budget, which is a requirement for particle detectors aiming at precise tracking at low particle momenta. The thesis has been focused on the characterization of the open-cell foams, thermal analysis, aeroelastic analysis, and the development of a novel turbulence model with potential applications to future particle detectors.

Characterization of open-cell foams

In the first chapter, a multiscale model for open-cell foams has been developed. The microscopic model is based on a periodic unit-cell geometry, and provides as outputs the pressure loss, the thermal conductivity, and the Nusselt number of open-cell foams. These parameters are universal and are used as inputs of a macroscopic model, that treats the foams as porous mediums with averaged properties, and gives as a result the thermal performance of a macroscopic system.

The microscopic approach is referred to characteristic lengths of the order of the foam cell length. The periodic unit cell has been modeled with a 14-sided truncated octahedron taken as a reference from the literature. The model uses as inputs the porosity, which can be easily measured with a precision balance, and the specific area, which can be obtained from microscope images or computer tomography scans. It has been shown that the accuracy of the model deteriorates when partially open-cell foams are considered. A comparison with experimental data obtained from the literature and from a setup built at CERN has shown that the model provides accurate results in all open-cell foams considered. A correlation to predict the Nusselt number as function of the pressure loss has been confirmed as valid in the cases where both experimental and numerical results are available. It has been concluded that the specific surface area of foams plays an important role in the thermal performance of systems where convective heat transfer is present.

The macroscopic model is applicable where the characteristic length is large enough so that the flow is fully developed. In this model, the foam is considered as a continuum, and the effect of the microscopic geometry on the macroscopic behavior is done with source terms in the governing equations. Since the entrance and exit effects are neglected in the microscopic model, the minimum ratio between the macroscopic and microscopic scales under which the macroscopic model is valid has been deduced. The results given by this model are accurate when compared with experimental data; in particular, in an experimental setup that represents a case of practical application in the ALICE ITS3 IB. When a foam is glued to a solid material, it has been shown that the thermal performance of the system is proportional to the penetration of the glue in the foam. An optimized assembly procedure developed at CERN has been shown to limit the thermal resistance of the joint.

Thermal analysis

The properties obtained from the foam characterization have been used to select adequate foams for the ITS3 IB and to design the cooling system in the second chapter. The non-uniform heat dissipation within the layers has motivated the incorporation of carbon foams, which act as localized heat exchangers combining conduction and convection. To the best of the author's knowledge,

this represents the first practical application in high-level engineering. These foams also serve as structural supports. This innovative approach leads to an 80% reduction in material budget compared to the previous version (ITS2 IB), resulting in enhanced measurement accuracy.

An experimental setup has been built to validate the proposed design. The heat dissipation of the layers has been modeled by including heaters of reduced thickness, and multiple temperature sensors have been installed to obtain the temperature distribution. The quality of the prototype in terms of dimensional tolerances has been verified with a Computed Tomography scan. The results of the scan have also been used to validate the quality of the gluing process between the foams and the layers. A numerical model has been implemented using the macroscopic foam model, and the geometry and parameters of the experimental setup have been used in numerical simulations; in particular, to determine the thermal performance of the system in a case of practical application. The mean deviation between the experiments and the simulations in the temperature distributions is lower than 0.5 K. The simulations overpredict the temperature values, and this has been ascribed to the thermal resistance induced by the glue between the temperature sensors and the layers.

The experimental setup, though close to the ITS3 IB setup, does not exactly represent the configuration of the final detector. It has been proven that the design requirement in terms of temperature distribution is met with freestream velocity values of more than 5 m/s. Since the layer heat dissipation values used in this work are approximate, a parametric study has been performed. An improvement in the baseline design has been proposed that provides almost a 50% reduction in the maximum temperature difference over the baseline configuration.

Aeroelastic analysis

The air flow applied to the low-mass structure of the ITS3 IB will cause vibrations, which requires an aeroelastic analysis that has been done in the fourth chapter. The displacement of the outermost layer of a prototype of the ITS3 IB has been measured with a confocal sensor. This is a non-invasive device that provides sub-micron accuracy, one order of magnitude higher than industry-standard devices such as laser displacement sensors. To the author's knowledge, this is the first example on the use of confocal sensors in a high-level engineering application. Experimental work has been complemented with a novel simplified mathematical model specifically designed for analyzing the fluid-structure interaction. This model is based on decoupling the structural and fluid problems, and a geometry of reduced size is defined in the fluid simulations to reduce the computational cost.

Experimental and simulation results of layer displacements have been compared in a prototype of the ITS3 IB. It has been shown that the developed model predicts the natural frequencies identified experimentally with an error lower than 10%, and that the risk of mechanical resonance is low due to the lack of aerodynamic coupling. The results demonstrate that the model gives an accurate prediction of the peaks of the displacement spectrum. Experimental data provide higher peak-to-peak values of the displacements than the simulations, which has been mainly attributed to the presence of low-frequency components in the experimental spectrum produced by the fan that generates the air flow. Simulations have also been performed to analyze the real configuration of the ALICE ITS3 IB, which differs slightly from the one used in the experimental setup. These results have demonstrated that the experimental setup is representative of the real behavior of the ALICE ITS3 IB, and that design requirements are met in all cases considered. Parametric studies have been performed to analyze the effect of the ITS3 IB layer composition and thickness on the structural response. In addition, it has been concluded that foam design can be tuned to find the required balance between structural displacements, energy consumption, and detector cooling.

The current study has led to the conclusion that the external noise contributes to layer displacements of the same order as the one of the aerodynamic loads. When installed in the ALICE detector, the ITS3 IB will be mechanically connected to other components, which are not considered in the prototype tested in this work. The external noise of the ALICE cavern could lead to displacements of the entire structure, which would imply additional displacements of the layers. Thus, future work will deal with the modeling of noise and structural properties of the ITS3 IB when integrated into other subsystems of the ALICE detector.

Turbulence model for industrial simulations

Motivated by the limitations of current turbulence models for industrial simulations, a generalized wall-modeled large simulation model (GWMLES) has been developed in the fifth chapter. The model improves and expands upon the classical WMLES approach, which models turbulence up to the inner part of the log-layer, by introducing a formulation that also allows for the modeling of the entire log-layer. This is particularly relevant for the industry, given the current needs and available computing power. The model is based on the main idea of the unpublished SBES model, which blends RANS and LES turbulent viscosities. The blending function has been designed to be independent of the mesh, thereby avoiding the grid-induced separation problem that is one of the main drawbacks of state-of-the-art models. Furthermore, GWMLES has been shown to have a computational cost up to 50% lower than other hybrid RANS/LES models such as DDES.

The numerical model has been validated with experimental data and DNS, WMLES, and LES simulations available in the literature of four test cases that represent industrial flows. Simulating a free shear flow has led to the conclusion that the model is consistent, since it provides a LES solution in the absence of boundary layers. The simulation of a periodic channel flow demonstrates the excellent performance of the model in a standard WMLES test case. Additionally, the advantages of resolving the inner part of the logarithmic layer in RANS instead of using wall functions or a mixing-length model have been presented. More complex test cases, such as the flow around the Ahmed body, which involves turbulent flow with separation and subsequent reattachment, have been studied. GWMLES has shown its ability to capture finer turbulence structures compared to other hybrid RANS/LES models. This has been attributed to the use of a more consistent LES model and a faster transition from modeled to resolved turbulence provided by the formulation. The results obtained by the model are in excellent agreement with experimental data, showing accuracy similar to LES simulations, but at a significantly lower computational cost. In addition, it has been shown to provide superior performance than URANS, even for coarse meshes. GWMLES is also promising as an alternative to LES in laminar-turbulent transitional flows, fully resolving laminar regions, and being able to solve the natural transition from laminar to fully turbulent flow.

The test cases considered have showcased the model's capabilities in various flow scenarios. However, further validation is necessary, in particular in different flow types that will be the basis of future work; first, additional standard test cases of turbulent flows such as the backward facing step (Davidson, 2011) allow additional comparison with experimental data and LES; second, complex flows with real geometries used in the aeronautical industry (Terracol and Manoha, 2020) serve as additional challenging cases using spectral analysis as basis for the result comparison; third, the instabilities generated by numerical schemes can be studied in detail in laminar-turbulent transitional flows with laminar separation bubbles (Lehmkuhl et al., 2013; Slaughter et al., 2023).

Appendix A

Turbulence models

Turbulence models are an alternative to the large computing power required by the Direct Numerical Simulations (DNS), in which the Navier-Stokes equations are solved directly without modeling. The turbulence scales that are explained in §1 form a basis for the development of these models, which are divided into three main approaches: Large Eddy Simulation (LES, §2), Reynolds-Averaged Navier Stokes Equations (RANS, §3), and Detached Eddy Simulation (DES, §4).

§1. Turbulence scales

§1.1. Kolmogorov's hypotheses

A fully turbulent flow is considered with characteristic velocity U and length scale L. Turbulence is considered to be composed of vorticity regions or eddies. The length scale of the largest eddies is $l_0 \sim L$, their characteristic velocity v_0 is of the order of the root mean square of the turbulence intensity $u' = (2k/3)^{1/2} \sim U$, and $Re_0 = v_0 l_0/\nu \gg 1$. The large eddies are unstable and break up, transferring their energy to the small eddies that are generated. As the eddy size decreases, the Reynolds number decreases, and on a sufficiently small length scale, it reaches a value $\mathcal{O}(1)$ (Richardson and Lynch, 2007). On these scales, the kinetic energy is dissipated into heat. The rate of kinetic energy transferred per unit of mass k is the turbulent dissipation rate ε. On the largest scales $k \sim v_0^2$, and the characteristic time scale involved in energy transfer is the eddy turnover time: $t_0 \sim l_0/v_0$. When turbulence reaches an equilibrium state, the energy transfer rate from the large scales is equal to the dissipated energy at the small scales ε, which gives as a result $\varepsilon \sim v_0^3/l_0$.

The scales of the largest eddies l_0 and v_0 depend on the geometry of the flow; in particular, l_0 is bounded by the characteristic size of the flow, while v_0 is limited by the mean velocity differences. Although the energy cascade concept implies that the Reynolds number $Re_l = u_l l/\nu$ decreases as the eddy size l decreases, there is not enough information neither to determine the trends of u_l and t_l, nor to estimate the size of the eddies where the energy is dissipated. The answer to these questions was given by A. N. Kolmogorov in 1941, who made three hypotheses in the case of flows at sufficiently high Reynolds numbers (Kolmogorov, 1991).

Hypothesis of local isotropy. *Small-scale turbulent motions satisfying $l/l_0 \ll 1$ are statistically isotropic.*

Local isotropy means that there is no preferential orientation for the small-scale eddies, which are assumed to be smaller than a limit scale $l_{\mathrm{EI}} < l_0$ with $l_{\mathrm{EI}} \sim l_0$.

First similarity hypothesis. *The statistical structure of small-scale eddies has a universal form that is uniquely determined by ν and ε.*

Given ε and ν, there are unique length, velocity, and time scales that can be formed:

$$\eta = \left(\frac{\nu^3}{\varepsilon}\right)^{1/4}, \quad v_\eta = (\varepsilon\nu)^{1/4}, \quad t_\eta = \left(\frac{\nu}{\varepsilon}\right)^{1/2}, \tag{A.1}$$

which characterize the small eddies, since $Re_\eta = v_\eta \eta/\nu = 1$ and $\varepsilon = \nu(v_\eta/\eta)^2$. The relationships (A.1) and $\varepsilon \sim v_0^3/l_0$ give:

$$\frac{\eta}{l_0} \sim Re_0^{-3/4}, \quad \frac{v_\eta}{v_0} \sim Re_0^{-1/4}, \quad \frac{t_\eta}{t_0} \sim Re_0^{-1/2}, \tag{A.2}$$

leading to the conclusion that the velocity and time scales of the small eddies are also smaller than those of the large eddies. In Eq. (A.2), the length scale ratio shows that, at sufficiently high Reynolds numbers, there is a range of scales l that satisfy $\eta \ll l \ll l_0$. Since in this range the eddies are much larger than the dissipative eddies, it can be assumed that $Re_l = v(l)l/\nu \gg 1$, and consequently that their motion is little affected by viscosity.

Second similarity hypothesis. *The statistical structure of the motions of scale l in the range $\eta \ll l \ll l_0$ has a universal form that is uniquely determined by ε independent of ν.*

It is convenient to introduce a length scale l_{DI} so that the range in the above hypothesis can be written $l_{\mathrm{DI}} < l < l_{\mathrm{EI}}$. This length scale divides the universal equilibrium range $l < l_{\mathrm{EI}}$ into two subranges: the inertial subrange ($l_{\mathrm{DI}} < l < l_{\mathrm{EI}}$) and the dissipation range $l < l_{\mathrm{DI}}$. According to the second similarity hypothesis, the motions in the inertial subrange are determined by inertial effects, whereas only motions in the dissipation range experience significant viscous effects.

§1.1.1. Energy spectrum

The turbulent kinetic energy is the integral of the energy spectrum:

$$k = \int_0^\infty E(K)\ \mathrm{d}K, \tag{A.3}$$

where $K = 2\pi/l$ is the wavenumber. In the universal equilibrium range, the spectrum is a universal function of ε and ν as a consequence of the first similarity hypothesis. In the inertial range, the second similarity hypothesis and dimensional arguments lead to the following spectrum:

$$E(K) = C\varepsilon^{2/3}K^{-5/3}, \tag{A.4}$$

with C referring to a constant. Eq. (A.4) is called Kolmogorov's -5/3 law, and is in many practical cases a good approximation of the spectrum in the inertial subrange (see Fig. A.1). The turbulent dissipation is given by the following integral (Pope, 2000):

$$\varepsilon = \int_0^\infty 2\nu K^2 E(K)\ \mathrm{d}K. \tag{A.5}$$

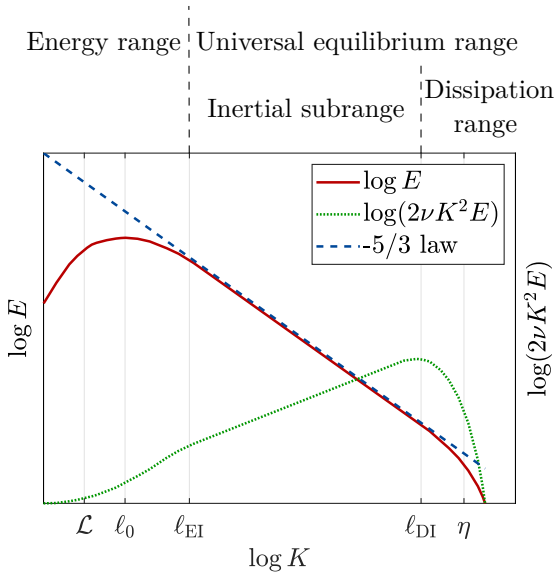

FIGURE A.1: Turbulence scales and energy and dissipation spectrums.

In what follows, the flow is assumed to be incompressible. Turbulence is a continuum problem, and the solution of all turbulence scales is called Direct Numerical Simulation (DNS). In this case, the Navier-Stokes equations are solved without modeling assumptions (Pope, 2000):

$$\begin{cases} \nabla \cdot \boldsymbol{v} = 0 & \text{(A.6)} \\ \dfrac{\partial \boldsymbol{v}}{\partial t} + \boldsymbol{v} \cdot \nabla \boldsymbol{v} = -\dfrac{1}{\rho} \nabla p + \nu \nabla^2 \boldsymbol{v} & \text{(A.7)} \\ \dfrac{\partial T}{\partial t} + \boldsymbol{v} \cdot \nabla T = \alpha \nabla^2 T, & \text{(A.8)} \end{cases}$$

where p is the pressure, ρ is the density, c_p is the specific heat capacity at constant pressure, T is the temperature, and α is the thermal diffusivity. Solving Eqs. (A.6) to (A.8) is computationally expensive, since the ratio between large and small length scales is of the order of $Re_0^{3/4}$ (see Eq. (A.2)). These scales have to be resolved in three dimensions, making the space resolution $\sim Re_0^{9/4}$. In addition, the turbulence scales have to be resolved in time; therefore, the computational cost scales like $\sim Re_0^{11/4}$, which is very expensive for flows at high Reynolds numbers. Turbulence models reduce the computational cost of the simulations, the main ones being:

- **Large Eddy Simulations (LES)**: a part of the energy spectrum is resolved. For accuracy and stability reasons, it usually requires solving more than 80% of the turbulent kinetic energy (Pope, 2000). The remaining part of the spectrum is modeled.
- **Reynolds-Averaged Navier Stokes (RANS)**: all energy spectrum is modeled.
- **Detached Eddy Simulation (DES)**: RANS and LES models are combined. Each model is used in a different portion of the computational domain.

§2. Large Eddy Simulation

In LES, the dynamics of the large-scale motions—which are affected by the flow geometry and are not universal—are computed explicitly, and the influence of the small scales—which have a universal character and follow Kolmogorov's hypotheses—are represented by simple models. These scales are separated by applying a low-pass filter to the exact solution. This filtering is represented mathematically in physical space as a convolution product (Leonard, 1975). The filtered part $\overline{\phi}(\boldsymbol{x}, t)$ of a variable $\phi(\boldsymbol{x}, t)$ in a domain Ω is defined formally by the following convolution:

$$\overline{\Phi}(\boldsymbol{x}, t) = (\Phi * G)(\boldsymbol{x}, t) = \int_\Omega \int_0^\infty \Phi(\boldsymbol{\xi}, \boldsymbol{x}) G(\boldsymbol{x} - \boldsymbol{\xi}, t - \tau) \, \mathrm{d}\tau \, \mathrm{d}\boldsymbol{\xi}, \tag{A.9}$$

for a class of filters that satisfy two constraints:

1. Conservation of constants:

$$\overline{C} = C \iff \int_\Omega \int_0^\infty G(\boldsymbol{\xi}, \boldsymbol{x}) \, \mathrm{d}\tau \, \mathrm{d}\boldsymbol{\xi} = 1. \tag{A.10}$$

2. Commutation with derivation:

$$\frac{\overline{\partial \Phi}}{\partial \boldsymbol{x}} = \frac{\partial \overline{\Phi}}{\partial \boldsymbol{x}} \quad \text{and} \quad \frac{\overline{\partial \Phi}}{\partial t} = \frac{\partial \overline{\Phi}}{\partial t}. \tag{A.11}$$

Using the above filter definition, any field Φ can be split into a filtered component $\overline{\Phi}$ and a residual component Φ':

$$\Phi = \overline{\Phi} + \Phi', \tag{A.12}$$

The substitution of Eq. (A.12) into the incompressible Navier–Stokes equations leads to the filtered incompressible Navier Stokes equations (Pope, 2000):

$$\begin{cases} \nabla \cdot \overline{\boldsymbol{v}} = 0 & \text{(A.13)} \\ \dfrac{\partial \overline{\boldsymbol{v}}}{\partial t} + \overline{\boldsymbol{v} \cdot \nabla \boldsymbol{v}} = -\dfrac{1}{\rho}\nabla \overline{p} + \nu \nabla^2 \overline{\boldsymbol{v}} & \text{(A.14)} \\ \dfrac{\partial \overline{T}}{\partial t} + \overline{\boldsymbol{v} \cdot \nabla T} = \alpha \nabla^2 \overline{T}, & \text{(A.15)} \end{cases}$$

Equations (A.13) to (A.15) differ from Eqs. (A.6) to (A.8) because the filtered products $\overline{\boldsymbol{v} \cdot \nabla \boldsymbol{v}}$ and $\overline{\boldsymbol{v} \cdot \nabla T}$ are not equal to the product of the filtered components $\overline{\boldsymbol{v}} \cdot \nabla \overline{\boldsymbol{v}}$ and $\overline{\boldsymbol{v}} \cdot \nabla \overline{T}$. The differences are the residual stress tensor $\rho \boldsymbol{\tau}^R$ and the residual heat flux $\boldsymbol{q}^R$ (Pope, 2000):

$$\rho \tau_{ij}^R = \rho(\overline{v_i v_j} - \overline{v_i}\ \overline{v_j}) \quad \text{and} \quad q_i^R = \rho c_p(\overline{v_i T} - \overline{v_i}\ \overline{T}). \tag{A.16}$$

The residual stress tensor can be decomposed into an isotropic part and a deviatoric part:

$$\tau_{ij}^R = \tau_{ij}^r + \frac{1}{3}\rho \tau_{kk}^R, \tag{A.17}$$

and the isotropic part is usually included in the modified filtered pressure. Assuming that the residual heat flux is isotropic, substituting Eq. (A.16) into Eqs. (A.13) to (A.15) leads to:

$$\begin{cases} \nabla \cdot \overline{\boldsymbol{v}} = 0 & \text{(A.18)} \\ \dfrac{\partial \overline{\boldsymbol{v}}}{\partial t} + \overline{\boldsymbol{v}} \cdot \nabla \overline{\boldsymbol{v}} = -\dfrac{1}{\rho}\nabla \overline{p} + \nu \nabla^2 \overline{\boldsymbol{v}} - \dfrac{1}{\rho}\nabla \cdot \boldsymbol{\tau}^r & \text{(A.19)} \\ \dfrac{\partial \overline{T}}{\partial t} + \overline{\boldsymbol{v}} \cdot \nabla \overline{T} = \alpha \nabla^2 \overline{T} - \dfrac{1}{\rho c_p}\nabla \cdot \boldsymbol{q}^r. & \text{(A.20)} \end{cases}$$

§2.1. Implicit and explicit filtering

There are three different approaches based on the filtering process:

- **Implicit LES**: the filter is the numerical scheme, and no residual stress tensor model is used. This is also called under-resolved DNS.
- **Implicitly-filtered LES**: the filter is the numerical scheme, and a residual stress tensor model is used.
- **Explicitly-filtered LES**: a filter satisfying the properties (A.10) and (A.11) is applied to the Navier-Stokes equations, and a residual stress tensor model is used.

Discrete derivative operators have a low-pass filtering effect, although the associated filter acts only in the single spatial direction in which the derivative is taken. This implies that each term in the Navier-Stokes equations is acted on by a distinct one-dimensional filter, and thus, there is no way to derive the discrete equations through the uniform application of a single three-dimensional filter. Further limitations related to implicit filtering are the inability to control the frequency content of convective terms or the numerical errors (Lund, 2003). These limitations motivate the use of explicit filtering, although its use is limited to academic studies. This is because for a grid size Δ, the simulation time scales with Δ^4, and the computational cost can be one order of magnitude higher than in the implicitly-filtered LES (Sagaut, 2006).

One standard LES test case is the decaying isotropic turbulence (DIT), where turbulence is generated in a box. The decay over time depends on the dissipation; therefore, it is possible to test the effectiveness of the dissipation of the numerical model in a simple periodic box. The energy flows down the spectrum, and if there is no residual stress tensor model, eventually arrives to the grid limit, which is larger than the Kolmogorov length scale. Since there is no resolution beyond that limit, this might lead to an unstable simulation and/or large errors (see Fig. A.2). To solve

this issue, the goal of the implicitly-filtered LES is that the turbulent dissipation rate of the LES at the grid limit is equal to the physics of the dissipation at the DNS limit:

$$\varepsilon_{\mathrm{DNS}} = \nu S^2 = \varepsilon_{\mathrm{LES}} = (\nu + \nu_t)\overline{S}^2, \tag{A.21}$$

where $S = \sqrt{2S_{ij}S_{ij}}$, S_{ij} are the components of the strain rate tensor, and ν_t is the turbulent kinematic viscosity. Since the gradients at the grid limit are smaller than the gradients at the Kolmogorov length scale, $\nu_t/\nu \geq 1$ to account for the same level of dissipation.

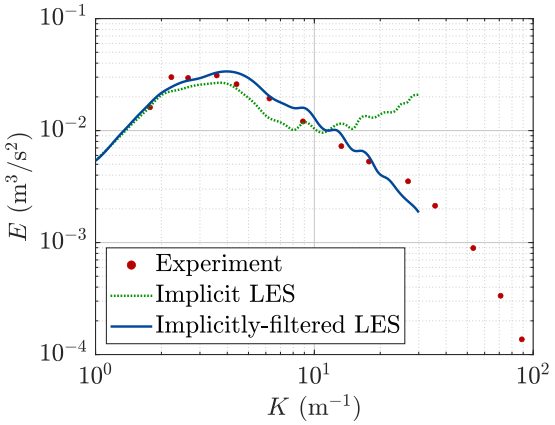

FIGURE A.2: Turbulence spectrum of DIT test case. Experimental data (Comte-Bellot and Corrsin, 1971) and numerical simulations of a grid of 64×64×64 elements.

§2.2. Residual stress tensor models

Models for the anisotropic residual stress tensor and heat flux are needed to close Eqs. (A.18) to (A.20). The most popular ones use the turbulent viscosity assumption (Boussinesq, 1877):

$$\boldsymbol{\tau}^r = -2\nu_t\overline{\boldsymbol{S}}, \qquad \boldsymbol{q}^r = -\kappa_t\nabla\overline{T}, \tag{A.22}$$

where κ_t is the turbulent thermal conductivity. For a wide range of flows, the expression $\kappa_t = \rho\nu_t c_p/Pr_t$ is valid, with Pr_t referring to the turbulent Prandtl number. For dimensional reasons, the turbulent kinematic viscosity scales like $\nu_t \sim \rho v_t l_t$. LES only models turbulence scales below the grid limit Δ; therefore, the relevant length scale in the model is $l_t \sim \Delta$. In case of an algebraic model, the only velocity scale is $v_t \sim l_t\nabla\boldsymbol{v}$, since the flow velocity is not Galilean invariant. The simplest residual stress model was proposed by Smagorinsky (Smagorinsky, 1963):

$$\nu_t = C_s\Delta^2\overline{S}, \tag{A.23}$$

which gives DNS results when $\Delta \to 0$. The model overpredicts the dissipation near walls, where the eddies are damped. Based on experimental data of wall-bounded flows (van Driest, 1956), the inclusion of the damping mechanism leads to the following expression (Moin and Kim, 1982):

$$\nu_t = C_s\Delta^2\overline{S}\left(1 - e^{-\tilde{y}^+/25}\right), \tag{A.24}$$

where C_s is the Smagorinsky constant, $\tilde{y}^+ = \tilde{y}u_\tau/\nu$ is the dimensionless wall distance, and $u_\tau = \sqrt{\tau_w/\rho}$ is the shear velocity, where τ_w is the wall shear stress.

LES models should only provide damping in underresolved turbulence and $\nu_t = 0$ in resolved turbulence and laminar shear flow. This is not the case with the Smagorinsky model, since the strain rate does not vanish in cases such as laminar shear flows. Moreover, the constant C_s varies between 0.1 and 0.25 and depends on the flow. More complex models have been developed to overcome these limitations, namely the dynamic Smagorinsky model (Germano et al., 1991). The expression derived from this model is the same as Eq. (A.23), but the coefficient C_s is replaced by a nonconstant C_d. The model is based on solving the equations in a coarser mesh, and the value

of C_d can be obtained assuming that the expression Eq. (A.23) is valid for both filtered tensors. If both solutions are the same, then the flow is fully resolved, and $C_d = 0$.

The dynamic Smagorinsky model increases the computational cost of the simulations with respect to the Smagorinsky model, and it can provide negative values of C_d that generate numerical instabilities. The WALE model (Nicoud and Ducros, 1999) was developed from invariants of the filtered velocity gradient tensor:

$$\nu_t = C_w \Delta^2 \frac{(\overline{\mathcal{S}}_{ij}^d \overline{\mathcal{S}}_{ij}^d)^{3/2}}{(\overline{S}_{ij}\overline{S}_{ij})^{5/2} + (\overline{\mathcal{S}}_{ij}^d \overline{\mathcal{S}}_{ij}^d)^{5/4}}, \tag{A.25}$$

where $\overline{\mathcal{S}}_{ij}^d$ are the components of the traceless symmetric part of the square of the velocity gradient tensor. The computational cost is not greater than the Smagorinsky model, and does not require adjustments to compute wall bounded flows. Moreover, it returns a zero turbulent viscosity for laminar shear flows. Equation (A.25) gives the correct near-wall scaling of the turbulent viscosity, $\nu_t = \mathcal{O}(\tilde{y}^3)$, unlike Eq. (A.24), which gives $\nu_t = \mathcal{O}(\tilde{y}^2)$ (Nicoud and Ducros, 1999). In Eq. (A.25), the value $C_w = 0.5$ was initially proposed by the cited authors, although intensive validation involving the original model has shown superior results in Ansys Fluent with $C_w = 0.325$. Subsequently, other models with similar features have been developed (Vreman, 2004).

§2.3. Wall-modeled LES

The mesh requirements of LES are restrictive in wall-bounded flows at high Reynolds numbers. The scaling problem near the wall is reduced in the Wall-Modeled LES (WMLES) models, which are usually divided into two different approaches: the first one is a modification of Eq. (A.24) that introduces a mixing-length model (Shur et al., 2008):

$$\nu_t = \min[(\underbrace{C_s\Delta^2}_{\text{LES}}), (\underbrace{\kappa y)^2}_{\text{RANS}})]\overline{S}\left(1 - e^{-\tilde{y}^+/25}\right), \tag{A.26}$$

where $\kappa \approx 0.4$ is the Von Kármán constant.
The second method uses *wall functions*. This consists of placing the first near-wall cell up to the innermost part of the log-layer. At the same time, instead of a no-slip boundary condition, a boundary condition for the wall-parallel velocity the law of the wall is applied:

$$v^+_{\text{sub}\parallel} = \tilde{y}^+, \quad v^+_{\text{log}\parallel} = \frac{1}{\kappa}\ln(\tilde{y}^+) + C^+, \tag{A.27}$$

where $C^+ \approx 5.2$ obtained from experimental data. Both velocity solutions are usually blended to ensure C^1-continuity (Lozano-Durán et al., 2022).

§3. Reynolds-Averaged Navier Stokes

The RANS equations use the Reynolds decomposition, in which a flow variable Φ is decomposed into its mean $\langle\Phi\rangle$ and fluctuating Φ' components (Pope, 2000):

$$\Phi = \langle\Phi\rangle + \Phi'. \tag{A.28}$$

Using the property $\langle\Phi'\rangle = 0$, the RANS equations take the following form:

$$\begin{cases} \nabla\cdot\langle\boldsymbol{v}\rangle = 0 & \text{(A.29)} \\ \dfrac{\partial\langle\boldsymbol{v}\rangle}{\partial t} + \langle\boldsymbol{v}\rangle\cdot\nabla\langle\boldsymbol{v}\rangle = -\dfrac{1}{\rho}\nabla\langle p\rangle + \nu\nabla^2\langle\boldsymbol{v}\rangle - \dfrac{1}{\rho}\nabla\cdot(\rho\langle\boldsymbol{v}'\otimes\boldsymbol{v}'\rangle) & \text{(A.30)} \\ \dfrac{\partial\langle T\rangle}{\partial t} + \langle\boldsymbol{v}\rangle\cdot\nabla\langle T\rangle = \alpha\nabla^2\langle T\rangle - \dfrac{1}{\rho c_p}\nabla\cdot(\rho c_p\langle\boldsymbol{v}'T'\rangle), & \text{(A.31)} \end{cases}$$

which are similar to the filtered LES equations (Eqs. (A.18) to (A.20)), but replacing the filtered variables by mean variables, and the residual terms by the Reynolds terms.

§3.1. Spalart-Allmaras model

The RANS models differ in the way the Reynolds stress tensor $\rho\langle \boldsymbol{v}' \otimes \boldsymbol{v}' \rangle$ is modeled. Many of them use the Boussinesq's turbulent viscosity assumption, and the differences depend on how the turbulent viscosity is computed. A popular model in aeronautics is the Spalart-Allmaras model (Spalart and Allmaras, 1992) that defines a transport equation for the turbulent kinematic viscosity:

$$\frac{\partial \nu_t}{\partial t} + \langle \boldsymbol{v} \rangle \nu_t = C_1 \nu_t \langle S \rangle - C_2 \frac{\nu_t^2}{\tilde{y}^2} + \nabla \cdot \left(\nu + \frac{\nu_t}{\sigma_v} \right) \nabla \langle \boldsymbol{v} \rangle. \tag{A.32}$$

The Spalart-Allmaras model is widely used for external aerodynamic flows; however, it is not suitable for laminar-turbulent transitional flows and does not provide accurate results in other applications (Malone, 1996; Godin et al., 1997; Fares and Schröder, 2005).

§3.2. Two-equation models

Two-equation models are nowadays the reference for industrial applications, in which transport equations are used for calculating two independent turbulence scales. The first is calculated from the turbulent kinetic energy $k = |\boldsymbol{v}'|^2/2$, and the second is obtained from the turbulent dissipation rate ε, or its turnover frequency: the specific turbulent dissipation rate ω. The first model published is the $k - \varepsilon$ model (Launder and Spalding, 1974) for $\nu_t = \beta^* k^2/\varepsilon$, where $\beta^* = 0.09$. It is derived from the application of the definition of turbulent kinetic energy in the Navier-Stokes equations. The approximation of turbulent diffusion by gradient diffusion leads to the following equation:

$$\frac{\partial k}{\partial t} + \langle \boldsymbol{v} \rangle \cdot \nabla k = \nabla \cdot \left[\left(\nu + \frac{\nu_t}{\sigma_{k\varepsilon}} \right) \nabla k \right] + \nu_t \langle S \rangle^2 - \varepsilon. \tag{A.33}$$

The exact ε-equation can be derived from the Navier-Stokes equations. This equation is complex and contains many higher-order terms. For this reason, the modeled ε-equation is formulated in analogy with the k-equation. Each of the source terms are modeled as proportional to the corresponding terms in the k-equation. The resulting ε-equation is:

$$\frac{\partial \varepsilon}{\partial t} + \langle \boldsymbol{v} \rangle \cdot \nabla \varepsilon = \nabla \cdot \left[\left(\nu + \frac{\nu_t}{\sigma_\varepsilon} \right) \right] \nabla \varepsilon + \frac{\varepsilon}{k} \left(C_{\varepsilon_1} \nu_t \langle S \rangle^2 - C_{\varepsilon_2} \varepsilon \right). \tag{A.34}$$

The constants of Eqs. (A.33) and (A.34) are determined from simple experiments in which the equations can be simplified. Additional corrections have also been done through computer optimizations and detailed comparison with complex experiments.

Another popular model is the $k - \omega$ model (Wilcox, 2006) for $\nu_t = k/\omega$:

$$\begin{cases} \dfrac{\partial k}{\partial t} + \langle \boldsymbol{v} \rangle \cdot \nabla k = \nabla \cdot \left[\left(\nu + \dfrac{\nu_t}{\sigma_{k\omega}} \right) \nabla k \right] + \nu_t \langle S \rangle^2 - \beta^* k \omega & \text{(A.35)} \\ \dfrac{\partial \omega}{\partial t} + \langle \boldsymbol{v} \rangle \cdot \nabla \omega = \nabla \cdot \left[\left(\nu + \dfrac{\nu_t}{\sigma_\omega} \right) \nabla \omega \right] + C_{\omega_1} \dfrac{\omega}{k} \nu_t \langle S \rangle^2 - C_{\omega_2} \omega^2. & \text{(A.36)} \end{cases}$$

The $k - \omega$ model provides good near-wall performance under adverse pressure gradients. However, it is highly sensible to the freestream values of ω (Menter, 1992). The baseline (BSL) $k - \omega$ model was developed to take advantage of the strong points of the $k - \omega$ and $k - \epsilon$ models (Menter, 1994). It uses the ω-equation near the wall, and then blends to the ε-equation near the boundary layer edge. Since it is undesirable to solve both at the same time, the ε-equation is transformed to an exact equivalent of the ω-formulation, and then blended with the original $k - \omega$ model to give:

$$\begin{cases} \dfrac{\partial k}{\partial t} + \langle \boldsymbol{v} \rangle \cdot \nabla k = \nabla \cdot \left[\left(\nu + \dfrac{\nu_t}{\tilde{\sigma}_{k\omega}} \right) \nabla k \right] + \nu_t \langle S \rangle^2 - \beta^* k\omega & \text{(A.37)} \\ \dfrac{\partial \omega}{\partial t} + \langle \boldsymbol{v} \rangle \cdot \nabla \omega = \nabla \cdot \left[\left(\nu + \dfrac{\nu_t}{\tilde{\sigma}_{\omega}} \right) \nabla \omega \right] + \tilde{C}_{\omega_1} \dfrac{\omega}{k} \nu_t \langle S \rangle^2 - \tilde{C}_{\omega_2} \omega^2 + \dfrac{2(1-F_1)}{\sigma_{\omega_2} \omega} \nabla k \nabla \omega. & \text{(A.38)} \end{cases}$$

The last term on the right-hand side of Eq. (A.38)—called *cross diffusion*—is the only term that varies between Eq. (A.36) and Eq. (A.38). It eliminates the freestream sensitivity of the original $k-\omega$ (Wilcox, 2006). The coefficients $1/\tilde{\sigma}_{k\omega}$, $1/\tilde{\sigma}_{\omega}$, $\tilde{C}_{\omega_1}$, and $\tilde{C}_{\omega_2}$ are blended:

$$\tilde{\varphi} = F_1 \varphi_1 + (1 - F_1) \varphi_2, \tag{A.39}$$

The function $F_1 = \tanh(\arg^4)$ depends on different arguments:

$$\arg = \min[\max(\arg_1, \arg_2), \arg_3] = \min \left[\max \left(\frac{\sqrt{k}}{\beta^* \omega y}, \frac{500\nu}{y^2 \omega} \right), \frac{4\rho k}{\sigma_{\omega 2} C D_{k\omega} y^2} \right], \tag{A.40}$$

$$CD_{k\omega} = \max \left(\frac{2\rho}{\sigma_{\omega 2} \omega} \nabla k \nabla \omega, 10^{-20} \right), \tag{A.41}$$

while the model constants for the limits of $k-\omega$ ($F_1 \to 1$) and $k-\varepsilon$ ($F_1 \to 0$) are given as follows:

$$C_{\omega_{11}} = \frac{5}{9},\ C_{\omega_{21}} = \frac{3}{40},\ \sigma_{k\omega_1} = \sigma_{\omega_1} = 2,\ C_{\omega_{12}} = 0.44,\ C_{\omega_{22}} = 0.083,\ \sigma_{k_2} = 1,\ \sigma_{\omega_2} = 1.17. \tag{A.42}$$

The BSL $k-\omega$ model needs further modifications to predict the onset and amount of flow separation from smooth surfaces. It was observed that the shear stress in a boundary layer is proportional to the turbulent kinetic energy (Bradshaw et al., 1967): $-\nabla \cdot (\rho \langle \boldsymbol{v}' \otimes \boldsymbol{v}' \rangle = k a_1$, and the turbulent stress given by the standard two-equation models is (Menter, 1994):

$$\tau = \mu_t \frac{\partial \langle \boldsymbol{v} \rangle}{\partial \tilde{y}} = \mu_t \langle S \rangle = \rho a_1 k \sqrt{\frac{\text{Production}}{\text{Dissipation}}}. \tag{A.43}$$

Standard models overpredict turbulent stress in adverse pressure gradient flows, leading to no or delayed separation. Turbulent stresses can be limited by clipping the turbulent viscosity so that $\mu_t \langle S \rangle \leq \rho a_1 k$. This is the motivation of the $k-\omega$ SST model, which takes the $k-\omega$ BSL model as a reference, and modifies the definition of the turbulent viscosity ($\mu_t = \rho k/\omega$) by the following:

$$\mu_t = \frac{\rho a_1 k}{\max(a_1 \omega, \langle S \rangle F_2)}, \qquad F_2 = \tanh[\max(2\arg_1, \arg_2)^2], \tag{A.44}$$

where $a_1 = 0.31$. The expressions of the arguments of the blending functions (see Fig. A.3) are based on perturbation analyses of the boundary layer (see (Menter, 1994) for general information and (Wilcox, 2006) for all the details):

- $\arg_1$: the equations for k and ω can be simplified in the log-layer by making the same assumptions as in the derivation of the law of the wall. As a result, the turbulence length scale $l_t = \sqrt{k}/(\beta^* \omega) \approx 2.5\tilde{y}$ in the log-layer. This means that $\tanh[(\sqrt{k}/(\beta^* \omega \tilde{y}))^2] \approx \tanh(2.5^2) \to 1$ holds in the log-layer (see Fig. A.3b). In Eq. (A.44), the coefficient equal to 2 acts as safeguard to ensure that $F_2 \to 1$ in the log-layer of all flows.

- $\arg_2$: the differential equations of the viscous sublayer are obtained as a limit $\tilde{y} \to 0$ of the log-layer equations. This expansion yields $\omega \approx 85\nu/\tilde{y}^2$. The coefficient equal to 500 in Eq. (A.40) avoids that $F_2 \to 0$ in the buffer layer.

- $\arg_3$: it ensures that the cross-diffusion term ($k-\varepsilon$ model) is activated in the outer layer to avoid the freestream dependence of the $k-\omega$ model (see Fig. A.3a).

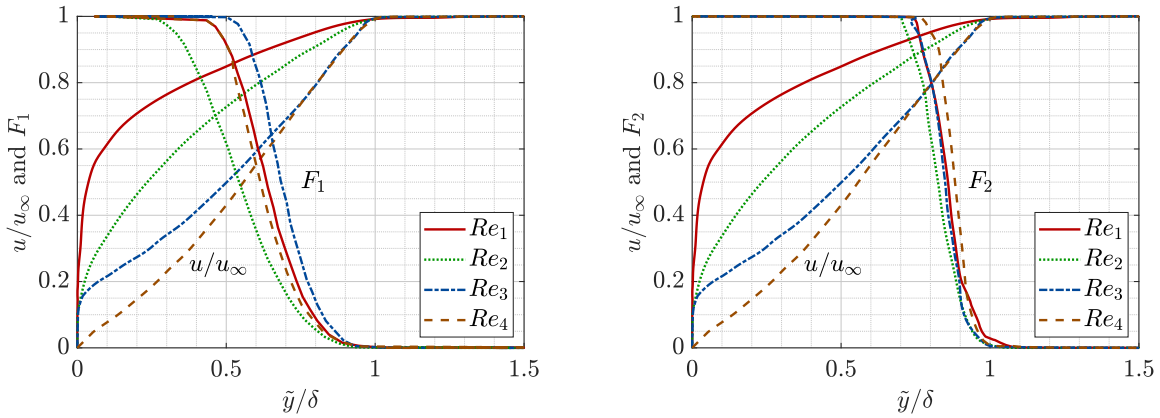

(A) F_1. (B) F_2.

FIGURE A.3: Blending functions of the $k-\omega$ SST model and velocity profiles at different Reynolds numbers, in flows exposed to an adverse pressure gradient. Adapted from (Menter, 1992).

§3.2.1. Near-wall modeling

In wall-bounded flows, the predictions of the turbulent variables in the boundary layer play a crucial role in the accuracy of the RANS models. The Spalart-Allmaras model was designed to provide a correct near-wall behaviour in aeronautical flows. In the most popular two-equation turbulence models, the following expressions hold in the viscous sublayer (Wilcox, 2006):

$$k \sim \tilde{y}^A \quad \text{and} \quad \frac{\beta \tilde{y}^2 \omega}{\nu} \sim B, \tag{A.45}$$

and the wall-parallel velocity in the log-layer is $v_{\parallel}^{+} = \log(\tilde{y}^{+})/\kappa + C^{+}$. The near-wall accuracy is determined by comparison of the constants A, B, and C^{+} with experimental data (see Table A.1).

Parameter	**Experiments**	$\boldsymbol{k-\varepsilon}$	$\boldsymbol{k-\omega}$
A	5 - 5.5	-2.2	5.1
B	2	1.39	3.23
C^{+}	2	0.53	7.20

TABLE A.1: Near-wall behaviour of the two-equation RANS turbulence models (Wilcox, 2006).

None of the models provide correct modeling of the viscous sublayer, and in the $k-\varepsilon$ model there is a large deviation from the log-law. This is critical for the prediction of wall-bounded flows, which means that modifications are required in the boundary layers. Solutions for this problem are the viscous sublayer models—usually named low-Re models—that are referred to the turbulent Reynolds number $Re_t = \nu_t/\nu$. Different formulations have been proposed (Launder and Sharma, 1974; Chien, 1982; Nagano and Tagawa, 1990) that modify the parameters of the equations near the walls. However, they are complex and non-linear formulations that can cause numerical problems, and they overpredict the wall shear stress in stagnation flows. Predictions for adverse pressure gradient flows require additional modifications (Patel et al., 1985), and model constants depend on the flow studied (Rodi and Mansour, 1993). To overcome these issues, V2F models add two additional differential equations to account for the near wall damping (Durbin, 1991), although the numerical stability is reduced, and the complex boundary conditions can lead to large errors (Lien and Kalitzin, 2001). Another alternatives are the two layer formulations, in which a mixing-length model is used for ε near the wall, and in the log-layer a blending is performed with the ε-equation (Rodi, 1991). The two-layer formulations can switch back to the mixing-length model for low Reynolds values outside the boundary layer, which is a source of instability and inconsistency.

Low-Re models have also been developed for the $k-\omega$ models (Peng et al., 1997), even though the accuracy improvement is not noticeable. The $k-\omega$ models have the advantage of providing analytical solutions for the ω values in the viscous sublayer and the logarithmic layer, and the wall function approach can be extended to the $k-\omega$ models (Wilcox, 2006):

$$\omega^+_{\text{sub}} = \frac{6}{C_{\omega_2}(\tilde{y}^+)^2}, \quad \omega^+_{\text{log}} = \frac{1}{\sqrt{\beta^*}\tilde{y}^+}, \tag{A.46}$$

with a blending function similar to that used in the velocity laws (Eq. (A.27)). The boundary condition of the turbulent kinetic energy is $k = 0$. The extension of the momentum boundary layer to the thermal boundary layer can be conducted following the method from (Kader, 1981).

§3.2.2. Laminar-turbulent transition

Multiple improvements have been developed for the two-equation models, namely the consideration of compressibility effects (Deck et al., 2002), buoyancy production (Hanjalić and Kenjereš, 2001), and corrections for flows with strong curvature (Smirnov and Menter, 2009) and wall roughness (Wilcox, 2006). Laminar-turbulent transitional flows are present in many industrial applications, for which specific models have been developed.

There are different types of laminar-turbulent transition, and the most relevant are natural transition (Kachanov and Levchenko, 1984), bypass transition (Jacobs and Durbin, 2001), crossflow transition (Dörr and Kloker, 2017), and separation-induced transition (Jones et al., 2008). The physics of these processes is very complex, and even if there are models that intend to capture them for a general case (Walters and Cokljat, 2008), most models available in the literature are based on correlations that are divided into two families: non-local and local.

The non-local formulations (Abu-Ghannam and Shaw, 1980) were developed first. In these models, the fully laminar boundary layer is solved in a preliminary simulation, and then the freestream turbulence intensity I, the momentum thickness θ, the pressure gradient λ_θ, and the Reynolds number referred to the momentum thickness Re_θ are calculated. By using correlations for the transition momentum thickness Reynolds number $Re_{\theta t} = f(I, \lambda_\theta)$, the point of transition can be determined. This procedure is complex and very difficult to implement efficiently in high-performance computing codes; thus, it is currently used only for specific applications.

The local models were developed to avoid the drawbacks of the non-local models. The most popular model is the $\gamma - Re_{\theta t}$ model (Langtry and Menter, 2009) that introduces two equations for the intermittency γ, which represents the fraction of turbulent flow, and the transition momentum thickness Reynolds number $Re_{\theta t}$, which contains the data from correlations as a function of freestream conditions. The model was built from the concept of vorticity Reynolds number:

$$Re_v = \frac{\rho\tilde{y}^2}{\mu}\left|\frac{\partial \boldsymbol{v}}{\partial \tilde{y}}\right|. \tag{A.47}$$

From studies of the Blasius boundary layer, it was deduced that $(Re_v)_{\max}$ is achieved in the middle of the boundary layer, and that $(Re_v)_{\max} \approx 2.193 Re_\theta$. The use of this approximation avoids the integration process to obtain Re_θ, since $(Re_v)_{\max}$ has an analytical expression that depends on the flow variables. To avoid the calculation of $(Re_v)_{\max}$, the following function is used:

$$F_{\text{onset}} \sim \max\left(\frac{Re_v}{2.193 Re_{\theta t}} - 1, 0\right), \tag{A.48}$$

which becomes active in the zones inside the boundary layer where $Re_\nu/2.193 > Re_{\theta t}$.

The transport equation for the intermittency γ is based on dimensional arguments:

$$\frac{\partial \gamma}{\partial t} + \langle \boldsymbol{v} \rangle \cdot \nabla\gamma = \nabla \cdot \left[\left(\nu + \frac{\nu_t}{\sigma_\gamma}\right)\nabla\gamma\right] + P_{\gamma 1}(1-\gamma) + P_{\gamma 2}(1 - c_{e2}\gamma), \tag{A.49}$$

and contains transition (subindex 1) and destruction/relaminarization (subindex 2) sources:

$$P_{\gamma 1} = 2F_{\text{length}} S\sqrt{\gamma F_{\text{onset}}}, \qquad P_{\gamma 2} = c_{a2}\Omega\gamma F_{\text{turb}}, \tag{A.50}$$

with F_{length} referred to the transition length, Ω to the vorticity rate magnitude, $F_{\text{turb}} = \exp(-\mu_t/\mu)$ to the laminar criterion, and σ_γ, c_{a2} and c_{e2} are model constants (Langtry and Menter, 2009).

The correlations for $Re_{\theta t}$ depend on the freestream conditions. The way to transfer the freestream conditions to the boundary layer is by defining a second transport equation. The concept is to treat $Re_{\theta t}$ as a scalar $\widetilde{Re}_{\theta t}$ that is given by the following equation:

$$\frac{\partial \widetilde{Re}_{\theta t}}{\partial t} + \langle \boldsymbol{v} \rangle \cdot \nabla \widetilde{Re}_{\theta t} = \nabla \cdot \left[\left(\nu + \frac{\nu_t}{\sigma_{\theta t}} \right) \nabla \widetilde{Re}_{\theta t} \right] + \frac{c_{\theta t}}{\tau} (Re_{\theta t} - \widetilde{Re}_{\theta t})(1 - F_{\theta t}), \tag{A.51}$$

where $\tau = 500\nu/(\rho|\boldsymbol{v}|^2)$ is a relaxation time, $F_{\theta t}$ is a blending function such that $F_{\theta t} \to 1$ in laminar boundary layers and $F_{\theta t} \to 0$ in the freestream, and $\sigma_{\theta t}$ and $c_{\theta t}$ are model constants. The reasoning behind the definition of Eq. (A.51) is that first $Re_{\theta t}$ is calculated from correlations; then, the source term of Eq. (A.51) ensures that $\widetilde{Re}_{\theta t} \to Re_{\theta t}$ outside the boundary layer, and, finally, the diffusion term transports that information from the freestream to the boundary layer.

In the separation-induced transition, even if the transition is correctly triggered, the $\gamma - Re_{\theta t}$ model predicts the reattachment location too far downstream. To solve this issue, the model contains a value of the intermittency at separation, γ_{sep}, so that $\gamma \to \gamma_{sep}$ in the separation bubbles. The blending from γ given by the transport equation and γ_{sep} is done with the function $F_{\theta t}$. It should be noted that $\gamma > 1$ in these zones. The coupling with the $k-\omega$ SST model is done through the modification of the source terms in the k-equation. In Eq. (A.37), the production $P_k = \nu_t \langle S \rangle^2$ and dissipation $D_k = \beta^* k\omega$ terms are replaced by γP_k and $\min[\max(\gamma, 0.1), 1]D_k$, respectively.

The $\gamma - Re_{\theta t}$ model has been validated in turbomachinery applications (Langtry et al., 2006), and has been shown to be capable of predicting some of the physics of the laminar-transition in further studies on wing profiles (Dong et al., 2019) and wind turbines (Rezaeiha et al., 2019b; Campobasso et al., 2022). However, since the turbulence intensity used as input for the correlation of $Re_{\theta t}$ depends on the flow velocity, the $\gamma - Re_{\theta t}$ model is not Galilean invariant. The γ model was developed to overcome this limitation and avoid the artificial equation for $\widetilde{Re}_{\theta t}$, consisting of only one transport equation for the intermittency (Menter et al., 2015). The equation is similar to Eq. (A.48), but instead of computing the correlation for $Re_{\theta t}$ outside the boundary layer, it is computed locally inside. For the calculation of the local turbulence intensity, the velocity is substituted by $\omega\tilde{y}$. Further simplifications are made in the recent algebraic model (Menter et al., 2022), which is based on two observations: that the boundary conditions for γ do not have a great impact on the solution, and that the source terms of the equation are dominant. This implies that no additional transport equations are required, so that the algebraic version is reasonable.

§3.3. Reynolds stress models

In the RANS equations (Eqs. (A.29) to (A.31)), the Reynolds stress tensor is an unknown quantity. Turbulent viscosity assumptions offer good predictions in shear flows but have limitations in complex flow interactions; in particular, when the Reynolds stress and strain rate tensor are not aligned, for example in flows with strong curvature or swirl, or impinging jets (Craft et al., 1996). Reynolds stress models (RSM) directly solve the transport equations for each of the components of the Reynolds stress tensor, aiming to capture the effect of anisotropy in the stresses (Pope, 2000). Because of the symmetry of the tensor, there are six independent quantities. It is possible to derive an exact equation for the Reynolds stresses, although higher-order terms are obtained that require modeling. In the same way as in the k-equation, the unsteady and convective terms are exact, and the general form of the equations are as follows:

$$\frac{\partial}{\partial t}(\rho\langle \boldsymbol{v}' \otimes \boldsymbol{v}' \rangle) + \nabla \cdot (\rho\langle \boldsymbol{v} \rangle \langle \boldsymbol{v}' \otimes \boldsymbol{v}' \rangle) = \nabla \cdot \left[\left(\mu + \frac{\mu_t}{\sigma_k} \right) \nabla(\rho\langle \boldsymbol{v}' \otimes \boldsymbol{v}' \rangle) \right] + \mathcal{P} - \mathcal{E} + \Pi \tag{A.52}$$

Unlike in the k-equations of the two-equation models, the production terms $\mathcal{P}$ are exact in Eq. (A.52). The turbulence diffusion term is usually modeled as gradient diffusion, and the turbulent dissipation term $\mathcal{E}$ is approximated by the turbulent dissipation rate. Compared to the equations of the $k-\varepsilon$ and $k-\omega$ models, a new redistribution term appears whose components are:

$$\Pi_{ij} = \left\langle p'\left(\frac{\partial v_i'}{\partial x_j} + \frac{\partial v_j'}{\partial x_i}\right)\right\rangle. \tag{A.53}$$

Equation (A.53) is usually called the *pressure-strain* term, which can be reformulated as two integral terms. The first term only contains fluctuating components, and tends to redistribute turbulence energy between the Reynolds stress components toward isotropy; that is, if there are no other terms, the term results into isotropic turbulence. This term is often formulated in terms of the anisotropy tensor (Pope, 2000):

$$a_{ij} = \frac{\langle v_i' v_j' \rangle}{2k} - \frac{\delta_{ij}}{3}, \tag{A.54}$$

where δ_{ij} are the components of the Kronecker delta. The general form of the second term is:

$$\Pi_{ij}^s = -\rho\varepsilon\left(C_{s1}a_{ij} - \frac{1}{3}C_{s2}\delta_{ij}a_{kl}a_{kl}\right), \tag{A.55}$$

and the most popular models are the Launder-Reece-Rodi, where $C_{s2} = 0$ (Launder et al., 1975), and the Speziale-Sarkar-Gatzki, where $C_{s2} \neq 0$ (Speziale et al., 1991). The second term depends also on the mean flow velocity gradients and is often modeled as proportional to the production term $\mathcal{P}$ and the anisotropy tensor. Reynolds stress models provide better accuracy in swirling flows, flows with rotating systems, or flows with sudden changes in the mean strain rate. Nevertheless, they are computationally more expensive and less robust and are not as widely validated as the two-equation models. In addition, the accuracy is as low as the one of the two-equation models in certain particular cases such as axisymmetric jets (Launder and Morse, 1979).

§4. Detached Eddy Simulation

A reference hybrid RANS/LES model is the Detached Eddy Simulation (DES) model, which was initially applied to the Spalart-Allmaras model (Spalart et al., 1997), and was later extended to two-equation models (Strelets, 2001). The two-equation DES model introduces the grid spacing $\Delta = \max(\Delta_x, \Delta_y, \Delta_z)$ in the dissipation term of the k-equation (Eq. (A.37)):

$$\frac{\partial k}{\partial t} + \langle \boldsymbol{v} \rangle \cdot \nabla k = \nabla \cdot \left[\left(\nu + \frac{\nu_t}{\tilde{\sigma}_{k\omega}}\right)\nabla k\right] + \nu_t |\langle S \rangle|^2 - \frac{k^{3/2}}{\min(l_t, C_{\mathrm{DES}}\Delta)}, \tag{A.56}$$

where Δ_i is the grid spacing in the i-direction, the constant $C_{\mathrm{DES}} = 0.61$, and $l_t = \sqrt{k}/(\beta^*\omega)$ is the turbulence length scale. The model switches to LES if $l_t > C_{\mathrm{DES}}\Delta$; therefore, it reduces to a RANS model in coarse meshes and to LES in fine meshes. However, for intermediate conditions, the transition from RANS to LES can happen without control.

If the original mesh satisfies $l_t < C_{\mathrm{DES}}\Delta$, then the model stays in RANS (see Fig. A.4a). If the mesh is refined so that $l_t > C_{\mathrm{DES}}\Delta$ in some regions of the boundary layer, then the model switches to LES. Since l_t reaches its maximum value in the middle of the boundary layer (Menter, 2018), a real situation can be the one shown in Fig. A.4b, where δ is the thickness of the boundary layer. This is a stable flow because there is no phenomenon that triggers an instability, so no vortex structures are generated, leading to early separation, especially in flows exposed to an adverse pressure gradient. This numerical behavior is called *grid-induced separation* (GIS) (Spalart et al., 2006). If the mesh is further refined, the switching of the model from RANS to LES formulations occurs closer to the wall; that is, the width of the LES zone is extended, while there is no certainty

that the mesh is fine enough for an accurate LES simulation. Thus, in DES, mesh refinement does not guarantee a more accurate prediction.

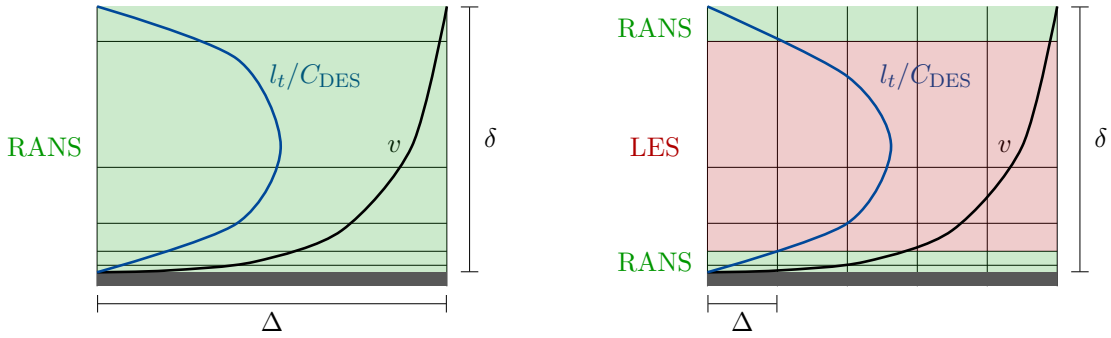

(A) Coarse mesh. (B) Fine mesh.

FIGURE A.4: Schematic of the grid-induced separation in DES.

An improvement of DES called Delayed-DES (DDES) was published later (Spalart et al., 2006). It introduces a shielding function f_{DDES} so that the dissipation term of the k-equation becomes:

$$\frac{k^{3/2}}{\min[l_t(1-f_{\mathrm{DDES}}), C_{\mathrm{DES}}\Delta]}. \tag{A.57}$$

While in DES the effect of GIS is noticeable from $\Delta \approx \delta$, in DDES it is reduced to $\Delta \approx 0.25\delta$ (Menter, 2018). However, the impact is much more drastic than in DES, since for $\Delta < 0.25\delta$ small changes in the mesh size produce significant variations in the solution. As a consequence, DES/D-DES can provide less accurate solutions than RANS (Browne et al., 2023). Another important aspect of DED/DDES is that the transition from RANS to LES takes place in a distance whose size is not negligible; in particular, in DDES it has been shown to be around 0.3δ on a flat plate (Gritskevich et al., 2012). This is called *gray area* in the literature.

Variants of the DDES model have been proposed using the functions of the $k-\omega$ SST model (Menter and Kuntz, 2004), that reduce the GIS down to $\Delta \approx 0.1\delta$, but the gray areas are not eliminated. More elaborated formulations involve the use of complex functions that depend on flow variables that act as sensors (Deck and Renard, 2020). The model cited solves the problem of gray areas, although the GIS is not addressed. Moreover, it includes multiple additional adjusting constants, and it has not been verified that the values proposed are universal. The Improved-DDES (IDDES) model is a modification of DES developed with the capability to run in WMLES mode (Shur et al., 2008), but with limited shielding against GIS. For meshes that are not suitable for WMLES, the accuracy of DDES and IDDES is similar (Schwamborn and Strelets, 2012), and recent studies have shown that IDDES does not solve completely the LLM (Han et al., 2020).

Appendix B

Finite volume method

One of the classical numerical approaches to solve the Navier-Stokes equations is the finite volume method, in which the computational domain is divided into a mesh consisting of a finite number of control volumes, also called cells (Ferzinger et al., 2020). The discretization methods explained in §1 reduce the Navier-Stokes equations to a system of linear algebraic equations that is solved by iteration. Different methodologies can be followed in the iterative process, which are discussed in §2. Finally, methods to solve the systems of linear algebraic equations are presented in §3.

§1. Discretization

In each cell, the Navier-Stokes equations are solved in integral form (Batchelor, 2000):

$$\begin{cases} \displaystyle\int_{S_c} \boldsymbol{v}\cdot\boldsymbol{n}\ \mathrm{d}\mathcal{S} = 0 & \text{(B.1)} \\ \displaystyle\frac{\mathrm{d}}{\mathrm{d}t}\int_{V_c}\boldsymbol{v}\ \mathrm{d}\mathcal{V} + \int_{S_c}\boldsymbol{v}(\boldsymbol{v}\cdot\boldsymbol{n})\ \mathrm{d}\mathcal{S} = -\frac{1}{\rho}\int_{S_c} p\boldsymbol{n}\ \mathrm{d}\mathcal{S} + \nu\int_{S_c}\nabla\boldsymbol{v}\cdot\boldsymbol{n}\ \mathrm{d}\mathcal{S} + \int_{V_c}\boldsymbol{M}\ \mathrm{d}\mathcal{V} & \text{(B.2)} \\ \displaystyle\frac{\mathrm{d}}{\mathrm{d}t}\int_{V_c}\left(e+\frac{1}{2}|\boldsymbol{v}|^2\right)\mathrm{d}\mathcal{V} + \int_{S_c}\left(e+\frac{1}{2}|\boldsymbol{v}|^2\right)(\boldsymbol{v}\cdot\boldsymbol{n})\ \mathrm{d}\mathcal{S} = \\ \displaystyle= -\frac{1}{\rho}\int_{S_c}(p\boldsymbol{n})\cdot\boldsymbol{v}\ \mathrm{d}\mathcal{S} + \nu\int_{S_c}\nabla\boldsymbol{v}\cdot\boldsymbol{n}\ \mathrm{d}\mathcal{S} + \alpha\int_{S_c}\nabla T\cdot\boldsymbol{n}\ \mathrm{d}\mathcal{S} + \int_{V_c} Q\ \mathrm{d}\mathcal{V}, & \text{(B.3)} \end{cases}$$

where V_c and S_c are the cell volumes and surfaces, respectively, e is the specific internal energy, $\boldsymbol{M}$ is the momentum source, and Q is the heat generation source. Spatial and temporal discretization schemes explained in §1.1 and §1.2 are needed to solve Eqs. (B.1) to (B.3), and the treatment of the non-linear terms is discussed in §1.3. Some combinations of spatial discretization schemes lead to oscillations, and a popular method to improve stability is discussed in §1.4.

§1.1. Spatial discretization

Flow variables are linear in space around a point P to obtain a second-order method:

$$\Phi(\boldsymbol{x}) = \Phi_P + (\boldsymbol{x}-\boldsymbol{x}_P)(\nabla\Phi)_P, \tag{B.4}$$

and the values are stored in cell centroids. The volume integrals are computed directly as the cell centroid value multiplied by the cell volume:

$$\int_{V_c}\Phi\ \mathrm{d}\mathcal{V} = \int_{V_c}[\Phi_P + (\boldsymbol{x}-\boldsymbol{x}_P)(\nabla\Phi)_P]\ \mathrm{d}\mathcal{V} = \Phi_P\int_{V_c}\mathrm{d}\mathcal{V} + (\nabla\Phi)_P\int_{V_c}(\boldsymbol{x}-\boldsymbol{x}_P)\ \mathrm{d}\mathcal{V} = \Phi_P V_c, \tag{B.5}$$

where the integral of the second term of Eq. (B.5) vanishes from the definition of cell centroid.

The surface integrals (fluxes) are equal to the sum of the fluxes over the faces of the cell:

$$\int_{S_c}(\Phi\cdot\boldsymbol{n})\ \mathrm{d}\mathcal{S} = \int_{S_c}\Phi_f\ \mathrm{d}\mathcal{S} = \sum_k\int_{S_{c_k}}\Phi_{f_k}\ \mathrm{d}\mathcal{S}. \tag{B.6}$$

Interpolation schemes exposed in §1.1.1 allow the definition of the values of the flow variables at the cell faces. In addition, since the Eqs. (B.1) to (B.3) involve terms that include the first derivatives, different procedures for calculating the gradients are presented in §1.1.2.

§1.1.1. Interpolation schemes

The most used interpolation schemes are four: first-order upwind, second-order upwind, central differencing, and hybrids between the central differencing and the first-order upwind.

First-order upwind

A flow variable Φ in the face e (see Fig. B.1) is approximated as follows:

$$\Phi_e^{1\mathrm{U}} = \begin{cases} \Phi_P & \text{if } (\boldsymbol{v}\cdot\boldsymbol{n})_e > 0 \\ \Phi_E & \text{if } (\boldsymbol{v}\cdot\boldsymbol{n})_e < 0. \end{cases} \tag{B.7}$$

Looking at the Taylor series expansion of Eq. (B.4), it is deduced that Eq. (B.7) is first-order accurate, and that the leading truncation error $\epsilon = (\Delta_x/2)(\nabla\Phi)_e$ term is a diffusive flux. Further numerical diffusion is added in two- and three-dimensional cases when the mesh grid is not aligned with the flow direction (de Vahl Davis and Mallinson, 1976).

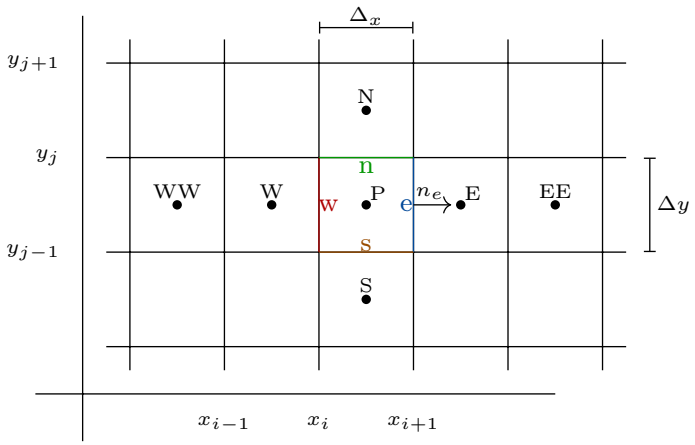

FIGURE B.1: Notation used in control volumes of a two-dimensional mesh

Second-order upwind

The second order approximation is obtained using a multidimensional linear reconstruction approach (Barth and Jespersen, 1989):

$$\Phi_e^{2\mathrm{U}} = \begin{cases} \Phi_P + \psi(\nabla\Phi)_P\cdot(\boldsymbol{x}_e - \boldsymbol{x}_P) & \text{if } (\boldsymbol{v}\cdot\boldsymbol{n})_e > 0 \\ \Phi_E + \psi(\nabla\Phi)_E\cdot(\boldsymbol{x}_e - \boldsymbol{x}_P) & \text{if } (\boldsymbol{v}\cdot\boldsymbol{n})_e < 0, \end{cases} \tag{B.8}$$

where ψ is the gradient limiter, which ensures that the face value does not exceed the minimum and maximum values of neighboring cells. This scheme is less diffusive than the first-order approximation (Liu, 2011), but at the expense of decreasing stability (Ferzinger et al., 2020).

Central differencing

The central differencing scheme uses the values of the variables in the two nearest cell centroids:

$$\Phi_e^{\mathrm{CD}} = \frac{1}{2}(\Phi_E + \Phi_P) + \frac{1}{2}[(\nabla\Phi)_E\cdot(\boldsymbol{x}_E - \boldsymbol{x}_e) + (\nabla\Phi)_P\cdot(\boldsymbol{x}_P - \boldsymbol{x}_e)]. \tag{B.9}$$

The standard definition given in the classical books (Patankar, 1980; Ferzinger et al., 2020) considers only the first term on the right-hand side of Eq. (B.9). However, this scheme provides second-order accuracy only if the grid is uniform (Ferzinger et al., 2020). The addition of the gradient term ensures second-order accuracy in all mesh configurations. In both cases no numerical diffusion is added to the equations, although the stability of the simulations is compromised

when using this scheme in the convective terms. This can be verified by studying the steady one-dimensional convection-diffusion equation coupled to the continuity equation:

$$\begin{cases} \displaystyle\int_{S_c} \boldsymbol{v}\cdot\boldsymbol{n}\ \mathrm{d}\mathcal{S} = 0 & \text{(B.10)} \\ \displaystyle\int_{S_c} \Phi(\boldsymbol{v}\cdot\boldsymbol{n})\ \mathrm{d}\mathcal{S} = D\int_{S_c} \nabla\boldsymbol{\Phi}\cdot\boldsymbol{n}\ \mathrm{d}\mathcal{S}. & \text{(B.11)} \end{cases}$$

The integration of Eq. (B.11) in the control volume of Fig. B.1 for $(\boldsymbol{v}\cdot\boldsymbol{n})_e > 0$ gives:

$$(u\Phi)_e - (u\Phi)_w = D\left(\left.\frac{\mathrm{d}\Phi}{\mathrm{d}x}\right|_e - \left.\frac{\mathrm{d}\Phi}{\mathrm{d}x}\right|_w \right). \tag{B.12}$$

The following discretized equation is obtained when approximating the convection and diffusion fluxes with the standard central differencing scheme:

$$\frac{1}{2}u_e(\Phi_E + \Phi_P) - \frac{1}{2}u_w(\Phi_P + \Phi_W) = \frac{D(\Phi_E - \Phi_P)}{\Delta_x} - \frac{D(\Phi_P - \Phi_W)}{\Delta_x}, \tag{B.13}$$

and Eq. (B.10) is equivalent to $u_e = u_w = u_\infty$. Using this condition in Eq. (B.13) leads to:

$$\frac{2D}{\Delta_x}\Phi_P = \left(\frac{D}{\Delta_x} - \frac{u_\infty}{2}\right)\Phi_E + \left(\frac{D}{\Delta_x} + \frac{u_\infty}{2}\right)\Phi_W. \tag{B.14}$$

In Eq. (B.14), the coefficient of Φ_E is lower than zero when $u_\infty > 2D/\Delta_x$. As will be seen later, if that condition is met, the convergence of Eq. (B.14) is not ensured when using an iterative method for solving systems of algebraic equations. The increase of the value of a variable in a neighbourhood implies the decrease of the variable in the reference cell, which does not have physical meaning. The convergence condition is usually expressed in terms of the Péclet number $Pe = u\Delta_x/D$, so that the central differencing scheme in the convective term provides a stable solution for $Pe < 2$. In iterative methods, this limitation can be alleviated by using the deferred correction approach, in which the explicit terms (from the previous iteration) are part of the source terms of the discretized equations (Ferzinger et al., 2020):

$$\Phi_e^{\mathrm{CD,D}} = \underbrace{\Phi_e^{\mathrm{1U}}}_{\text{Implicit}} + \underbrace{(\Phi_e^{\mathrm{CD}} - \Phi_e^{\mathrm{1U}})}_{\text{Explicit}}. \tag{B.15}$$

Hybrid

It has been shown that the first-order upwind scheme adds numerical diffusion, while the central differencing scheme is not unconditionally stable, and the second-order upwind stays between these two in terms of stability and numerical diffusion. The deficiencies of these schemes can be solved by using hybrid discretizations. Different formulations have been developed using second-order upwind and central differencing, namely the Quadratic Upstream Interpolation for Convective Kinematics (QUICK) (Leonard, 1979) scheme, although numerical stability is guaranteed in none of these schemes. This is a consequence of the Godunov's theorem, which states that the linear schemes that ensure the monotonicity of the solution can be at most first-order accurate (Godunov and Bohachevsky, 1959). Thus, the most popular schemes are based on the combination of the first-order upwind and the central differencing. One of the first proposals consisted of using the stability condition of the central differencing scheme (Spalding, 1972). In the case $(\boldsymbol{v}\cdot\boldsymbol{n})_e > 0$:

$$\Phi_e = \begin{cases} \left[\left(1 + \dfrac{2}{Pe_e}\right)\dfrac{\Phi_P}{2} + \left(1 - \dfrac{2}{Pe_e}\right)\dfrac{\Phi_E}{2}\right] & \text{if } Pe < 2 \\ \Phi_P & \text{if } Pe \geq 2, \end{cases} \tag{B.16}$$

although multiple stable simulations have been obtained for $Pe \gg 1$ in entire domains (Yu et al., 2001); therefore, the condition $Pe < 2$ is restrictive in practical applications.

More elaborated models use the concept of Total Variation (TV), which is an important parameter in the proofs of theorems related to the convergence of differencing schemes (Harten, 1983):

$$TV(\Phi^n) = \sum_f (\Phi_E^n - \Phi_P^n), \tag{B.17}$$

where E and P are the points around the face f, and the superindex n refers to the time step. The Total Variation Diminishing schemes (TVD) satisfy the following condition at every time step:

$$TV(\Phi^{n+1}) \leq TV(\Phi^n), \tag{B.18}$$

and is applied to the combination of the first-order upwind the central differencing schemes (Sweby, 1984):

$$\Phi_e = \Phi^{1\mathrm{U}} + \Psi(\Phi^{\mathrm{CD}} - \Phi^{1\mathrm{UD}}), \tag{B.19}$$

where $\Psi = \Psi(r)$ for $r = (\Phi_P - \Phi_W)/(\Phi_E - \Phi_P)$ based on the notation of Fig. B.1.

Controlling the numerical diffusion in the TVD schemes is a challenge. Depending on the problem, these schemes can provide either excessive or negative diffusion. The latter is an important problem, since oscillations can be produced in smooth solutions (Leonard, 1991).

Another type of hybrid discretizations use the Convection Boundedness Criterion (CBC) (Gaskell and Lau, 1988). It is obtained from the Normalized Variable Diagram (NVD) (Leonard, 1988), in which normalized variables are defined as follows:

$$\hat{\Phi} = \frac{\Phi - \Phi_W}{\Phi_E - \Phi_W}. \tag{B.20}$$

Equation (B.20) was extended to unstructured meshes (Jasak et al., 1999):

$$\hat{\Phi} = 1 - (\nabla\Phi)_e \cdot \frac{(\Phi_E - \Phi_P)|\boldsymbol{x}_p - \boldsymbol{x}_E|}{\boldsymbol{x}_p - \boldsymbol{x}_E}. \tag{B.21}$$

To avoid non-physical oscillations in the solution, the principal condition of the CBC is that the cell values are bounded by those of the neighbors. In terms of the function $\hat{\Phi}_e = f(\hat{\Phi}_P) \in C^0(\mathbb{R})$, the set of conditions of the CBC are (Gaskell and Lau, 1988):

$$\hat{\Phi}_e = \begin{cases} 0 & \text{if } \hat{\Phi}_P = 0 \quad \text{(B.22)} \\ 1 & \text{if } \hat{\Phi}_P = 1 \quad \text{(B.23)} \\ < 1 \text{ and } > \hat{\Phi}_P & \text{if } 0 < \hat{\Phi}_P < 1 \quad \text{(B.24)} \\ \hat{\Phi}_P & \text{if } \hat{\Phi}_P < 0 \text{ or } \hat{\Phi}_P > 1. \quad \text{(B.25)} \end{cases}$$

The CBC conditions are sufficient to deduce that a convective differencing scheme is bounded (convective boundedness), although later work has shown that only Eqs. (B.22) and (B.23) are necessary conditions, and Eqs. (B.24) and (B.25) can be relaxed (Yu et al., 2001).

Other hybrid models such as the Gamma Differencing Scheme (Jasak et al., 1999) use the CBC to blend the first-order upwind and central differencing schemes:

$$\hat{\Phi}_e^{\gamma\mathrm{D}} = \begin{cases} -\dfrac{\hat{\Phi}_P^2}{2\beta_m} + \left(1 + \dfrac{1}{2\beta_m}\right)\hat{\Phi}_P & \text{if } 0 < \hat{\Phi}_P < \beta_m \quad \text{(B.26)} \\ \dfrac{1}{2} + \dfrac{1}{2}\hat{\Phi}_P & \text{if } \beta_m \leq \hat{\Phi}_P \leq 1 \quad \text{(B.27)} \\ \hat{\Phi}_P & \text{if } \hat{\Phi}_P \leq 0 \text{ or } \hat{\Phi}_P \geq 1. \quad \text{(B.28)} \end{cases}$$

In the Gamma Diffrencing Scheme, the transition from one scheme to another depends on the value of the constant β_m (see Fig. B.2). The stability of the simulations is improved when β_m is increased, although at the expense of the decrease in resolution. For accuracy reasons, it is

recommended that $\beta_m \leq 1/2$, while it has been deduced that $\beta_m \geq 1/10$ to avoid instabilities; consequently, the optimal range is $1/10 \leq \beta_m \leq 1/2$. The amount of numerical diffusion added by the hybrid schemes is difficult to quantify; thus, the numerical settings should be adapted to use central differencing whenever possible.

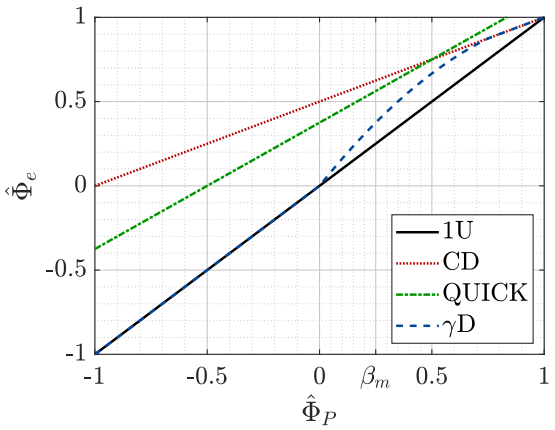

FIGURE B.2: Normalized Variable Diagram (NVD) of popular spatial discretization schemes in finite volume methods.

§1.1.2. Calculation of gradients

Gradients are required for constructing the flow variables at cell centers (see Eqs. (B.8) and (B.9)) and cell faces (see Eqs. (B.2) and (B.3)). The classical models use the Stokes' theorem to calculate the gradient of a scalar in a cell:

$$(\nabla\Phi)_P = \frac{1}{V_c}\sum_f \Phi_f \boldsymbol{n}_f, \tag{B.29}$$

and the face value is usually calculated with one of the following methods:

$$\Phi_f = \begin{cases} (\nabla\Phi)_P \dfrac{|\boldsymbol{x}_e - \boldsymbol{x}_P|}{|\boldsymbol{x}_P - \boldsymbol{x}_E|} + (\nabla\Phi)_e \left(1 - \dfrac{|\boldsymbol{x}_e - \boldsymbol{x}_P|}{|\boldsymbol{x}_P - \boldsymbol{x}_E|}\right) & \text{Cell-based approach} \quad \text{(B.30)} \\ \dfrac{1}{n_f}\displaystyle\sum_n^{n_f} \Phi_n & \text{Node-based approach.} \quad \text{(B.31)} \end{cases}$$

In the cell-based calculation, the face values are obtained at the intersection of the vector joining the centroids with the face. This point differs from the center of the face in skewed cells, leading to the *skewness error* (see Fig. B.3). In the node-based approach, Φ_n refers to the nodal value, and n_f is the number of nodes of a face. The nodal values are constructed from the weighted average of the cell values surrounding the nodes (Holmes and Connell, 1989), leading to higher accuracy, although at the expense of the increase in computational cost.

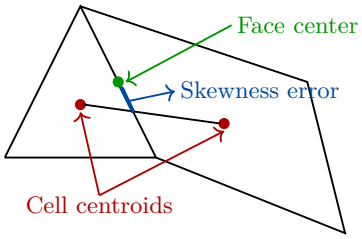

FIGURE B.3: Skewness error of the cell-based approach for gradient calculation.

An alternative method with a similar accuracy to the node-based approach presented before is the least-squares cell-based method (Syrakos et al., 2017). Assuming that the solution varies linearly, in each cell (c_0), the gradient is given by the following expression:

$$(\nabla\Phi)_{c_0} \cdot (\boldsymbol{x}_{c_i} - \boldsymbol{x}_{c_0}) = \Phi_{c_i} - \Phi_{c_0}, \tag{B.32}$$

where c_i is a cell that surrounds the cell c_0. Equation (B.32) applied to all cells and the corresponding neighbors leads to a system of linear algebraic equations. This system, which is over-determined, is solved using the Gram-Schmidt process (Anderson and Bonhaus, 1994).

§1.2. Temporal discretization

After discretizing Eqs. (B.2) and (B.3), the following general form is obtained:

$$\frac{\mathrm{d}\Phi}{\mathrm{d}t} = F(t, \Phi). \tag{B.33}$$

Explicit methods are not frequently used in the finite volume method, especially when second order spatial discretization methods are applied. This is because the resulting numerical scheme inherits the stability limitations of both the spatial and the temporal discretizations. The most popular schemes are three: the Euler implicit, the Crank-Nicholson, and the second-order implicit. For each cell centroid P and time n, Eq. (B.33) is discretized with a time step Δt as follows:

$$\Phi_f = \begin{cases} \dfrac{\Phi_P^{n+1} - \Phi_P^n}{\Delta t} = F(t, \Phi_P^{n+1}, \Phi_{NB}^{n+1}) & \text{Euler implicit} \quad \text{(B.34)} \\ \dfrac{\Phi_P^{n+1} - \Phi_P^n}{\Delta t} = \dfrac{1}{2}\left[F(t, \Phi_P^{n+1}, \Phi_{NB}^{n+1}) + F(t, \Phi_P^n, \Phi_{NB}^n)\right] & \text{Crank Nicholson} \quad \text{(B.35)} \\ \dfrac{3\Phi_P^{n+1} - 4\Phi_P^n + \Phi_P^{n-1}}{\Delta t} = 2F(t, \Phi_P^{n+1}, \Phi_{NB}^{n+1}) & \text{Second-order implicit,} \quad \text{(B.36)} \end{cases}$$

where subindex NB refers to the neighbour cell centroids. The Euler implicit and the second-order implicit are the first- and second-order backward differentiation formulas (BDF), respectively. Two are the main factors that determine the choice of the scheme: the accuracy and the stability.

The accuracy of the method is given by the order of the truncation error. The Euler implicit method is first-order accurate, while the Crank-Nicholson and the second-order implicit methods are second-order accurate. However, the truncation error of the Crank-Nicholson scheme is four times smaller than the one of the second-order implicit (Ferzinger et al., 2020).

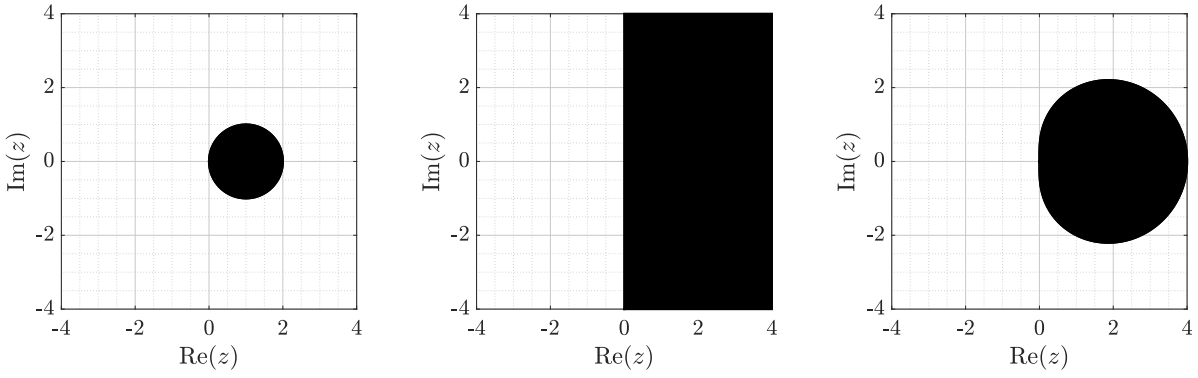

(A) Euler implicit (B) Crank-Nicholson (C) Second-order implicit

FIGURE B.4: Non-stable regions of time-discretization methods used in the finite volume method.

The stability of a temporal integration method is determined by studying the stability region. First, the discretized expression of the scheme is substituted into a simplified ordinary differential equation: $\mathrm{d}\Phi/\mathrm{d}t = \lambda\Phi$ (Butcher, 2016); then, the stability function is represented in terms of the

complex numbers $S(z) = S(\lambda\Delta t) = \Phi^{n+1}/\Phi^n$, and the stability region is $\mathcal{S} = \{z \in \mathbb{C} : |S(z)| \leq 1\}$ (Wanner and Hairer, 1996). The unstable regions of the schemes mentioned are shown in Fig. B.4.

An important concept related to the stability region of temporal discretization schemes is the A-stability. A scheme is said to be *A-stable* if the stability domain satisfies $\mathrm{Re}(z) \leq 0$. It can be verified in Fig. B.4 that all three schemes are A-stable. The definition is closely related to the fact that the eigenvalues of stable solutions satisfy the condition $\mathrm{Re}(z) \leq 0$. Similar to the Godunov's theorem about the monotonicity of spatial discretization schemes, the Dalquist theorem states that backward difference schemes of higher order than two are not A-stable (Wanner and Hairer, 1996). This limits the temporal discretization of finite-volume schemes to second order. A stronger concept of stability is the L-stability. A scheme is said to be *L-stable* if it is A-stable and $S(z) \to 0$ when $z \to \infty$. The first and second order BDF are L-stable, while the Crank-Nicholson is not (Jameson, 2022). Thus, even if the truncation error is higher, BDF are the preferred choise because they are more stable than the Crank-Nicholson scheme. This can be expected, since the non-stable region of the Crank-Nicholson scheme is unbounded (see Fig. B.4c). In addition, since the flow variables from neighbour cells of the previous time steps are used in the formulation (see Eq. (B.35)), the Crank-Nicholson scheme is not suitable for dynamic meshes.

§1.3. Non-linear terms

The objective of spatial and temporal discretization is to obtain a linear system of algebraic equations. However, the convective terms of Eqs. (B.2) and (B.3) and the unsteady term of Eq. (B.3), and possibly the source terms M and Q of these equations, are not linear. When iterative methods such as those explained in §2 are used, the solution is based on using a mixed explicit-implicit form, usually called *Picard iteration* (Ferzinger et al., 2020). In the case of the convective term:

$$\boldsymbol{v}^{m+1}(\boldsymbol{v}^{m+1} \cdot \boldsymbol{n}) \approx \underbrace{\boldsymbol{v}^{m}}_{\text{Explicit}} \underbrace{(\boldsymbol{v}^{m+1} \cdot \boldsymbol{n})}_{\text{Implicit}} \tag{B.37}$$

where m refers to the iteration number. The same reasoning applies to other nonlinear terms. Provided that the iterative method converges, the approximation does not give any error.

§1.4. Rhie-Chow interpolation

Except for the convection terms, whose discretization depends on the goals of the simulation, the rest of the terms of the Navier-Stokes equations are usually discretized with central differences. This is done to achieve second-order accuracy without the addition of numerical diffusion. However, the use of central differences in the pressure terms without additional corrections leads to numerical instabilities. To show this, Eq. (B.2) is considered in the x-direction of Fig. B.1:

$$A_P v_P = \sum_{NB} A_{NB} v_{NB} - \nabla p, \tag{B.38}$$

and the velocity at the cell center is:

$$v_P = \frac{1}{A_p}(\sum_{NB} A_{NB} v_{NB} - \nabla p) = \tilde{v}_P - d_P \frac{\mathrm{d}p}{\mathrm{d}x}\bigg|_P . \tag{B.39}$$

The continuity equation is simply $v_e = v_w$. The discretization of the face velocities with the standard central differences and the use of Eq. (B.39) lead to:

$$v_E = v_W \longrightarrow \tilde{v}_E - d_E \frac{\mathrm{d}p}{\mathrm{d}x}\bigg|_E = \tilde{v}_W - d_W \frac{\mathrm{d}p}{\mathrm{d}x}\bigg|_W . \tag{B.40}$$

Finally, the use of standard central differences in the pressure gradient term (see Fig. B.1) gives the final form of the discretized continuity equation at the cell center P:

$$\tilde{v}_E - d_E \frac{p_{EE} - p_P}{\Delta_x} = \tilde{v}_W - d_W \frac{p_P - p_{WW}}{\Delta_x}. \tag{B.41}$$

In Eq. (B.41), the pressure at the cell center does not depend on the values of the neighboring cell. The same reasoning in two dimensions leads to the same conclusion, since the equations are linear (Ferzinger et al., 2020). Thus, there are two independent solutions of the pressure field. Both satisfy the discretized momentum equation, but non-physical oscillations can appear in the pressure. This numerical behavior is called *checkerboard oscillations*, since the pressure field looks like a checkerboard, with each of the colors representing a smooth solution of the pressure gradient.

Checkerboard oscillations do not appear when an upwind scheme is used for the pressure, although this approach leads to the addition of numerical diffusion. An alternative is to use a *staggered grid* (Ferzinger et al., 2020), in which not all of the flow variables are stored at cell centers; in particular, the velocity components are stored at cell faces. However, staggered grids have multiple limitations such as the requirement of using cells with zero skewness and cartesian meshes for accuracy reasons, which are limiting factors in complex geometries.

The idea of the staggered grids of solving momentum equations at cell faces can be used to derive a correction for the central differencing scheme used in the continuity equation (Rhie and Chow, 1983; Bartholomew et al., 2018). The face velocity reads:

$$v_e = v_e^{\mathrm{CD}} + F, \tag{B.42}$$

where $F = F(\nabla p)$ is a correction. The starting point for its derivation are the momentum equations in the P and E cells, as well as in the e face, obtained from Eq. (B.39):

$$\begin{cases} v_P = \tilde{v}_P - d_P \left.\dfrac{\mathrm{d}p}{\mathrm{d}x}\right|_P & \text{(B.43)} \\ v_E = \tilde{v}_E - d_E \left.\dfrac{\mathrm{d}p}{\mathrm{d}x}\right|_E & \text{(B.44)} \\ v_e = \tilde{v}_e - d_e \left.\dfrac{\mathrm{d}p}{\mathrm{d}x}\right|_e . & \text{(B.45)} \end{cases}$$

The key of the procedure is to interpolate the value of $\tilde{v}_e$ with the central differencing scheme $\tilde{v}_e = (\tilde{v}_E + \tilde{v}_P)/2$. Thus, taking Eqs. (B.43) and (B.44) into account, Eq. (B.45) becomes:

$$\tilde{v}_e = \frac{1}{2}\left[v_P + d_P \left.\frac{\mathrm{d}p}{\mathrm{d}x}\right|_P + v_E + d_E \left.\frac{\mathrm{d}p}{\mathrm{d}x}\right|_E \right] = v_e^{\mathrm{CD}} + \frac{1}{2}\left[d_P \left.\frac{\mathrm{d}p}{\mathrm{d}x}\right|_P + d_E \left.\frac{\mathrm{d}p}{\mathrm{d}x}\right|_E \right]. \tag{B.46}$$

The last term of Eq. (B.46) is the pressure gradient of a central differencing scheme:

$$\tilde{v}_e = v_e^{\mathrm{CD}} + d \left.\frac{\mathrm{d}p}{\mathrm{d}x}\right|_e^{\mathrm{CD}}, \tag{B.47}$$

and Eq. (B.47) can be substituted into Eq. (B.45) to give:

$$v_e = v_e^{\mathrm{CD}} - \left(d_e \left.\frac{\mathrm{d}p}{\mathrm{d}x}\right|_e - d \left.\frac{\mathrm{d}p}{\mathrm{d}x}\right|_e^{\mathrm{CD}} \right) \approx v_e^{\mathrm{CD}} - d_e^{\mathrm{CD}} \left(\left.\frac{\mathrm{d}p}{\mathrm{d}x}\right|_e - \left.\frac{\mathrm{d}p}{\mathrm{d}x}\right|_e^{\mathrm{CD}} \right). \tag{B.48}$$

The last term of Eq. (B.48) is the correction that is applied to the central differencing scheme for the velocity in the momentum equation. In each face, $\mathrm{d}p/\mathrm{d}x|_e^{\mathrm{CD}}$ is the gradient of one of the two solutions of the problem, which does not depend on the neighbour cells. In contrast, the term $\mathrm{d}p/\mathrm{d}x|_e = (p_E - p_P)/\Delta_x$ depends on the pressure value at the neighbour cell. When the checkerboard oscillations occur, the correction term of Eq. (B.48) activates and smooths out the pressure field. When convergence is achieved, the oscillations disappear and the correction vanishes.

§2. Pressure-velocity coupling

For a general scalar transport equation, in each cell, the discretization methods explained in §1.1 and §1.2 lead to a system of linear algebraic equations:

$$\mathcal{A}_P \Phi_P = \sum_{NB} \mathcal{A}_{NB} \Phi_{NB} + b_P \tag{B.49}$$

that is solved with one of the methods explained in §3. The use of Picard iterations implies that the equations need to be solved iteratively. There are two main approaches that differ on how the momentum and continuity equations are solved: the segregated solvers (§2.1), where the momentum and the pressure correction equations—which is equivalent to the continuity equation—are solved separately, and the coupled solvers (§2.2), which solve both equations in a single step (see Fig. B.5). The basics for the extension of the algorithms to compressible flows are mentioned in §2.3.

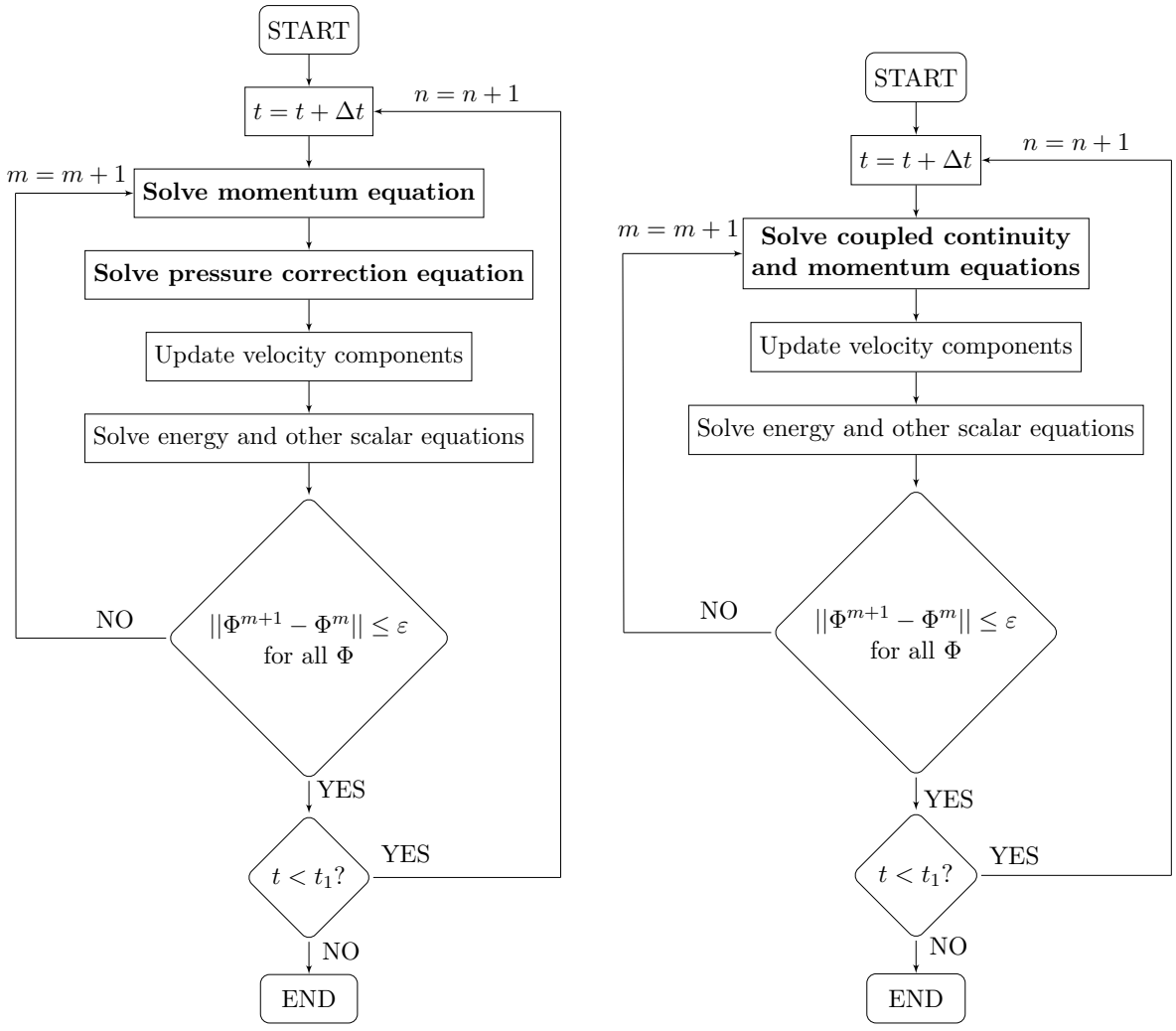

(A) Segregated solvers (B) Coupled solver

FIGURE B.5: Solution methods for the incompressible Navier-Stokes equations

§2.1. Segregated algorithms

In each iteration, the discretized continuity and momentum equations in matrix form are:

$$\begin{cases} \boldsymbol{\mathcal{C}}^m \boldsymbol{v}^{m+1} = 0 & \text{(B.50)} \\ (\boldsymbol{\mathcal{A}}^m + \boldsymbol{\mathcal{H}}^m)\boldsymbol{v}^{m+1} = -\nabla p^{m+1} + \boldsymbol{\mathcal{S}}^m, & \text{(B.51)} \end{cases}$$

where $\boldsymbol{\mathcal{A}}^m$ and $\boldsymbol{\mathcal{H}}^m$ are diagonal and non-diagonal matrices, respectively. The matrix $\boldsymbol{\mathcal{S}}$ includes the source terms of the momentum equation, as well as other terms coming from Picard iterations or deferred corrections that can be computed explicitly in terms of $\boldsymbol{v}^n$. In the segregated algorithms, the iterative process is done defining pressure and velocity corrections:

$$p^{m+1} = p^m + p', \quad \boldsymbol{v}^{m+1} = \boldsymbol{v}^{m+1/2} + \boldsymbol{v}', \tag{B.52}$$

where $\boldsymbol{v}^{m+1/2}$ indicates an intermediate velocity field that does not satisfy the continuity equation. The methods differ on how the iteration process is done and the equations that are solved. The most popular ones are SIMPLE (§2.1.1), SIMPLEC (§2.1.2), and PISO (§2.1.3).

§2.1.1. SIMPLE

In each iteration of the SIMPLE algorithm (Semi-Implicit Method for Pressure-Linked Equations), an intermediate velocity field $\boldsymbol{v}^{m+1/2}$ is defined. It is obtained by solving Eq. (B.51) using the pressure gradient from the previous iteration:

$$(\boldsymbol{\mathcal{A}}^m + \boldsymbol{\mathcal{H}}^m)\boldsymbol{v}^{m+1/2} = -\nabla p^m + \boldsymbol{\mathcal{S}}^m, \tag{B.53}$$

and the subtraction of Eq. (B.53) from Eq. (B.51) gives:

$$(\boldsymbol{\mathcal{A}}^m + \boldsymbol{\mathcal{H}}^m)\boldsymbol{v}' = -\nabla p', \tag{B.54}$$

Then, $\boldsymbol{\mathcal{H}}^m$ is neglected in Eq. (B.54) (Patankar, 1980), and the velocity correction reads:

$$\boldsymbol{v}' = -(\boldsymbol{\mathcal{A}}^m)^{-1}\nabla p'. \tag{B.55}$$

Calculating $(\boldsymbol{\mathcal{A}}^m)^{-1}$ is a simple task because $\boldsymbol{\mathcal{A}}$ is a diagonal matrix. The substitution of Eq. (B.55) into Eq. (B.52) gives:

$$\boldsymbol{v}^{m+1} = \boldsymbol{v}^{m+1/2} - (\boldsymbol{\mathcal{A}}^m)^{-1}\nabla p', \tag{B.56}$$

and Eq. (B.56) is substituted into Eq. (B.50) to obtain the equation for the pressure correction:

$$\boldsymbol{\mathcal{C}}^m(\boldsymbol{v}^{m+1/2} - (\boldsymbol{\mathcal{A}}^m)^{-1}\nabla p') = 0. \tag{B.57}$$

After Eq. (B.57) is solved, $\boldsymbol{v}^{m+1}$ and p^{m+1} are obtained from Eq. (B.52), and the iterative process starts again once convergence is achieved.

§2.1.2. SIMPLEC

In the SIMPLEC algorithm (Semi-Implicit Method for Pressure-Linked Equations-Consistent), the methodology is the similar. Instead of considering that the non-diagonal matrix $\boldsymbol{\mathcal{H}}^m = 0$, it is replaced by a diagonal matrix $\boldsymbol{\mathcal{D}}^m$ (Van Doormaal and Raithby, 1984). The components of $\boldsymbol{\mathcal{D}}^m$ are the sum of the off-diagonal elements of $\boldsymbol{\mathcal{H}}^m$, and the velocity correction (Eq. (B.55)) becomes:

$$\boldsymbol{v}' = -(\boldsymbol{\mathcal{A}}^m + \boldsymbol{\mathcal{D}}^m)^{-1}\nabla p'. \tag{B.58}$$

§2.1.3. PISO

The neglection of the matrix $\boldsymbol{\mathcal{H}}^m$ in the SIMPLE algorithm implies that, in each iteration, Eq. (B.51) is equivalent to (Ferzinger et al., 2020):

$$\boldsymbol{\mathcal{A}}^m\boldsymbol{v}^{m+1} + \boldsymbol{\mathcal{H}}^m\boldsymbol{v}^{m+1/2} = -\nabla p^{m+1} + \boldsymbol{\mathcal{S}}^m. \tag{B.59}$$

The PISO algorithm (Pressure-Implicit with Splitting of Operators) considers SIMPLE as a predictor step, and a second correction is applied in each iteration (Issa, 1986):

$$p^{m+1} = p^m + p' + p'', \qquad \boldsymbol{v}^{m+1} = \boldsymbol{v}^{m+1/2} + \boldsymbol{v}' + \boldsymbol{v}''. \tag{B.60}$$

In PISO, the equation equivalent to Eq. (B.51) is:

$$\boldsymbol{\mathcal{A}}^m \boldsymbol{v}^{m+1} + \boldsymbol{\mathcal{H}}^m(\boldsymbol{v}^{m+1/2} + \boldsymbol{v}') = -\nabla p^{m+1} + \boldsymbol{\mathcal{S}}^m, \tag{B.61}$$

and the relationships between the second velocity and pressure corrections are obtained by subtracting Eq. (B.59) from Eq. (B.61):

$$\boldsymbol{\mathcal{A}}^m \boldsymbol{v}'' + \boldsymbol{\mathcal{H}}^m \boldsymbol{v}' = -\nabla p'' \longrightarrow \boldsymbol{v}'' = -(\boldsymbol{\mathcal{A}}^m)^{-1}(\boldsymbol{\mathcal{H}}^m \boldsymbol{v}' + \nabla p''), \tag{B.62}$$

Taking Eq. (B.62) into account, the equation for the pressure correction is obtained by substituting Eq. (B.60) into Eq. (B.50):

$$\boldsymbol{\mathcal{C}}^m \boldsymbol{\mathcal{A}}^m(\boldsymbol{\mathcal{H}}^m \boldsymbol{v}' - \nabla p') = 0. \tag{B.63}$$

In summary, the standard PISO algorithm is equal to the SIMPLE algorithm plus additional corrections. In the procedure explained above, only one additional correction for the velocity and the pressure has been defined, although the number of additional corrections can be increased.

§2.2. Coupled algorithms

In the coupled approach, the continuity and momentum equations are solved simultaneously (Darwish et al., 2009), while the remaining equations are solved separately in the same way as in the segregated solver. Since the velocity components and the pressure are considered as variables in the solution process, coupled solvers require more memory and more computing time in each iteration. The overall performance with respect to the segregated algorithms depends on the application.

§2.3. Extensions to compressible flow

When density is not constant, before the iterative process starts, the value is obtained from the equation of state before the equations are solved. In compressible flows, the implementation of the coupled algorithms is straightforward by substituting the update of velocity components by the update of mass fluxes in Fig. B.5b. The same modification applies to that part in Fig. B.5a.

In the segregated methods, the same procedure of the incompressible flow case is followed. The density is corrected in the same way as the pressure and velocity: $\rho^{m+1} = \rho^m + \rho'$, and the pressure-correction equation contains density corrections. The standard approach consists of assuming that the corrections are small. In each iteration, the momentum and energy equations are solved separately, which means that the temperature is constant when solving the pressure correction equation. In addition, the equation of state gives $\rho = \rho(p, T)$. Thus:

$$\rho' = \frac{\partial \rho}{\partial T}\cancelto{0}{T'} + \frac{\partial \rho}{\partial p} p' = \frac{\partial \rho}{\partial p} p', \tag{B.64}$$

and the value of $\partial\rho/\partial p$ is given by the equation of state. The speed of sound is $a = \sqrt{\partial p/\partial \rho|_s}$, where s is the specific entropy. The usual approximation is to consider $\partial\rho/\partial p|_T = \partial\rho/\partial p|_s$.

§3. Resolution of systems of linear algebraic equations

The reference methods for solving the systems of linear algebraic equations are presented in §3.1. Solution methodologies have been improved by combining those methods with additional techniques that lead to multigrid methods that are presented in §3.2. Some of the variant of these methods require additional modifications for stability improvement that are explained in §3.3.

§3.1. Iterative methods

The most-used methods in CFD are two iterative methods: Gauss-Seidel and incomplete lower upper decomposition. The reference linear algebraic system of equations is:

$$\boldsymbol{\mathcal{A}\Phi} = \boldsymbol{b}. \tag{B.65}$$

§3.1.1. Gauss-Seidel

The Gauss-Seidel method applied to Eq. (B.65) is defined by (Demmel, 1997):

$$\mathcal{A}_{i,i}\Phi_i^{m+1} = b_i - \sum_{j=1}^{i-1} \mathcal{A}_{i,j}\Phi_j^{m+1} - \sum_{j=i+1}^{n} \mathcal{A}_{i,j}\Phi_j^{m}, \quad i = 1, 2, \ldots, n \ , \tag{B.66}$$

For each row, the variable of the diagonal is solved as a function of the rest of the variables. The variables whose coefficients are below the diagonal correspond to the iteration $m+1$, while the rest correspond to the previous iteration m. The process done for all rows of the matrix is called a *sweep*, which can be done in backward and forward direction. The process is implemented numerically in terms of matrices. The matrix $\boldsymbol{\mathcal{A}}$ is expressed as the matrix sum:

$$\boldsymbol{\mathcal{A}} = \boldsymbol{\mathcal{D}} + \boldsymbol{\mathcal{L}} + \boldsymbol{\mathcal{U}}, \tag{B.67}$$

where $\boldsymbol{\mathcal{D}}$ is a diagonal matrix, $\boldsymbol{\mathcal{L}}$ is a strictly lower triangular matrix, and $\boldsymbol{\mathcal{U}}$ is a strictly upper triangular matrix. In terms of $\boldsymbol{\mathcal{D}}$, $\boldsymbol{\mathcal{L}}$, and $\boldsymbol{\mathcal{U}}$, Eq. (B.66) is:

$$(\boldsymbol{\mathcal{D}} + \boldsymbol{\mathcal{L}})\boldsymbol{\Phi^{m+1}} = \boldsymbol{b} - \boldsymbol{\mathcal{U}\Phi}^n \longrightarrow \boldsymbol{\Phi^{m+1}} = (\boldsymbol{\mathcal{D}} + \boldsymbol{\mathcal{L}})^{-1}(\boldsymbol{b} - \boldsymbol{\mathcal{U}\Phi}^n), \tag{B.68}$$

or equivalently:

$$(\boldsymbol{\mathcal{D}} + \boldsymbol{\mathcal{L}})\boldsymbol{\mathcal{D}}^{-1}(\boldsymbol{\mathcal{D}} + \boldsymbol{\mathcal{U}})(\boldsymbol{\Phi^{m+1}} - \boldsymbol{\Phi^{m}}) = \boldsymbol{b} - \boldsymbol{\mathcal{A}\Phi^{m}}. \tag{B.69}$$

§3.1.2. Incomplete lower upper decomposition

As will be shown in next sections, modern CFD codes solve the systems of linear algebraic equations by combining different approaches; in particular, methods such as the Gauss-Seidel are used up to a certain level of the residual value. Another popular method is the incomplete lower upper decomposition (ILU), where Eq. (B.69) is solved with a modification:

$$\boldsymbol{\tilde{\mathcal{A}}}(\boldsymbol{\Phi^{m+1}} - \boldsymbol{\Phi^{m}}) = \boldsymbol{b} - \boldsymbol{\mathcal{A}\Phi^{m}}, \tag{B.70}$$

with $\boldsymbol{\tilde{\mathcal{A}}}$ referring to an incomplete lower upper factorization of $\boldsymbol{\mathcal{A}}$, so that the approximation matrix $\boldsymbol{\tilde{\mathcal{A}}} - \boldsymbol{\mathcal{A}}$ satisfies certain constraints. The usual approach consists of eliminating certain non-diagonal elements to facilitate the calculation of $\boldsymbol{\tilde{\mathcal{A}}}^{-1}$ in Eq. (B.69) (Saad, 2003).

§3.2. Multigrid methods

The iterative methods for solving systems of linear algebraic equations such as the Gauss-Seidel method have a slow asymptotic convergence. Looking at the norm of the error of Eq. (B.65), $\boldsymbol{e}^m = ||\boldsymbol{\Phi^m} - \boldsymbol{\Phi}||$, it can be proved that the high-frequency errors are removed rapidly in a few iterations, while the low-frequency components take much more iterations to be removed (McCormick, 1987).

The key of multigrid methods is that the low-frequency components of the solution error become high-frequency in coarser meshes. Thus, Eq. (B.65) can be solved first in the original mesh to remove the high-frequency components; then, the low-frequency components are removed by performing additional iterations in a coarser mesh. This procedure gives a correction $\boldsymbol{\phi}$ to the solution of the original mesh as a result; finally, the solution is transferred back to the fine mesh. In that process, called *cycle*, the iterative solvers act as *smoothers*.

For a matrix $\boldsymbol{\mathcal{A}}$ of size $n \times n$, it can be shown that, while the computational cost of the iterative methods scales $\mathcal{O}(n^2)$, in the case of multigrid methods it is $\mathcal{O}(n)$ (McCormick, 1987). The transfer of the coefficients of the matrices between the meshes is done with the use of restriction $\boldsymbol{\mathcal{R}}$ and prolongation $\boldsymbol{\mathcal{P}}$ matrices. In what follows, the subindex h will refer to the fine mesh, and $2h$ to the coarse mesh. The simplest cycle is called *V-Cycle*, which consists of the following steps:

1. Realization of few iterations—usually less than 10—in $\boldsymbol{\mathcal{A}_h \Phi} = \boldsymbol{b_h}$ to obtain $\boldsymbol{\Phi_h}$.
2. Restriction of the residual $\boldsymbol{r_h} = \boldsymbol{b_h} - \boldsymbol{\mathcal{A}_h \Phi_h}$ to the coarse grid: $\boldsymbol{r_{2h}} = \boldsymbol{\mathcal{R} r_h}$.
3. Resolution of $\boldsymbol{\mathcal{A}_{2h} \phi_{2h}} = \boldsymbol{r_{2h}}$.
4. Prolongation of $\boldsymbol{\phi_{2h}}$ back to $\boldsymbol{\phi_h} = \boldsymbol{\mathcal{P} \phi_{2h}}$ to obtain the corrected solution $\boldsymbol{\Phi_h} + \boldsymbol{\phi_h}$.
5. Realization of few iterations in $\boldsymbol{\mathcal{A}_h \Phi} = \boldsymbol{b_h}$ using the corrected solution as initial guess.

The usual approach for computing the restriction and prolongation matrices is by piecewise constant interpolation, which leads to the identity $\boldsymbol{\mathcal{P}} = \boldsymbol{\mathcal{R}}^T$. The maximum computational performance is obtained by combining restriction and prolongation steps at different coarsening levels. This leads to different types of multigrid cycles (see Fig. B.6). The full multigrid cycle gives the lowest computational cost (Briggs et al., 2000).

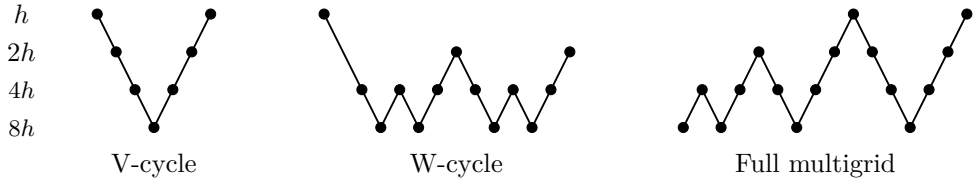

FIGURE B.6: Multigrid cycles (Briggs et al., 2000).

§3.2.1. Algebraic multigrid

In unstructured grids of complex geometries, deriving the $\boldsymbol{\mathcal{A}_{2h}}$ matrix is not straighforward. In addition, it requires significant amount of memory. A solution consists of approximating this matrix, which is the idea behind the Algebraic Multigrid (AMG) methods. The natural choice that follows variational principles is given by the *Galerkin projection* (Briggs et al., 2000):

$$\boldsymbol{\mathcal{A}_{2h}} = \boldsymbol{\mathcal{R} \mathcal{A}_h \mathcal{I}}. \tag{B.71}$$

§3.3. Under-relaxation

Apart from the stability limits of the temporal and spatial discretization methods, another limiting factor for the resolution of the Navier-Stokes equations is the stability properties of the iterative methods such as the Gauss-Seidel method. A sufficient condition for the convergence of this method is that the $\boldsymbol{\mathcal{A}}$ matrix is *diagonally dominant*, which means that:

$$|a_{ii}| = \sum_{\substack{j=1 \\ j \neq i}}^{n} |a_{ij}| \quad \forall i = 1, \ldots, n. \tag{B.72}$$

In the SIMPLE algorithm, the neglection of the off-diagonal elements in the pressure-correction equation is a restrictive approximation, and in many cases it leads to the divergence of the numerical method. The coupled algorithms also suffer from stability issues. A solution to improve the convergence in each iteration is to make use under-relaxation techniques, which are divided into two categories: explicit and implicit (Ferzinger et al., 2020).

In the explicit under-relaxation, the flow variables between successive iterations are limited:

$$\mathbf{\Phi}^{m+1} = \mathbf{\Phi}^{m} + \alpha_{\Phi}(\mathbf{\Phi}^{*} - \mathbf{\Phi}^{m}), \tag{B.73}$$

where α_{Φ} is the under-relaxation factor, and $\mathbf{\Phi}^{*}$ is the result obtained when solving Eq. (B.65).

In the implicit under-relaxation, there is no need of storing $\mathbf{\Phi}^{m}$ and $\mathbf{\Phi}^{*}$ in the memory at the same time. This technique consists of solving for Φ_P^{*} directly from Eq. (B.49):

$$\Phi_P^{*} = \frac{\sum_{NB} \mathcal{A}_{NB}\Phi_{NB} + b}{\mathcal{A}_P}, \tag{B.74}$$

and leads to the modified equation at node P:

$$\underbrace{\frac{\mathcal{A}_P}{\alpha_{\Phi}}}_{\mathcal{A}_P^{*}}\Phi_P^{m+1} + \sum_{NB}\mathcal{A}_{NB}\Phi_{NB}^{m+1} = \underbrace{b_P + \frac{1-\alpha_{\Phi}}{\alpha_{\Phi}}\mathcal{A}_P\Phi_P^{m}}_{b_P^{*}}, \tag{B.75}$$

where $\mathcal{A}_P^{*}$ and b_P^{*} are the modified main diagonal matrix and source term components. The under-relaxation increases the values in the diagonal components; therefore, it improves the convergence of iterative methods. Implicit and explicit under-relaxation are usually combined in the modern CFD codes. PISO and SIMPLEC are designed so that no under-relaxation is applied, although this implies the use of time steps that satisfy $Co = v_{\text{cell}}\Delta t / L_{\text{cell}} < 1$.

§3.3.1. Pseudo-transient

When a steady state is reached, another approach for improving the convergence of the iterative methods is based on physical principles. The idea of the pseudo-transient simulations is to consider the steady state solution as the one of an unsteady simulation for $t \to \infty$. The discretization of the time derivative with an Euler implicit method leads to the increase in the diagonal elements:

$$V_c\frac{\Phi_P^{m+1} - \Phi_P^{m}}{\Delta t} + \mathcal{A}_P^{*}\Phi_P^{m+1} + \sum_{NB}\mathcal{A}_{NB}\Phi_{NB}^{m+1} = b_P^{*}, \tag{B.76}$$

with $\Delta t = L_c / v_c$ referring to the pseudo time step that depends on the length and velocity scales L_c and v_c. A conservative L_c is obtained from the domain volume V_d and lengths L_x, L_y, and L_z:

$$L_c = \min[V^{1/3}, \max(L_x, L_y, L_z)], \tag{B.77}$$

while the velocity scale is the maximum velocity between the molecular diffusion, the maximum cell velocity in the domain, and the speed of sound (for compressible flows):

$$v_c = \max\left[\frac{\nu}{L_c}, U_{\text{cell}}^{\max}, a\right]. \tag{B.78}$$

The pseudo-transient approach combined with coupled algorithms has been verified to provide superior performance with respect to segregated algorithms in steady-state simulations.

§3.4. Residuals

In each iteration, the globally-scaled residual of Eq. (B.49) is defined as:

$$R_{\Phi}^{m} = \frac{\sum_{\text{cells } P}|\sum_{NB}\mathcal{A}_{NB}\Phi_{NB}^{m}|}{\sum_{\text{cells}P}|\mathcal{A}_p\Phi_p^{m}|}. \tag{B.79}$$

Other approaches to calculate the residuals include the local scaling, that replaces the fluxes of the denominator of Eq. (B.79) by the difference between the maximum and the minimum of Φ in the domain. Normalization of scaled or unscaled residuals is another approach, which consists of dividing those residuals by the maximum residual after a number of p iterations: $\overline{R}_{\Phi}^{m} = R_{\Phi}^{m}/R_{\Phi}^{p}$.

Bibliography

Abe, K. (2021). Detailed investigation of subgrid scale models in large-eddy simulation using high aspect-ratio grid spacing. *Physics of Fluids*, 33(115120). DOI: 10.1063/5.0070183.

Abu-Ghannam, B. J. and Shaw, R. (1980). Natural transition of boundary layers—the effects of turbulence, pressure gradient, and flow history. *Journal of Mechanical Engineering Science*, 22(5):213–228. DOI: 10.1243/JMES_JOUR_1980_022_043.

Achenbach, E. (1968). Distribution of local pressure and skin friction around a circular cylinder in cross-flow up to $Re = 5 \times 10^6$. *Journal of Fluid Mechanics*, 34(4):625–639. DOI: 10.1017/S0022112068002120.

Ahmed, S. R., Ramm, G., and Faltin, G. (1984). Some Salient Features of the Time-Averaged Ground Vehicle Wake. *SAE Transactions*, 93:473–503. DOI: 10.4271/840300.

ALICE Collaboration (2013). Technical Design Report for the Upgrade of the ALICE Inner Tracking System. Technical Report CERN-LHCC-2013-024, CERN.

ALICE Collaboration (2019). Letter of intent for an ALICE ITS Upgrade in LS3. Technical Report CERN-LHCC-2019-018, CERN.

ALICE Collaboration (2022). Letter of intent for ALICE 3: A next generation heavy-ion experiment at the LHC. Technical Report CERN-LHCC-2022-009, CERN.

Amani, Y., Takahashi, A., Chantrenne, P., Maruyama, S., Dancette, S., and Maire, E. (2018). Thermal conductivity of highly porous metal foams: Experimental and image based finite element analysis. *International Journal of Heat and Mass Transfer*, 122:1–10. DOI: 10.1016/j.ijheatmasstransfer.2018.01.050.

Ami Ahmadi, H., Variji, N., Kaabinejadian, A., Moghimi, M., and Siavashi, M. (2021). Optimal design and sensitivity analysis of energy storage for concentrated solar power plants using phase change material by gradient metal foams. *Journal of Energy Storage*, 35(102233). DOI: 10.1016/j.est.2021.102233.

Anderson, W. K. and Bonhaus, D. L. (1994). An implicit upwind algorithm for computing turbulent flows on unstructured grids. *Computers & Fluids*, 23(1):1–21. DOI: 10.1016/0045-7930(94)90023-X.

Ansys Inc. (2023a). *Ansys Fluent Theory Guide, 2023R1.*

Ansys Inc. (2023b). *Ansys Mechanical Theory Guide, 2023R1.*

Arndt, K., Augustin, H., Baesso, P., Berger, N., Berg, F., Betancourt, C., et al. (2021). Technical design of the phase I Mu3e experiment. *Nuclear Instruments and Methods in Physics Research Section A: Accelerators, Spectrometers, Detectors and Associated Equipment*, 1014(165679). DOI: 10.1016/j.nima.2021.165679.

ASM (1991). *ASM Handbook, Volume 2: Nonferrous Alloys and Special-Purpose Materials.* ASM International, 10th edition. DOI: 10.31399/asm.hb.v02.9781627081627.

ATLAS Collaboration (2012). Observation of a new particle in the search for the Standard Model Higgs boson with the ATLAS detector at the LHC. *Physics Letters B*, 716(1):1–29. DOI: 10.1016/j.physletb.2012.08.020.

ATLAS Collaboration (2017a). Technical Design Report for the ATLAS Inner Tracker Pixel Detector. Technical Report CERN-LHCC-2017-021, CERN.

ATLAS Collaboration (2017b). Technical Design Report for the ATLAS Inner Tracker Strip Detector. Technical Report CERN-LHCC-2017-005, CERN.

ATLAS Collaboration (2018). Observation of $h \to b\bar{b}$ decays and VH production with the ATLAS detector. *Physics Letters B*, 786:59–86. DOI: 10.1016/j.physletb.2018.09.013.

ATLAS Collaboration (2023). Combined measurement of the Higgs boson mass from the $h \to \gamma\gamma$ and $h \to zz^* \to 4\ell$ decay channels with the ATLAS detector using $\sqrt{s} = 7$, 8 and 13 tev pp collision data. Technical Report ATLAS-CONF-2023-037, CERN.

Avin, O., Raveh, D. E., Drachinsky, A., Ben-Shmuel, Y., and Tur, M. (2022). Experimental aeroelastic benchmark of a very flexible wing. *AIAA Journal*, 60(3):1745–1768. DOI: 10.2514/1.J060621.

Bacchetta, N., Collins, P., and Riedler, P. (2022). Tracking and vertex detectors at FCC-ee. *The European Physical Journal Plus*, 137(231). DOI: 10.1140/epjp/s13360-021-02323-w.

Barth, T. and Jespersen, D. (1989). The design and application of upwind schemes on unstructured meshes. In *27th Aerospace Sciences Meeting*. DOI: 10.2514/6.1989-366.

Bartholomew, P., Denner, F., Abdol-Azis, M. H., Marquis, A., and van Wachem, B. G. M. (2018). Unified formulation of the momentum-weighted interpolation for collocated variable arrangements. *Journal of Computational Physics*, 375:177–208. DOI: 10.1016/j.jcp.2018.08.030.

Batchelor, G. K. (2000). *An Introduction to Fluid Dynamics*. Cambridge University Press. DOI: 10.1017/CBO9780511800955.

Bathe, K. L. and Zhang, H. (2009). A mesh adaptivity procedure for CFD and fluid-structure interactions. *Computers & Structures*, 87(11):604–617. DOI: 10.1016/j.compstruc.2009.01.017.

Bazilevs, Y., Hsu, M. C., Zhang, Y., Wang, W., Liang, X., Kvamsdal, T., Brekken, R., and Isaksen, J. G. (2010). A fully-coupled fluid-structure interaction simulation of cerebral aneurysms. *Computational Mechanics*, 46:3–16. DOI:10.1007/s00466-009-0421-4.

Bear, J. (2018). *Modeling Phenomena of Flow and Transport in Porous Media*. Springer. DOI: 10.1007/978-3-319-72826-1.

Bernardini, M., Pirozzoli, S., and Orlandi, P. (2014). Velocity statistics in turbulent channel flow up to $Re_\tau = 4000$. *Journal of Fluid Mechanics*, 742:171–191. DOI: 10.1017/jfm.2013.674.

Bisplinghoff, R. L., Ashley, H., and Halfman, R. L. (2013). *Aeroelasticity*. Courier Corporation.

Bodart, J. and Larsson, J. (2012). Sensor-based computation of transitional flows using wall-modeled large eddy simulation. *Center for Turbulence Research Annual Briefs*, pages 229–240.

Bonaad, I. (2012). *Thermo-mechanical characterisation of low density carbon foams and composite materials for the ATLAS upgrade*. PhD thesis, University of Glasgow.

Bonnet, J. P., Topin, F., and Tadrist, L. (2008). Flow Laws in Metal Foams: Compressibility and Pore Size Effects. *Transport in Porous Media*, 73:233–254. DOI: 10.1007/s11242-007-9169-5.

Boomsma, K. and Poulikakos, D. (2001). On the effective thermal conductivity of a three-dimensionally structured fluid-saturated metal foam. *International Journal of Heat and Mass Transfer*, 44(4):827–836. DOI: 10.1016/S0017-9310(00)00123-X.

Bose, S. T. and Park, G. I. (2018). Wall-Modeled Large-eddy simulation for Complex Turbulent Flows. *Annual Review of Fluid Mechanics*, 50(1):535–561. DOI: 10.1146/annurev-fluid-122316-045241.

Boss, R. B. (1991). *Metallic Materials Specification Handbook*. Springer, 4th edition.

Bouchard, M., Marty, J., Deck, S., and Costes, M. (2022). Numerical investigation of self-sustained oscillations of stall cells around a leading edge-separating airfoil. *Physics of Fluids*, 34(11). DOI: 10.1063/5.0111550.

Boussinesq, J. (1877). *Essai sur la theorie des eaux courantes*. Imprimerie Nationale.

Bradshaw, P., Ferriss, D. H., and Atwell, N. P. (1967). Calculation of boundary-layer development using the turbulent energy equation. *Journal of Fluid Mechanics*, 28(3):593–616. DOI: 10.1017/S0022112067002319.

Brennen, C. E. (2005). *Fundamentals of Multiphase Flows*. Cambridge University Press. 10.1017/CBO9780511807169.

Bres, G. A., Bose, S. T., Emory, M., Ham, F. E., Schmidt, O. T., Rigas, G., and Colonius, T. (2018). Large-eddy simulations of co-annular turbulent jet using a Voronoi-based mesh generation framework. In *2018 AIAA/CEAS Aeroacoustics Conference*. DOI:10.2514/6.2018-3302.

Breuer, M. (2000). A challenging test case for large eddy simulation: high Reynolds number circular cylinder flow. *International Journal of Heat and Fluid Flow*, 21(5):648–654. DOI: 10.1016/S0142-727X(00)00056-4.

Breuer, M., De Nayer, G., Münsch, M., Gallinger, T., and Wüchner, R. (2012). Fluid–structure interaction using a partitioned semi-implicit predictor–corrector coupling scheme for the application of large-eddy simulation. *Journal of Fluids and Structures*, 29:107–130. DOI: 10.1016/j.jfluidstructs.2011.09.003.

Bridges, J. and Wernet, M. P. (2011). The NASA Subsonic Jet Particle Image Velocimetry (PIV) Dataset. Technical Report TM-2011-216807, NASA.

Bridges, J. E. and Wernet, M. P. (2021). Noise of Internally Mixed Exhaust Systems With External Plug For Supersonic Transport Applications. In *AIAA Aviation 2021 Forum*. DOI: 10.2514/6.2021-2218.

Briggs, W. L., Henson, V. E., and McCormick, S. F. (2000). *A Multigrid Tutorial, Second Edition*. Society for Industrial and Applied Mathematics, 2nd edition. DOI: 10.1137/1.9780898719505.

Brooks, N. R., Bottura, L., Perez, J. G., Dunkel, O., and Walckiers, L. (2008). Estimation of mechanical vibrations of the LHC fast magnetic measurement system. *IEEE Transactions on Applied Superconductivity*, 18(2):1617–1620. DOI: 10.1109/TASC.2008.921296.

Browne, O. M. F., Housman, J. A., Kenway, G. K., Ghate, A. S., and Kiris, C. C. (2023). Numerical investigation of $c_{L,max}$ Prediction on the NASA High-Lift Common Research Model. *AIAA Journal*, 61(4):1639–1658. DOI: 10.2514/1.J062508.

Bursnall, W. J. and Loftin, L. K. (1951). Experimental investigation of the pressure distribution about a yawed circular cylinder in the critical reynolds number range. Technical Report TN-2463, NACA.

Burton, T., Jenkins, N., Sharpe, D., and Bossanyi, E. (2011). *Wind Energy Handbook*. Wiley. DOI: 10.1002/9781119992714.

Butcher, J. C. (2016). *Numerical Methods for Ordinary Differential Equations*. Wiley, 3rd edition. DOI: 10.1002/9781119121534.

Calmidi, V. V. and Mahajan, R. L. (1999). The Effective Thermal Conductivity of High Porosity Fibrous Metal Foams. *Journal of Heat Transfer*, 121(2):466–471. DOI: 10.1115/1.2826001.

Calmidi, V. V. and Mahajan, R. L. (2000). Forced Convection in High Porosity Metal Foams. *International Journal of Heat and Mass Transfer*, 122(3):3781–3793. DOI: 10.1115/1.1287793.

Campbell, R. L. and Paterson, E. G. (2011). Fluid–structure interaction analysis of flexible turbomachinery. *Journal of Fluids and Structures*, 27(8):1376–1391. DOI: 10.1016/j.jfluidstructs.2011.08.010.

Campobasso, M. S., Castorrini, A., Cappugi, L., and Bonfiglioli, A. (2022). Experimentally validated three-dimensional computational aerodynamics of wind turbine blade sections featuring leading edge erosion cavities. *Wind Energy*, 25(1):168–189. DOI: 10.1002/we.2666.

Cantwell, B. and Coles, D. (1983). An experimental study of entrainment and transport in the turbulent near wake of a circular cylinder. *Journal of Fluid Mechanics*, 136:321–374. DOI: 10.1017/S0022112083002189.

CERN (2021). FAQ-LHC The Guide. Technical Report CERN-Brochure-2021-004-Eng.

Chaouat, B. (2017). The state of the art of hybrid RANS/LES modeling for the simulation of turbulent flows. *Flow, Turbulence and Combustion*, 99(2):279–327. DOI: 10.1007/s10494-017-9828-8.

Chien, K. Y. (1982). Predictions of Channel and Boundary-Layer Flows with a Low-Reynolds Number Turbulence Model. *AIAA Journal*, 20(1):33–38. DOI: 10.2514/3.51043.

Choi, H. and Moin, P. (2012). Grid-point requirements for large eddy simulation: Chapman's estimates revisited. *Physics of Fluids*, 24(011702). DOI: 10.1063/1.3676783.

Chávez-Modena, M., González, L. M., Valero, E., Broatch, A., García-Tíscar, J., and Felgueroso, A. (2023). Experimental and numerical methodology for the aero-thermal analysis of a SACOC heat exchanger. *Applied Thermal Engineering*, 219(119409). DOI: 10.1016/j.applthermaleng.2022.119409.

CMS Collaboration (2012). Observation of a new boson at a mass of 125 GeV with the CMS experiment at the LHC. *Physics Letters B*, 716(1):30–61. DOI: 10.1016/j.physletb.2012.08.021.

CMS Collaboration (2017). The Phase-2 Upgrade of the CMS Tracker. Technical Report CERN-LHCC-2017-009, CERN.

CMS Collaboration (2021). Evidence for Higgs boson decay to a pair of muons. *Journal of High Energy Physics*, 2021(1):1–68. DOI: 10.1007/JHEP01(2021)148.

Comte-Bellot, G. and Corrsin, S. (1971). Simple Eulerian time correlation of full-and narrow-band velocity signals in grid-generated, 'isotropic' turbulence. *Journal of Fluid Mechanics*, 48(2):273–337. DOI: 10.1017/S0022112071001599.

Conan, B., Anthoine, J., and Planquart, P. (2011). Experimental aerodynamic study of a car-type bluff body. *Experiments in Fluids*, 50:1273–1284. DOI: 10.1007/s00348-010-0992-z.

Contento, G., Oliviero, M., Bianco, N., and Naso, V. (2014). The prediction of radiation heat transfer in open cell metal foams by a model based on the Lord Kelvin representation. *International Journal of Heat and Mass Transfer*, 76:499–508. DOI: 10.1016/j.ijheatmasstransfer.2014.04.058.

Contin, G., Greiner, L., Schambach, J., Szelezniak, M., Anderssen, E., Bell, J., et al. (2018). The STAR MAPS-based PiXel detector. *Nuclear Instruments and Methods in Physics Research Section A: Accelerators, Spectrometers, Detectors and Associated Equipment*, 907:60–80. DOI: 10.1016/j.nima.2018.03.003.

Coquard, R. and Baillis, D. (2005). Modeling of Heat Transfer in Low-Density EPS Foams. *Journal of Heat Transfer*, 128(6):538–549. DOI: 10.1115/1.2188464.

Cornejo, A., Franci, A., Zárate, F., and Oñate, E. (2021). A fully Lagrangian formulation for fluid-structure interaction problems with free-surface flows and fracturing solids. *Computers & Structures*, 250(106532). DOI: 10.1016/j.compstruc.2021.106532.

Corson, D., Jaiman, R., and Shakib, F. (2009). Industrial application of RANS modelling: capabilities and needs. *International Journal of Computational Fluid dynamics*, 23(4):337–347. DOI: 10.1080/10618560902776810.

Craft, T. J., Launder, B. E., and Suga, K. (1996). Development and application of a cubic eddy-viscosity model of turbulence. *International Journal of Heat and Fluid Flow*, 17(2):108–115. DOI: 10.1016/0142-727X(95)00079-6.

Crosetto, P., Reymond, P., Deparis, S., Kontaxakis, D., Stergiopulos, N., and Quarteroni, A. (2011). Fluid–structure interaction simulation of aortic blood flow. *Computers & Fluids*, 43(1):46–57. DOI: 10.1016/j.compfluid.2010.11.032.

Dang, H., Yang, Z., and Li, Y. (2010). Accelerated loosely-coupled CFD/CSD method for nonlinear static aeroelasticity analysis. *Aerospace Science and Technology*, 14(4):250–258. DOI: 10.1016/j.ast.2010.01.004.

Darwish, M., Sraj, I., and Moukalled, F. (2009). A coupled finite volume solver for the solution of incompressible flows on unstructured grids. *Journal of Computational Physics*, 228(1):180–201. DOI: 10.1016/j.jcp.2008.08.027.

Davidson, L. (2006). Evaluation of the SST-SAS model: channel flow, asymmetric diffuser and axi-symmetric hill. In *European Conference on Computational Fluid Dynamics*. Springer.

Davidson, L. (2011). How to estimate the resolution of an LES of recirculating flow. In *Quality and Reliability of Large-Eddy Simulations II*, pages 269–286. Springer. DOI: 10.1007/978-94-007-0231-8_25.

de la Llave Plata, M., Lamballais, E., and Naddei, F. (2019). On the performance of a high-order multiscale DG approach to LES at increasing Reynolds number. *Computers & Fluids*, 194(104306). DOI: 10.1016/j.compfluid.2019.104306.

De Schampheleire, S., De Jaeger, P., Huisseune, H., Ameel, B., T'Joen, C., De Kerpel, K., and De Paepe, M. (2013). Thermal hydraulic performance of 10 PPI aluminium foam as alternative for louvered fins in an HVAC heat exchanger. *Applied Thermal Engineering*, 51(1):371–382. DOI: 10.1016/j.applthermaleng.2012.09.027.

de Vahl Davis, G. and Mallinson, G. (1976). An evaluation of upwind and central difference approximations by a study of recirculating flow. *Computers & Fluids*, 4(1):29–43. DOI: 10.1016/0045-7930(76)90010-4.

Deck, S., Duveau, P., d'Espiney, P., and Guillen, P. (2002). Development and application of Spalart–Allmaras one equation turbulence model to three-dimensional supersonic complex configurations. *Aerospace Science and Technology*, 6(3):171–183. DOI: 10.1016/S1270-9638(02)01148-3.

Deck, S. and Renard, N. (2020). Towards an enhanced protection of attached boundary layers in hybrid RANS/LES methods. *Journal of Computational Physics*, 400(108970). DOI: 10.1016/j.jcp.2019.108970.

Degroote, J., Bathe, K. L., and Vierendeels, J. (2009). Performance of a new partitioned procedure versus a monolithic procedure in fluid–structure interaction. *Computers & Structures*, 87(11):793–801. DOI: 10.1016/j.compstruc.2008.11.013.

Delany, N. K. and Sorensen, N. E. (1953). Low-speed Drag of Cylinders of Various Shapes. Technical Report TN-3038, NACA.

Della Torre, A., Montenegro, G., Tabor, G., and Wears, M. (2014). Cfd characterization of flow regimes inside open cell foam substrates. *International Journal of Heat and Fluid Flow*, 50:72–82. DOI: 10.1016/j.ijheatfluidflow.2014.05.005.

Demmel, J. (1997). *Applied Numerical Linear Algebra*. SIAM. DOI: 10.1137/1.9781611971446.

Di Girolamo, B., Boudagov, J. A., Lyablin, M. V., and Vlachos, S. (2021). The precision laser inclinometer. In *Proceedings of the 12th International Particle Accelerator Conference*. DOI: 10.18429/JACoW-IPAC2021-WEPAB281.

Dong, H., Xia, T., Chen, L., Liu, S., Cui, Y. D., Khoo, B. C., and Zhao, A. (2019). Study on flow separation and transition of the airfoil in low Reynolds number. *Physics of Fluids*, 31(10). DOI: 10.1063/1.5118736.

Dongellini, M., Naldi, C., Cancellara, S., and Morini, G. L. (2022). Experimental measurements of thermal-hydraulic performance of aluminum-foam water-to-air heat exchangers for a HVAC application. *Applied Thermal Engineering*, 213(118716). DOI: 10.1016/j.applthermaleng.2022.118716.

Dorf, R. and Bishop, R. (2016). *Modern Control Systems*. Pearson, 13th edition.

Dörr, P. C. and Kloker, M. J. (2017). Crossflow transition control by upstream flow deformation using plasma actuators. *Journal of Applied Physics*, 121(063303). DOI: 10.1063/1.4975791.

Dowell, E. H. and Hall, K. C. (2001). Modelling of Fluid-Structure Interaction. *Annual Review of Fluid Mechanics*, 33(1):445–490. DOI: 10.1146/annurev.fluid.33.1.445.

Dukhan, N. (2006). Correlations for the pressure drop for flow through metal foam. *Experiments in Fluids*, 41:665–672. DOI: 10.1007/s00348-006-0194-x.

Durbin, P. A. (1991). Near-wall turbulence closure modeling without damping functions. *Theoretical and Computational Fluid Dynamics*, 3:1–13. DOI: 10.1007/BF00271513.

Egorov, Y., Menter, F. R., Lechner, R., and Cokljat, D. (2010). The Scale-Adaptive Simulation Method for Unsteady Turbulent Flow Predictions. Part 2: Application to Complex Flows. *Flow, Turbulence and Combustion*, 85(1):139–165. DOI: 10.1007/s10494-010-9265-4.

Ekman, P., Wieser, D., Virdung, T., and Karlsson, M. (2020). Assessment of hybrid RANS-LES methods for accurate automotive aerodynamic simulations. *Journal of Wind Engineering and Industrial Aerodynamics*, 206:104301. DOI: 10.1016/j.jweia.2020.104301.

Englert, F. and Brout, R. (1964). Broken Symmetry and the Mass of Gauge Vector Mesons. *Physical Review Letters*, 13(9). DOI: 10.1103/PhysRevLett.13.321.

Evans, L. R. (2009). *The Large Hadron Collider: A Marvel of Technology*. EPFL Press.

Fage, A. (1930). Drag of Circular Cylinders and Spheres. Technical Report R & M 1370, Aeronautical Research Council.

Fares, E. and Schröder, W. (2005). A general one-equation turbulence model for free shear and wall-bounded flows. *Flow, Turbulence and Combustion*, 73:187–215. DOI: 10.1007/s10494-005-8625-y.

Ferzinger, J. H., Peric, M., and Street, R. (2020). *Computational Methods for Fluid Dynamics*. Springer, 4th edition. DOI: 10.1007/978-3-319-99693-6.

Fox, R. O. (2012). Large-Eddy-Simulation Tools for Multiphase Flows. *Annual Review of Fluid Mechanics*, 44(1):47–76. DOI: 10.1146/annurev-fluid-120710-101118.

Fröhlich, J. and von Terzi, D. (2008). Hybrid LES/RANS methods for the simulation of turbulent flows. *Progress in Aerospace Sciences*, 44(5):349–377. DOI: 10.1016/j.paerosci.2008.05.001.

Gaskell, P. H. and Lau, A. K. C. (1988). Curvature-compensated convective transport: SMART, a new boundedness-preserving transport algorithm. *International Journal for Numerical Methods in Fluids*, 8(6):617–641. DOI: 10.1002/fld.1650080602.

Germano, M., Piomelli, U., Moin, P., and Cabot, W. H. (1991). A dynamic subgrid-scale eddy viscosity model. *Physics of Fluids A: Fluid Dynamics*, 3(7):1760–1765. DOI: 10.1017/S0022112082001116.

Gilchriese, M., Miller, W., and Shih, W. (2012). New Proposed Foam Developments. *Berkeley meeting on tracker materials and FEA - LSWG*.

Girimaji, S. S. (2006). Partially-averaged Navier-Stokes model for turbulence: A Reynolds-averaged Navier-Stokes to direct numerical simulation bridging method. *Journal of Applied Mechanics*, 73(3):413–421. DOI: 10.1115/1.2151207.

Glück, M., Breuer, M., Durst, F., Halfmann, A., and Rank, E. (2001). Computation of fluid–structure interaction on lightweight structures. *Journal of Wind Engineering and Industrial Aerodynamics*, 89(14):1351–1368. DOI: 10.1016/S0167-6105(01)00150-7.

Godin, P., Zingg, D. W., and Nelson, T. E. (1997). High-Lift Aerodynamic Computations with One-and Two-Equation Turbulence Models. *AIAA Journal*, 35(2). DOI: 10.2514/2.113.

Godunov, S. K. and Bohachevsky, I. (1959). A difference method for numerical calculation of discontinuous solutions of the equations of hydrodynamics. *Matematičeskij Sbornik*, 47(3):271–306.

Grega, R., Krajňák, J., Žuľová, L., Fedorko, G., and Molnár, V. (2017). Failure analysis of driveshaft of truck body caused by vibrations. *Engineering Failure Analysis*, 79:208–215. DOI: 10.1016/j.engfailanal.2017.04.023.

Gritskevich, M. S., Garbaruk, A. V., Schütze, J., and Menter, F. R. (2012). Development of DDES and IDDES formulations for the $k - \omega$ shear stress transport model. *Flow, Turbulence and Combustion*, 88(3):431. DOI: 10.1007/s10494-011-9378-4.

Guinchard, M., Cabon, M., Charrondière, C., Develle, K., Fessia, P., Lacny, L., et al. (2018). Investigation and estimation of the LHC magnet vibrations induced by HL-LHC civil engineering activities. In *Proceedings of the 9th International Particle Accelerator Conference*. DOI: 10.18429/JACoW-IPAC2018-WEPMF080.

Gupta, G. (2010). Calculation of radiation length in materials. Technical Report PH-EP-Tech-Note-2010-013, CERN.

Hall, M. J. and Hiatt, J. P. (1996). Measurements of pore scale flows within and exiting ceramic foams. *Experiments in Fluids*, 20:433–440. DOI: 10.1007/BF00189382.

Han, J. C. (2014). Recent Studies in Turbine Blade Cooling. *International Journal of Rotating Machinery*, 10(517231). DOI: 10.1155/S1023621X04000442.

Han, Y., He, Y., and Le, J. (2020). Modification to Improved Delayed Detached-Eddy Simulation Regarding the Log-Layer Mismatch. *AIAA Journal*, 58(2):712–721. DOI: 10.2514/1.J058535.

Hanjalić, K. and Kenjereš, S. (2001). Simulation of Deterministic Eddy Structure in Flows Driven by Thermal Buoyancy and Lorentz Force. *Flow, Turbulence and Combustion*, 66:427–451. DOI: 10.1023/A:1013570705813.

Harten, A. (1983). High resolution schemes for hyperbolic conservation laws. *Journal of Computational Physics*, 49(3):357–393. DOI: 10.1016/0021-9991(83)90136-5.

Hauser, S., Robertson, M., Ijspeert, A., and Paik, J. (2017). JammJoint: A Variable Stiffness Device Based on Granular Jamming for Wearable Joint Support. *IEEE Robotics and Automation Letters*, 2(2):849–855. DOI: 10.1109/LRA.2017.2655109.

Higgs, P. W. (1964). Broken symmetries, massless particles and gauge fields. *Physics Letters*, 12(2):132–133. DOI: 10.1016/0031-9163(64)91136-9.

Holmes, D. and Connell, S. (1989). Solution of the 2D Navier-Stokes equations on unstructured adaptive grids. In *9th Computational Fluid Dynamics Conference*. DOI: 10.2514/6.1989-1932.

Hopcroft, M. A., Nix, W. D., and Kenny, T. W. (2010). What is the Young's Modulus of Silicon? *Journal of microelectromechanical systems*, 19(2):229–238. DOI: 10.1109/JMEMS.2009.2039697.

Hoyas, S. and Jiménez, J. (2006). Scaling of the velocity fluctuations in turbulent channels up to Re_τ=2003. *Physics of Fluids*, 18(1). DOI: 10.1063/1.2162185.

Hu, H., Weng, X., Zhuang, D., Ding, G., Lai, Z., and Xu, X. (2016). Heat transfer and pressure drop characteristics of wet air flow in metal foam under dehumidifying conditions. *Applied Thermal Engineering*, 93:1124–1134. DOI: 10.1016/j.applthermaleng.2015.09.019.

Iasiello, M., Bianco, N., Chiu, W. K. S., and Naso, V. (2020). Anisotropic convective heat transfer in open-cell metal foams: Assessment and correlations. *International Journal of Heat and Mass Transfer*, 154(119682). DOI: 10.1016/j.ijheatmasstransfer.2020.119682.

Inayat, A., Klumpp, M., Lämmermann, M., Freund, H., and Schwieger, W. (2016). Development of a new pressure drop correlation for open-cell foams based completely on theoretical grounds: Taking into account strut shape and geometric tortuosity. *Chemical Engineering Journal*, 287:704–719. DOI: 10.1016/j.cej.2015.11.050.

Incera Garrido, G., Patcas, F. C., Lang, S., and Kraushaar-Czarnetzki, B. (2008). Mass transfer and pressure drop in ceramic foams: A description for different pore sizes and porosities. *Chemical Engineering Science*, 63(21):5202–5217. DOI: 10.1016/j.ces.2008.06.015.

Issa, R. I. (1986). Solution of the implicitly discretised fluid flow equations by operator-splitting. *Journal of Computational Physics*, 62(1):40–65. DOI: 10.1016/0021-9991(86)90099-9.

Jacobs, R. G. and Durbin, P. A. (2001). Simulations of bypass transition. *Journal of Fluid Mechanics*, 428:185–212. DOI: 10.1017/S0022112000002469.

Jameson, A. (2022). *Computational Aerodynamics*. Cambridge University Press. DOI: 10.1017/9781108943345.

Jasak, H., Weller, H. G., and Gosman, A. D. (1999). High resolution NVD differencing scheme for arbitrarily unstructured meshes. *International Journal for Numerical methods in Fluids*, 31(2):431–449. DOI: 10.1002/(SICI)1097-0363(19990930)31:2

Jeong, J. and Hussain, F. (1995). On the identification of a vortex. *Journal of Fluid Mechanics*, 285:69–94. DOI: 10.1017/S0022112095000462.

Jones, L. E., Sandberg, R. D., and Sandham, N. D. (2008). Direct numerical simulations of forced and unforced separation bubbles on an airfoil at incidence. *Journal of Fluid Mechanics*, 602:175–207. DOI: 10.1017/S0022112008000864.

Jonsson, E., Riso, C., Lupp, C. A., Cesnik, C. E. S., Martins, J. R. R. A., and Epureanu, B. I. (2019). Flutter and post-flutter constraints in aircraft design optimization. *Progress in Aerospace Sciences*, 109(100537). DOI: 10.1016/j.paerosci.2019.04.001.

Kachanov, Y. S. and Levchenko, V. Y. (1984). The resonant interaction of disturbances at laminar-turbulent transition in a boundary layer. *Journal of Fluid Mechanics*, 138:209–247. DOI: 10.1017/S0022112084000100.

Kader, B. (1981). Temperature and concentration profiles in fully turbulent boundary layers. *International Journal of Heat and Mass Transfer*, 24(9):1541–1544. DOI: 10.1016/0017-9310(81)90220-9.

Kandlikar, S. G. (2012). History, Advances, and Challenges in Liquid Flow and Flow Boiling Heat Transfer in Microchannels: A Critical Review. *Journal of Heat Transfer*, 134(3). DOI: 10.1115/1.4005126.

Kays, W. M. (1994). Turbulent Prandtl Number—Where Are We? *Journal of Heat Transfer*, 116(2):284–295. DOI: 10.1115/1.2911398.

Keating, A. and Piomelli, U. (2006). A dynamic stochastic forcing method as a wall-layer model for large-eddy simulation. *Journal of Turbulence*, 7. DOI: 10.1080/14685240612331392460.

Kluge, A. (2022). ALICE - ITS3 — A bent, wafer-scale CMOS detector. *Nuclear Instruments and Methods in Physics Research Section A: Accelerators, Spectrometers, Detectors and Associated Equipment*, 1041(167315). DOI: 10.1016/j.nima.2022.167315.

Kolanoski, H. and Wermes, N. (2020). *Particle Detectors: Fundamentals and Applications*. Oxford University Press. DOI: 10.1093/oso/9780198858362.001.0001.

Kolmogorov, A. N. (1991). The local structure of turbulence in incompressible viscous fluid for very large Reynolds numbers. *Journal of Materials Science*, 434:9–13. DOI: 10.1098/rspa.1991.0075.

Kolmogorov, D. K., Hüppe, A., Menter, F., and Garbaruk, A. V. (2021a). Large Eddy Simulation with wall functions of Ahmed body. *Journal of Physics: Conference Series*, 2103(012213). DOI: 10.1088/1742-6596/2103/1/012213.

Kolmogorov, D. K., Menter, F., and Garbaruk, A. V. (2021b). On mesh requirements for large eddy simulation with wall functions. *Journal of Physics: Conference Series*, 2103(012212). DOI: 10.1088/1742-6596/2103/1/012212.

Kovács, R., Fehér, A., and Sobolev, S. (2022). On the two-temperature description of heterogeneous materials. *International Journal of Heat and Mass Transfer*, 194(123021). DOI: 10.1016/j.ijheatmasstransfer.2022.123021.

Kumar, P. and Topin, F. (2016). Thermal conductivity correlations of open-cell foams: Extension of Hashin–Shtrikman model and introduction of effective solid phase tortuosity. *International Journal of Heat and Mass Transfer*, 92:539–549. DOI: 10.1016/j.ijheatmasstransfer.2015.08.085.

Kuruneru, S. T. W., Vafai, K., Sauret, E., and Gu, Y. (2020). Application of porous metal foam heat exchangers and the implications of particulate fouling for energy-intensive industries. *Chemical Engineering Science*, 228(115968). DOI: 10.1016/j.ces.2020.115968.

Lacroix, M., Nguyen, P., Schweich, D., Huu, C. P., Savin-Poncet, S., and Edouard, D. (2007). Pressure drop measurements and modeling on SiC foams. *Chemical Engineering Science*, 62(12):3259–3267. DOI: 10.1016/j.ces.2007.03.027.

Lahooti, M., Bao, Y., D.Scott, Palacios, R., and Sherwin, S. J. (2023). LES/DNS fluid-structure interaction simulation of non-linear slender structures in *Nektar++* framework. *Computer Physics Communications*, 282(108528). DOI: 10.1016/j.cpc.2022.108528.

Landau, L. D. and Lifshitz, E. M. (1980). *The Classical Theory of Fields*. Elsevier, 4th edition.

Langtry, R. B. and Menter, F. R. (2009). Correlation-based transition modeling for unstructured parallelized computational fluid dynamics codes. *AIAA Journal*, 47(12):2894–2906. DOI: 10.2514/1.42362.

Langtry, R. B., Menter, F. R., Likki, S. R., Suzen, Y. B., Huang, P. G., and Völker, S. (2006). A Correlation-Based Transition Model Using Local Variables—Part II: Test Cases and Industrial Applications. *Journal of Turbomachinery*, pages 423–434. DOI: 10.1115/1.2184353.

Lardeau, S., Leschziner, M., and Zaki, T. (2012). Large eddy simulation of transitional separated flow over a flat plate and a compressor blade. *Flow, Turbulence and Combustion*, 88:19–44. DOI: 10.1007/s10494-011-9353-0.

Launder, B. E. and Morse, A. (1979). Numerical Prediction of Axisymmetric Free Shear Flows with a Reynolds Stress Closure. In *Turbulent Shear Flows I*, pages 279–294. DOI: 10.1007/978-3-642-46395-2_21.

Launder, B. E., Reece, G. J., and Rodi, W. (1975). Progress in the development of a Reynolds-stress turbulence closure. *Journal of Fluid Mechanics*, 68(3):537–566. DOI: 10.1017/S0022112075001814.

Launder, B. E. and Sharma, B. I. (1974). Application of the energy-dissipation model of turbulence to the calculation of flow near a spinning disc. *Letters in Heat and Mass Transfer*, 1(2):131–137. DOI: 10.1016/0094-4548(74)90150-7.

Launder, B. E. and Spalding, D. B. (1974). The numerical computation of turbulent flows. *Computer Methods in Applied Mechanics and Engineering*, 3(2):269–289. DOI: 10.1016/0045-7825(74)90029-2.

Lawson, S., Greenwell, D., and Quinn, M. K. (2016). Characterisation of buffet on a civil aircraft wing. In *54th AIAA Aerospace Sciences Meeting*. DOI: 10.2514/6.2016-1309.

Lehmkuhl, O., Houzeaux, G., Owen, H., Chrysokentis, G., and Rodriguez, I. (2019). A low-dissipation finite element scheme for scale resolving simulations of turbulent flows. *Journal of Computational Physics*, 390:51–65. DOI: 10.1016/j.jcp.2019.04.004.

Lehmkuhl, O., Rodríguez, I., Baez, A., Oliva, A., and Pérez-Segarra, C. D. (2013). On the large-eddy simulations for the flow around aerodynamic profiles using unstructured grids. *Computers & Fluids*, 84:176–189. DOI: 10.1016/j.compfluid.2013.06.002.

Leishman, J. G., Bhagwat, M. J., and Bagai, A. (2002). Free-Vortex Filament Methods for the Analysis of Helicopter Rotor Wakes. *Journal of Aircraft*, 39(5):759–775. DOI: 10.2514/2.3022.

Leonard, A. (1975). Energy Cascade in Large-Eddy Simulations of Turbulent Fluid Flows. In Frenkiel, F. N. and Munn, R. E., editors, *Turbulent Diffusion in Environmental Pollution*, volume 18 of *Advances in Geophysics*, pages 237–248. DOI: 10.1016/S0065-2687(08)60464-1.

Leonard, B. P. (1979). A stable and accurate convective modelling procedure based on quadratic upstream interpolation. *Computer Methods in Applied Mechanics and Engineering*, 19(1):59–98. DOI: 10.1016/0045-7825(79)90034-3.

Leonard, B. P. (1988). Simple high-accuracy resolution program for convective modelling of discontinuities. *International Journal for Numerical Methods in Fluids*, 8(10):1291–1318. DOI: 10.1002/fld.1650081013.

Leonard, B. P. (1991). The ULTIMATE conservative difference scheme applied to unsteady one-dimensional advection. *Computer Methods in Applied Mechanics and Engineering*, 88(1):17–74. DOI: 10.1016/0045-7825(91)90232-U.

LHCb Collaboration (2021). Observation of New Resonances Decaying to $j/\psi K^+$ and $j/\psi\phi$. *Physical Review Letters*, 127. DOI: 10.1103/PhysRevLett.127.082001.

Li, H. Y. and Leong, K. C. (2011). Experimental and numerical study of single and two-phase flow and heat transfer in aluminum foams. *International Journal of Heat and Mass Transfer*, 54(23):4904–4912. DOI: 10.1016/j.ijheatmasstransfer.2011.07.002.

Lien, F. S. and Kalitzin, G. (2001). Computations of transonic flow with the v^2–f turbulence model. *International Journal of Heat and Fluid Flow*, 22(1):53–61. DOI: 10.1016/S0142-727X(00)00073-4.

Lienhart, H., Stoots, C., and Becker, S. (2002). Flow and Turbulence Structures in the Wake of a Simplified Car Model (Ahmed Modell). In *New Results in Numerical and Experimental Fluid Mechanics III*, pages 323–330. Springer. DOI: 10.1007/978-3-540-45466-3_39.

Liu, H., Qu, Y., Gao, H., Xie, F., and Meng, G. (2024). Nonlinear aeroelastic fluid-structure-acoustic interaction analysis of a coupled composite panel with an acoustic cavity in supersonic flow. *Journal of Sound and Vibration*, 569(118086). DOI: 10.1016/j.jsv.2023.118086.

Liu, M. (2011). Computational study of convective–diffusive mixing in a microchannel mixer. *Chemical Engineering Science*, 66(10):2211–2223. DOI: 10.1016/j.ces.2011.02.036.

Lodato, G., Castonguay, P., and Jameson, A. (2014). Structural wall-modeled LES using a high-order spectral difference scheme for unstructured meshes. *Flow, turbulence and combustion*, 92:579–606. DOI: 10.1007/s10494-013-9523-3.

Lozano-Durán, A., Bose, S. T., and Moin, P. (2022). Performance of Wall-Modeled LES with Boundary-Layer-Conforming Grids for External Aerodynamics. *AIAA Journal*, 60(2):747–766. DOI: 10.2514/1.J061041.

Lozano-Durán, A. and Jiménez, J. (2014). Effect of the computational domain on direct simulations of turbulent channels up to Re_τ=4200. *Physics of Fluids*, 26(011702). DOI: 10.1063/1.4862918.

Lozovskiy, A., Olshanskii, M. A., and Vassilevski, Y. V. (2019). Analysis and assessment of a monolithic FSI finite element method. *Computers & Fluids*, 179:277–288. DOI: 10.1016/j.compfluid.2018.11.004.

Lund, T. S. (2003). The use of explicit filters in large eddy simulation. *Computers & Mathematics with Applications*, 46(4):603–616. DOI: 10.1016/S0898-1221(03)90019-8.

Malone, M. B. (1996). Turbulence model evaluation for free shear dominated flows. In *AIAA Fluid Dynamics Conference*. DOI: 10.2514/6.1996-2038.

Mancin, S., Zilio, C., Diani, A., and Rossetto, L. (2013). Air forced convection through metal foams: Experimental results and modeling. *International Journal of Heat and Mass Transfer*, 62:112–123. DOI: 10.1016/j.ijheatmasstransfer.2013.02.050.

Mangiarotti, F. J., Willering, G., Fiscarelli, L., Bajko, M., Bottura, L., Desbiolles, V., et al. (2022). Power test of the first two HL-LHC insertion quadrupole magnets built at CERN. *IEEE Transactions on Applied Superconductivity*, 32(6):1–5. DOI: 10.1109/TASC.2022.3157574.

Martin, H. (2002). The generalized Lévêque equation and its practical use for the prediction of heat and mass transfer rates from pressure drop. *Chemical Engineering Science*, 57(16):3217–3223. DOI: 10.1016/S0009-2509(02)00194-X.

Masolin, A., Bouchard, P. O., Martini, R., and Bernacki, M. (2013). Thermo-mechanical and fracture properties in single-crystal silicon. *Journal of Materials Science*, 48:979–988. DOI: 10.1007/s10853-012-6713-7.

McCormick, S. F. (1987). *Multigrid Methods*. SIAM. DOI: 10.1137/1.9781611971057.

McKeon, B. J., Zagarola, M. V., and Smits, A. J. (2005). A new friction factor relationship for fully developed pipe flow. *Journal of Fluid Mechanics*, 538:429–443. DOI: 10.1017/S0022112005005501.

Menon, S., Yeung, P. K., and Kim, W. W. (1996). Effect of subgrid models on the computed interscale energy transfer in isotropic turbulence. *Computers & Fluids*, 25(2):165–180. DOI: 10.1016/0045-7930(95)00036-4.

Menter, F. (2018). Stress-Blended Eddy Simulation (SBES)—A New Paradigm in Hybrid Rans-LES Modeling. In *Progress in Hybrid RANS-LES Modelling*, pages 27–37. Springer.

Menter, F. R. (1992). Influence of Freestream Values on $k - \omega$ Turbulence Model Predictions. *AIAA Journal*, 30(6):1657–1659. DOI: 10.2514/3.11115.

Menter, F. R. (1994). Two-Equation Eddy-Viscosity Turbulence Models for Engineering Applications. *AIAA Journal*, 32(8):1598–1605. DOI: 10.2514/3.12149.

Menter, F. R. and Egorov, Y. (2010). The Scale-Adaptive Simulation Method for Unsteady Turbulent Flow Predictions. Part 1: Theory and Model Description. *Flow, turbulence and combustion*, 85(1):113–138. DOI: 10.1007/s10494-010-9264-5.

Menter, F. R. and Kuntz, M. (2004). Adaptation of eddy-viscosity turbulence models to unsteady separated flow behind vehicles. In *The aerodynamics of heavy vehicles: trucks, buses, and trains*, pages 339–352. Springer. DOI: 10.1007/978-3-540-44419-0_30.

Menter, F. R., Matyushenko, A., Lechner, R., Stabnikov, A., and Garbaruk, A. (2022). An Algebraic LCTM Model for Laminar–Turbulent Transition Prediction. *Flow, Turbulence and Combustion*. DOI: 10.1007/s10494-022-00336-8.

Menter, F. R., Smirnov, P. E., Liu, T., and Avancha, R. (2015). A One-Equation Local Correlation-Based Transition Model. *Flow, Turbulence and Combustion*, 95:583–619. DOI: 10.1007/s10494-015-9622-4.

Micro-Epsilon (2023). confocalDT IFS2404 datasheet.

Mohmmed, A. O., Al-Kayiem, H. H., Ahmed, O., and Sabir, O. (2020). One-way coupled fluid–structure interaction of gas–liquid slug flow in a horizontal pipe: Experiments and simulations. *Journal of Fluids and Structures*, 97(103083). DOI: 10.1016/j.jfluidstructs.2020.103083.

Moin, P. and Kim, J. (1982). Numerical investigation of turbulent channel flow. *Journal of Fluid Mechanics*, 118:341–377. DOI: 10.1017/S0022112082001116.

Monteil, S. and Wilkinson, G. (2021). Heavy-quark opportunities and challenges at FCC-ee. *The European Physical Journal Plus*, 136(837). DOI: 10.1140/epjp/s13360-021-01814-0.

Mudawar, I., Bharathan, D., Kelly, K., and Narumanchi, S. (2009). Two-phase spray cooling of hybrid vehicle electronics. *IEEE Transactions on Components and Packaging Technologies*, 32(2):501–512. DOI: 10.1109/ITHERM.2008.4544399.

Mussgiller, A. (2016). The CMS Outer Tracker Detector for HL-LHC. In *International Workshop on Vertex Detectors*.

Nagano, Y. and Tagawa, M. (1990). An Improved $k - \varepsilon$ Model for Boundary Layer Flows. *Journal of Fluids Engineering*, 112(1):33–39. DOI: 10.1115/1.2909365.

Nagaya, S., Hirano, N., Naruse, M., Watanabe, T., and Tamada, T. (2012). Development of a high-efficiency conduction cooling technology for SMES coils. *IEEE Transactions on Applied Superconductivity*, 23(3). DOI: 10.1109/TASC.2012.2235751.

Ng, C. F. and Hui, C. K. (2008). Low frequency sound insulation using stiffness control with honeycomb panels. *Applied Acoustics*, 69(4):293–301. DOI: 10.1016/j.apacoust.2006.12.001.

Nicoud, F. and Ducros, F. (1999). Subgrid-Scale Stress Modelling Based on the Square of the Velocity Gradient Tensor Flow. *Flow Turbulence, and Combustion*, 62(3):183–200. DOI: 10.1023/A:1009995426001.

Nishizawa, S., Yashiro, H., Sato, Y., Miyamoto, Y., and Tomita, H. (2015). Influence of grid aspect ratio on planetary boundary layer turbulence in large-eddy simulations. *Geoscientific Model Development*, 8(10):3393–3419. DOI: 10.5194/gmd-8-3393-2015.

Norton, M. P. and Karczub, D. G. (2003). *Fundamentals of Noise and Vibration Analysis for Engineers*. Cambridge University Press.

Otter, A., Murphy, J., Pakrashi, V., Robertson, A., and Desmond, C. (2022). A review of modelling techniques for floating offshore wind turbines. *Wind Energy*, 25(5):831–857. DOI: 10.1002/we.2701.

Paek, J. W., Kang, B. H., Kim, S. Y., and Hyun, J. M. (2000). Effective Thermal Conductivity and Permeability of Aluminum Foam Materials. *International Journal of Thermophysics*, 21:453–464. DOI: 10.1023/A:1006643815323.

Palkin, E., Mullyadzhanov, R., Hadžiabdić, M., and Hanjalić, K. (2016). Scrutinizing URANS in shedding flows: the case of cylinder in cross-flow in the subcritical regime. *Flow, Turbulence and Combustion*, 97(4):1017–1046. DOI: 10.1007/s10494-016-9772-z.

Papagiannopoulos, G. A. and Hatzigeorgiou, G. D. (2011). On the use of the half-power bandwidth method to estimate damping in building structures. *Soil Dynamics and Earthquake Engineering*, 31(7):1075–1079. DOI: 10.1016/j.soildyn.2011.02.007.

Patankar, S. (1980). *Numerical Heat Transfer and Fluid Flow*. CRC Press. DOI: 10.1201/9781482234213.

Patankar, S. V., Liu, C. H., and Sparrow, E. M. (1977). Fully Developed Flow and Heat Transfer in Ducts Having Streamwise-Periodic Variations of Cross-Sectional Area. *Journal of Heat Transfer*, 99:180–186. DOI: 10.1115/1.3450666.

Patel, V. C., Rodi, W., and Scheuerer, G. (1985). Turbulence Models for Near-Wall and Low Reynolds Number Flows: A Review. *AIAA Journal*, 23(9):1308–1319. DOI: 10.2514/3.9086.

Peng, S. H., Davidson, L., and Holmberg, S. (1997). A modified low-Reynolds-number $k-\omega$ model for recirculating flows. *Journal of Fluids Engineering*, 119(4). DOI: 10.1115/1.2819510.

Perrot, C., Panneton, R., and Olny, X. (2007). Periodic unit cell reconstruction of porous media: Application to open-cell aluminum foams. *Journal of Applied Physics*, 101(113538). DOI: 10.1063/1.2745095.

Pety, S. J., Tan, M. H. Y., Najafi, A. R., Barnett, P. R., Geubelle, P. H., and White, S. R. (2017). Carbon fiber composites with 2D microvascular networks for battery cooling. *International Journal of Heat and Mass Transfer*, 115:513–522. DOI: 10.1016/j.ijheatmasstransfer.2017.07.047.

Phanikumar, M. S. and Mahajan, R. L. (2002). Non-Darcy natural convection in high porosity metal foams. *International Journal of Heat and Mass Transfer*, 45(18):3781–3793. DOI: 10.1016/S0017-9310(02)00089-3.

PHENIX Collaboration (2019). Creation of quark–gluon plasma droplets with three distinct geometries. *Nature Physics*, 15:214–220. DOI: 10.1038/s41567-018-0360-0.

Piomelli, U., Balaras, E., Pasinato, H., Squires, K. D., and Spalart, P. R. (2003). The inner–outer layer interface in large-eddy simulations with wall-layer models. *International Journal of Heat and Fluid Flow*, 24(4):538–550. DOI: 10.1016/S0142-727X(03)00048-1.

Pont, G., Brenner, P., Cinnella, P., and Robinet, J. C. (2018). High-order hybrid RANS/LES strategy for industrial applications. In *Direct and Large-Eddy Simulation X*, pages 313–319. Springer.

Pope, S. B. (2000). *Turbulent Flows*. Cambridge University Press.

Powell, A. (1958). On the Fatigue Failure of Structures due to Vibrations Excited by Random Pressure Fields. *The Journal of the Acoustical Society of America*, 30(12):1130–1135. DOI: 10.1121/1.1909481.

Rafelski, J. (2016). *Melting Hadrons, Boiling Quarks - From Hagedorn Temperature to Ultra-Relativistic Heavy-Ion Collisions at CERN*. Springer. DOI: 10.1007/978-3-319-17545-4.

Ramlau, R. and Niebsch, J. (2009). Imbalance Estimation Without Test Masses for Wind Turbines. *Journal of Solar Energy Engineering*, 131(1). DOI: 10.1115/1.3028042.

Rawal, S. P., Johnson, K. S., and Makowski, K. (2005). Multifunctional Carbon-Carbon Foam-Core Space Radiator Development. In *AIP Conference Proceedings 746, 3*. DOI: 10.1063/1.1867112.

Reddy, J. N. (2006). *Theory and Analysis of Elastic Plates*. CRC Press. DOI: 10.1201/9780849384165.

Rehman, T. and Ali, H. M. (2020). Experimental study on the thermal behavior of RT-35HC paraffin within copper and Iron-Nickel open cell foams: Energy storage for thermal management of electronics. *International Journal of Heat and Mass Transfer*, 146(118852). DOI: 10.1016/j.ijheatmasstransfer.2019.118852.

Rezaeiha, A., Montazeri, H., and Blocken, B. (2019a). CFD analysis of dynamic stall on vertical axis wind turbines using Scale-Adaptive Simulation (SAS): Comparison against URANS and hybrid RANS/LES. *Energy Conversion and Management*, 196:1282–1298. DOI: 10.1016/j.enconman.2019.06.081.

Rezaeiha, A., Montazeri, H., and Blocken, B. (2019b). On the accuracy of turbulence models for CFD simulations of vertical axis wind turbines. *Energy*, 180:838–857. DOI: 10.1016/j.energy.2019.05.053.

Rhie, C. M. and Chow, W. L. (1983). Numerical Study of the Turbulent Flow Past an Airfoil with Trailing Edge Separation. *AIAA Journal*, 21(11):1525–1532. DOI: 10.2514/3.8284.

Richardson, L. F. and Lynch, P. (2007). *Weather Prediction by Numerical Process*. Cambridge University Press, 2nd edition. DOI: 10.1017/CBO9780511618291.

Richter, T. (2013). A fully Eulerian formulation for fluid–structure-interaction problems. *Journal of Computational Physics*, 233:227–240. DOI: 10.1016/j.jcp.2012.08.047.

Rodi, W. (1991). Experience with two-layer models combining the $k-\varepsilon$ model with a one-equation model near the wall. In *AIAA 29th Aerospace Sciences Meeting*. DOI: 10.2514/6.1991-216.

Rodi, W. and Mansour, N. N. (1993). Low reynolds number $k-\varepsilon$ modeling with the aid of direct simulation data. *Journal of Fluid Mechanics*, 250:509–529. DOI: 10.1017/S0022112093001545.

Rolek, P., Bruni, S., and Carboni, M. (2016). Condition monitoring of railway axles based on low frequency vibrations. *International Journal of Fatigue*, 86:88–97. DOI: 10.1016/j.ijfatigue.2015.07.004.

Rossitto, G., Sicot, C., Ferrand, V., Borée, J., and Harambat, F. (2016). Influence of afterbody rounding on the pressure distribution over a fastback vehicle. *Experiments in Fluids*, 57(43). DOI: 10.1007/s00348-016-2120-1.

Rudzki, T. T., Aeschbacher, F. M., Deflorin, M., and Flucher, N. (2023). Successful cooling of a pixel tracker using gaseous helium: Studies with a mock-up and a detector prototype. *Nuclear Instruments and Methods in Physics Research Section A: Accelerators, Spectrometers, Detectors and Associated Equipment*, 168405. DOI: 10.1016/j.nima.2023.168405.

Ryzhakov, P. B., Rossi, R., Idelsohn, S. R., and Oñate, E. (2010). A monolithic lagrangian approach for fluid–structure interaction problems. *Computational Mechanics*, 446. DOI: 10.1007/s00466-010-0522-0.

Saad, J. (2003). *Iterative Methods for Sparse Linear Systems*. SIAM. DOI: 10.1137/1.9780898718003.

Sadeghi, E., Hsieh, S., and Bahrami, M. (2011). Thermal conductivity and contact resistance of metal foams. *Journal of Physics D: Applied Physics*, 44(12). DOI: 10.1088/0022-3727/44/12/125406.

Sagaut, P. (2006). *Large Eddy Simulation for Incompressible Flows*. Springer. DOI: 10.1007/b137536.

Scheffer, C. and Girdhar, P. (2004). *Practical Machinery Vibration Analysis & Predictive Maintenance*. Elsevier. DOI: 10.1016/B978-0-7506-6275-8.X5000-0.

Schewe, G. (1983). On the force fluctuations acting on a circular cylinder in crossflow from subcritical up to transcritical reynolds numbers. *Journal of Fluid Mechanics*, 133:265–285. DOI: 10.1017/S0022112083001913.

Schlichting, H. (1979). *Boundary Layer Theory*. McGraw-Hill, 7th edition.

Schwamborn, D. and Strelets, M. (2012). ATAAC – An EU-Project Dedicated to Hybrid RANS/LES Methods. In *Progress in Hybrid RANS-LES Modelling*, pages 59–75. Springer. DOI: 10.1007/978-3-642-31818-4.

Shangguan, W. B. and Lu, Z. H. (2004). Experimental study and simulation of a hydraulic engine mount with fully coupled fluid–structure interaction finite element analysis model. *Computers & Structures*, 82(22):1751–1771. DOI: 10.1016/j.compstruc.2004.05.017.

Sheta, E. F., Harrand, V. J., Thompson, D. E., and Strganac, T. W. (2002). Computational and experimental investigation of limit cycle oscillations of nonlinear aeroelastic systems. *Journal of Aircraft*, 39(1):133–141. DOI: 10.2514/2.2907.

Shur, M. L., Spalart, P. R., Strelets, M. K., and Travin, A. K. (2008). A hybrid RANS-LES approach with delayed-DES and wall-modelled LES capabilities. *International Journal of Heat and Fluid Flow*, 29(6):1638–1649. DOI: 10.1016/j.ijheatfluidflow.2008.07.001.

Shyy, W., Chen, M. H., Mittal, R., and Udaykumar, H. S. (1992). On the Suppression of Numerical Oscillations Using a Non-Linear Filter. *Journal of Computational Physics*, 102(1):49–62. DOI: 10.1016/S0021-9991(05)80004-X.

Slaughter, J., Moxey, D., and Sherwin, S. (2023). Large Eddy Simulation of an Inverted Multi-Element Wing in Ground Effect. *Flow, Turbulence and Combustion*, 110(4):917–944. DOI: 10.1007/s10494-023-00404-7.

Smagorinsky, J. (1963). General Circulation Experiments with the Primitive Equations. *Monthly Weather Review*, 91(3):99–164. DOI: 10.1175/1520-0493(1963)091<0099:GCEWTP>2.3.CO;2.

Smirnov, P. E. and Menter, F. R. (2009). Sensitization of the SST Turbulence Model to Rotation and Curvature by Applying the Spalart–Shur Correction Term. *Journal of Turbomachinery*, 131(4). DOI: 10.1115/1.3070573.

Smith, T. A. and Ventikos, Y. (2019). Boundary layer transition over a foil using direct numerical simulation and large eddy simulation. *Physics of Fluids*, 31(12). DOI: 10.1063/1.5126663.

Spalart, P. R. (2009). Detached-eddy simulation. *Annual Review of Fluid Mechanics*, 41(1):181–202. DOI: 10.1146/annurev.fluid.010908.165130.

Spalart, P. R. and Allmaras, S. R. (1992). A One-Equation Turbulence Model for Aerodynamic Flows. In *AIAA 30th Aerospace Sciences Meeting and Exhibit*. DOI: 10.2514/6.1992-439.

Spalart, P. R., Deck, S., Shur, M. L., Squires, K. D., Strelets, M. K., and Travin, A. (2006). A New Version of Detached-eddy Simulation, Resistant to Ambiguous Grid Densities. *Theoretical and Computational Fluid Dynamics*, 20(181). DOI: 10.1007/s00162-006-0015-0.

Spalart, P. R., Jou, W., Strelets, W. M., and Allmaras, S. (1997). Comments on the Feasibility of LES for Wings, and on a Hybrid RANS/LES Approach. In *Proceedings of the First AFOSR International Conference on DNS/LES*.

Spalding, D. B. (1972). A novel finite difference formulation for differential expressions involving both first and second derivatives. *International Journal for Numerical Methods in Engineering*, 4(4):551–559. DOI: 10.1002/nme.1620040409.

Speziale, C. G., Sarkar, S., and Gatski, T. B. (1991). Modelling the pressure–strain correlation of turbulence: an invariant dynamical systems approach. *Journal of Fluid Mechanics*, 227:245–272. DOI: 10.1017/S0022112091000101.

Spitzer, R. E. (1965). *Measurements of Unsteady Pressures and Wake Fluctuations for Flow Over a Cylinder at Supercritical Reynolds Number*. PhD thesis, California Institute of Technology. DOI: 10.7907/WT4K-6337.

Stein, K., Tezduyar, T., and Benney, R. (2003). Mesh moving techniques for fluid-structure interactions with large displacements. *Journal of Applied Mechanics*, 70(1):58–63. DOI: 10.1115/1.1530635.

Stich, G. D., Ghate, A. S., Housman, J. A., and Kiris, C. C. (2022). Wall Modeled Large Eddy Simulations for NASA's jet noise consensus database of single-stream, round, convergent jets. In *AIAA SCITECH 2022 Forum*.

Strelets, M. (2001). Detached Eddy Simulation of Massively Separated Flows. In *39th AIAA Aerospace Sciences Meeting and Exhibit*. DOI: 10.2514/6.2001-879.

Sullivan, P. P., McWilliams, J. C., and Moeng, C. H. (1994). A subgrid-scale model for large-eddy simulation of planetary boundary-layer flows. *Boundary-Layer Metheorology*, 71:247–276. DOI: 10.1007/BF00713741.

Swanson, R. C. and Turkel, E. (1992). On central-difference and upwind schemes. *Journal of Computational Physics*, 101(2):292–306. DOI: 10.1016/0021-9991(92)90007-L.

Sweby, P. K. (1984). High resolution schemes using flux limiters for hyperbolic conservation laws. *SIAM Journal on Numerical Analysis*, 21(5):995–1011. DOI: 10.1137/0721062.

Syrakos, A., Varchanis, S., Dimakopoulos, Y., Goulas, A., and Tsamopoulos, J. (2017). A critical analysis of some popular methods for the discretisation of the gradient operator in finite volume methods. *Physics of Fluids*, 29(127103). DOI: 10.1063/1.4997682.

Terracol, M. (2006). A zonal RANS/LES approach for noise sources prediction. *Flow, Turbulence and Combustion*, 77(1):161–184. DOI: 10.1007/s10494-006-9042-6.

Terracol, M. and Manoha, E. (2020). Wall-Resolved Large-eddy Simulation of a Three-Element High-Lift Airfoil. *AIAA Journal*, 58(2):517–536. DOI: 10.2514/1.J058340.

Thompson, D. J. (2008). A continuous damped vibration absorber to reduce broad-band wave propagation in beams. *Journal of Sound and Vibration*, 311(3):824–842. DOI: 10.1016/j.jsv.2007.09.038.

Thompson, K. W. (1987). Time dependent boundary conditions for hyperbolic systems. *Journal of Computational Physics*, 68(1):1–24. DOI: 10.1016/0021-9991(87)90041-6.

Thomson, W. (1887). On the division of space with minimum partitional area. *Acta Mathematica*, 11:121–134.

Tong, Z., Zhang, Y., Zhang, Z., and Hua, H. (2007). Dynamic behavior and sound transmission analysis of a fluid–structure coupled system using the direct-BEM/FEM. *Journal of Sound and Vibration*, 299(3):645–655. DOI: 10.1016/j.jsv.2006.06.063.

Townsend, S., R. Picelli, B., Stanford, and Kim, H. A. (2019). Structural Optimization of Platelike Aircraft Wings Under Flutter and Divergence constraints. *Progress in Aerospace Sciences*, 56(8). DOI: 10.2514/1.J056748.

Trilok, G., Kumar, K. K., Gnanasekaran, N., and Mobedi, M. (2022). Numerical assessment of thermal characteristics of metal foams of orderly varied pore density and porosity under different convection regimes. *International Journal of Thermal Sciences*, 172(107288). DOI: 10.1016/j.ijthermalsci.2021.107288.

Tschisgale, S., Löhrer, B., Meller, R., and Fröhlich, J. (2021). Large eddy simulation of the fluid–structure interaction in an abstracted aquatic canopy consisting of flexible blades. *Journal of Fluid Mechanics*, 916(A43). DOI: 10.1017/jfm.2020.858.

Uzun, A., Lyrintzis, A. S., and Blaisdell, G. A. (2004). Coupling of Integral Acoustics Methods with LES for Jet Noise Prediction. *International Journal of Aeroacoustics*, 3(4):297–346. DOI: 10.1260/1475472043499290.

Vallone, G., Anderssen, E., Boettcher, D. N., Claybaugh, T., Janda, M., and Veale, K. L. (2023). Mechanical Vibrations of the ATLAS ITk Structures Under Transportation Loads. In *Forum on Tracking Detector Mechanics*.

van Brummelen, E. H. (2011). Partitioned iterative solution methods for fluid–structure interaction. *International Journal for Numerical Methods in Fluids*, 65(1-3):3–27. DOI: 10.1002/fld.2465.

Van Doormaal, J. P. and Raithby, G. D. (1984). Enhancements of the SIMPLE method for predicting incompressible fluid flows. *Numerical Heat Transfer*, 7(2):147–163. DOI: 10.1080/01495728408961817.

van Driest, E. (1956). On Turbulent Flow Near a Wall. *Journal of the Aeronautical Sciences*, 23:1007–1011. DOI: 10.2514/8.3713.

Vaz, G., Mabilat, C., van der Wal, R., and Gallagher, P. (2007). Viscous Flow Computations on a Smooth cylinders: A Detailed Numerical Study With Validation. *International Conference on Offshore Mechanics and Arctic Engineering*, pages 849–860. DOI: 10.1115/OMAE2007-29275.

Viswanathan, K. (2004). Aeroacoustics of hot jets. *Journal of Fluid Mechanics*, 516:39–82. DOI: 10.1017/S0022112004000151.

Von Kármán, T. (1948). Progress in the Statistical Theory of Turbulence. *Proceedings of the National Academy of Sciences*, 34(11):530–539.

Vreman, A. W. (2004). An eddy-viscosity subgrid-scale model for turbulent shear flow: Algebraic theory and applications. *Physics of Fluids*, 16:3670–3681. DOI: 10.1063/1.1785131.

Wagner, J. L., Casper, K. M., Beresh, S. J., Hunter, P. S., Spillers, R. W., Henfling, J. F., and Mayes, R. L. (2015). Fluid-structure interactions in compressible cavity flows. *Physics of Fluids*, 27(6). DOI: 10.1063/1.4922021.

Wall, W. A., Genkinger, S., and Ramm, E. (2007). A strong coupling partitioned approach for fluid–structure interaction with free surfaces. *Computers & Fluids*, 36(1):169–183. DOI: 10.1016/j.compfluid.2005.08.007.

Walters, D. K. and Cokljat, D. (2008). A three-equation eddy-viscosity model for Reynolds-averaged Navier–Stokes simulations of transitional flow. *Journal of Fluids Engineering*, 130(12). DOI: 10.1115/1.2979230.

Wang, X., Zhang, J., Chen, Y., and Kuai, Z. (2023). Numerical study of rising Taylor bubbles driven by buoyancy and additional pressure. *International Journal of Multiphase Flow*, 159(104309). DOI: 10.1016/j.ijmultiphaseflow.2022.104309.

Wang, Y., Yu, Y., Jing, Z., Wang, C., Zhou, G., and Zhao, W. (2021). Thermal performance of lithium-ion batteries applying forced air cooling with an improved aluminium foam heat sink design. *International Journal of Heat and Mass Transfer*, 167(120827). DOI: 10.1016/j.ijheatmasstransfer.2020.120827.

Wanner, G. and Hairer, E. (1996). *Solving Ordinary Differential Equations II: Stiff and Differential-Algebraic Problems*. Springer, 2nd edition. DOI: 10.1007/978-3-642-05221-7.

Webb, R. L. and Chung, K. (2005). Two-Phase Flow Distribution to Tubes of Parallel Flow Air-Cooled Heat Exchangers. *Heat Transfer Engineering*, 26(4):3–18. DOI: 10.1080/01457630590916239.

Wieselsberger, C. (1922). New Data on the Laws of Fluid Resistance. Technical Report TN-84, NACA.

Wijesooriya, K., Mohotti, D., Amin, A., and Chauhan, K. (2021). Comparison between an uncoupled one-way and two-way fluid structure interaction simulation on a super-tall slender structure. *Engineering Structures*, 229(111636). DOI: 10.1016/j.engstruct.2020.111636.

Wilcox, D. C. (2006). *Turbulence Modeling for CFD*. DCW Industries, 3rd edition.

Wypych, G. (2022). *Handbook of Foaming and Blowing Agents*. ChemTec Publishing, 2nd edition.

Xu, C. Y., Zhang, T., Yu, Y. Y., and Sun, J. H. (2019). Effect of von Karman length scale in scale adaptive simulation approach on the prediction of supersonic turbulent flow. *Aerospace Science and Technology*, 86:630–639. DOI: 10.1016/j.ast.2019.01.030.

Yang, J., Sun, S. S., Du, H., Li, W. H., Alici, G., and Deng, H. X. (2014). A novel magnetorheological elastomer isolator with negative changing stiffness for vibration reduction. *Smart Materials and Structures*, 23(10). DOI: 10.1088/0964-1726/23/10/105023.

Yoder, D. A., DeBonis, J. R., and Georgiadis, N. J. (2015). Modeling of turbulent free shear flows. *Computers & Fluids*, 117:212–232. DOI: 10.1016/j.compfluid.2015.05.009.

Yoshizawa, A. (1986). Statistical theory for compressible turbulent shear flows, with the application to subgrid modeling. *Physics of Fluids*, 29(7):2152–2164. DOI: 10.1063/1.865552.

Younis, L. B. and Viskanta, R. (1993). Experimental determination of the volumetric heat transfer coefficient between stream of air and ceramic foam. *International Journal of Heat and Mass Transfer*, 36(6):1425–1434. DOI: 10.1016/S0017-9310(05)80053-5.

Yu, B., Tao, W. Q., Zhang, D. S., and Wang, Q. W. (2001). Discussion on numerical stability and boundedness of convective discretized scheme. *Numerical Heat Transfer: Part B: Fundamentals*, 40(4):343–365. DOI: 10.1080/104077901317091721.

Zarruk, G. A., Brandner, P. A., Pearce, B. W., and Phillips, A. (2014). Experimental study of the steady fluid–structure interaction of flexible hydrofoils. *Journal of Fluids and Structures*, 51:326–343. DOI: 10.1016/j.jfluidstructs.2014.09.009.

Zhang, F., Blanchot, G., Higginbotham, S., Honma, A., Kalogeropoulos, A., Kovacs, M., et al. (2022). Prototyping and qualification of 2S modules for the CMS Outer Tracker upgrade at the HL-LHC. *Journal of Instrumentation*, 17. DOI: 10.1088/1748-0221/17/05/C05019.

Zhang, H., Liu, L., Dong, M., and Sun, H. (2013). Analysis of wind-induced vibration of fluid–structure interaction system for isolated aqueduct bridge. *Engineering Structures*, 46:28–37. DOI: 10.1016/j.engstruct.2012.07.019.

Zhang, J., Shaw, A. D., Wang, C., Gu, H., Amoozgar, M., Friswell, M. I., and Woods, B. K. S. (2021). Aeroelastic model and analysis of an active camber morphing wing. *Aerospace Science and Technology*, 111(106534). DOI: 10.1016/j.ast.2021.106534.

Zhao, C. Y. (2012). Review on thermal transport in high porosity cellular metal foams with open cells. *International Journal of Heat and Mass Transfer*, 55(13):3618–3632. DOI: 10.1016/j.ijheatmasstransfer.2012.03.017.

Zienkiewicz, O. C., Taylor, R. L., and Zhu, J. Z. (2005). *The Finite Element Method: Its Basis and Fundamentals*. Elsevier. DOI: 10.1016/C2009-0-24909-9.

Šekutkovski, B., Kostić, I., Simonović, A., Cardiff, P., and Jazarević, V. (2016). Three-dimensional fluid–structure interaction simulation with a hybrid RANS–LES turbulence model for applications in transonic flow domain. *Aerospace Science and Technology*, 49:1–16. DOI: 10.1016/j.ast.2015.11.028.